# MULTI-SCALE TILT DEPTH ESTIMATION

Reece van Buren

A Dissertation submitted to the Faculty of Science, University of the Witwatersrand, Johannesburg, in fulfilment of the requirements for the Degree of Master of Science.

Johannesburg, 2013

## DECLARATION

I declare that this Dissertation is my own, unaided work. It is being submitted for the Degree of Master of Science at the University of the Witwatersrand, Johannesburg. It has not been submitted before for any degree or examination at any other University.

_____

(Signature of candidate)

_____ day of _____ 20_____ in _____

## ABSTRACT

Many an approach to the estimation of magnetic source depths from magnetic data has been investigated over the past half a century. These approaches have been shown to have particular strengths and weaknesses with few implemented on a wide scale, commercial basis. A review of many of the more popular, as well as a few of the more obscure methods, is presented within this work.

The history of multi-scale computation, with emphasis on its application to potential fields is summarized. A newly developed depth estimation technique dubbed Multi-Scale Tilt Depth Estimation is offered. The method has been shown to derive suitable depth estimates when applied to modelled data computed from a range of simple synthetic models. Sensitivity of the method to model type, dip, interference and noise has been tested. A number of mitigating strategies to improve and stabilize the method's performance have been proposed. Results of the successful application of the method to field datasets from the Bushveld Complex and surrounding areas in South Africa are shown. Code to execute the method, written in Matlab is offered in Appendix A. Figures of the application of the method to all synthetic models have been included in Appendix B and C.

A portion of this work has been presented at the South African Geophysical Association's 11$^{th}$ Biennial Technical Meeting and Exhibition in the form of verbal and poster presentations accompanied by a short paper which is included here in Appendix D.

## ACKNOWLEDGMENTS

I would like to thank all those who assisted in the conceptualisation, compilation and proofing of this dissertation, especially my supervisor, Gordon Cooper. A special thanks to my wife, Diana, for allowing me the time to complete the research and writing.

# TABLE OF CONTENTS

## LIST OF FIGURES

## NOMENCLATURE

**A(B)** – Indicates operation A applied to object B

**AS** – Analytic Signal amplitude

**CGS** – Centimeter-Gram-Second system of units

**CPS** – Center Point of Similarity

**FDST** – Finite Difference Similarity Transforms

**FFT** – Fast Fourier Transform

**HD** – Horizontal Derivative

**MSTD** – Multi-Scale Tilt Depth

**MSTDE** – Multi-Scale Tilt Depth Estimation

**nT** – nanotesla

**QSP** – Quasi-Singular Points

**RTP** – Pole-reduced total magnetic intensity

**SI** – Structural Index / SI system of units (Le Système International d'Unités)

**SPI** – Source Parameter Imaging

**T** – Tilt

**TMI** – Total Magnetic Intensity

**VD** – Vertical Derivative

# CHAPTER 1: INTRODUCTION

This study is concerned with the field of source depth estimation from magnetic data. Magnetic data, especially when acquired from an airborne platform, is the most common and widely employed geophysical technique in the exploration for economically viable deposits of both minerals and petroleum. This is primarily due to the low cost, high reliability of acquisition and the wealth of information derivable from airborne magnetic data. The estimation of source depth from such data is a long and intensely studied field due to a number of factors, namely, the significance of cover thickness (depth) on the economic viability of mineral deposits, its major contribution to the understanding of the regional geology of an area and the comparative computational efficiency of such estimation methods.

Herein, a newly developed source depth estimation method named, “Multi-Scale Tilt Depth Estimation” is presented. It is illustrated by application to synthetic data generated from applicable model types and its robustness and accuracy assessed in the presence of added noise and interfering regional signals. This method is also applied to observed data acquired over structures of known geometries.

## Werner Deconvolution

The concept of deriving source parameter information directly from measured field data was presented by Werner (1953). In this landmark work he presented a mathematical framework for the parameter estimation of thin, thick and multiple sheets; the common occurrence of magnetic geologic elements in this geometry was given as justification of the usefulness of the method. The pre-existing alternatives to this method made use of characteristic points (i.e. minimum, maximum and inflection points) on the anomaly curve, most of which were approximations.

**Werner deconvolution reviewed**

Pasteka (2000) includes a review of Werner and Euler deconvolution as well as the Total Normalized Gradient method. Before commencing with the details of each method, a review of inverse methods is presented in order to contextualize the nature of the problems faced. A short reference is made to the theoretical non-uniqueness of potential field sources which is related to the instability of inversion algorithms. In essence, small perturbations in the resultant potential field may be generated by large reorganizations of the source distributions. This is one of the characteristics of ill-posed problems, which may violate any of the three following conditions of well-posed problems:

- There exists a solution
- The solution is unique
- The solution is stable

An exact solution to the specific problem may easily not exist due to measurement errors in the observed data or due to the limited number of model types that may be solved for. Due to inversion belonging to the set of ill-posed problems, the solution approach is based on regularization, introduced by Tikhonov (1963). However, this solution approach does require the introduction of supplementary conditions (often referred to as norms) in order to stabilize the solution.

The first of the three methods described by Pasteka is that of Werner deconvolution. He reiterates the two principal problems that Werner sought to solve, namely the separation of the anomaly from the background signal and the consideration of the whole anomaly, not only the few characteristic points. Equation 1.1 describes the potential for sheet-like bodies upon which the Werner method is based:

$$\Delta \boldsymbol{T} = \frac{\boldsymbol{A}(\boldsymbol{x} - \boldsymbol{x_0}) + \boldsymbol{B}\boldsymbol{z_0}}{(\boldsymbol{x} - \boldsymbol{x_0})^2 + \boldsymbol{z_0}^2} \quad 1.1$$

where $A$ and $B$ are functions of magnetization and geometry as follows:

$$\boldsymbol{A} = -2\boldsymbol{b}\left(\boldsymbol{M_x}\boldsymbol{sin}(\boldsymbol{I}) + \boldsymbol{M_z}\boldsymbol{cos}(\boldsymbol{I})\boldsymbol{sin}(\boldsymbol{a})\right) \quad 1.2$$

$$\boldsymbol{B} = 2\boldsymbol{b}\left(-\boldsymbol{M_x}\boldsymbol{cos}(\boldsymbol{I})\boldsymbol{sin}(\boldsymbol{a}) + \boldsymbol{M_z}\boldsymbol{sin}(\boldsymbol{I})\right) \quad 1.3$$

where $M_x$ and $M_z$ are the vector components of the magnetization, $2b$ represents the thickness and $I$ and $a$ are the magnetic inclination and profile azimuth respectively.

Equation 1.1 is then reformulated by substitution as follows:

$$\boldsymbol{x}^2\Delta\boldsymbol{T} = \boldsymbol{a_0} + \boldsymbol{a_1}\boldsymbol{x} + \boldsymbol{b_0}\Delta\boldsymbol{T} + \boldsymbol{b_1}\boldsymbol{x}\Delta\boldsymbol{T} \quad 1.4$$

which allows the unknowns to be found using four or more points of the curve and subsequently related to the original unknowns (source parameters). The strength of the method lies in its ability to solve for the dip and susceptibility requiring only the assumption of zero remanence.

The background signal removal is addressed by the addition of an interference polynomial (P) to the right side of the original formulation (Werner, 1953):

$$\boldsymbol{P} = \boldsymbol{C_0} + \boldsymbol{C_1}\boldsymbol{x} + \cdots + \boldsymbol{C_n}\boldsymbol{x}^{\boldsymbol{n}} \quad 1.5$$

which translates into an equation involving not only $a_0 + a_1 x$, but $a_0 + a_1 x + \cdots + a_i x^i$. The author quotes a number of published sources when it is stated that a polynomial of order two is sufficient for most purposes, implying that the solved equation is now in seven unknowns $a_0 - a_4, b_0 \& b_1$. Pasteka presents solutions derived with the 4, 5, 6, 7 & 8-point operators, illustrating the improvement in spatial resolving power due to the effective higher order residual. There may be scope here to include higher order terms on the left of the equation (or subtracted from the right) in order to compensate for high frequency noise inevitably present within observed data. An explanation of the applicability of Werner deconvolution to contacts (or thick dyke-like features) follows. Pasteka highlights the intuitive arguments made by Hartman et al. (1971), and the formal derivation thereof by Ku et al. (1983), that by applying the Werner method to the horizontal derivative of the field, depths may be derived for contacts as opposed to the intended dyke-type. Pasteka ends the section on Werner by summarizing the five most important points to consider when applying the method, namely:

- factors affecting the stability of the operator, size, length and step, small operators leading to overestimated depths and vice versa with optimal operators giving the most focused solutions
- attempting to solve for geometries that are ill-suited to the method, i.e. not dikes or contacts
- the correct use of the interference polynomial as in equation 1.5 and its poor results when used to remove the effects of depth limited structures
- the influence of shallow anomalies on the estimates of deeper structures stating that if the effect of the shallow source is less than one tenth of the deeper then both are resolved, although with increased uncertainty
- and finally, the influence of noise, which is similar to the previous point but with varying solution approaches being filtering of the data

and possible ‘controlled filtering’ suggested by Jain (1976) where solutions derived from the application to unfiltered and filtered data are compared and solutions that differ greatly are rejected. Figure 1 illustrates the effect of incorporating the interference polynomial on the solution distribution.

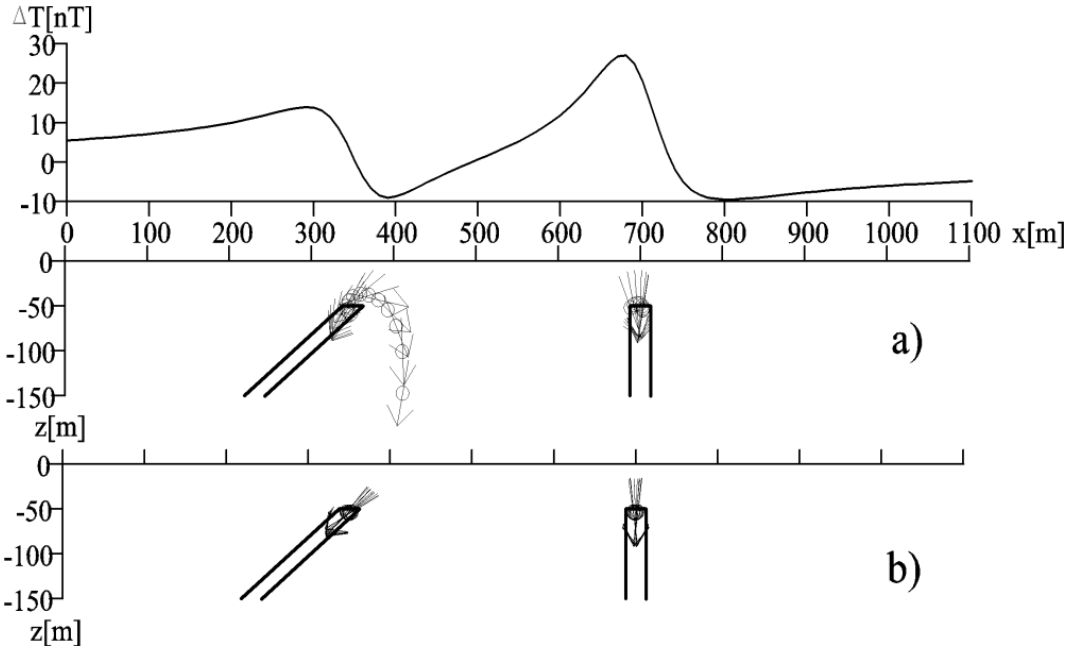


**Figure 1. Extracted from Pasteka (2000) Figure 4, this shows the solutions derived over dyke-like structures with (b) and without (a) the interference polynomial terms.**

### 3D multiple source Werner deconvolution

Hansen shows that the matrix form of the Nabighian et al. (2001) Euler equations is in fact a statement of the single-source 3D Werner equation. Hansen then goes about generalizing this to multiple sources by beginning with the proof for the two-source case and generalizing to many sources by an inductive proof. As with the multiple-source Euler algorithm, the solution is conducted in two steps, the first being a linear least-squares fit providing data for the second, nonlinear, but tractable solution which generalizes the process of finding the roots of a complex polynomial. The advantage that Werner has over the Euler implementation is that it has the

ability to solve for many sources, with subsequent truncation providing solutions to a small finite number. The practical implementation is however dependent on analytically derived orthogonalization tables which limit the number of sources per window to five, which is conjectured to be adequately large for any dataset.

## Euler Deconvolution

### First mention of Euler's equation applied to depth estimation

Breiner (1962) compiles a review of the uses of magnetic derivatives in geophysical interpretation. The third part of his review addresses the conundrum of quantitative applications and, in particular, to magnetic source depth determination. He states that "if" the potential can be described by a homogenous function it will satisfy Euler's theorem on homogeneous functions. This is the earliest reference found to Euler's equation being used to solve this problem. He presents Euler's equation and comments on a number of characteristic points for each of its terms i.e. where either the positions or derivatives are zero, providing simplifications of the original equation. Stated explicitly, this is a method for solving the system of equations when more than one variable is independent. The scheme involves the evaluation of the equation at various points producing a set of straight lines (e.g. in z and n), the solution being at the intersection of these lines. The analytic equivalent of solving simultaneous equations is also presented.

### The computerization of Euler depth estimation

Thompson (1982) published a well referenced paper on the determination of magnetic source depths using an algorithm named EULDPH. The approach utilised the previously reported Euler homogeneity equation in

conjunction with the structural index term in order to solve for the depths of simple sources. It is stressed in this work that the EULDPH technique does not assume a particular geologic model and that the results of the application can be interpreted usefully even though the simple models may not properly represent the actual source geology. Thompson notes that at this point in time, the EULDPH method was the only method which could be directly applied to gridded magnetic data.

The theory of the method commenced with the original homogeneity condition:

$$\boldsymbol{f(tx, ty, tz) = t^n f(x, y, z)} \quad 1.6$$

The original form of Euler's homogeneity equation is then presented:

$$\boldsymbol{x\frac{\partial f}{\partial x} + y\frac{\partial f}{\partial y} + z\frac{\partial f}{\partial z} = nf} \quad 1.7$$

The final form of this equation, presented as equation 6 in the original paper, makes the assumption that the transverse gradient is zero. This is the case if, as with other methods at the time, the source is 2D, or if the field is simply symmetric about the profile. This simplified form was presented as follows:

$$\boldsymbol{x_0\frac{\partial \Delta T}{\partial x} + z_0\frac{\partial \Delta T}{\partial z} = x\frac{\partial \Delta T}{\partial x} + N\Delta T(x)} \quad 1.8$$

Many comments on the performance of the method are made in the original paper, but little elaboration on mitigating usage is put forward. These mitigating strategies were presented in more detail by later authors on the topic. Examples of the performance limitations acknowledged for

the method include limitations due to unknown regional signal contribution and the improved performance ($x, y$ location) at higher structural indices even though the depth estimates are worse. Thompson does comment on a number of the mitigating strategies presented by later authors and he suggests:

- the use of multiple indices (five were presented) to determine the optimal selection
- the addition of a constant term to the definition of the field
- the use of over-determined equation sets to improve the stability of the method when multiple sources contribute to the anomalous field
- and incorporating the standard deviation ($\sigma_z$) of the solution depths as an error estimate.

These conditions, collectively referred to as acceptance criteria, are determined empirically and it is suggested that these are to be relaxed relative to the solved depth. A minimum tolerance value (TOL) of 20 is suggested where:

$$\boldsymbol{TOL = \frac{z_0}{N\sigma_z}} \qquad 1.9$$

Thompson also compares the accuracy of the depth estimates when conducted on total intensity and on pole-reduced data. He noted that the pole-reduced data returns shallower estimates, and considering that Thompson (1973) illustrated the overestimating tendency of the simple model solution approach, it is conjectured that the pole-reduced solutions were more accurate. The comparison of these estimated depths was suggested as a method to determine whether the sources were 2D in nature and/or remanent. Figure 2, from Thompson (1982) shows the variation in solution distribution with a variety of structural indices.

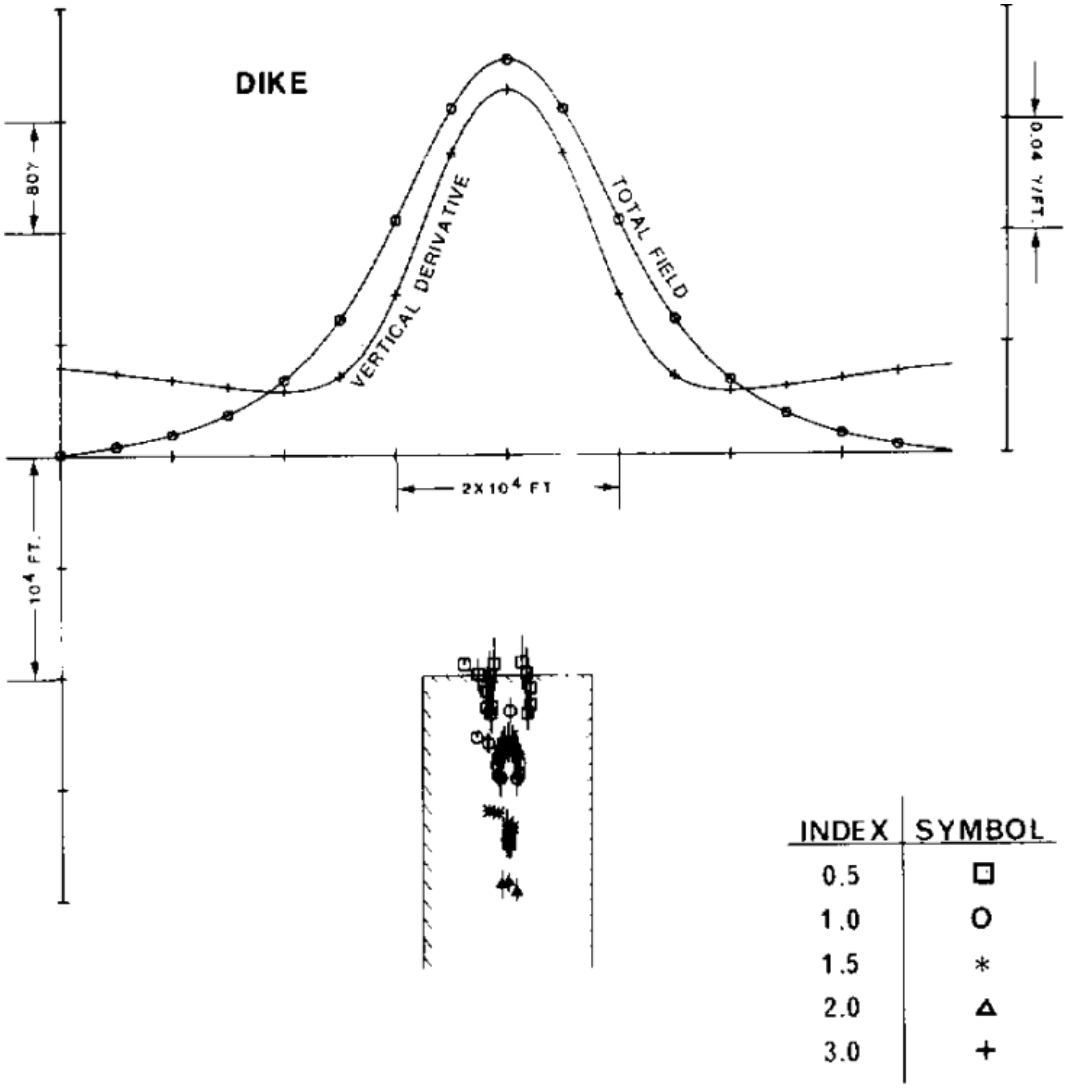


**Figure 2. Extracted from Thompson (1982), this figure shows the response of Euler deconvolution to an anomaly due to a 2D dyke.**

## Euler deconvolution formalised

After EULDPH was described by Thompson (1982), its implementation to gridded data (in 3D) was described by Reid et al. (1990) and dubbed the method “Euler deconvolution”. In this paper they show their moving window solution strategy and comment upon the correct use of the Structural Index (SI). They describe an equation to be used in the zero SI case for non-zero offsets and illustrate that a SI chosen too small will lead to depths that are too shallow and vice versa. They also note that for correctly chosen SI values, the solutions are more precise, but that higher

values of the SI produce more focused solutions. This suggests that a choice of SI higher than the correct value may lead to more focused trends even though the absolute depth estimates may be incorrect. Comment is made that, contrary to Thompson's (1982) preferences to work with pole-reduced data, the method returns accurate source positions despite its application to the TMI, illustrating its independence of the field direction. They further show that the method is also independent of dip and strike of the magnetic feature, leading to the realization that the method cannot return any dip information. An attempt is also made to suggest selection criteria enabling the separation of higher and lower accuracy solutions. Two significant applications of the technique are proposed, structural delineation and accurate depth estimation. The trade-off between these is suggested to be a result of the strength of the criteria. Figure 3 (Reid, 1990) shows the Euler solution distribution when applied to 2D data.

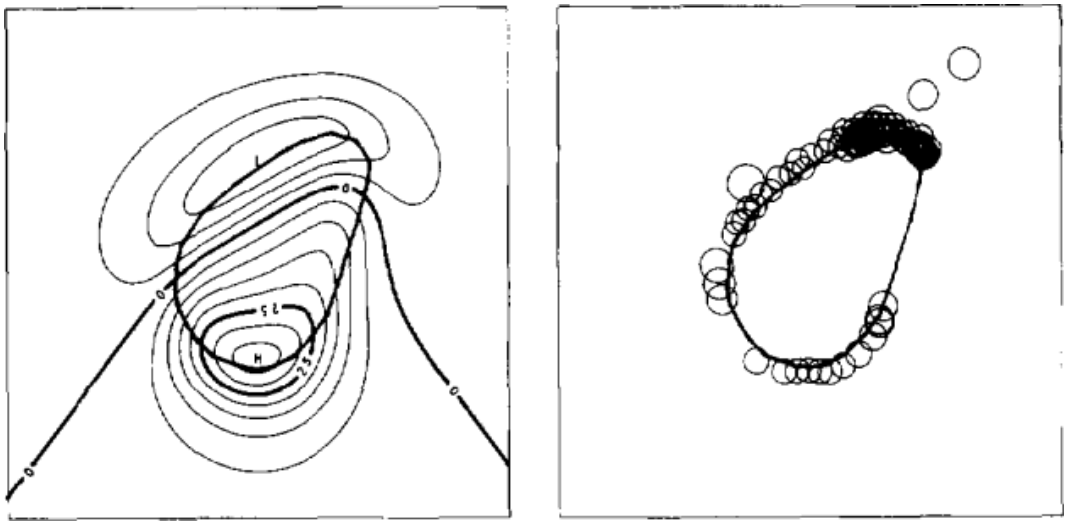

**Figure 3. Extracted from Reid (1990) Figure 1, the illustration shows the implementation of Euler deconvolution to the mapping of the extent of magnetic sources. This figure shows the outline of the source along with the computed magnetic intensity and Euler solutions.**

### 3D Euler deconvolution

The two-dimensional version of Euler deconvolution defined by Thompson (1982) is easily extended to three dimensions and was alluded to in his 1982 paper. Around this time this extension was becoming increasingly useful due to the ever increasing use of tight line-spaced airborne magnetic surveys. From such surveys, gridded products of sufficient quality could be produced to warrant the use of automated techniques such as Euler deconvolution. The extension was published by Reid et al. (1990) and suggests an algorithm comprising a number of steps in order to arrive at a set of good solutions. Herein they state the error in the use of a SI of 0.5 for a contact model as suggested by Thompson (1982) and the resulting overestimation of the depth. Reid et al. also suggest a method for empirically determining the optimal SI by solving for a range of values and then making use of the most well focussed set of solutions for each feature. They do not propose any technique for automating this selection. Due to the method's ability to treat gridded data, various advantages are presented, shown by the application to field data and illustrating the use of the 3D Euler deconvolution method in delineating structures in plan, as well as determining the structure depth. It is suggested that the numerous selection criteria are varied in order to achieve optimal results for both structure delineation and depth determination.

### Extended Euler deconvolution

Mushayandebvu et al. (1999) develop the method of Euler deconvolution further and introduce Extended Euler deconvolution for 2D structures. This method makes use of the relationship of potential fields when rotated. The rotated forms of the differential equations pair the $x$ differences with the derivative in the $z$ direction and vice versa. Making use of these relations, and if the field properties are known, the dip and susceptibility contrast of

the contact or dyke can be found, assuming no remanent magnetization. The original and rotated forms are as follows:

$$(\boldsymbol{x}-\boldsymbol{x_0})\frac{\boldsymbol{\partial M}}{\boldsymbol{\partial x}}+(\boldsymbol{z}-\boldsymbol{z_0})\frac{\boldsymbol{\partial M}}{\boldsymbol{\partial z}}=\boldsymbol{\alpha} \quad 1.10$$

$$(\boldsymbol{z}-\boldsymbol{z_0})\frac{\boldsymbol{\partial M}}{\boldsymbol{\partial x}}+(\boldsymbol{x}-\boldsymbol{x_0})\frac{\boldsymbol{\partial M}}{\boldsymbol{\partial z}}=\boldsymbol{\beta} \quad 1.11$$

**Multi-source Euler deconvolution**

Hansen (2000) presents a mathematically rigorous derivation of a multi-source implementation of the Euler deconvolution method. The derivation is made for the 2D source case, after which the method is extended to 3D and then by an inductive proof to many sources. In order to arrive at a useful form of the equation, motivation was sought from the multi-source Werner deconvolution of Hansen and Simmonds (1993) which implemented the Hilbert transform. $x, z$ and the potential are then represented in complex form, along with the use of the Hilbert transform in order to arrive at a generalized multi-source form of the equations. A further constraint which is not implicitly required by standard Euler deconvolution is that the field satisfy Laplace's equation as well as being homogeneous. A restriction is imposed by an assumption that the sources produce fields of equal degree of homogeneity. The final solution also requires a higher order derivative per source making the deconvolution of many sources extremely sensitive to noise.

In solving for the required parameters, they state that in principal, the system may be solved directly by using a nonlinear optimization scheme. However, due to their experience with other such problems, chose to seek a solution making use of a two-stage solution, linear least-squares fitting followed by a less trivial nonlinear search for coordinates from the parameters solved for in the least-squares step. This nonlinear step was

attempted using a number of approaches but one was more suited to the exact problem. It possesses the ability to solve for all of the roots of the equation simultaneously and ensures the roots separate, thereby aiding the definitions of all of the roots in the presence of highly dominant roots. An added functionality is the ability to define an error covariance for each solution position.

**Euler deconvolution applied to the analytic signal**

Keating et al. (2004) investigate the application of Euler deconvolution to the analytic signal. Deconvolution of the analytic signal is analogous to Euler deconvolution of the magnetic field with a background field. Because the analytic signal computation essentially removes the background field (long wavelengths), the deconvolution can solve for both depth and structural index of the magnetic source. Keating et al. mention that Huang et al. (1995) show that if a function is homogenous of degree N, then its analytic signal is also homogenous, and of degree N+1. They proceed to reference verifications of this property for simple models (2D contacts, sheets and horizontal cylinders). Equations are presented to solve for the dip and susceptibility contrast (or susceptibility-thickness product) once the depth and structural index are found. They also note that the depth may be obtained by the ratio of the analytic signal to its vertical gradient. This is a re-statement of equations 7a-d of Salem et al. (2003). Reid et al. (1990) propose making use of the relative error in the depths calculated in order to attribute a confidence rating to the solution from each moving window. Keating et al. (2004) extend this notion by including a similar term for the structural indices.

**Analytic Euler deconvolution**

The AN_EUL method, proposed by Salem (2003), makes use of orthogonal derivatives of the Euler equation and of its first vertical derivative.

Following definitions of the analytic signal by Roest et al. (1992) and Debeglia and Corpel (1997), the amplitude of the $n^{th}$-order derivative analytic signal is restated as follows:

$$|\boldsymbol{AAS_n}(\boldsymbol{x},\boldsymbol{y})| = \sqrt{\left(\frac{\boldsymbol{\partial T_n^z}}{\boldsymbol{\partial x}}\right)^{\boldsymbol{2}} + \left(\frac{\boldsymbol{\partial T_n^z}}{\boldsymbol{\partial y}}\right)^{\boldsymbol{2}} + \left(\frac{\boldsymbol{\partial T_n^z}}{\boldsymbol{\partial z}}\right)^{\boldsymbol{2}}} \quad 1.12$$

Two equations are derived for the epi-centroid ($x = x_0, y = y_0, z = 0$):

$$\boldsymbol{z_0}|\boldsymbol{AAS_1}| = (\boldsymbol{\eta} + \boldsymbol{1})|\boldsymbol{AAS_0}| \quad 1.13$$

$$\boldsymbol{z_0}|\boldsymbol{AAS_2}| = (\boldsymbol{\eta} + \boldsymbol{2})|\boldsymbol{AAS_1}| \quad 1.14$$

From these two relationships the following can be shown:

$$\boldsymbol{\eta} = \frac{\boldsymbol{2}|\boldsymbol{AAS_1}|^{\boldsymbol{2}} - |\boldsymbol{AAS_2}||\boldsymbol{AAS_1}|}{|\boldsymbol{AAS_2}||\boldsymbol{AAS_0}| - |\boldsymbol{AAS_1}|^{\boldsymbol{2}}} \quad 1.15$$

$$\boldsymbol{z_0} = \frac{|\boldsymbol{AAS_1}||\boldsymbol{AAS_0}|}{|\boldsymbol{AAS_2}||\boldsymbol{AAS_0}| - |\boldsymbol{AAS_1}|^{\boldsymbol{2}}} \quad 1.16$$

therefore illustrating that the depth and structural index of the source may be calculated at the epi-centroid. The only restriction of this being that it

requires the computation of third order derivatives of the magnetic field which make it more sensitive to high frequency noise. Results of the application of this method to synthetic and field data are presented and an attempt made to estimate the validity of the solutions by making use of various upward continued versions of the field. Solutions were derived from each of the upward continuation levels and the stability of these assessed in order to determine the optimal continuation level. There is potential to derive an algorithm in order to automatically vary the chosen continuation level across a survey based on the local solution statistics.

**Unification of Werner and Euler deconvolution**

Nabighian et al. (2001) state that the equations of Mushayandebvu et al. (1999) are identical to those of Hansen et al. (1993), therefore for a structural index of zero, the extended Euler deconvolution method is that of Werner deconvolution and therefore generalizes it. They then, for the case where the index is non-zero, show that the rotated form of the Euler equation can be rewritten in the same form as the original Euler equation. This is done by making use of the Hilbert transform pairs of the field derivatives as defined by Nabighian (1972), which is also applicable to the case where the index is zero. The generalized relation is therefore as follows:

$$(\boldsymbol{x}-\boldsymbol{x_0})\frac{\boldsymbol{\partial M}}{\boldsymbol{\partial x}}+(\boldsymbol{z}-\boldsymbol{z_0})\frac{\boldsymbol{\partial M}}{\boldsymbol{\partial z}}+\boldsymbol{nM}=\boldsymbol{\alpha} \qquad 1.17$$

$$(\boldsymbol{x}-\boldsymbol{x_0})\frac{\boldsymbol{\partial H(M)}}{\boldsymbol{\partial x}}+(\boldsymbol{z}-\boldsymbol{z_0})\frac{\boldsymbol{\partial H(M)}}{\boldsymbol{\partial z}}+\boldsymbol{nH(M)}=\boldsymbol{\beta} \qquad 1.18$$

This form implies that provided the field is homogenous with Euler index $n$, then its Hilbert transform is too. The form of the equation is also derived for the 3D case which simply includes the respective $y$ terms and extends

Werner deconvolution to 3D. Benefits of making use of this form include improved stability due to the availability of three equations at each point, and the insensitivity of this form to the constant portion of the field as the Hilbert transform of a constant is zero.

**Euler deconvolution reviewed**

Following on from the review of the Werner method in Pasteka (2000), focus is shifted to the original formulation of Euler deconvolution. A review is presented of the original derivations of the method and the dependence upon the correct usage of the structural index. Stavrev (1997) tabulates ideal SI values and reference is made to the degrees of freedom in each model type. Attention is then given to the correct value for the structural index of a step in gravimetry. This is a topic that has drawn much scrutiny by a number of the leading authors in this field. Reference is made to the accepted value of $N = 1$, derived by Reid et al. (1990) and widely used thereafter (e.g. Keating, 1998). Pasteka states that he disagrees with the interpretation of the result considering that the generally accepted result from model studies would have the value as $N = -1$ which is impossible as this would imply an increase in the field amplitude with distance. A derivation in the style of Reid et al. (1990) ($N = 1$) is followed but is compared in the case of a vertically thin step to a sill of zero thickness having a structural index of zero ($N = 0$). He therefore suggests a study of the behaviour of the solution as the thickness tends to zero. Due to each of the terms on the right of his formula tending to zero as the thickness approaches zero, the result is:

$$\lim_{z_0 - z_1 \to 0} (N) = 0 \qquad 1.19$$

which is in agreement with the accepted result for a sill. Due to the response from a finite step being the sum of the responses from two

singularities, it is not homogeneous and therefore violates the conditions upon which the Euler method is based (homogeneity and a single singular point). An equation is then presented which accounts for the thickness of a finite step:

$$\boldsymbol{g(x,z) = 2G\rho\left[(z-z_t)(\Phi_0-\Phi_u) + (x-x_0)\ln\frac{R_u}{R_0}\right] - 2G\rho\Phi_u\Delta t} \quad 1.20$$

The second term in equation 1.20 reflects the contribution from the lower edge. The right hand side of the equation may be rewritten in Thompson's form. In this form, the field ($f$) is replaced by $f(x,y,z) - B$, where $B$ represents a constant regional. An important substitution is made hereafter, the $B$ term being replaced by the interference polynomial used in Werner deconvolution. Therefore $f(x,y,z) - B$ becomes:

$$\boldsymbol{f(x,y,z) + A_0 + A_1x + A_2x^2 + \ldots} \quad 1.21$$

The significance of the interference polynomial when applied to gravity data is emphasized by the Taylor series expansion of the second term in equation 1.20:

$$\boldsymbol{-2G\rho\Phi_u\Delta t = -2G\rho\Delta t\left(\frac{\pi}{2} + arctan\frac{x}{z_T}\right) \approx} \quad 1.22$$
$$-2G\rho\Delta t\left(\frac{\pi}{2} + \frac{x}{z_T} + \left(\frac{x}{z_T}\right)^3 + \ldots\right)$$

Pasteka draws a similarity between this form and the interference polynomial providing justification for its use. He states that model studies

have shown the use of a third order expansion to be of use in focusing solutions around the upper contact of the step. The solution strategy adopted is that of least squares and is identical to that of the Werner case when the interference polynomial is used; an additional benefit being the covariance matrix allowing the solution confidence to be assessed.

**Selection criteria**

Fitzgerald et al. (2004) propose a number of new selection criteria in order to cull spurious solutions. Instead of focusing simply on one implementation of the Euler algorithm, they make use of the original Euler algorithm, recast in the form of Nabighian et al. (2001) along with the two forms of the extended Euler equation which incorporate the Hilbert transforms of the field in two orthogonal directions (here $Hx$ and $Hy$). These three equations solved within a square, moving kernel of 5 by 5 up to 10 by 10 cells produce 75 – 300 equations with 6 unknowns. Due to the incorporation of the additional equations the solution clustering is improved, however culling is still required. The discrimination techniques proposed make use of the increased number of parameters solved for to impose additional constraints on the solution set.

They state the existing criteria to be:

1) Rejection of estimated depth error/depth greater than a threshold
2) Solutions falling outside the convolution window
3) Solutions falling outside the observed survey data
4) Signal strength lower than a threshold
5) Spatial binning/selection of solutions
6) Low pass filtering prior to deconvolution
7) Rejection based on reliability (derived from the least-squares technique)

They suggest a number of additions to this list:

8) Rejection of bodies with inadmissible SI

9) Rejection of bodies with an SI of no interest
10) Rejection on the basis of the singularity ratio (derived from the least-squares technique)
11) Co-variance of the XY equations within the convolution window above a threshold
12) Rejection if SI error is above a threshold
13) Rejection based on histogram analysis of local parameters
14) Clustering of solutions (already proposed, see point 5 above)
15) Rejection if solution vector dips too shallowly
16) Rejection based on α and β values
17) Downward continuation to enhance anomalies

They conclude with an interesting observation that due to the non-homogeneity of the gravity anomaly over an infinite step, Euler deconvolution is merely an approximation, but when the Hilbert transform pairs are included the quality of the solutions improve. They also note that the uncertainty in depth estimates is a poor discriminator of quality.

**Cluster analysis**

The approach adopted by Ugalde et al. (2008) is one of clustering the solutions derived from any depth estimation routine. Therefore this method operates within the solution space and has no a-priori knowledge of the data. In order to achieve the desired clustered output, a two-step approach is used, the first being the application of a 3D kernel density distribution. Once the solution set has been classified in terms of its density, the second step of clustering is conducted using the method of Balasko et al. (2005), the outputs of which are eigenvectors and eigenvalues. The eigenvectors are used directly to derive the orientation of each cluster, while the eigenvalues relate to the overall density of the cluster which may further be utilized as a discriminator.

**Degrees of homogeneity**

A rigorous proof of the degrees of homogeneity associated with simple models is presented by Stavrev et al. (2007). The formal derivation is conducted for the gravity field of point, line, surface and solid mass distributions, after which the degrees for the magnetic field are inferred due to the illustrated congruency of the forms of the equations. By analysing the applicable degree of homogeneity ($n_k$) for derivatives of order $k$ of the potentials, they show that the degree of the derivative is decreased by the order $k$ from the degree of the original potential:

$$\boldsymbol{n_k = n_0 - k}, \qquad \boldsymbol{where\ k = 0, 1, 2, \ldots} \tag{1.23}$$

This is applicable not only to integer order derivatives but can be generalized by the definition of $k$, where the referenced derivative may take the form:

$$\frac{\boldsymbol{\partial^k V}}{\boldsymbol{\partial x^\alpha \partial y^\beta \partial z^\chi}}, \qquad \boldsymbol{where\ \alpha + \beta + \chi = k} \tag{1.24}$$

This illustrates the more rapid falloff in the field of higher order derivatives and is manifested as an increasing exponent of the reciprocal $1/r$.
This is followed by the definition of a generalized gravitational form as follows:

$$\boldsymbol{n_g = p - k - 1} \tag{1.25}$$

where $p$ is now a term describing the property distribution as follows:

- $p = 0$ for a mass
- $p = 1$ for a line density

- $p = 2$ for a surface density
- $p = 3$ for a solid density

In order to perform the inference to magnetic potentials the following relationship is shown:

$$\boldsymbol{n_m = n_g - 1 = p - k - 2} \quad 1.26$$

Following from the above conditions, they state that the summary field produced by a collection of sources may be homogenous if they have the same degree of homogeneity.

Stavrev et al. (2007) show that homogeneity may be used as a potential field transform if all geometries are accounted for. They give an example of such a transform having a central point $0$, a coefficient of similarity $t$, and a degree of homogeneity $n$. Given a dataset $A(x, y, z)$, its direct similarity transform is:

$$\boldsymbol{A(tx, ty, tz) = t^n A(x, y, z)} \quad 1.27$$

In applying this theory to Euler deconvolution, they state explicitly that Euler deconvolution assumes that, locally at least, the field is produced by one singular point (point, line, sheet edge or contact top). A conversion from the more general concept of degree of homogeneity to structural index ($N$) is then presented:

$$\boldsymbol{N = k + s - d} \quad 1.28$$

where $s = 1$ for masses and $s = 2$ for magnetic dipoles and

- $d = 0$ for points and equivalent spheres

- $d = 1$ for lines and equivalent cylinders
- $d = 2$ for plates and equivalent thin layers, dykes and steps
- $d = 3$ for contacts

**Stability analysis of the SI**

Barbosa et al. (1999) present a detailed study of the stability of the estimated parameters $x_0, y_0, z_0$ and $b$ from standard Euler deconvolution. They follow this by proposing a method to compute the correct structural index. This involves estimating the regional value given variable assumed values of the structural index. The most applicable structural index is shown to occur when the correlation between the derived regional value and the original anomaly is at its lowest. It is also shown that the horizontal solution position is insensitive to the chosen structural index and although the vertical solution position is sensitive to this (linearly dependent), it does not affect the correlation qualitatively.

**Semi-automatic Euler interpretation**

Cooper (2004) presents a method of estimating the position of simple sources by simulating a solution set for each data point. The method relies on the property that for any data point, there exists an infinite set of combinations of model parameters which may satisfy it. The $x, z$ solution position is computed for a chosen mass/SI, for each data point, which produces a set of trade-off curves. These curves intersect at the source location as the data is produced by a single source. On real data these curves may not all intersect at the same point, so a line density may be used to visualize the solution location. If an incorrect choice of mass/SI is made, the intersections will become defocused so multiple values should be assessed in order to determine the optimal value.

**Optimization of Euler**

Pracha (1995) undertook a study on the use of the Euler deconvolution method, the aim of which was to determine if any further information regarding the parameters of the magnetic sources could be extracted from the application of the Euler deconvolution method. This involved studying the non-focused solutions which were previously disregarded and often excluded from the solution set. He presents empirical results which link the geometry of the defocused solutions with the dip and dip direction of a contact plane or dyke. Due to the similarity of the effect of varying dip and inclination of the inducing magnetizing field, these must be treated separately. These results were derived by varying the dip for a fixed inducing inclination, and subsequently varying the inducing inclination for a fixed dip. These perturbations in the model parameters can be represented in matrix form, each column element representing a particular distribution of solutions as in Figure 4 below.

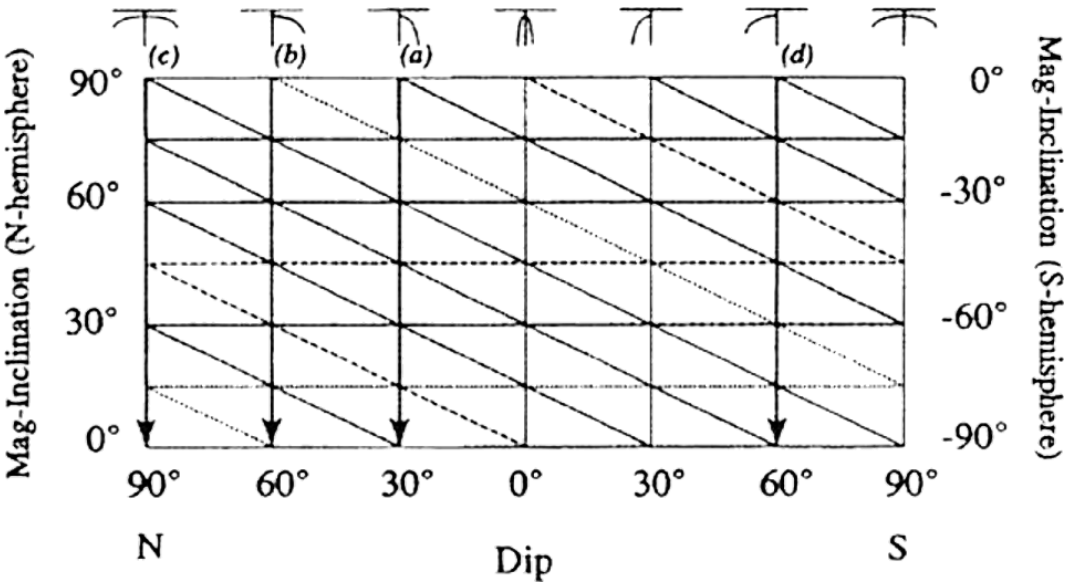


**Figure 4. Extracted from Pracha (1995) Figure 16, Euler solution geometry - dip vs. inducing magnetic field inclination. The relevant solution distributions are shown along the top of the figure.**

The method that Prasha (1995) developed to estimate the throw of a vertical step, where the depth:throw ratio is greater than 1, makes use of multiple structural indices. From empirical studies it was shown by Prasha that the use of the correct structural index for a step, 0.5, focuses solutions at the top of the step, while using the structural index for a dyke (1) focuses solutions at the centre of the step. The same method was applied to a dipping step with less successful results due to the inaccurate location of the characteristic points of the source. However, one observation was that the solutions from the application of the structural index of 1 shifted laterally in the down-dip direction. Another was that the separation between the two solution clusters decreased to less than half the throw of the step. Prasha (1995) noted this limiting case where the throw of the step is strictly more than twice the separation between the solution clusters generated from the use of a value of 0.5 and of 1 for the structural index.

Further optimisation of the algorithm includes the estimation of the optimal cell size for interpolation, and finds that the choice of window size is dependent upon the correct choice of cell size. Prasha (1995) shows that a 10 by 10 cell window returns more focused solutions when the optimal cell size is used than a 5 by 5 cell window. Further to this, rejection criteria were presented in order to minimise the number of spurious solutions. The most effective method, more so than making use of the standard deviations of the $X,Y$ and $Z$ locations, was to only make use of the solutions generated from windows located within the region of positive curvature of the analytic signal amplitude. Prasha (1995) also suggests this as a means of improving the performance of the estimation by eliminating the windows in regions where the curvature of the analytic signal amplitude is negative. The sign used by Pracha (1995) with respect to the curvature of the analytic signal amplitude is in fact not in accordance with convention and when the curvature is stated as ‘positive’ it should rather be ‘negative’.

It is evident, from the extensive publications incorporating the Euler deconvolution method, that the method is widely utilised and is still the most popular estimation employed when interrogating large magnetic datasets. The method has been extensively modified and applied to various derived products of the magnetic field including the vertical and horizontal derivatives, analytic signal amplitude and the tilt angle of the magnetic field. Further mention of the application to the tilt angle is made in a later section devoted to the use of this quantity.

## Multiridge Analysis and Reduced Euler Deconvolution

Fedi and Florio (2007) present a generalized version of the pre-existing geometric method. The method involves tracking of extrema of the absolute field or derivatives thereof in a vertical plane (or volume). Within a vertical section, these extrema of simple models occur along straight lines deemed ridges and diverge with increasing height separation. These ridges, depending on the order of the potential being utilized, intersect in the subsurface region at the position of the source. The roots of the various parametric equations representing the fields (or derivatives thereof) are then found analytically. Furthermore, they introduce the concept of computing Euler deconvolution solutions along these ridges, enabling simplification of the original Euler deconvolution method. This simplified version is called Reduced Euler deconvolution. They represent the field of order $n$ by $f_n$. and the corresponding structural index $N$ by $S_n$. The following are then the simplified Euler equations along the respective ridges:

$$(\boldsymbol{z - z_0})\frac{\boldsymbol{\partial f_n}}{\boldsymbol{\partial z}} = -\boldsymbol{S_n f_n} \qquad 1.29$$

at zeros of the first-order horizontal derivative,

$$(\boldsymbol{x}-\boldsymbol{x_0})\frac{\boldsymbol{\partial f_n}}{\boldsymbol{\partial x}}=-\boldsymbol{S_n f_n} \tag{1.30}$$

at zeros of the first-order vertical derivative,

$$(\boldsymbol{x}-\boldsymbol{x_0})\frac{\boldsymbol{\partial f_n}}{\boldsymbol{\partial x}}=-(\boldsymbol{z}-\boldsymbol{z_0})\frac{\boldsymbol{\partial f_n}}{\boldsymbol{\partial z}} \tag{1.31}$$

at zeros of the field.

Fedi et al. (2007) suggest that this set of equations can be used separately or in conjunction to derive the various source parameters, the first involving depth and structural index, the second involving horizontal position and structural index and the third involving only the positional parameters and being independent of the structural index. Due to the combination of upward continuation and derivation, the resultant process resembles that of a band-pass filter attenuating both the high and low wave number spectra components. Due to this property, the method is quite robust when applied to noise contaminated data. Figure 5 illustrates the section with respect to vertical altitude whereupon the extrema are traced.

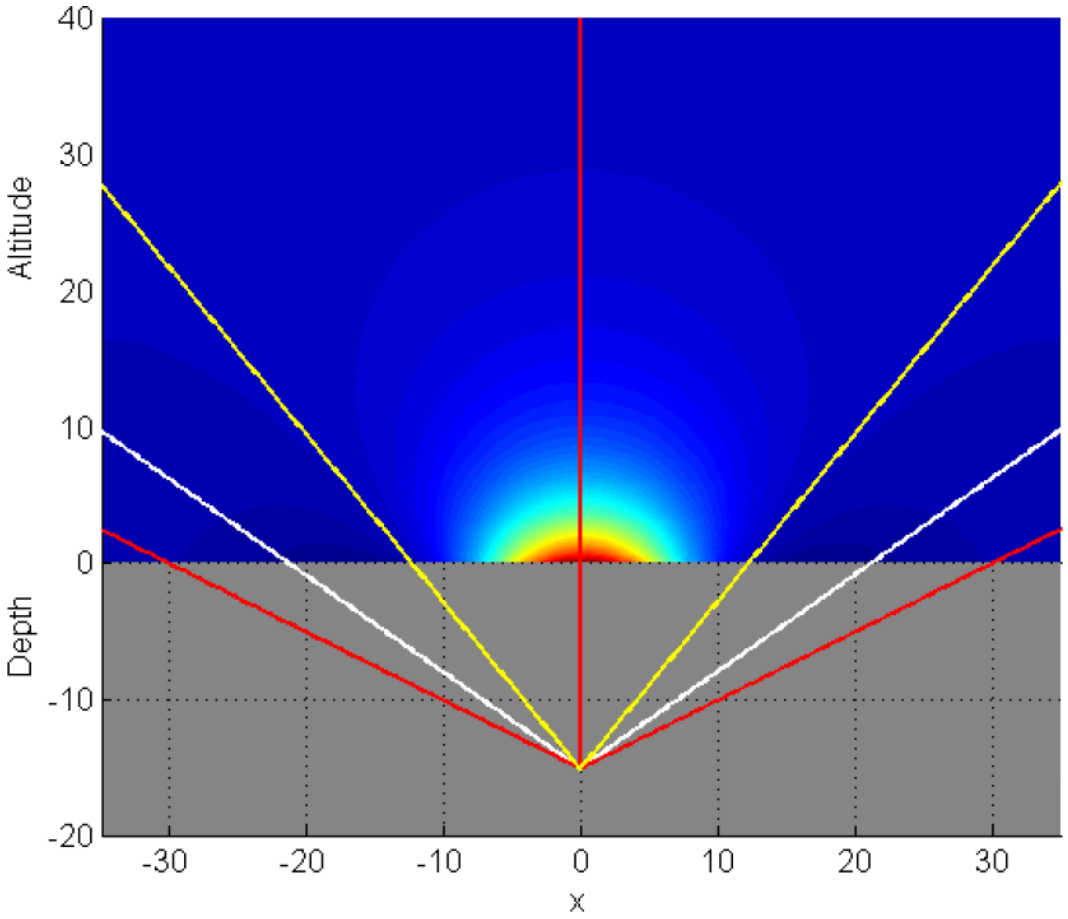


**Figure 5. Extracted from Fedi and Florio (2007) Figure 1, this illustration shows the Geometric Multiridge Method for determining depth.**

## Source Parameter Imaging

Source Parameter Imaging (SPI), first described by Thurston and Smith (1997), is another method capable of estimating not only depth to magnetic source, but dip and susceptibility contrast as well. Thurston and Smith note that due to the dipolar nature of the magnetic potential, characteristic points may be hard to identify. To mitigate this, SPI uses the source parameters deconvolved from the magnetic potential which describe the source. Various profile methods exist such as Naudy, Werner and Euler but these assume 2D structures and require correction for the apparent strike relative to the profile direction. Grid based methods have been developed such as 3D Euler and the 3D analytic signal method, and

have an advantage over profile methods as they do not require correction for the strike direction of the source. The SPI method is applied to gridded data but still has various constraints. The method assumes that the observed field is due to a susceptibility contrast in the form of either a 2D sloping contact or a 2D dipping thin sheet and the dip and susceptibility estimates assume no remanent magnetization. The depth estimate however is independent of the magnetic inclination, declination dip, strike or remanent magnetization. Another advantage is that solutions are produced without the need to define a window size as in the Naudy and Euler methods. The output images may also be further processed to enhance structural detail.

Thurston and Smith (1997) state that the SPI method extends the theory of the complex analytic signal by Nabighian by computing an additional three attributes, the local amplitude, phase and frequency. Due to the method being based on the complex analytic signal which assumes a 2D source, the method is applicable to either the total field (assuming a thin sheet model) or the horizontal derivative (assuming a sloping contact with infinite depth extent).
The analytic signal amplitude and local phase are quoted by Thurston and Smith in equations 3 and 4 as:

$$|\boldsymbol{A}| = \sqrt{\left(\frac{\boldsymbol{\partial M}}{\boldsymbol{\partial x}}\right)^{\mathbf{2}} + \left(\frac{\boldsymbol{\partial M}}{\boldsymbol{\partial z}}\right)^{\mathbf{2}}} \qquad 1.32$$

$$\boldsymbol{\theta} = \mathbf{tan}^{-\mathbf{1}}\left(\frac{\dfrac{\boldsymbol{\partial M}}{\boldsymbol{\partial z}}}{\dfrac{\boldsymbol{\partial M}}{\boldsymbol{\partial x}}}\right) \qquad 1.33$$

$M(x, z)$ is the magnitude of the total magnetic field.

They then define the local frequency and local wave number in equations 5 and 6 as:

$$\boldsymbol{f = \frac{\frac{\partial \theta}{\partial x}}{2\pi}} \quad 1.34$$

$$\boldsymbol{k = 2\pi f} \quad 1.35$$

and proceed to show that the local depth is the inverse of the local wave number at the body's edge. Definitions for the local dip and local susceptibility contrast are also presented.

Subsequently, Smith et al. published an improvement to the SPI method, iSPI ("i" for improved), in 1998 which extends the method to include the field of a horizontal cylinder and allowing the determination of the most appropriate model type. The most appropriate model type is determined from analysing the analytic signal and the second derivative analytic signal. This allows the calculation of an additional local wave number and when solved simultaneously a model independent (only for the applicable model types) depth may be obtained. A quantity $n_k$ (SPI structural index) is defined as:

$$\boldsymbol{n_k = \frac{k_1}{k_2 - k_1} - 1} \quad 1.36$$

and then the model independent depth becomes:

$$\boldsymbol{h = \left. \frac{1}{k_2 - k_1} \right|_{x=0}} \quad 1.37$$

It must be stressed that even though the depth is deemed “model independent”, that this is still only applicable to the three 2D source types i.e. contact, thin sheet and horizontal cylinder. In order to ensure that this depth estimation method is applicable efforts should be made to ensure that the magnetic field contours are roughly straight and parallel. Due to the use of second order derivatives of the magnetic potential, the results are somewhat less robust in the presence of noise than those of the original SPI method and it is suggested that this method be used with caution. Figure 6, taken from Thurston and Smith (1997), shows the various quantities utilised by the SPI method when computed for a dipping contact.

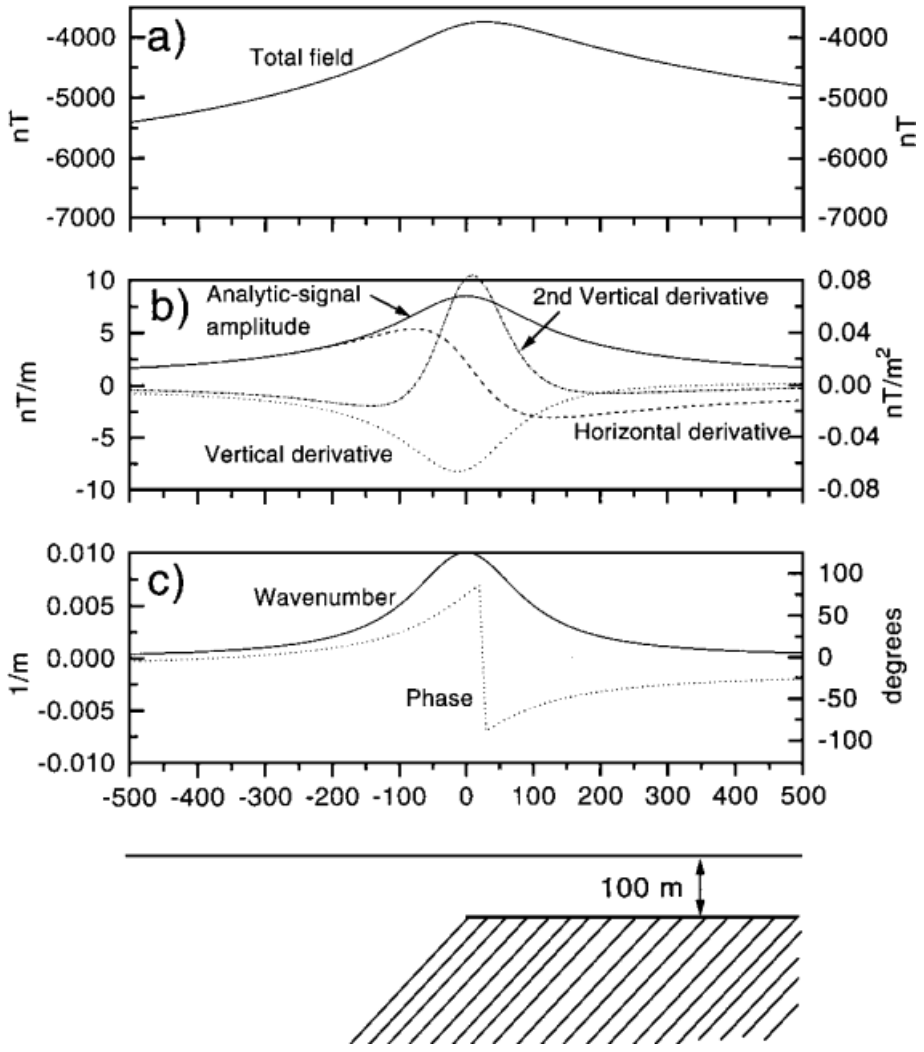


**Figure 6. The illustration taken from Thurston and Smith (1997) shows the quantities used in the SPI method.**

## Potential Field Tilt

### Tilt depth

The tilt angle of the magnetic potential was first described by Miller and Singh (1994). They comment on the properties of the horizontal derivative of the potential and its relationship to source body edges as well as the positivity of the vertical derivative over sources. The tilt is described as superior to these as it has the added property of being normalized for small and large amplitude anomalies, therefore it has a similar amplitude response over deep and shallow targets and has a range $\frac{-\pi}{2} > TILT > \frac{\pi}{2}$. It also crosses zero near or at source body edges. A further suggestion is the concurrent use of the tilt and the apparent strike plotted on a stereo plot in order to summarize the orientation statistics of the magnetic sources in a dataset.

The tilt-depth method was introduced by Salem et al. (2007) and is described as a simple method of estimating the magnetic source depth. It makes use of a quantity called the magnetic tilt angle (also known as the local phase). The assumptions are that the source is that of a vertical magnetic contact with a vertical inducing field and no remanent magnetization. The terms are defined in three dimensions where $M(x, y, z)$ is the magnetic potential as follows:

$$\frac{\partial M}{\partial h} = \sqrt{\left(\frac{\partial M}{\partial x}\right)^2 + \left(\frac{\partial M}{\partial z}\right)^2} \qquad 1.38$$

$$\boldsymbol{\theta = \tan^{-1}\left(\frac{\frac{\partial M}{\partial z}}{\frac{\partial M}{\partial h}}\right)} \qquad 1.39$$

Due to the properties of the arctan function the tilt angle has a normalizing effect, reducing the amplitudes to the range $\frac{-\pi}{2} > \theta > \frac{\pi}{2}$ while preserving the spectral integrity of the data in either profile or grid form. They further show (in equation 6) that in the special case when the field and contact are vertical, the tilt angle reduces to:

$$\boldsymbol{\theta = \tan^{-1}\left(\frac{h}{z_c}\right)} \qquad 1.40$$

and this implies the tilt angle has a zero value over the contact $(h = 0)$ and that the depth ($z_c$) is equal to half the distance between the positive and negative contours having a value of $\frac{\pi}{4}$. A recent development on the technique published by Cooper et al. (2011) is that the distance between any pair of contours separated by $\frac{\pi}{2}$ may be utilized and the choice thereof may be optimized. The geometric method of the tilt-depth is well illustrated by Salem (2007) and shown here in Figure 7.

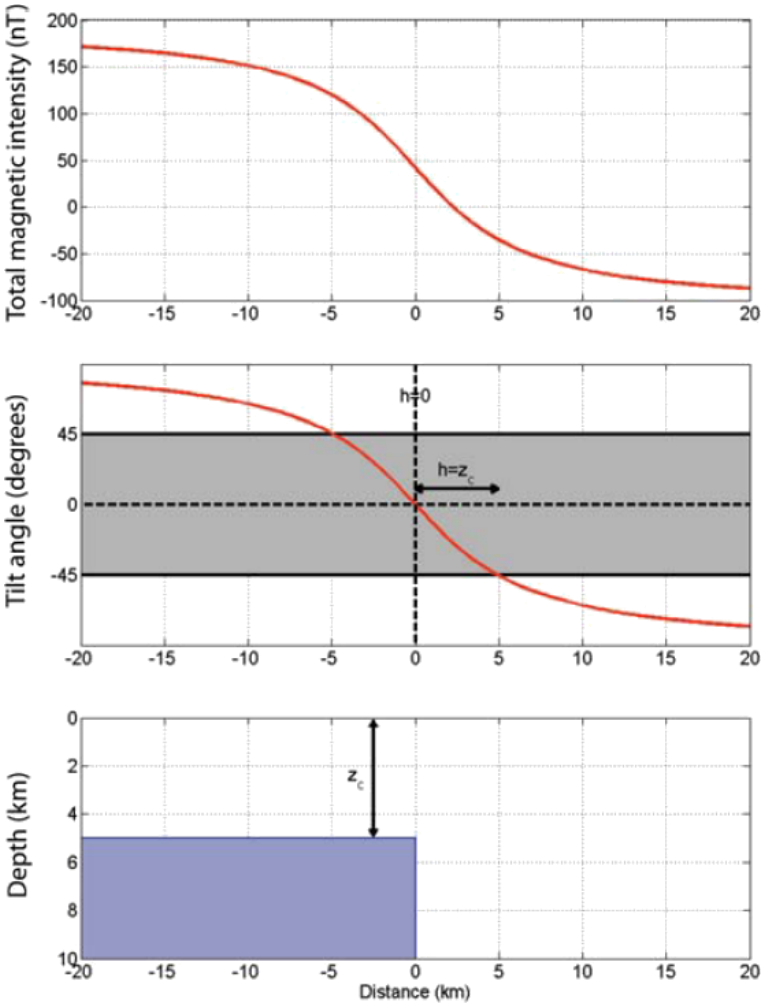


**Figure 7. Salem (2007) shows the simple application of the tilt-depth method.**

## Generalized Tilt-Euler deconvolution

This method of depth estimation was introduced by Salem et al. (2007) and makes use of Euler deconvolution of the magnetic tilt angle (or generalized local phase). The concept was originally restricted to the interpretation of profile data but was then generalized to include gridded data. A major advantage of this method is that no structural index is required. In order to achieve this, the method makes use of second order derivatives of the field which are less sensitive to noise than the third order derivatives upon which other structurally independent methods rely.

The method begins by computing the first order derivatives of the tilt in the $x, y$ and $z$ directions which are identical to the local wave number in 2D cases. These equations are substituted into derived forms of the 3D Euler equation and after some manipulation and collecting terms the form is as follows:

$$\boldsymbol{k_x x + k_y y + k_z z = k_x x_0 + k_y y_0 + k_z z_0} \qquad 1.41$$

The method is illustrated by application to synthetic data from a single, square prism model striking at 45° and to the popular Bishop model, a synthetic model created using the topographic data from an area north of Bishop, California by G. Flanagan.

Lee et al. (2010) shows the magnetic amplitude dependence of the tilt depth estimates and highlights the structural influence on this amplitude dependence. The concept of depth to top and depth to bottom of the magnetic source is however mixed with that of 2D vs. 3D sources and the referenced edge effects are likely due to the 3D nature of the source. There seems to be a directional dependence of the computed tilt which requires investigation and might be due to the computation of multiple models simultaneously.

**Enhanced Local Wavenumber analysis**

Pal (2006) introduces a method called Enhanced Local Wavenumber analysis. The approach adopted here is to make use of not only the local wave number, but the phase rotated version as well. In order to achieve this, the vertical derivative of the local phase is taken along with the traditional horizontal derivative. These two quantities are shown to contain a variable dependence upon the model type (structural index). To remove the model dependency the two equations are ratioed leaving an expression as follows:

$$\boldsymbol{k_x x + k_z z = k_x x_0 + k_z z_0} \quad 1.42$$

Equation 1.42 is identical to that of Generalized Tilt-Euler deconvolution by Salem et al. (2007) which generalizes this relationship in three dimensions.

## Differential Similarity Transforms

Following from work by Stavrev published in 1997 on the application of differential similarity transforms (DST) to magnetic data, Stavrev et al. presented the concept of finite-difference similarity transforms (FDST) in 2006. The method, as with many other estimation methods, makes use of the homogeneity property of the potential field of simple sources. The FDST method differs from that of the most popular Euler deconvolution method in that it makes use of the principal form of the homogeneity relationship before taking the derivatives. The FDST requires the computation of two levels of upward analytical continuation of the anomalous field $\Delta T(x, y, z)$. The calculation follows:

$$\boldsymbol{\Delta T'(x', y', z') = t^n \Delta T(x, y, z)} \quad 1.43$$

Then the FDST is:

$$\boldsymbol{D(x', y', z') \; = \; \Delta T'(x', y', z') - \Delta T(x', y', z')} \quad 1.44$$

Stavrev et al. (2006) show the ability to transform the principal form of the relation by dividing by (creating a ratio of) one of the independent variables resulting in a straight line plot, intersecting characteristic points of the potential at multiple heights as well as a singular point of the source, e.g. the top of a 2D thin sheet. This is similar to the application of

Multiridge Analysis by Fedi and Florio (2007). Stavrev likens the FDST to the difference between the anomalies generated by two equal sources located proximally. One of these source's anomalies is generated via the similarity transform, achieved through the projection of the observed anomaly, using an assumed structural index, from a chosen central point of similarity (CPS). The FDST then approaches zero (for sources having only a single singular point) when the synthetic source approaches the real. For sources with multiple singular points the FDST simplifies to a straight line. The amplitude of the FDST is then dependent on the chosen location of the CPS and the structural index. Stavrev therefore proposes a method which minimises the FDST with respect to the CPS location and chosen structural index.

The method presented by Stavrev et al. (2006) involves a sliding, overlapping windowed search for the optimal CPS and SI by creating what might be akin to a vertical magnetic sounding. The resultant FDST is inspected for linearity by making use of a normalised residual standard deviation with respect to its linear regression ($Q$). This parameter is called the estimator of linearity and is gridded to produce an image which, is interrogated for minima corresponding to the singular points. The value of the estimator of similarity is compared for proximal minima generated with different values of the structural index and the lowest chosen. This is then the optimal combination of CPS and SI describing both the location and shape of the source.

From the relations above, a profile (or grid) of data may be used to produce a pseudo-section (-volume) containing these zero points (or minima) corresponding to the source locations. This is a useful method, as unlike Euler deconvolution and most other depth estimation methods, it does not rely upon the computation of derivatives of the field which are sensitive to noise. The result of this is an increased relative stability of this method when applied to data containing high frequency noise. Figure 8

provides a well-illustrated example of the data quantities and Q field calculated for two dyke-like structures.

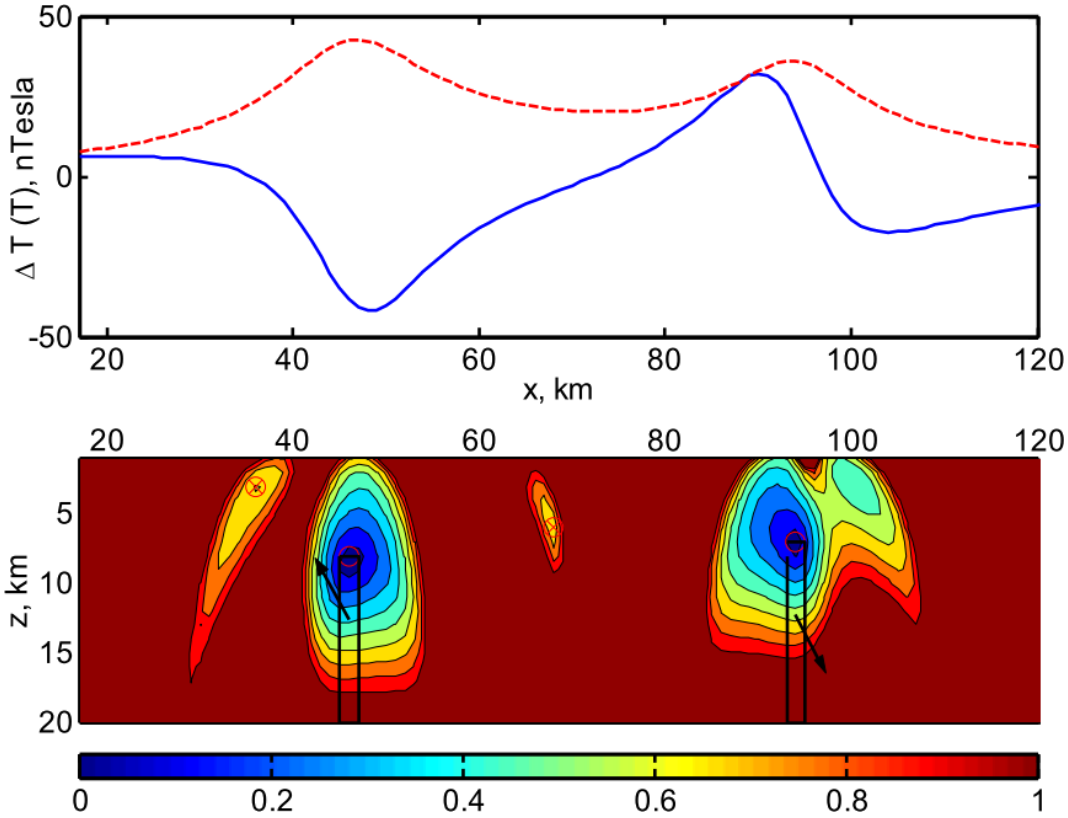


**Figure 8. The figure from Stavrev et al. (2004) illustrates the DST from two dyke-like structures. The anomalous magnetic field (Blue -) and the field magnitude (Red --) are shown above the $Q$ field where $0 \leq Q \leq 1$.**

## SLUTH

The SLUTH method defined by Thurston and Smith (2007) makes use of the homogeneity property of the amplitude of a potential field and interrogates the behaviour of the field in a vertical plane above the source. They define a construct called a “level curve”. The level curve is a contour (a line tracing equal values) in the vertical plane. The unique property of level curves of homogenous fields is that when any number of curves intersect a straight line (ray) passing through the origin, they have equal gradient. This implies the straight line is a level curve of the gradient of the

level curves of the magnetic potential. The method of locating the source position (origin) involves finding two or more of these straight contours which intersect in the sub-surface, thereby defining the origin. In order to represent the computations graphically, the authors made use of the arctangent of the gradient of the field represented on the vertical plane with straight line contours extrapolated to the source position. The method may make use of numerous points from varying continuation levels to define a best-fit ray. Furthermore, the authors suggest the use of a linear least-squares fit due to its innate association with straight line equations. A significant advantage that the SLUTH method has is that it does not require a quantity akin to the structural index. The depths derived from the rays can be determined independent of this biasing quantity. The authors do suggest that the method should work for degrees of homogeneity $n = 0, -1$ and -2. The graphical nature of the SLUTH method is illustrated in Figure 9, taken from Thurston and Smith (2007).

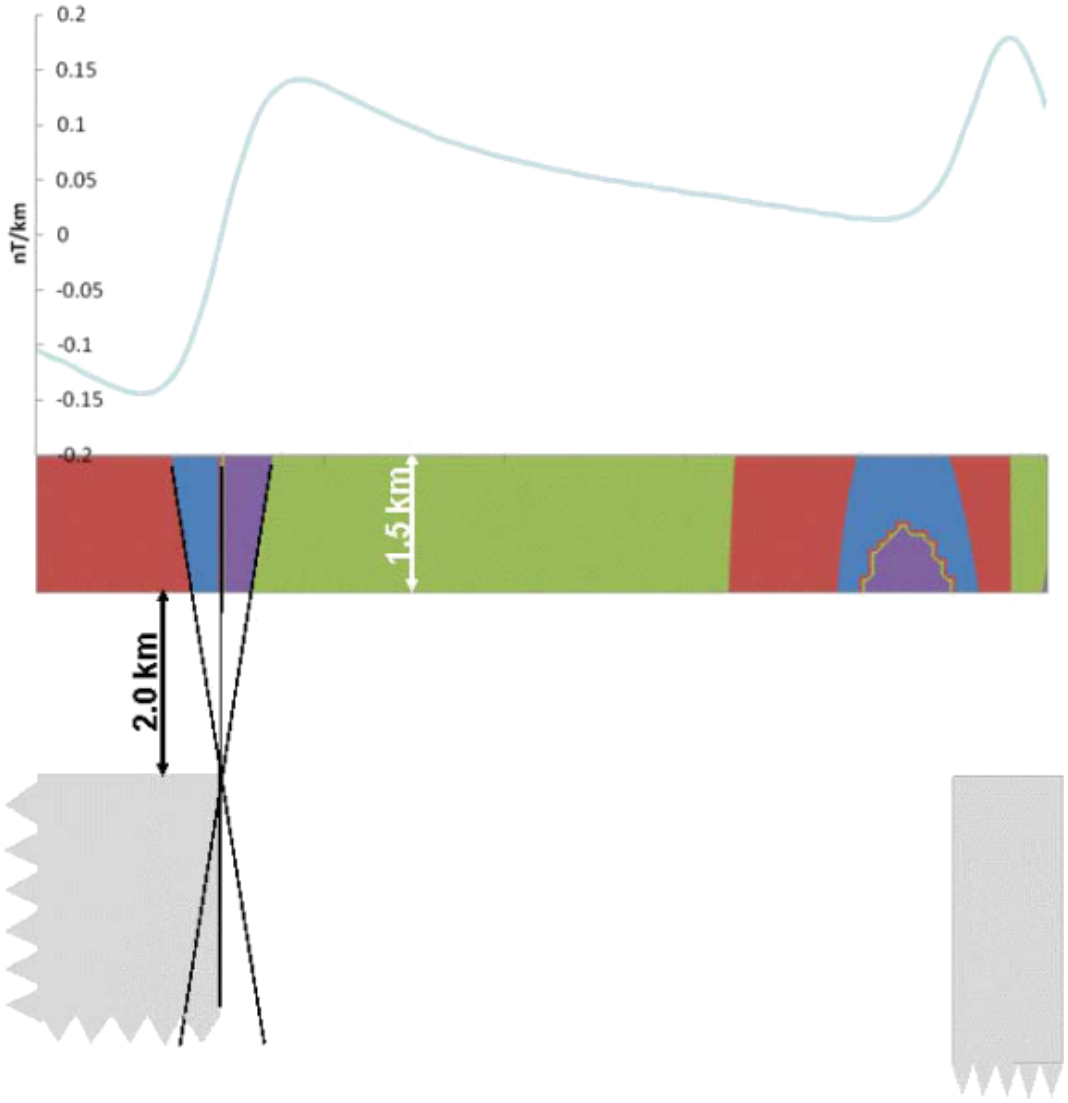


**Figure 9. Thurston and Smith (2007) illustrates the SLUTH method applied to synthetic data**

The SLUTH method as described by Thurston and Smith (2007) is identical to that of Multiridge Analysis by Fedi et al. (2007), however Thurston and Smith fail to identify the simplification of the Euler equations possible along these rays.

## Linear Least Squares

Salem et al. (2004) present a method of source parameter estimation similar to that of Euler deconvolution. The method is able to solve for either the depth (assuming a shape factor), or depth and shape factor simultaneously. The method utilizes a symmetric anomaly and its first order horizontal derivative. For magnetic data, the analytic signal is used instead of the potential due to its symmetrical nature about a 2D source. The symmetric potential is quoted as:

$$\boldsymbol{f(x) = \frac{F}{(x^2 + z^2)^q}} \tag{1.45}$$

Then its horizontal derivative is given by:

$$\boldsymbol{\frac{\partial f(x)}{\partial x} = \frac{-2qxF}{(x^2 + z^2)^{q+1}}} \tag{1.46}$$

The potential is then related to its horizontal gradient as follows:

$$\boldsymbol{\frac{f(x)}{\frac{\partial f(x)}{\partial x}} = \frac{x^2 + z^2}{-2qx}} \tag{1.47}$$

or

$$\boldsymbol{x^2 \frac{\partial f(x)}{\partial x} = -2qxf(x) - z^2 \frac{\partial f(x)}{\partial x}} \tag{1.48}$$

The final form is somewhat similar to Euler's equation but is not homogeneous preventing all of the source parameters being estimated simultaneously. The horizontal position is therefore estimated using the

turning point of the field (or zero of the horizontal derivative). The shape factor here denoted by $q$ is related to the structural index of Euler deconvolution by:

$$\boldsymbol{q = (\eta + 1)/2} \tag{1.49}$$

If $q$ is assumed then the depth may be obtained from the following form:

$$\boldsymbol{z^2 = \sum_{i=1}^{N} \frac{\left(-2qx_i f(x_i) - {x_i}^2 \frac{\partial f(x_i)}{\partial x}\right)\frac{\partial f(x_i)}{\partial x}}{\sum_{i=1}^{N}\left(\frac{\partial f(x_i)}{\partial x}\right)^2}} \tag{1.50}$$

or both depth and shape factor may be derived by linear matrix inversion of equation 1.48:

$$\boldsymbol{\bar{d} = G\bar{m}} \tag{1.51}$$

where $\bar{d}$ is a vector of $N$ elements where:

$$\boldsymbol{\bar{d}_i = {x_i}^2 \frac{\partial f(x_i)}{\partial x}} \tag{1.52}$$

and $\boldsymbol{G}$ is a $N \times 2$ matrix given by:

$$\boldsymbol{G_i = \left[-2x_i f(x_i) \quad -\frac{\partial f(x_i)}{\partial x}\right]} \tag{1.53}$$

$\bar{m}$ then being the vector of unknowns namely $q$ and $z^2$.

The method is applied to synthetic and field datasets with much success. Upward continuation of the potential is utilized in order to suppress high noise content to a suitable level and improved performance is achieved when more points within the isolated anomaly are used.

## Total Normalised Gradient

After reviewing the traditional Werner and Euler deconvolution methods, mostly employed in the “western” geophysical fraternity, Pasteka (2000) turns to one of the most popular and successful methods used in the “Russian” fraternity, that of the Total Normalized Gradient (also known as Quasi-Singular Points). The method, originally introduced by Berezkin et al. (1965) was developed by him and many others and aims to determine singular points of potential fields. Pasteka acknowledges the method's similarity to the analytic signal method of Nabighian (1972, 1974) because of the method's dependence upon the analytic signal of the potential. The analytic signal is employed to stabilize the oscillations produced when the scalar potential is continued toward the source. Intuitively, the potential cannot be continued deeper than the source but nevertheless, this may be done numerically if the distortions which arise are recognized and appropriately treated. Pasteka delves into the analytic computation of the continued gradient field $F^N$ which is beyond the scope of this review which aims to summarize the main points.

The downward continuation is achieved using the standard Fourier series routine in the wave number domain. The downward continued fields ($f, f_x \& f_z$) are presented showing the unwanted perturbations, followed by the total gradient illustrating the ability to remove these perturbations. However, the problem of the field amplitude increasing with continuation distance still remains. The continuation is represented analytically and the inverse Fourier transforms of the potential and its orthogonal derivatives

calculated. The sum of the squares of these derivatives is then computed containing 3 components, the first containing the correct derivatives of the field, the second containing the exponential disturbance without the oscillatory part, and the third containing the oscillatory terms which decrease rapidly with increasing horizontal distance and with increasing $z$ where $z > h$. The last step is taken to normalize the total gradient field and is achieved by dividing the field at each level by its mean. A smoothing term (Lanczos) was also introduced into the Fourier series by Berezkin (1967), which suppresses the contributions of the high wave number components.

A fundamental observation by Berezkin (1967) was that by varying the number of terms in the Fourier summation, the $F^N$ field changes and its maxima migrate upward along the contacts of the model toward the upper surface. Berezkin's criterion therefore follows that the position of a singularity is related to the position of the greatest local maxima, obtained by varying the number of Fourier terms (N).

Pasteka recounts that following this observation, Eliseeva (1982) defined an expanded empirical algorithm for tracking these maxima through changing $F^N$. The local maxima, situated approximately beneath each other on subsequent levels are connected with lines forming a zone. These zones have start, end and maximum points which are used to determine the location of the singular points. The zones were categorized into two types, one for sub-vertical and the other for sub-horizontal density/susceptibility contacts. The sub-vertical zones are more omnipresent throughout the range of N and have the highest values while the sub-horizontal zones are only present in some of the levels and are of lower value. Studies have shown that the zones move with varying rate with respect to N. The rate of variation was shown to increase significantly at the base of the model layer while the maximum amplitude was reached at approximately its centre.

Pasteka reviews the work of Eliseeva (1995, 1997) where she has defined on this basis the Quasi-Singular Points method (QSP) and in doing so highlighted the shortcomings of the classical Berezkin method:

- No clear criteria for selecting N
- Low variability of the spectral characteristics of the operator (Lanczos operator, exponent limited to 2, only first derivatives used)
- No analytic criteria for locating the singular positions

Many of these shortcomings were addressed by the more general QSP method. A fundamental condition imposed by the method is that the result of applying the chosen non-linear operator to the continued data must be constant for the depth level containing the singularity. The search for the optimal operator involves maximizing the number of coefficients of the spectral response where this condition holds. A more complete explanation of the independent variables affecting the spectral operator may be found in the work of Pasteka 2000. Once the optimal operator has been identified, it may be used to form generalized derivatives of the field, thereby producing the optimized total gradient (and total normalized gradient). Eliseeva not only succeeded in deriving analytic expressions describing the behaviour of the zones, but also automating the recognition and digitization of these zones. Pasteka proposes that further work is required to better understand how the zones' behaviour is best interpreted. Eliseeva (1995) defined two criteria which may be used in determining the location of the singularity from the zones' characteristics, namely the $\alpha$-criterion and the $F^N$-criterion. These criterions are then evaluated graphically with the help of a set of master curves. Figure 10 shows the various solution types obtained from the application of the QSP method to a rectangular prism.

Pasteka concludes with a review of a number of model studies where the Werner, Euler and QSP methods are applied and compared. The conclusions arrived at as a result of this work being:

- Werner deconvolution is a stable method producing highly clustered results and is best suited to ore-type problems (Stavrev 1997).
- Euler deconvolution offers a similar product to Werner but often achieving more dispersed solutions. The flexibility of Euler deconvolution (due to its structural index) when applied to differing model types is attractive.
- The Quasi-Singular Points method is possibly the best for interpreting structural-type problems (Stavrev 1997) due to its spectral considerations.

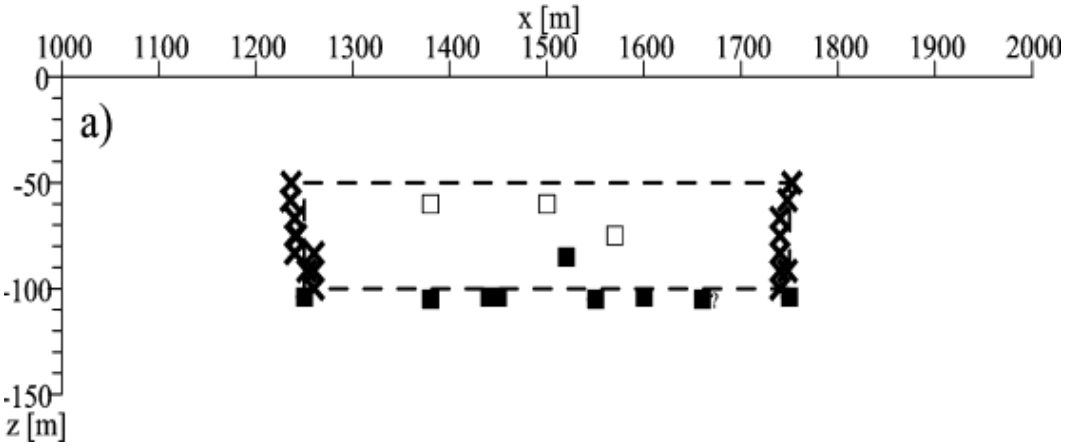


**Figure 10. Extracted from Pasteka (2000) Figure 23, this illustrates the ability of the QSP method to resolve the lower contact of the source**

## Window Curves

The window curves method was introduced by Abdelrahman et al. (2001) and adopts a novel approach to simultaneous depth and shape estimation from gravity data. The method involves the calculation of residual anomalies using a defined second moving average filter ($R_2$), the equation of which is:

$$\boldsymbol{R_2(X_i, Z, q, s) = \frac{A}{4}[6\left(X_i{}^2 - Z^2\right)^{-q}} \quad 1.54$$

$$-4((X_i - s)^2 + Z^2)^{-q} - 4((X_i + s)^2 + Z^2)^{-q}$$
$$+((X_i - 2s)^2 + Z^2)^{-q} + ((X_i + 2s)^2 + Z^2)^{-q}]$$

where $s \in 0,1,2 \ldots$, and $q$ is the shape factor. The authors divide the second moving average values and produce the following reformulated expression:

$$\boldsymbol{Z = \left[\frac{4}{B}\right]^{1/2q}} \tag{1.55}$$

where

$$\boldsymbol{B = [7(s^2 - Z^2)^{-q} - 4(4s^2 - Z^2)^{-q} + (9s^2 - Z^2)^{-q}]}$$
$$-2F[3Z^{-2q} - 4(s^2 - Z^2)^{-q} + (4s^2 - Z^2)^{-q}] \tag{1.56}$$

and

$$\boldsymbol{F = \frac{R_2(s)}{R_2(0)}} \tag{1.57}$$

The solution strategy involves using multiple values of $s$ to produce a number of second moving average residual anomalies, each solved using the above equation for a set of $q$ values within a reasonable domain. This produces a set of curves in $(q, Z)$ space which intersect at the source depth and shape factor. Abdelrahman et al. (2001) illustrate the method on synthetic data with varying order regional fields and on data contaminated with substantial noise.

# CHAPTER 2: THEORY OF MULTI-SCALE TILT DEPTH ESTIMATION

## History of Multi-Scale Computation

Multi-scale computation of the magnetic potential has been widely utilised as an interpretive tool. The concept of multi-scale edges is presented as a set of detectable edges (local maxima) within the transform of a dataset at a variety of scales. These scales have been determined in numerous ways including via wavelet transformation and vertical continuation. Mallet et al. (1989) presents a comprehensive review of the signal content available within a set of multi-scale edges derived from one and two dimensional data. They present a verification of the formal completeness of a set of adequately derived edges and proceed to formalise the reconstruction of a signal from such a set. The concept is presented once more, but with a slightly altered focus in Mallet et al. (1992), where the emphasis is on the ability to characterize the edges. In essence, the edges are characterized on the basis of their evolution across multiple scales.

Evidence of multi-scale edge detection applied to potential field data has been found dating back to McGrath (1991), where edges were determined using the maxima of the horizontal derivative of upward continued gravity data. Dip as well as extent information were determined using the technique. Archibald et al. (1999) present the analysis of potential field data with the use of multi-scale edges. This work extends the concept of worms, frequently used in magnetic interpretation, to three dimensions. They show that the edges derived in two dimensions at a unique spatial scale, migrate in three dimensions across scales to form surfaces. The work of Hornby et al. (1998) shows the application of the wavelet transform to potential fields and its equivalence to more commonly utilized Fourier-based processes. Archibald et al. (1999) extend the use of the

wavelet transform to multi-scale edge analysis. The manner of visualization includes plotting the three dimensional location as well as the intensity of the edges. They show that the maxima of the wavelet transform diverge with increased scale to forma characteristic curve. This curve is characteristic to different geometries, i.e. the edges diverge at different rates if the body/contact has a non-vertical dip. Inversion techniques are proposed whereby the inversion is initially constrained by extrapolating the multi-scale edges toward the source's location. Holden et al. (2000) continues the topic with more contemporary illustrations of the nature of the multi-scale, wavelet transform maxima in three dimensions for a number of forward models, illustrated in Figure 11. The figure below is extracted from this paper and clearly shows the geometric dependence of the multi-scale edge surface on the dip of the source.

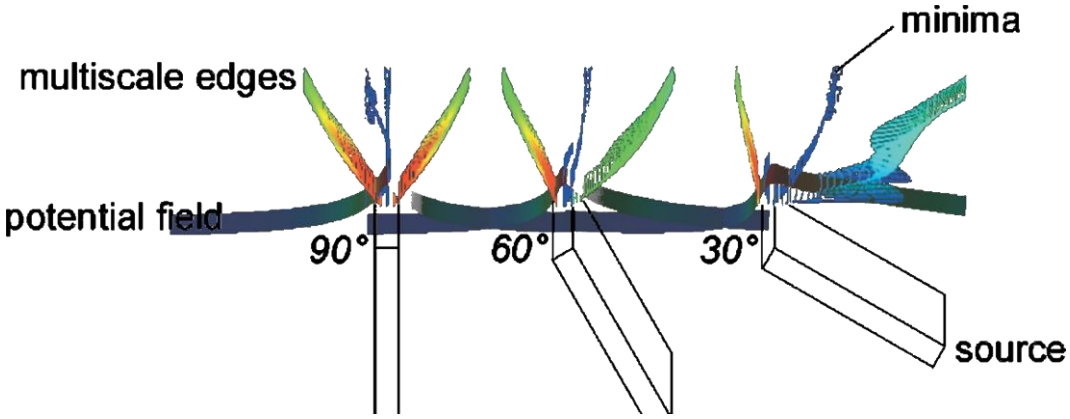


**Figure 11. Holden at al. (2000) Figure 7 illustrates the nature of traditional multi-scale edges**

Boschetti et al. (2000) present work on improved edge detection and graphically illustrate the method of determining the depth-to-top of a source by making use of the tangents to the lower portion of the multi-scale edge section. Here I note that the line/surface created in two/three dimensions by the migration of the maxima is not linear/flat. Estimation of the depth if the tangent is taken at a higher scale will be greater than the true depth to the source.

Fedi and Florio, as detailed earlier in this text, make use of a similar method of geometric solution in the Geometric Multiridge Method. Lahti and Karinen (2010) merge the application of multi-scale edge determination with the tilt of the potential field. They compute the tilt of the upward continued, pole reduced field and extract the zero crossing/contours in order to construct a multi-scale edge set. The tilt is utilised due to its zero crossing/contour being closely associated with the edge of a source as well as to stabilise and normalise the amplitudes of the maxima.

These methods all have one element in common: the maxima, however derived, diverge with increased scale. It is shown in the following sections that the zero crossing of the tilt, when upward continued, converges. This is fundamental to the method of Multi-Scale Tilt Depth Estimation.

## Theoretical Formulation of Multi-Scale Tilt Depth Estimation

Multi-Scale Tilt Depth Estimation (MSTDE), first reported by van Buren (2009), is a method to approximate the depth to the source of a magnetic anomaly. It is an empirical method derived on the basis of experimentation with tilt and continuation of the magnetic field intensity. The method constructs a vertical distribution via upward-continuation of the tilt of the pole-reduced total magnetic intensity.

The tilt is computed as defined by Miller and Singh (1994):

$$\mathbf{T}(\boldsymbol{f}) = \boldsymbol{tan}^{-1}\left[\frac{\partial \boldsymbol{f}}{\partial \boldsymbol{z}} \Big/ \sqrt{\left(\frac{\partial \boldsymbol{f}}{\partial \boldsymbol{x}}\right)^{2}}\right] \qquad 2.1$$

where $f$ is the reduced-to-pole magnetic intensity.

The upward-continuation of the tilt of the pole-reduced total magnetic intensity is conducted in the frequency domain with the following standard equation:

$$\boldsymbol{U = Ae^{-ikz_j}} \qquad 2.2$$

where $A$, $U$, $k$ & $z_j$ are the original and continued frequency domain amplitude coefficients, the wavenumber and the continuation distance respectively.

The method originally reported by van Buren (2009) made use of the AREA quantity and was defined as follows:

$$\mathbf{AREA} = \boldsymbol{tan^{-1}\left[tan\left[\frac{\pi}{2} - tan^{-1}(RTP\_TDR)\right]\right]} \qquad 2.3$$

where $RTP\_TDR$ is the tilt of the reduced to pole magnetic intensity.

The sign of the MSTD distribution above a correctly pole-reduced magnetic source is positive, but the lateral extent of the positive region decreases with increased upward-continuation. This is illustrated in the following figure and may be otherwise stated as follows: for the continuation distance less than the depth to the source, $Z_j < d_0$, as the continuation distance increases, the x-intercepts of the tilt approach each other.

$$\left|\boldsymbol{X_b^j - X_a^j}\right| > \left|\boldsymbol{X_b^{j+\Delta j} - X_a^{j+\Delta j}}\right| \qquad 2.4$$

for $Z_{j+\Delta j} < d_0$.

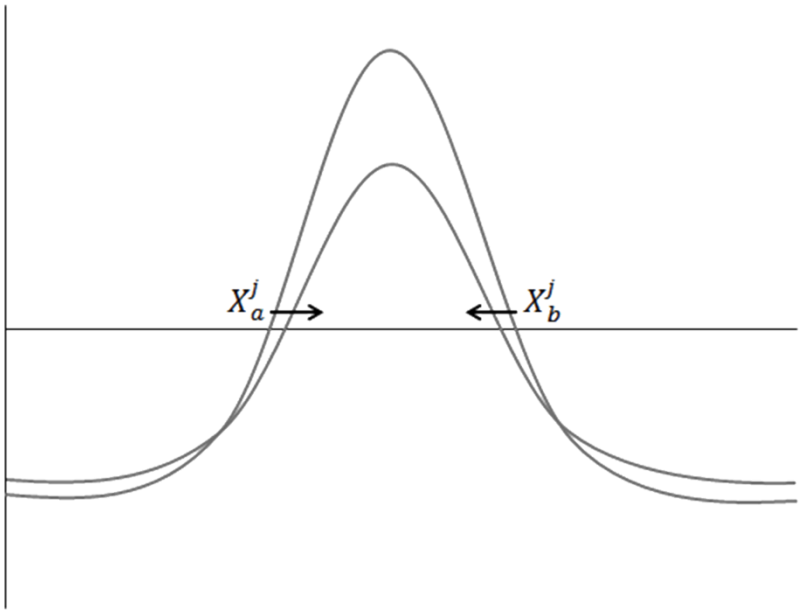


**Figure 12. Illustration of the migration of the x-intercepts of the tilt, $X_a^j$&$X_b^j$ with upward continuation.**

The x-intercepts tend toward the centre of the anomaly which, for a vertical sheet / dike-like feature is centred on the source. At some continuation distance the positive area vanishes and all values become negative. This continuation distance corresponds to the depth of the source. The upward-continued distribution is therefore transformed to a distribution in depth by simply substituting the depth with the continuation distance. It will be shown that the method, as applied to pole-reduced total magnetic intensity returns correct depth estimates for vertical sheet / dyke-like features, i.e. features where the depth-to-top is far greater than the width. The peak location of the analytic signal amplitude, for vertical sheet / dyke-like features, is located over the centre of the source.

Algorithmically, the lateral solution location may be determined by making use of the peaks of the analytic signal amplitude but, in the code distributed herein, the solutions are located via the gradient of the zero contour of the tilt distribution. Points coincident at, and surrounding the turning points of the zero contour, while the curvature is positive, are selected as solutions.

The sign of the AREA quantity defined above is the same as that of the tilt from which it is computed. Due to the method's dependence upon the change of sign of the distribution, the AREA quantity is therefore not required for the proper functioning of the method and making use of the MSTD distribution is sufficient.

## Strengths and Weaknesses of Multi-Scale Tilt Depth Estimation

### Model types

The method, applied to the pole-reduced total magnetic intensity, has proven effective when applied to sheet / dyke-like models but fails to return correct depth estimates when applied to contact models. These model types have been shown, by Stavrev et al. (2007), to vary in terms of their degree of homogeneity, when applied to the pole-reduced total magnetic intensity, as follows:

- 1 for plates, equivalent thin layers and dykes
- 2 for contacts

When applied to higher order derivatives, the degree of homogeneity changes by the order of the derivative. Making use of this relationship, the MSTDE method has been applied to the analytic signal amplitude of the first vertical derivative of the total magnetic intensity in order to improve the estimation of the depth of contacts. There is an obvious disadvantage when applied to derivatives of the original field - derivatives have relatively higher levels of noise than the original field due to the high pass effects. This is, in part, mitigated by the application of further smoothing iterations, as described in the following section, to the original field prior to the computation of the vertical derivative and analytic signal amplitude, which then forms the input to the depth estimation algorithm. This is by no means

the most effective method of noise suppression and this aspect has potential for further improvement and optimization, but falls outside the scope of this work. The variation in the MSTD distribution is illustrated in Figure 13 and Figure 14 for the model shown in Figure 15.

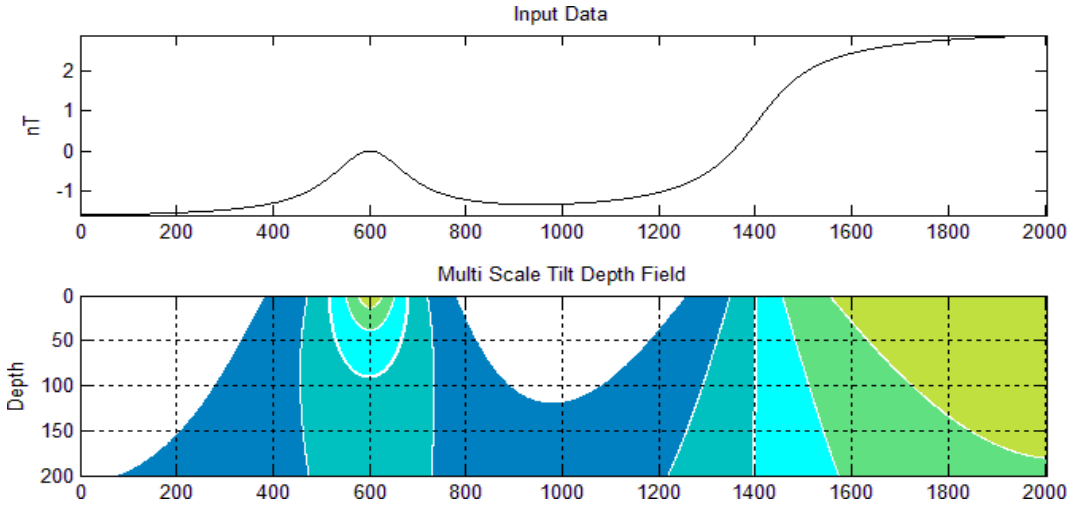


**Figure 13. The Multi-Scale Tilt Depth distribution computed from the total magnetic intensity for a dyke/sheet and for a step of the same depth of 100 units.**

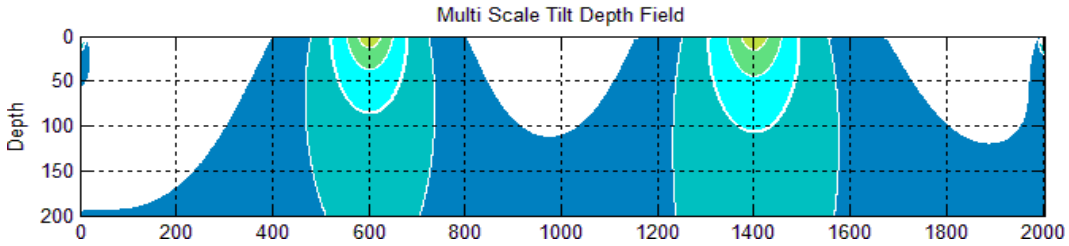


**Figure 14. The Multi-Scale Tilt Depth distribution computed from the AS(VD(TMI)) for a dyke/sheet and for a step of the same depth of 100 units.**

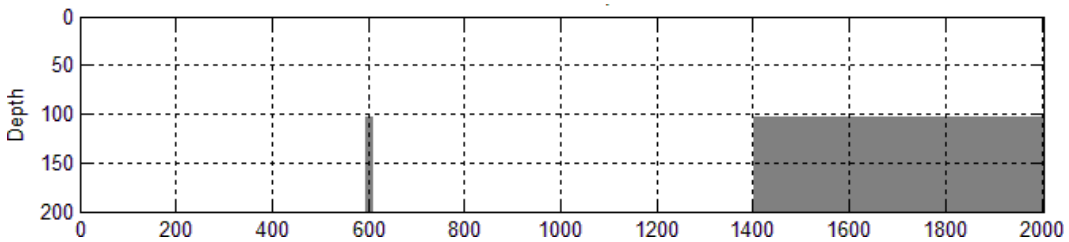


**Figure 15. The model used to produce the dyke/sheet and step responses shown in Figure 13.**

**Noise**

In the original paper by van Buren (2009), various implementations of the method were presented as listed below:

- MSDepth – the standard algorithm (MSTDE) making use of the known centre positions of the source models
- MSDepth_RG – designed as a response to the poor performance of the standard algorithm in the case of added noise, also solved at the known centre positions of the source models
- MSDepth_E3D – the standard algorithm, but solved at positions derived from the peaks of the analytic signal amplitude (as with 3D Euler)

The aim of the MSDepth_RG implementation was to mitigate the dramatic reduction in accuracy due to added high frequency noise. This was achieved by conservatively, spatially, low-pass filtering the pole-reduced total magnetic intensity at a wavelength equal to the upward-continued distance, for each continuation step before computing the tilt. The reason for applying this filtering prior to the computation of the tilt is due to its strong normalization effect. If noise is present in the original data, it is greatly accentuated in the tilt. This approach gave drastically improved results and it was indicated by van Buren (2009) that there existed scope for improvement by better defining the wavelength of interest.

The option of implementing a frequency domain smoothing at a cut-off wavelength equal to the upward continuation distance was investigated. The smoothing filter was defined by making all frequency coefficients corresponding to wavelengths greater than the continuation distance 1 with a cosine roll-off to 0 and is illustrated in Figure 16. The effect of this filter when applied to noise polluted data is shown in Figure 17. The application of a subsequent iterative spatial smoothing was introduced to handle data with extreme noise amplitudes. This spatial smoothing is

achieved by iteratively applying a three element kernel [0.25 0.5 0.25] to the input data. However, the data is smoothed by an increasing number of iterations as the continuation distance increases. The number of iterations increases stepwise and linearly from 1 iteration at the first level of continuation, up to the number chosen by the user at the final level. Within the code presented here, both the frequency domain and spatial smoothing loop may be bypassed by choosing zero iterations.

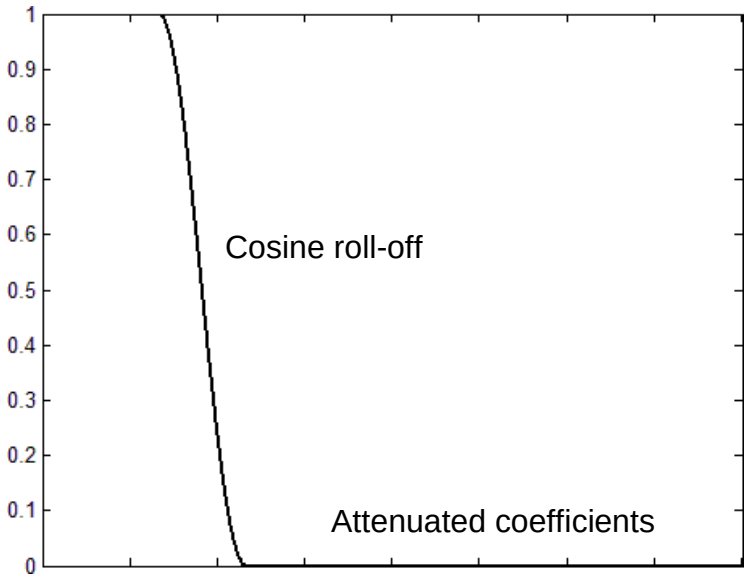


**Figure 16. Example of the frequency domain filter used to low-pass data prior to tilt computation.**

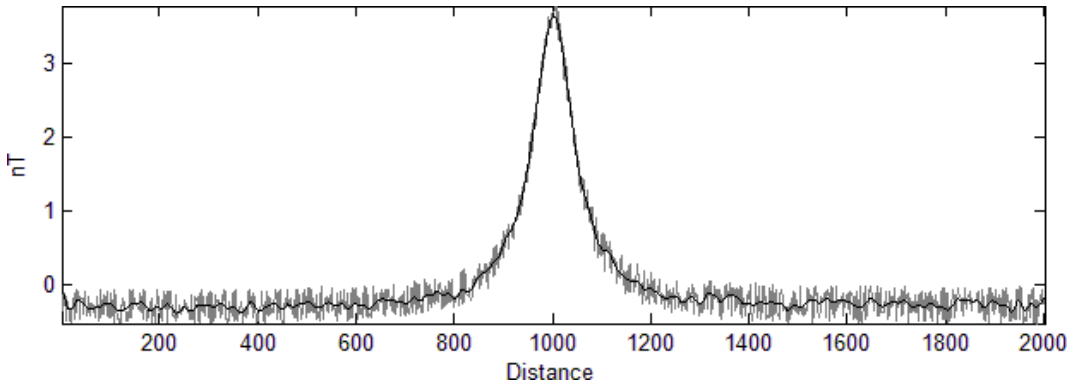


**Figure 17. Original noise polluted data and low-pass filtered data at a cut-off wavelength of 100 distance units.**

**Interference**

The effect of a regional, non-constant field can in many instances be equated with interference of the anomalous responses from proximal sources. The effect of proximal source fields is poorly handled by the method. The interference at lower frequencies from a fixed multi-source distribution is more significant than at the higher frequency components. Due to the method's dependence upon the lower frequency information in the field, which is retained during upward-continuation, proximal source fields have a substantial effect on the estimated source depth. This effect is visibly manifested in the continued distribution, which is noticeably distorted as per Figure 18.

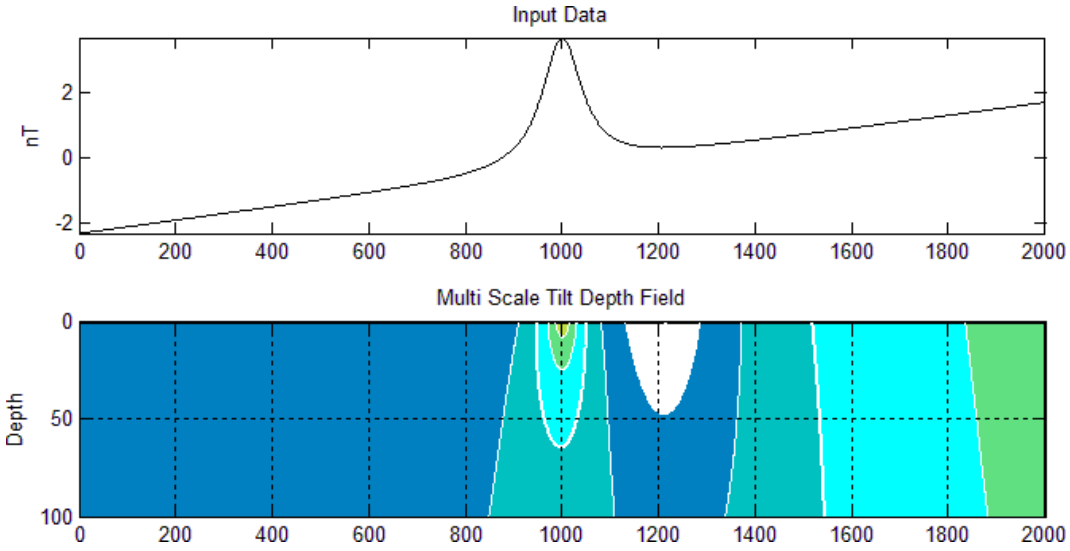


**Figure 18. Linear trend added to synthetic anomalous data produces a trend in the MSTD distribution .**

# CHAPTER 3: USE OF THE PROGRAM

The code for the execution of the program, which may be found in the Appendix A, was compiled in Matlab. The code accepts a 2-column ascii, comma delimited data file, the name of which must be fully qualified including the file extension. The format of the columns is such that the 1-dimensional position of a data point along the profile is specified in the first column with the corresponding magnetic field intensity in the second column. The units of distance output by the code will correspond with those specified in the input data. The assumptions are made that the data are specified monotonically with respect to distance and that the magnetic field intensity is in nanotesla. The code makes provision for data specified at non-regular intervals, interpolating the data onto regularly spaced positions equal in number and overall profile length to the original data. Prior to this interpolation, the data are conditioned to remove outliers by ensuring that within a 3 element kernel, the difference between the centre point and the median of the kernel is less than the standard deviation of the same kernel. Care is taken at the extremes of the profile where the two end points at each end are smoothed by extending the gradients of the previous two data points as shown in Figure 19.

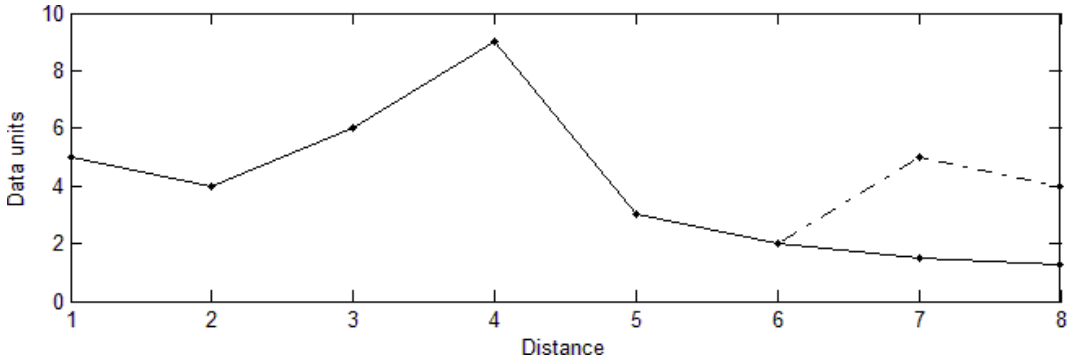


**Figure 19. An example of the conditioning applied at the two endpoints of the profile (Solid line connects the conditioned points, dashed line connects the original data).**

In order to perform the required frequency domain operations, Fast Fourier Transforms, herein referred to by the standard abbreviation, FFT, are applied to the data. Due to the use of FFT processes, the data requires further conditioning. This conditioning should ensure that the data are continuous, smooth and differentiable at every point. In order to achieve this, the data are padded out by one and one half lengths of the original profile. The data values are inverted about the nearest endpoint value and in respect of distance. These inverted profiles are attached to each end of the profile along with additional zeros, half the length of the original profile. This padded profile is then tapered with the piecewise function, making use of cosine tapers, shown in Figure 20.

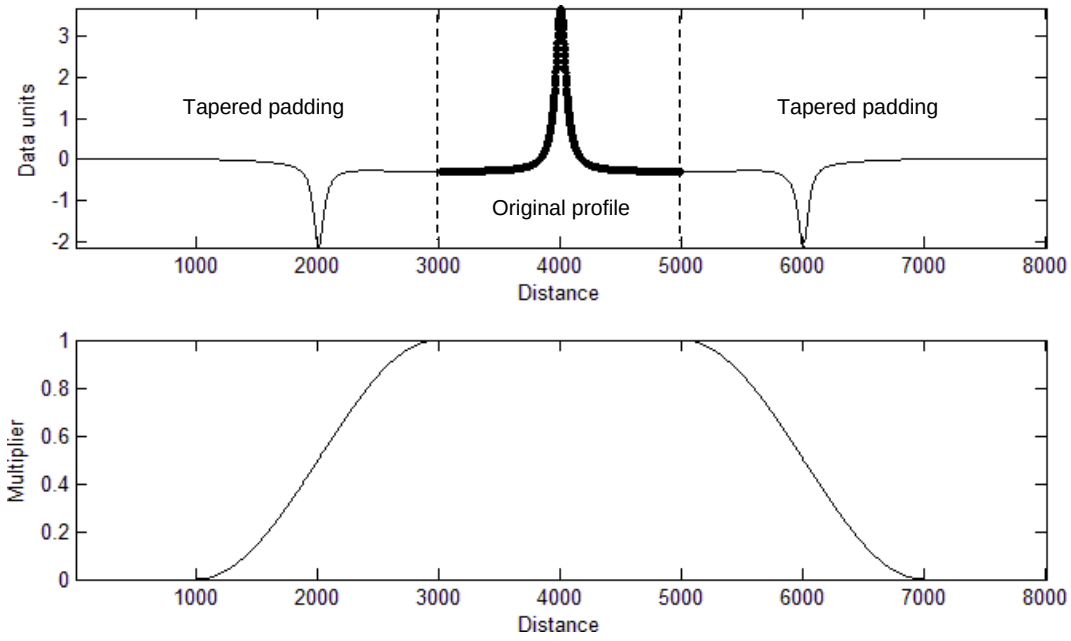


**Figure 20. An example of data which has been padded and tapered (Top), the attenuation factor applied to the padded data (Bottom).**

Once the data are properly conditioned for the subsequent use of Fourier type filters, the option is presented to the user to remove a regional field. The regional field is created via upward continuation of the data by a distance equal to one eighth of the profile length. This distance was decided upon empirically based on the assumption that such a continuation distance would sufficiently separate signals of interest from

those inadequately represented by the profile given its length. This regional removal may be done in a more tailored fashion externally and prior to executing the program. This regional field is then subtracted from the original data resulting in the residual data utilised from here on. At this stage the option has been inserted to allow the addition of random white noise. The amplitude of this noise is determined as a percentage of the standard deviation of the data. Once the noise component has been added to the data the entire padded profile is re-tapered using a similar function to the one shown in the figure above to ensure proper conditioning at the edges. It should be noted that the frequency of the noise which is added is controlled at the high end by the data spacing.

The data are now ready for input into the chosen algorithm. Here the choice is presented to the user to compute the tilt field from the original total magnetic intensity or from the analytic signal amplitude of the vertical derivative of the total magnetic intensity (AS(VD(TMI))). This choice, as elaborated upon within Chapter 2, is due to the method not solving for the depth to step-like features from the total magnetic intensity. The use of this second option is cautioned due to the high order of derivatives employed. Some care is taken here to reduce the noise amplification by allowing the user to specify the amount of smoothing prior to the derivative computations. During the iterative derivations the profiles are also re-padded and tapered which has been found to be necessary.

The subsequent operation sets up the 2D array of stacked profiles which will be transformed into the 2D tilt field. In this step, depth-variable low-pass filtering is applied both in the frequency domain and spatial domain as described in Chapter 2. The tilt field is then computed from this filtered array as per equation 2.1. Now that the data are adequately prepared the final transformation into the Multi-Scale Tilt Depth (MSTD) field can be conducted. Each level of the conditioned tilt array is upward continued by an incremental amount as per equation 2.2. In this code, each level

represents an increment of 1 distance unit; therefore the number of levels computed will be equal to the total depth requested by the user and the problem would have an order proportional to $d1$ ($d =$ total depth). This topic is highlighted by van Buren (2009), wherein it states that an improvement in computational efficiency may be had by increasing the interval of continuation in a non-linear fashion at subsequent levels. This recommendation was made primarily due to the reduction in vertical resolution at increased depths. A scheme might be easily implemented where the continuation interval were increased to 110% of the previous interval. A simple modification such as this would achieve a four times increase in speed to compute to a continuation level of 100 distance units and would have a vertical resolution of 10 units at the last level. Figure 21 illustrates the improvement achieved by such modification.

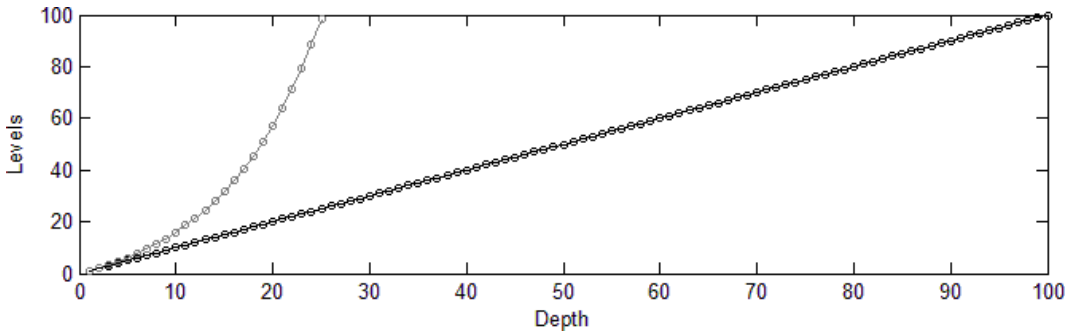


**Figure 21. Non-linear increase in the continuation distance per level to achieve improvements in the speed of computation.**

Now that the MSTD distribution is computed the solution locations may be determined. van Buren (2009) assessed the solution positions by either querying the distribution at the known lateral position of the synthetic sources, or by solving at the peaks of the analytic signal amplitude of the input data. This second solution strategy was again attempted but found to be quite sensitive to noise in the input data, therefore, a new solution strategy was adopted where the turning point of the zero contour of the MSTD distribution is sought. This is done by computing the horizontal derivative of the zero contour and choosing locations where the product of

adjacent derivative points is negative or zero. A plot of such solution locations is shown in Figure 22.

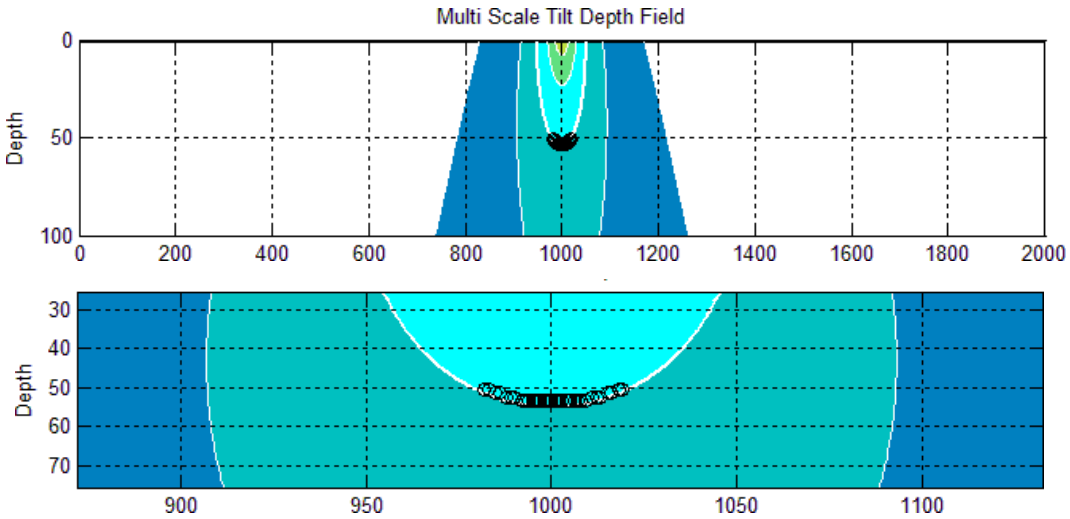


**Figure 22. MSTD distribution with solution locations determined at the turning point of the zero contour (Above), Zoomed into solution locations (Below).**

Late in the development of the solution strategy it was decided to iterate the entire procedure facilitating the addition of a number of permutations. The user may choose to have a different random noise (with the same statistical distribution) generated at each iteration, and the dataset run through the program. A further choice is given to the user, independent of the noise addition, to increment the smoothing per iteration by a fixed number of smoothing passes. The combination of these options results in at least four distinct permutations. The result of each iteration is assimilated and after all the iterations, the results are plotted as a solution density image, an example of which may be seen in Figure 23 and Figure 24. The assimilated solutions are also plotted as a histogram of their depths as in Figure 25. This approach allows the user to gain further understanding as to the variability of the solution location set with respect to noise as well as the extent of smoothing. This noise may be chosen to approximate the amplitude of the noise in the source data.

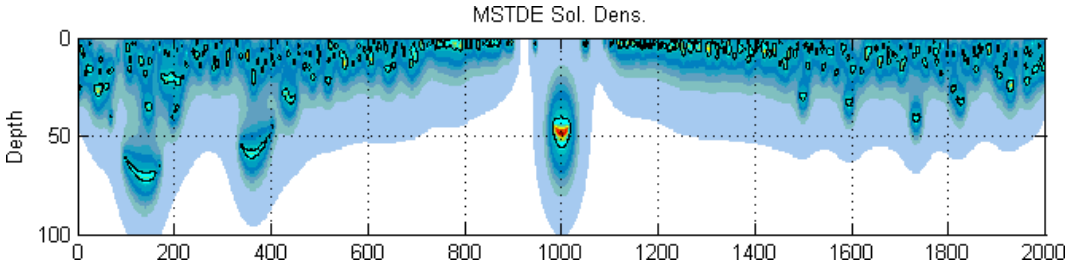


**Figure 23. Solution density image illustrating a high solution density near the source's location.**

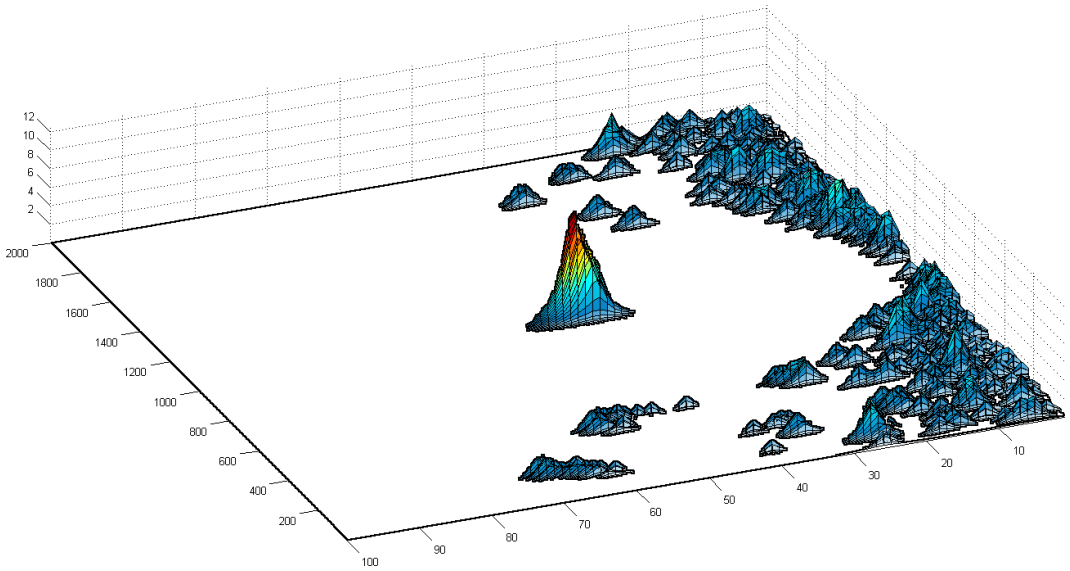

**Figure 24. 3D view of solution density illustrating a high solution density near the source's location.**

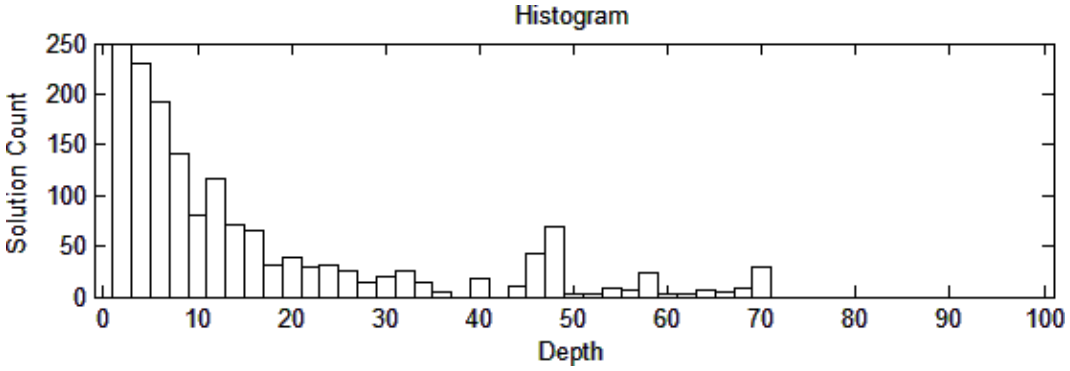


**Figure 25. A histogram of solution depths illustrating an increased solution density near the source's depth (50 distance units).**

# CHAPTER 4: APPLICATION OF MULTI-SCALE DEPTH ESTIMATION TO SYNTHETIC DATA

## Creation of the Synthetic Data

Synthetic data have been created to test the performance of the program to various model types and sources of interference. The data have been computed in Encom's ModelVision, Version 11.00, Release Build 1. The profile length is kept constant for the various models at 2000 distance units. The data spacing are also kept constant at 1 distance unit, ensuring significantly oversampled responses in most cases. All data were computed with a vertical inducing field of 10 000 nT and a susceptibility of 0.0010 CGS (0.0126 SI).

The various model profiles computed include:

- A sheet 10 distance units wide at a depth of 10, 20, 30, 40, 50, 60, 70 & 80 distance units
- The same sheet at a depth of 50 distance units with a dip of 10°, 20°, 30°, 40°, 50°, 60°, 70° & 80°
- The same sheet at a depth of 50 distance units with uniform noise added, the amplitude range of which is equal to 10%, 25%, 50% & 100% of the standard deviation of the original data
- Two sheets as specified above with variable centreline separation about the profile centre of 20, 50, 100, 200 & 400 distance units
- Data were produced over an infinite step at a depth of 50 distance units

## Results and Comparison of the Application of Multi-Scale Tilt Depth Estimation to Synthetic Data

The results of the application of the MSTDE method to the synthetic model data described in the previous section are collated and presented here. Summaries of the results of the depth estimation are presented in two standard graph types (See Figure 31). The first is a plot of the estimated depth while the second represents the error in the depth as a percentage of the true depth of the model. For each of the model types an example of the model response and various derived products as per Figure 27, as well as the MSTD distribution and solution densities as per Figure 28, are shown. Schematics of the various model types are illustrated in Figure 26.

### Synthetic model types

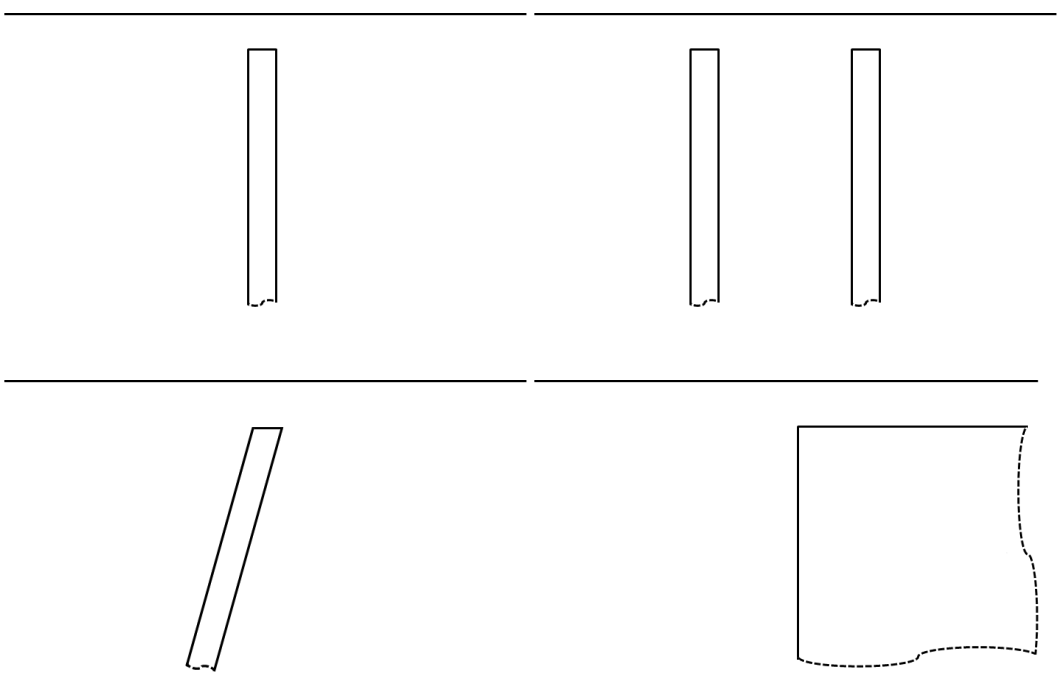

**Figure 26. Schematics of the various synthetic model types employed in this study are shown. Single vertical sheet (Top left), Multiple vertical sheets (Top right), Dipping sheet (Bottom left) and Contact in the form of a step (Bottom right).**

## Schematic of figures

The following figures represent a standard format for the figures to follow and are here described.

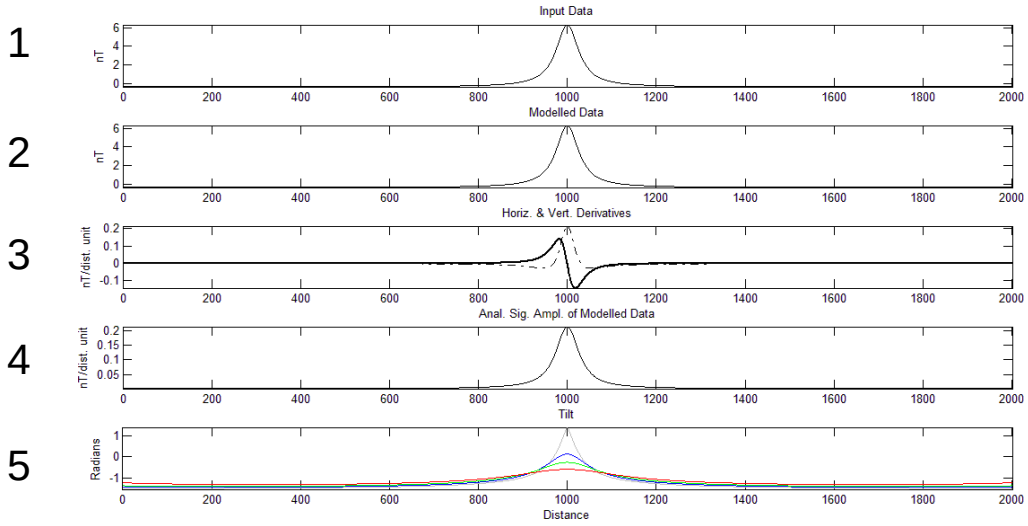


**Figure 27. Schematic of data and various derivatives.**

The subplots within Figure 27 contain:

1. A line plot of the input data profile to the program
2. A line plot of the modelled data quantity
3. Horizontal (Solid) and vertical (Dashed) derivatives of the modelled data quantity
4. The analytic signal amplitude of the modelled data quantity
5. Various upward continuations of the tilt of the modelled data quantity (distance equal to 0, 25, 50 and 100% of the total section depth)

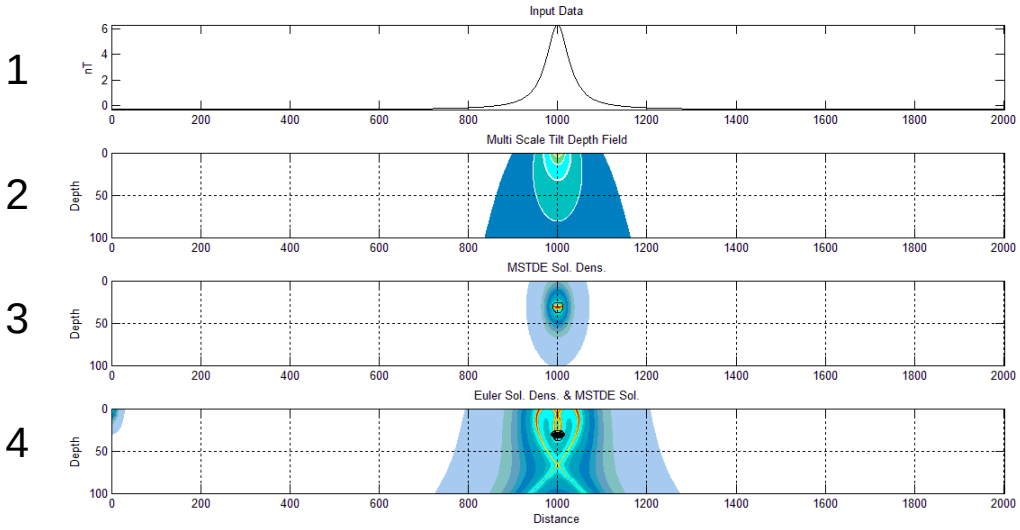


**Figure 28. Schematic of data and various section images.**

The subplots within Figure 28 contain:

1. A line plot of the input data profile to the program
2. The MSTD distribution plotted as a solid contour plot; The zero contour is plotted thicker
3. The MSTDE solution density plotted as a colour image with an arbitrary contour surrounding regions of high solution density for correlation across subplots
4. The Euler solution density plotted as a colour image with an instance of MSTDE solutions plotted as circles. The contour from the MSTDE solution density plot is replicated here

It must be stressed that only the intensities of the fields and not their geometries are affected by homogeneously varying the unit of distance. In this work, the generic distance unit was chosen to be the SI distance unit of 1 meter, resulting in the magnetic fields being reported in nanotesla.

On the use of colour images in order to portray the MSTD distribution and solution density, the author would like to provide explanation for the absence of colour bars for each of the images. The intent of the use of the

colour solution density images is to provide more clarity to the diagrams, especially when presenting solution locations as symbols, the plots would rapidly degrade into thick lines of solution symbols, preventing the determination of the densest region of solutions. A clear comparison of locations from different methods on the same plot would consequently be hindered. The use of colour density images then facilitates the determination of the location of the densest region of solutions by showing the relative solution densities. It is stressed that the location and not the absolute density of solutions is in fact what is intended to be emphasised to the reader.

The colour table shown in Figure 29 has been applied to the MSTD distribution and solution density plots and is illustrated here in order that the reader may be aware of the relative ordering of colours.


**Figure 29. Colour table applied to the MSTD distribution and solution density plots, cool colours on the left are associated with low values and warm colours on the right are associated with high values of the applicable quantity.**

## Vertical sheet at various depths

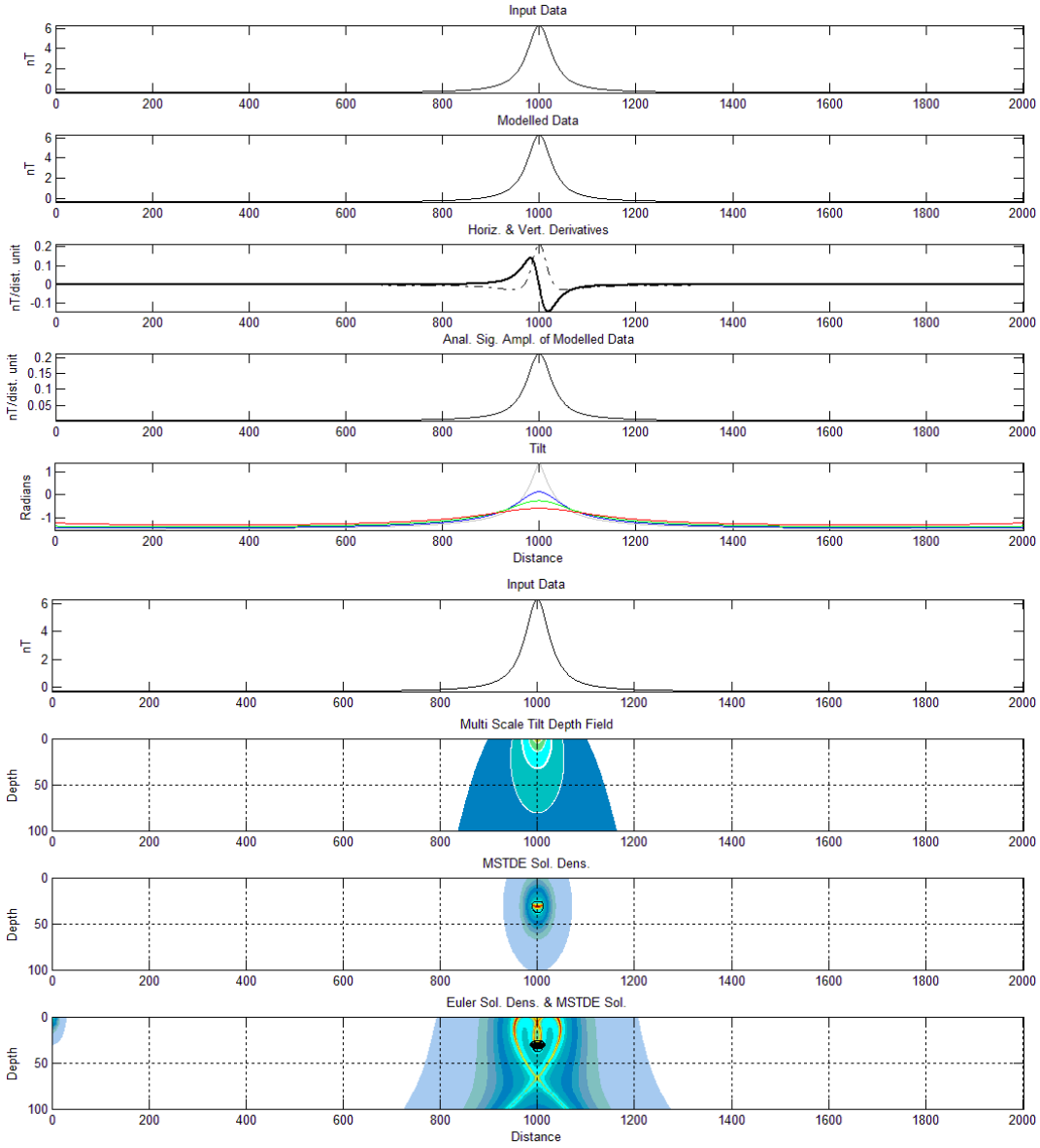


**Figure 30. Synthetic model data (Depth of 30 dist. units) with plots of the spatial derivatives, analytic signal amplitude and various continued tilt products (Top), Synthetic model data with MSTD distribution, MSTDE solution density and Euler solution density with MSTDE solution locations (Bottom).**

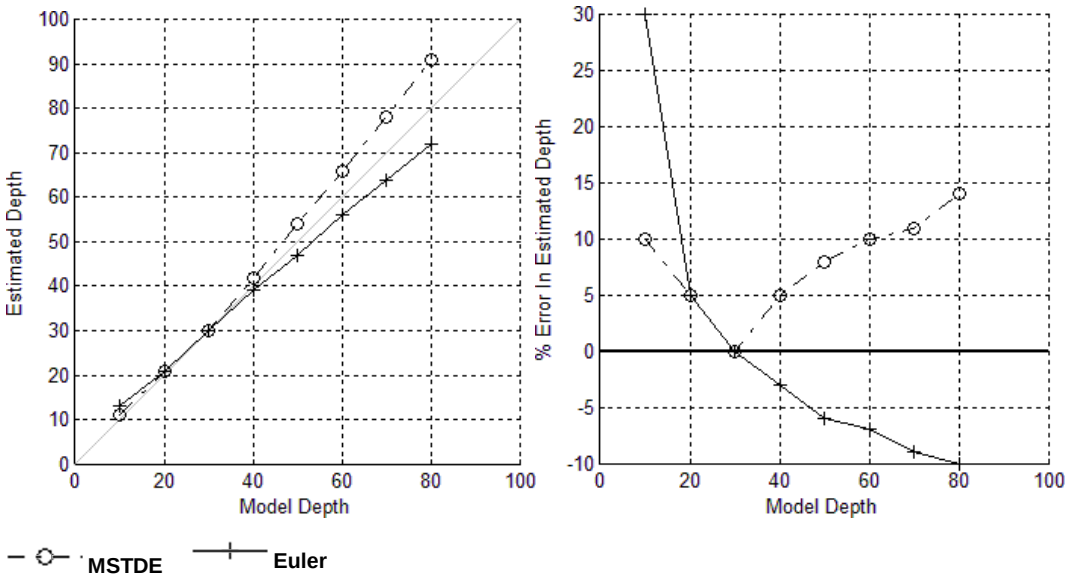


**Figure 31. Solution depths from MSTDE and Euler (Left), Percentage error in estimated depths (Right).**

## Sheet with various dips

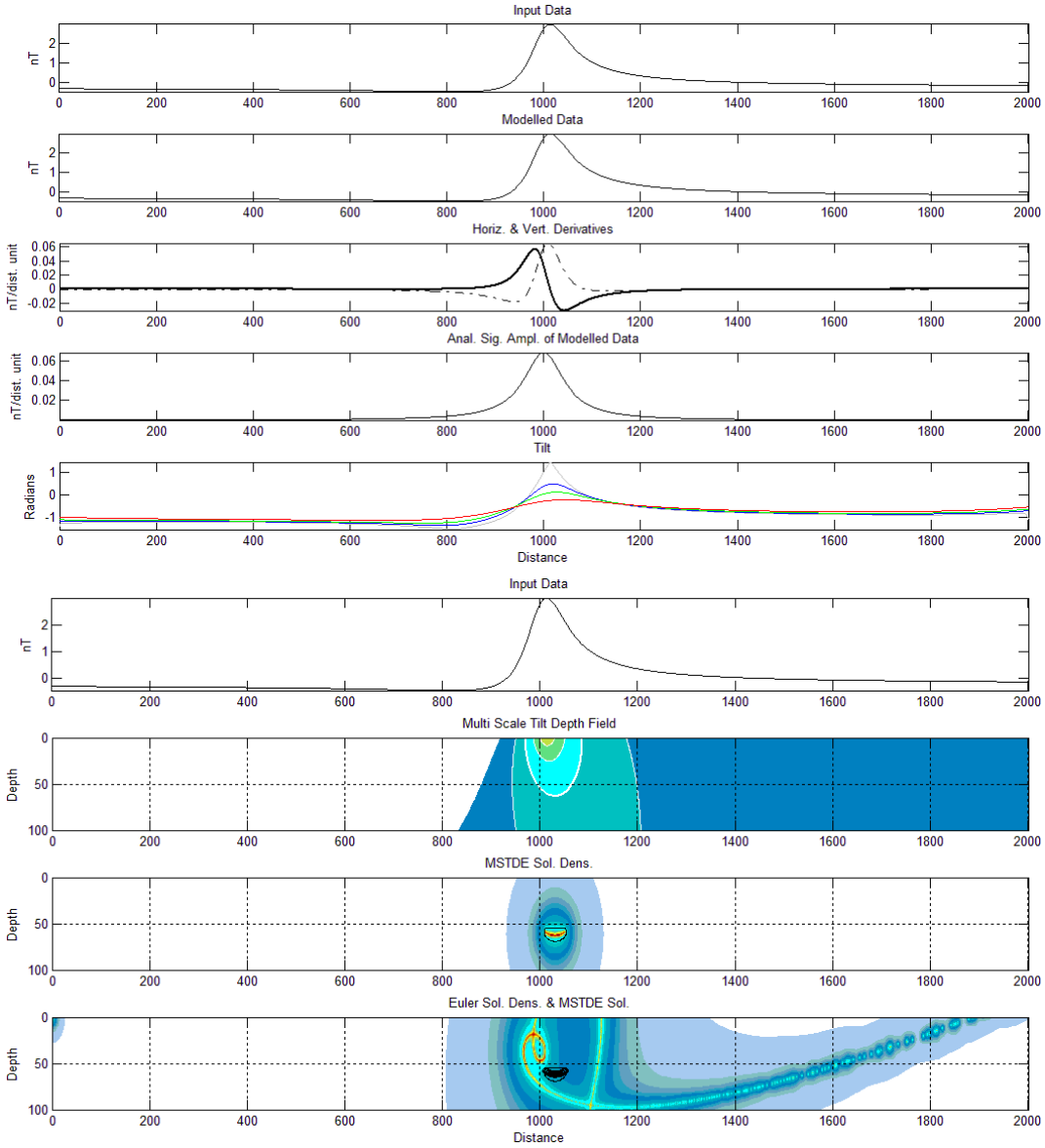


**Figure 32. Synthetic model data (60° dip, Depth of 50 dist. units) with plots of the spatial derivatives, analytic signal amplitude and various continued tilt products (Top), Synthetic model data with MSTD distribution, MSTDE solution density and Euler solution density with MSTDE solution locations (Bottom).**

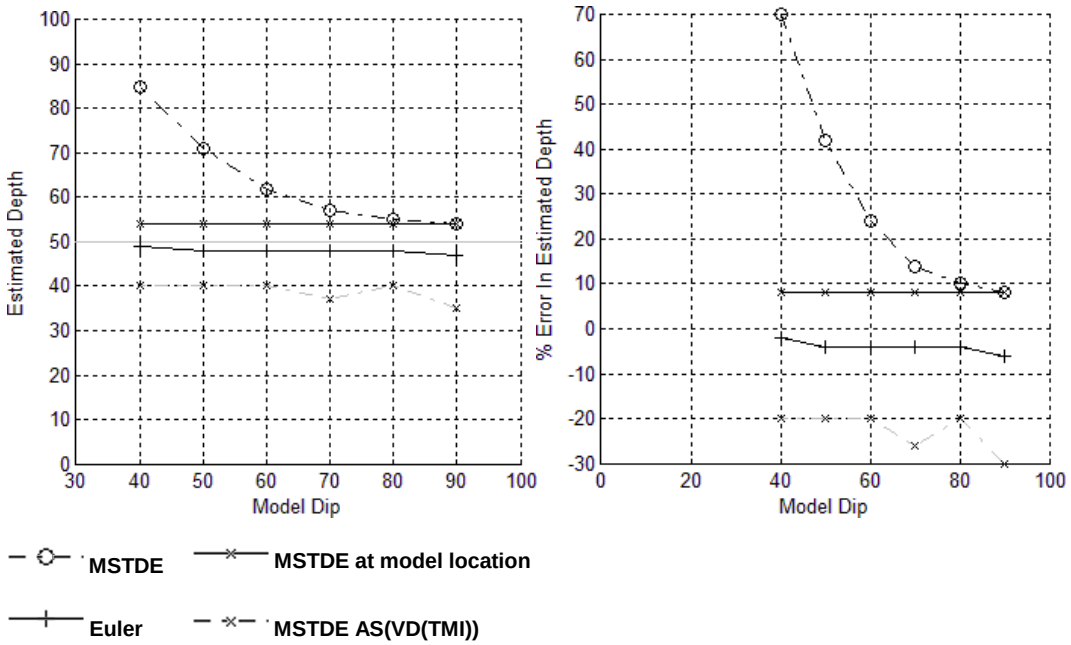


**Figure 33. Solution depths from MSTDE, MSTDE at known model location, MSTDE applied to the AS(VD(TMI)) and Euler (Left), Percentage error in estimated depths (Right).**

## Vertical sheet with various noise amplitudes

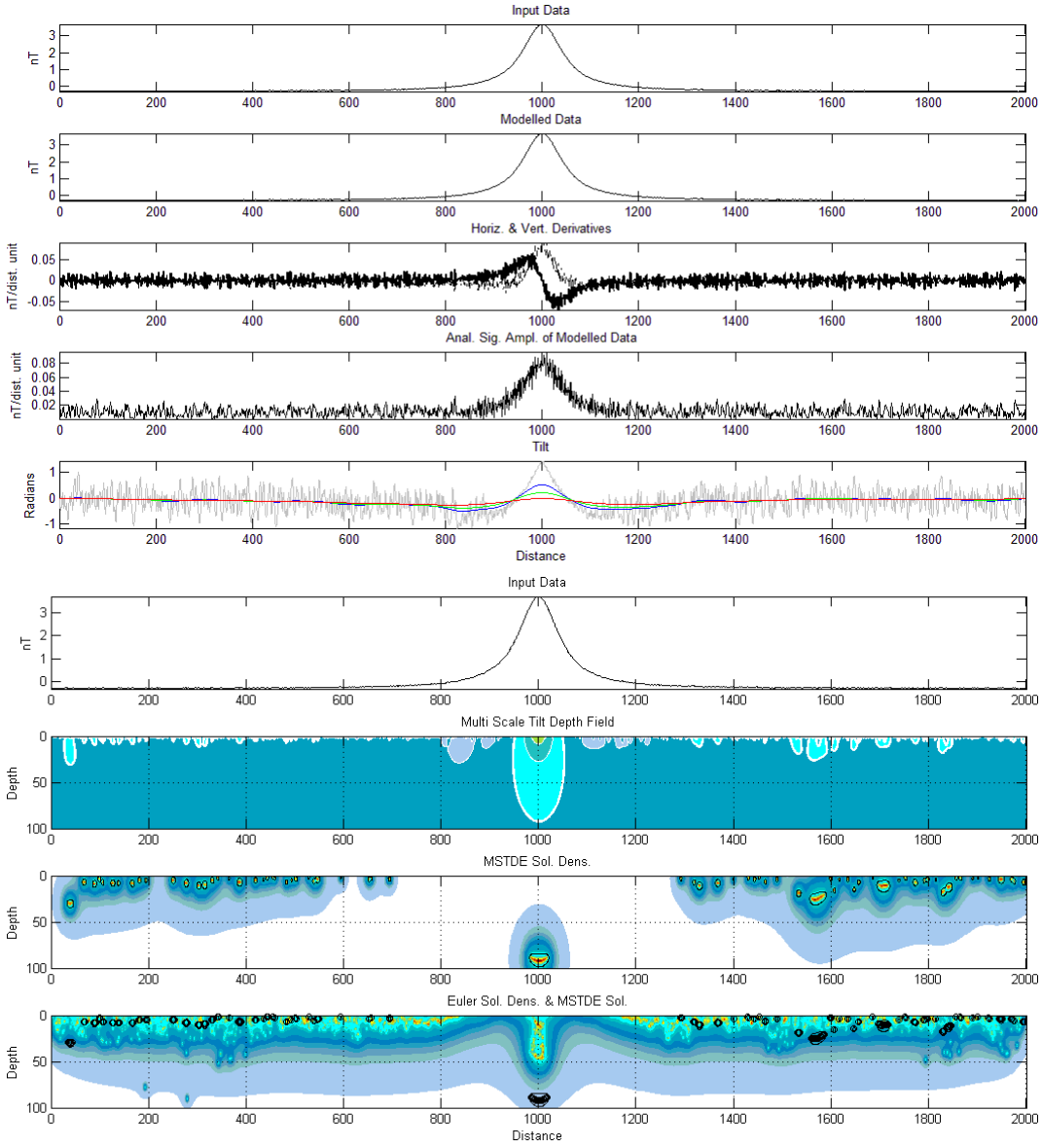


**Figure 34. Noise contaminated synthetic model data (Noise range of 10% of the standard deviation, Depth of 50 dist. units) with no smoothing applied. Plots of the spatial derivatives, analytic signal amplitude and various continued tilt products (Top), Synthetic model data with MSTD distribution, MSTDE solution density and Euler solution density with MSTDE solution locations (Bottom).**

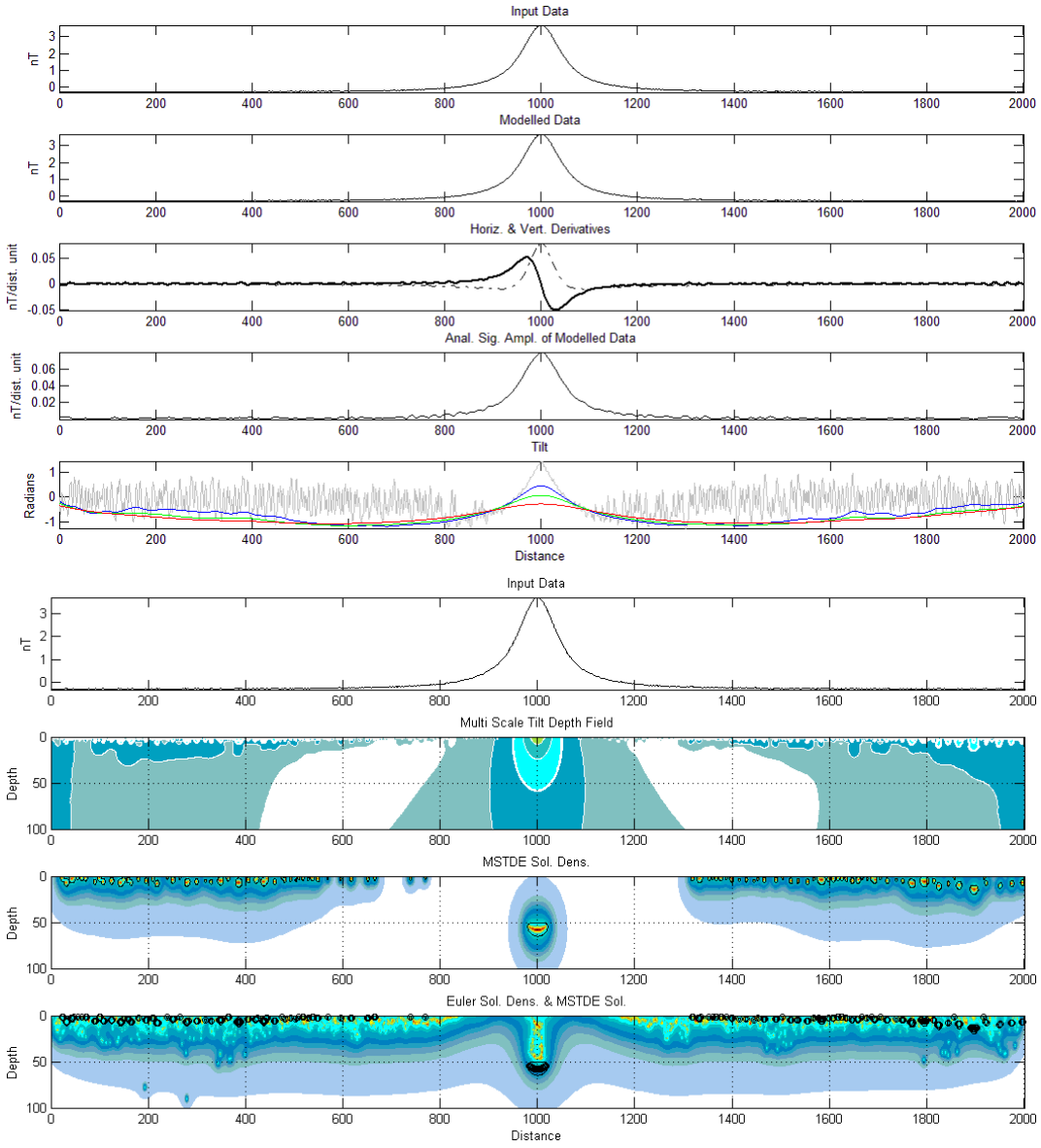


**Figure 35. Noise contaminated synthetic model data (Noise range of 10% of the standard deviation, Depth of 50 dist. units) with frequency domain and up to 100 iterations of spatial domain smoothing applied. Plots of the spatial derivatives, analytic signal amplitude and various continued tilt products (Top), Synthetic model data with MSTD distribution, MSTDE solution density and Euler solution density with MSTDE solution locations (Bottom).**

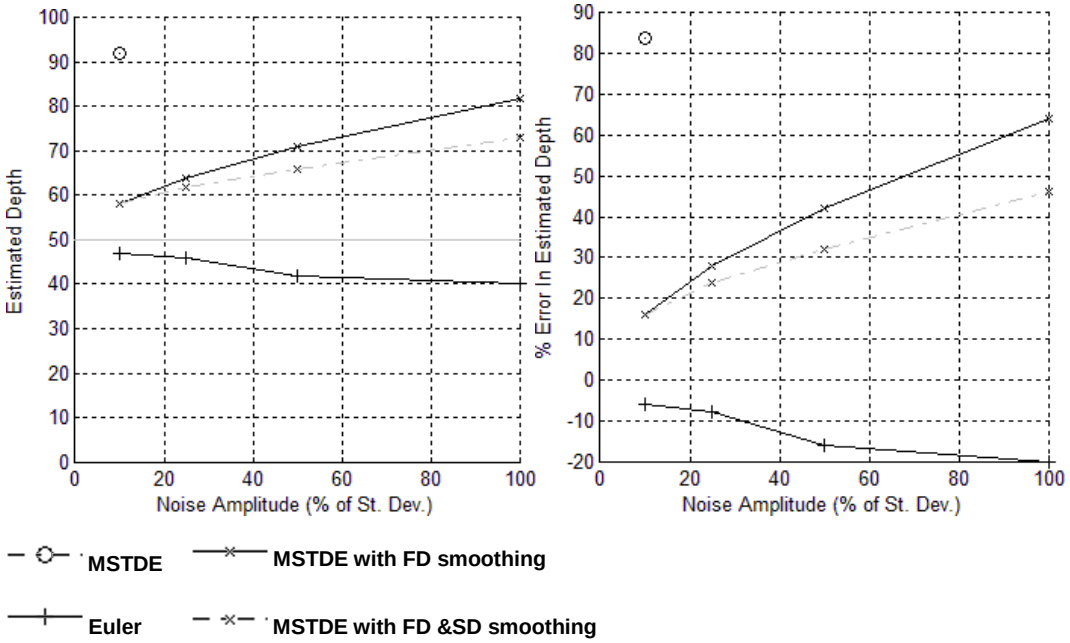


**Figure 36. Solution depths from MSTDE, MSTDE with frequency / spatial domain smoothing and Euler (Left), Percentage error in estimated depths (Right).**

## Multiple vertical sheets with various separations

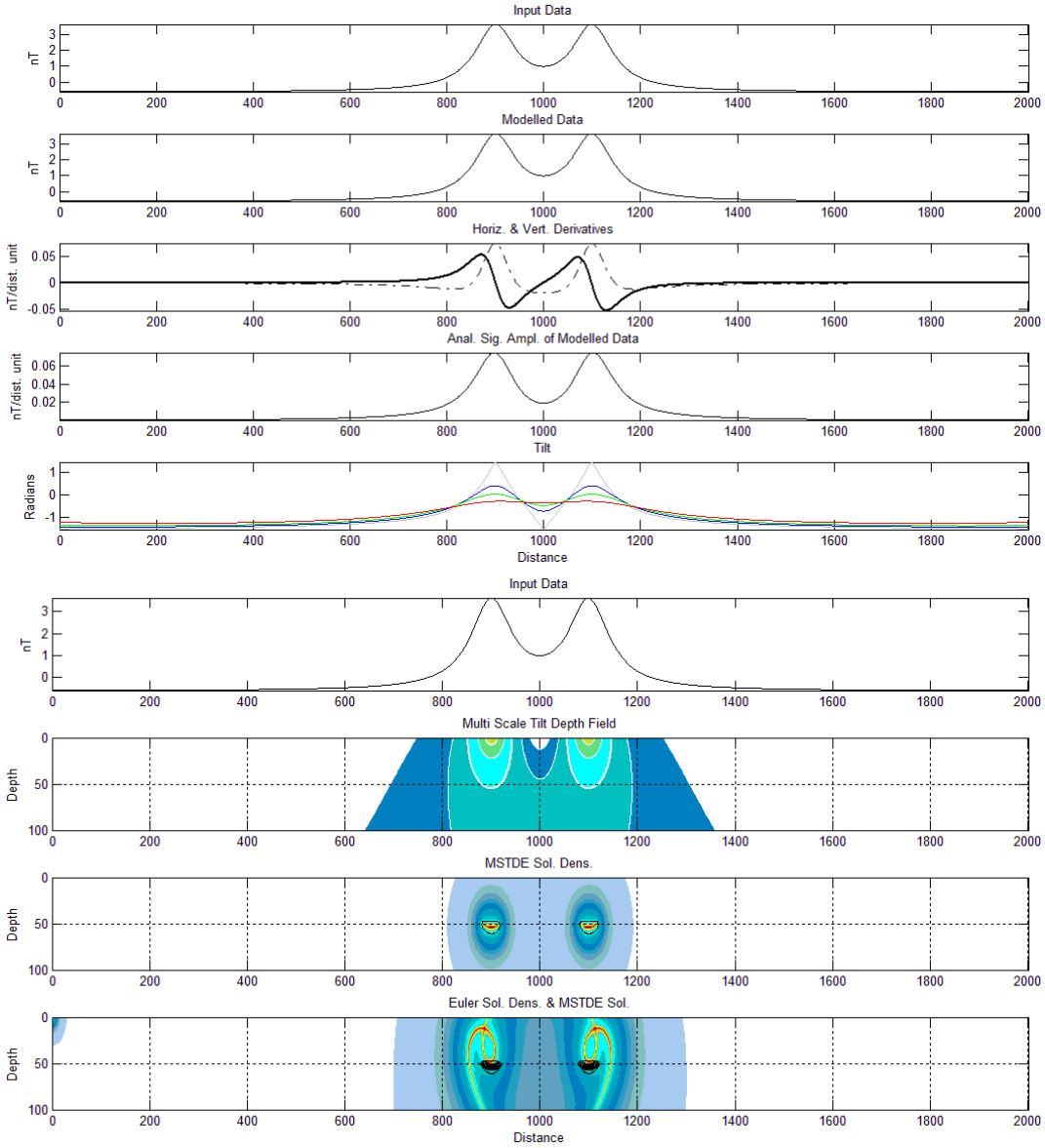


**Figure 37. Synthetic model data of two vertical sheets, the centres separated by 100 distance units. Plots of the spatial derivatives, analytic signal amplitude and various continued tilt products (Top), Synthetic model data with MSTD distribution, MSTDE solution density and Euler solution density with MSTDE solution locations (Bottom).**

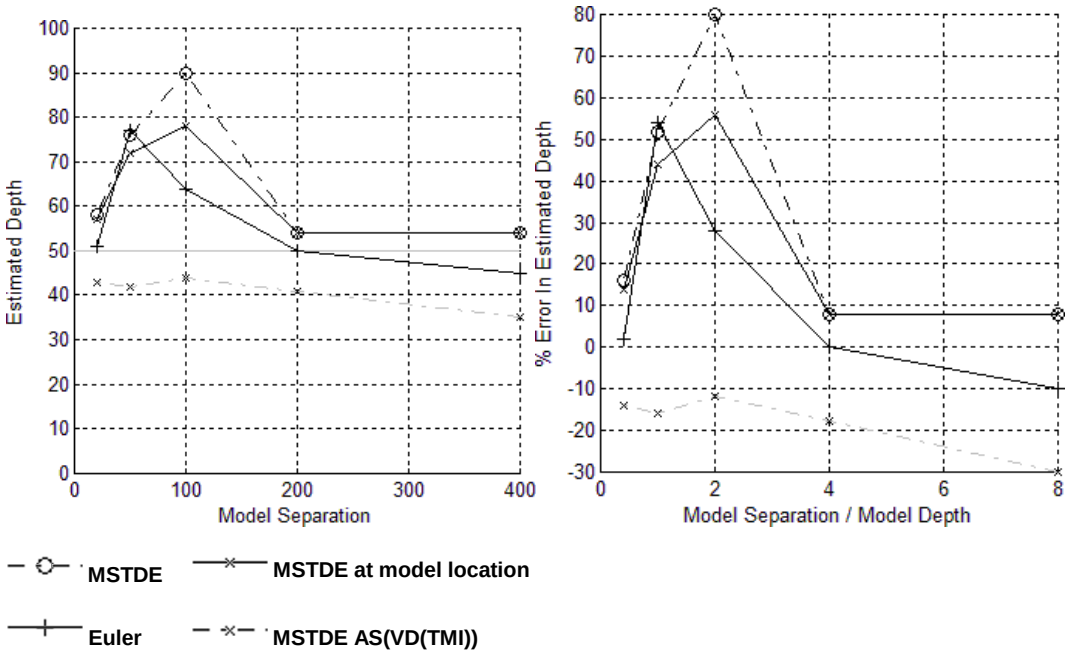


**Figure 38. Solution depths from MSTDE, MSTDE at known model location, MSTDE applied to the AS(VD(TMI)) and Euler (Left), Percentage error in estimated depths (Right).**

## Regional / residual separation

The regional field may be removed from the data prior to computation of the solutions in order to decrease the sensitivity to long wavelength interference due to proximal sources as well as to portions of sources at depths significantly deeper than the depth to top of the sources of interest.

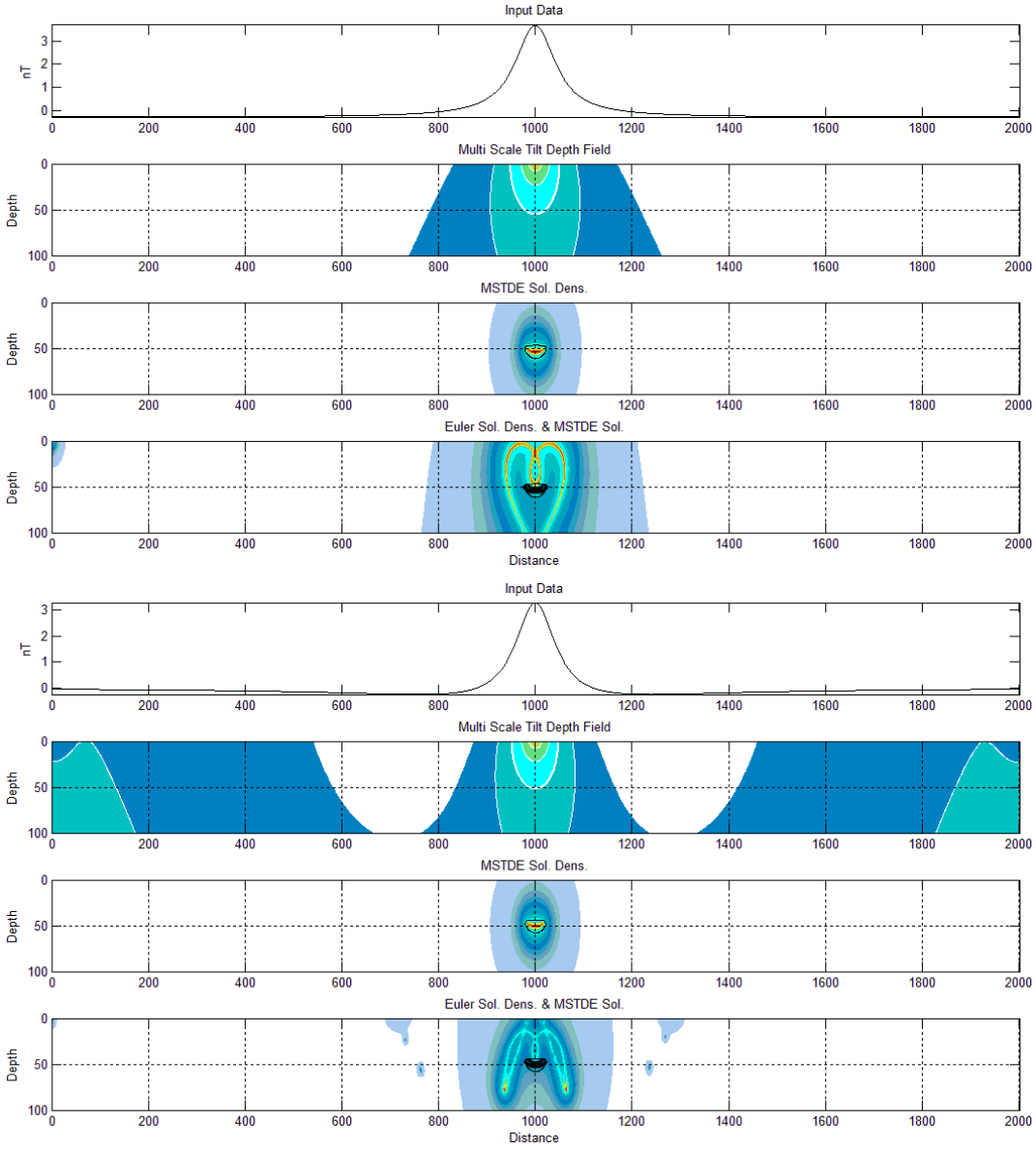


**Figure 39. Synthetic model data with MSTD distribution, MSTDE solution density and Euler solution density with MSTDE solution locations when applied to the total magnetic intensity (Top). The same quantities but applied to the residual intensity after removal of the regional field (Bottom). The estimated depths are 54 and 51 distance units respectively.**

## Contact model

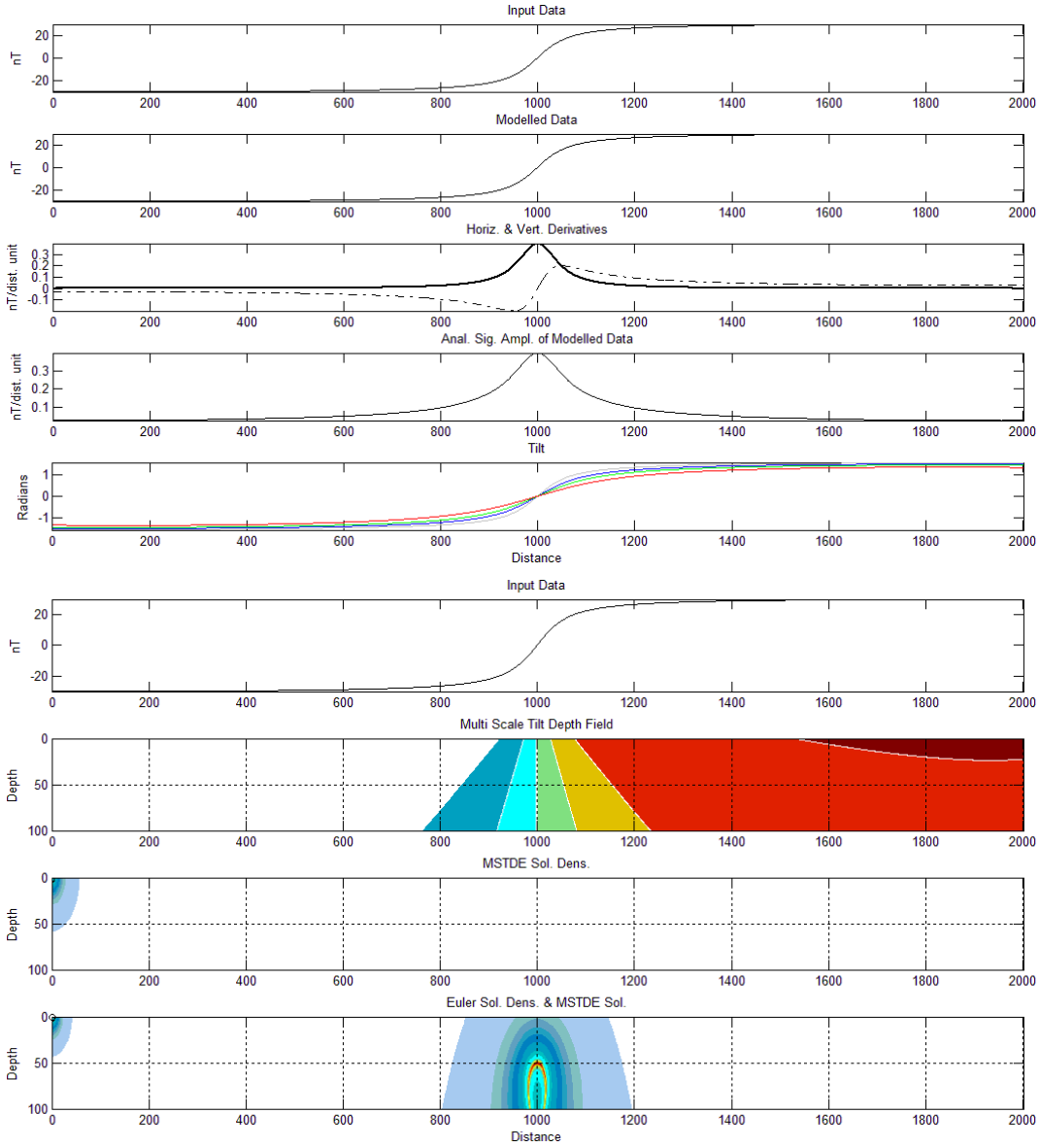


**Figure 40. Synthetic model data (Step at a depth of 50 dist. units) with plots of the spatial derivatives, analytic signal amplitude and various continued tilt products (Top), Synthetic model data with MSTD distribution, MSTDE solution density and Euler solution density with MSTDE solution locations (Bottom).**

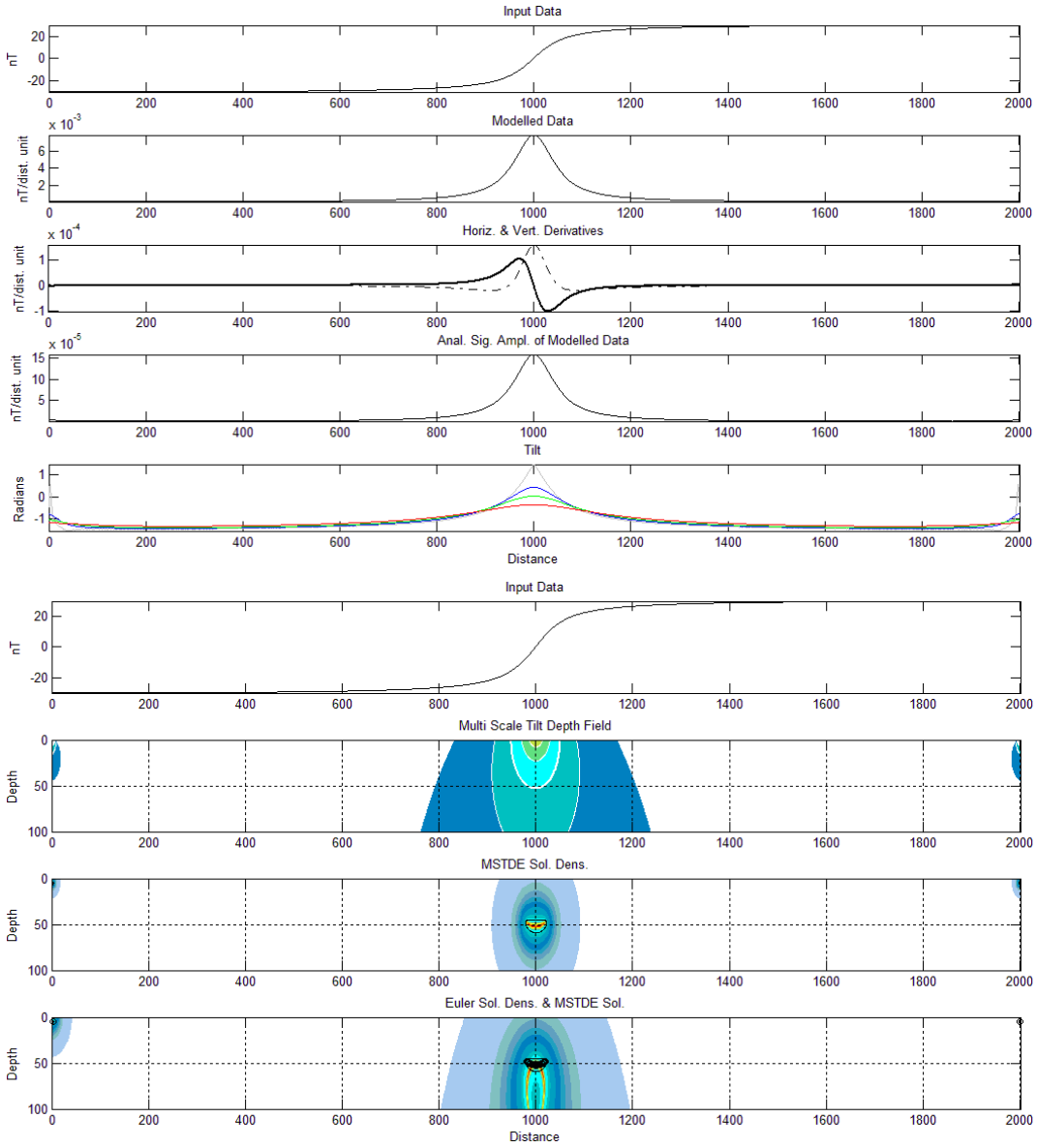


**Figure 41. Synthetic model data (Step at a depth of 50 dist. units) with plots of the spatial derivatives, analytic signal amplitude and various continued tilt products (Top), Synthetic model data with MSTD distribution, MSTDE solution density and Euler solution density with MSTDE solution locations (Bottom). The input data to the algorithm was the AS(VD(TMI)).**

# CHAPTER 5: APPLICATION OF MULTI-SCALE DEPTH ESTIMATION TO OBSERVED DATA AND PERFORMANCE REVIEW

## Field Example 1

### Choice of observed data

Due to the method being applicable to two-dimensional, correctly pole reduced data, data were chosen over dyke-like features with a near vertical magnetizing field. Such data was made available over a portion of the Bushveld Complex in South Africa and may be seen in Figure 43, which also shows the location of the profile. The data are in a map projection measured in meters, received in gridded format at a 15 m cell size and was acquired at a flight height of 50 m above the terrain. All depths stated herein are relative to the survey platform and not to the actual ground level. Figure 42 is a schematic of the near surface geology in the vicinity of the profile.

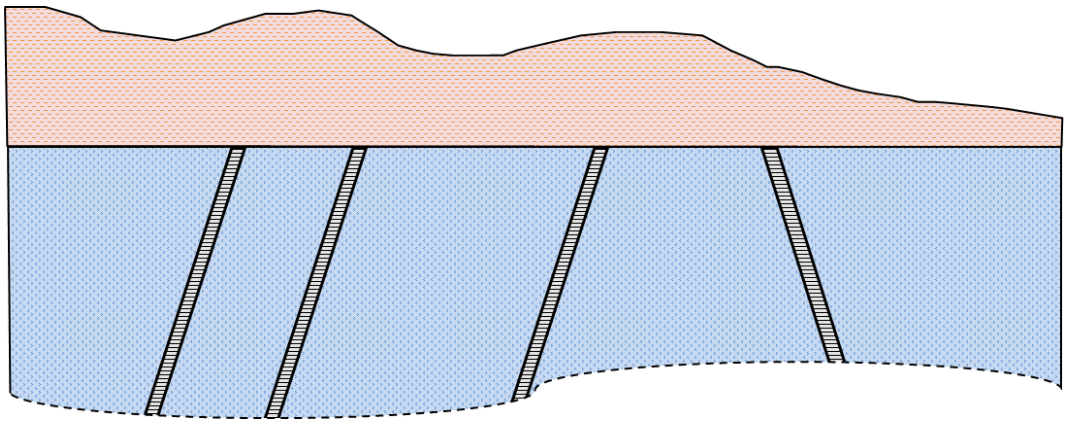

**Figure 42. Schematic representation of the near surface geology of the Bushveld in the immediate vicinity of the field data. The thin cover sequence (Red) overlies the igneous rocks of the Bushveld Complex (Blue) which have been cross-cut by mafic, magnetically susceptible dykes (Black).**

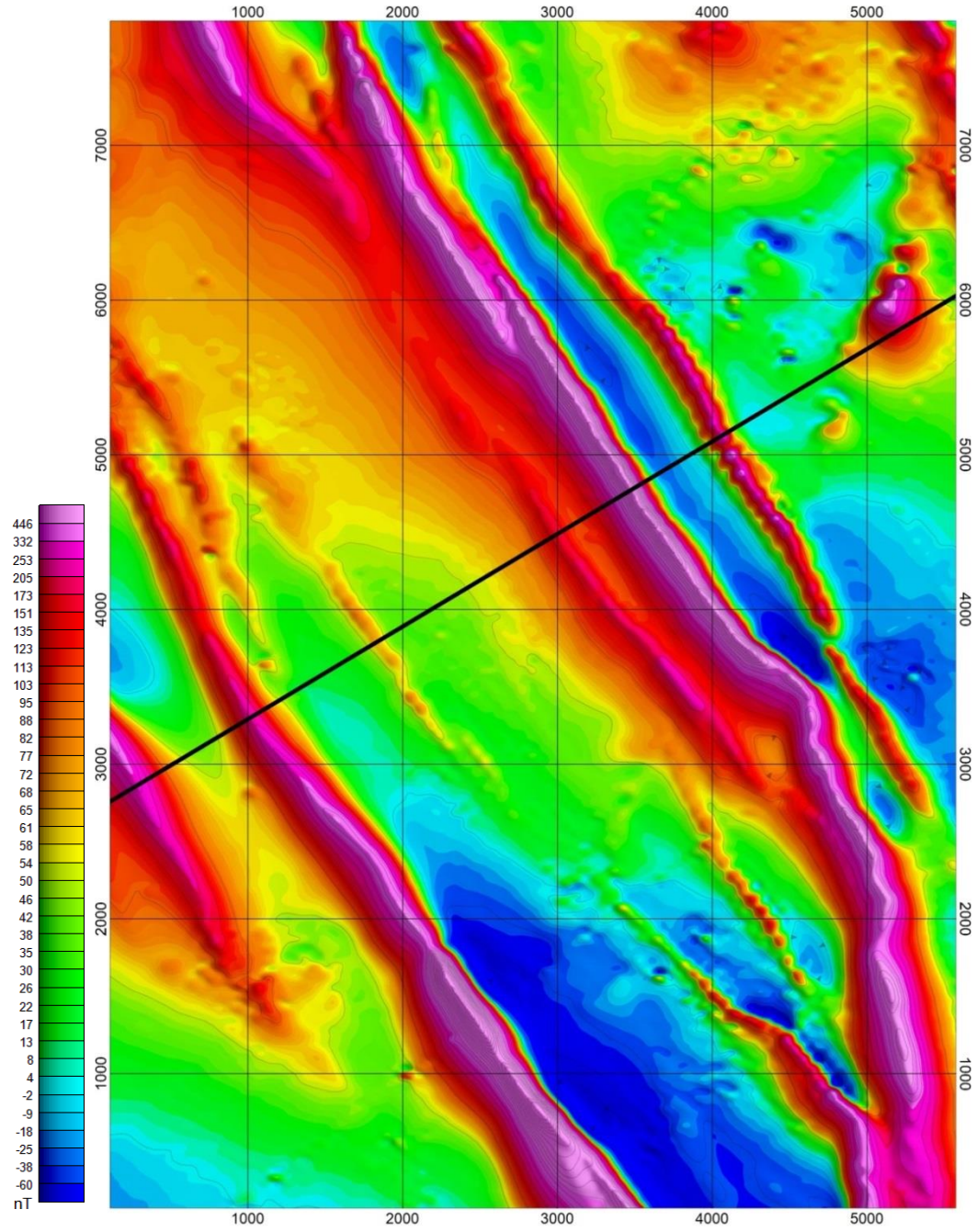


**Figure 43. Pole-reduced total magnetic intensity data over a region of the Bushveld Complex in South Africa showing the profile extracted for use in this example.**

## Modelling of observed data

The data were modelled using Encom's ModelVision, Version 11.00, Release Build 1. Bodies of type 'tabular' were used to represent the likely sources of the linear magnetic anomalies and their properties optimised via inversion. The anomaly located at a distance of approximately 6000 m along the profile was not modelled as it is not sufficiently 2D in nature. The inducing field intensity used in the modelling was 28370 nT with an inclination of -63° and a declination of -18°, as derived from the available IGRF information for the region. No remanence was introduced during the modelling. Table 1 and Figure 44 below illustrate the results obtained from this modelling. Figure 45 and Figure 46 illustrate the MSTDE results for the profile.

**Table 1 Positions, widths and susceptibilities of the modelled sources**

| Distance (m) | Depth (m) | Susceptibility (SI) | Width (m) | Susceptibility x width product |
|---|---|---|---|---|
| 382.6 | 149.1 | 0.52 | 25.2 | 13.1 |
| 1229.6 | 106.0 | 0.29 | 24.9 | 7.2 |
| 2141.0 | 72.4 | 0.17 | 8.3 | 1.4 |
| 3517.3 | 125.5 | 0.22 | 11.2 | 2.5 |
| 4096.8 | 78.2 | 0.50 | 37.8 | 18.9 |
| 4763.0 | 49.5 | 0.47 | 9.2 | 4.3 |

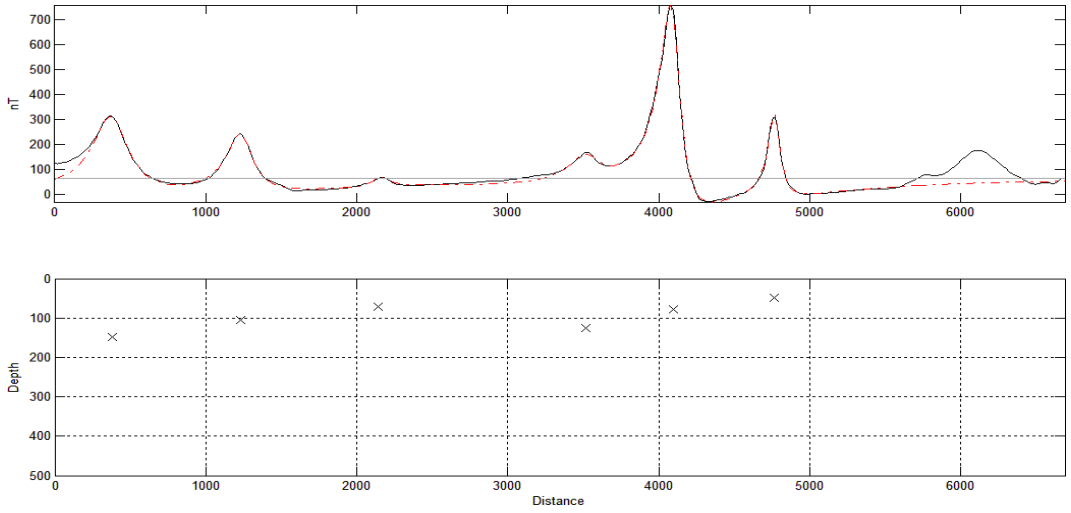


**Figure 44. Observed total magnetic intensity data (Black) with regional (Gray) and modelled intensity (Red, dashed) (Top). Modelled source locations are plotted as "x" (Bottom).**

**Results of the application of Multi-Scale Tilt Depth Estimation to observed data**

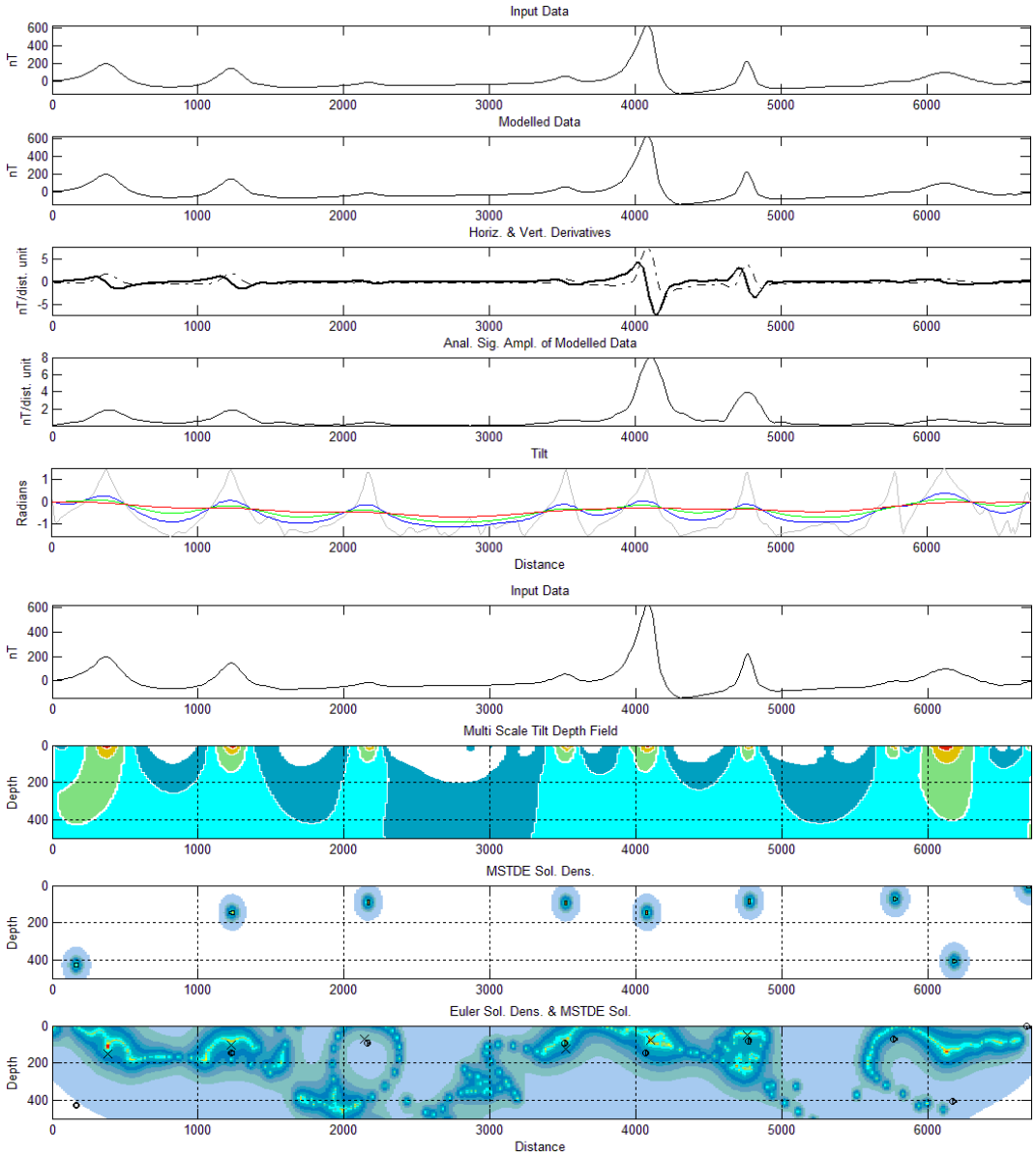


**Figure 45. Observed data with plots of the spatial derivatives, analytic signal amplitude and various continued tilt products (Top), Observed data with MSTD distribution, MSTDE solution density and Euler solution density with MSTDE solution locations (Bottom). On the bottom subplot, modelled source locations are plotted as "x".**

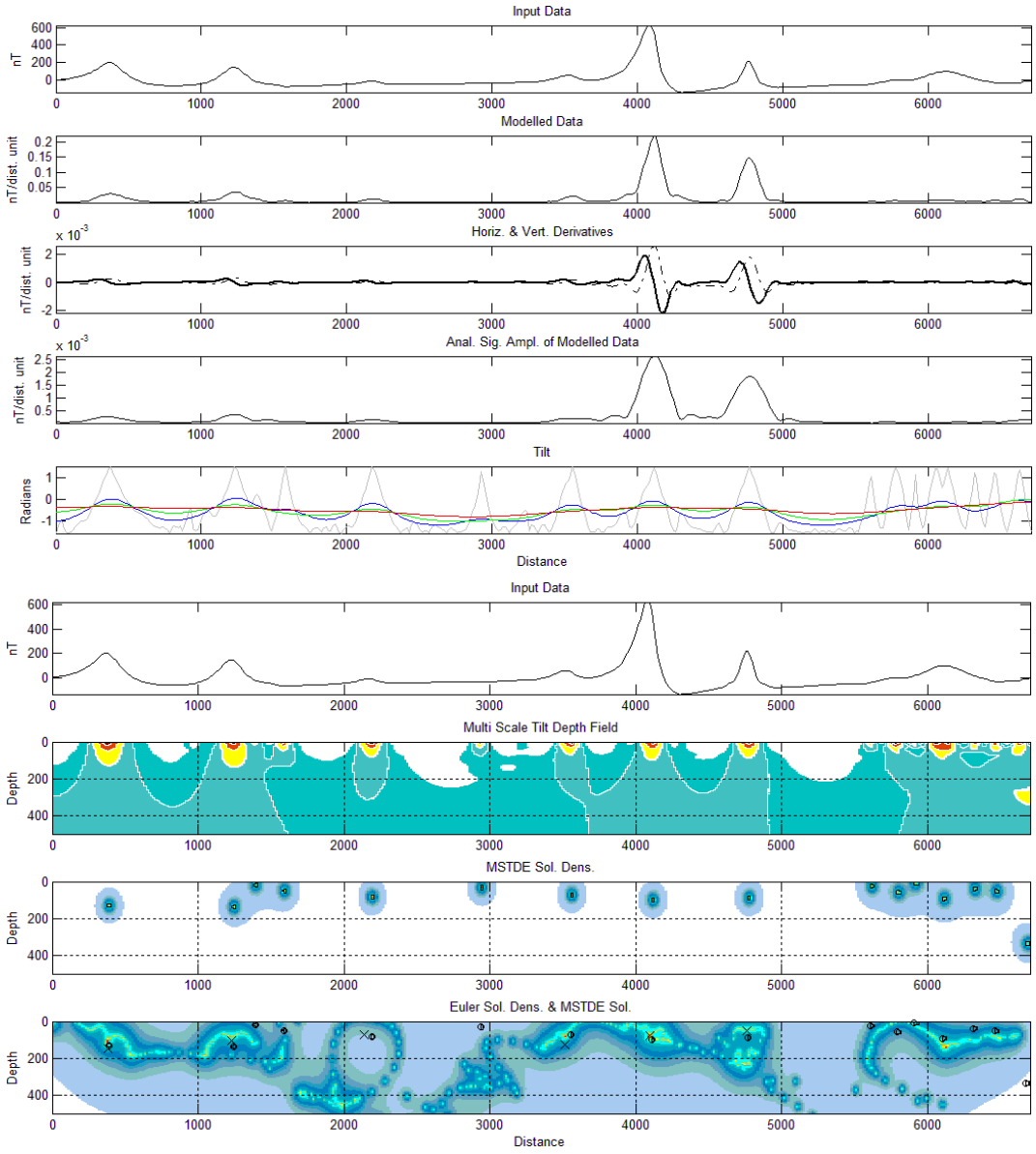


**Figure 46. Observed data with plots of the spatial derivatives, analytic signal amplitude and various continued tilt products (Top), Observed data with MSTD distribution, MSTDE solution density and Euler solution density with MSTDE solution locations (Bottom). On the bottom subplot, modelled source locations are plotted as "x". The input data to the algorithm was the analytic signal amplitude of the vertical derivative of the pole-reduced total magnetic intensity.**

In Figure 47 it may be seen that the solutions derived from the application of the MSTDE method to the TMI and to the AS(VD(RTP)) differ to varying degrees for different anomalies. Some understanding may be gained as to the geometry of the source from this variation. For step/contact like features the variation is expected to be larger than for sheet-like sources. There is generally good agreement between the modelled locations and those estimated from the MSTDE method.

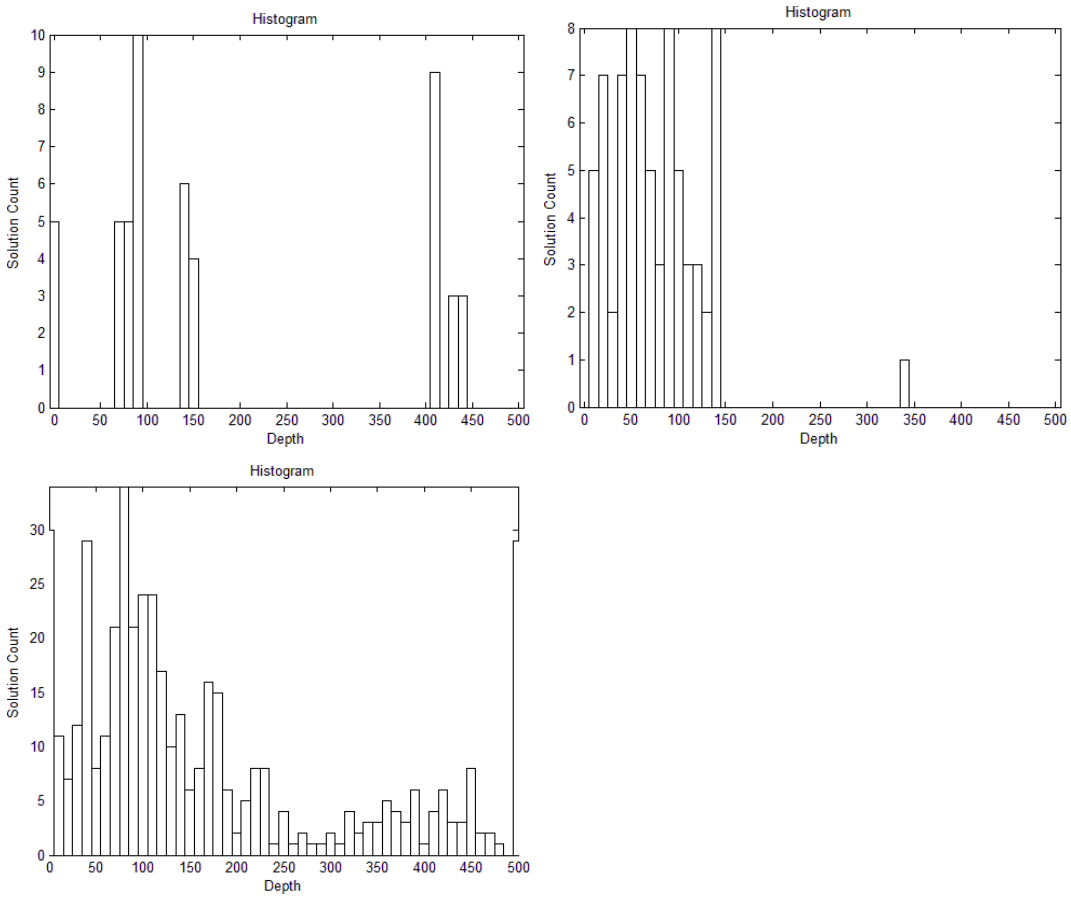


**Figure 47. Histograms of the MSTDE solutions with respect to depth for the application to the pole-reduced total magnetic intensity (Top left), The same histogram but of the application to the AS(VD(RTP)) (Top right), The same histogram but of the Euler solutions when applied to the pole-reduced total magnetic intensity (Bottom).**

## Field Example 2

### Choice of observed data

The data used in this example was acquired in 1993 approximately 200 km north-west of Johannesburg, see Figure 48. The region includes the western limb of the Bushveld Complex in the north-east of the survey area overlying the floor rocks of the Transvaal Supergroup. The circular region of high anomalous magnetic intensity due to the Pilanesberg Complex is located in the centre of the survey area. Three profiles have been extracted, all in a north-south orientation to be approximately perpendicular to the mafic dykes that crosscut the region. The data are in a geographic projection measured in meters; gridded to a 200 m cell size and while the flight height is not precisely known it was likely in the order of a few hundred meters (150 m +60 m, Atlas of Magnetic Data - Council for Geoscience). These data are of significantly poorer quality than those used in example 1 and thereby serve as a test of the methods ability to perform in a robust fashion in the presence of an elevated level of noise.

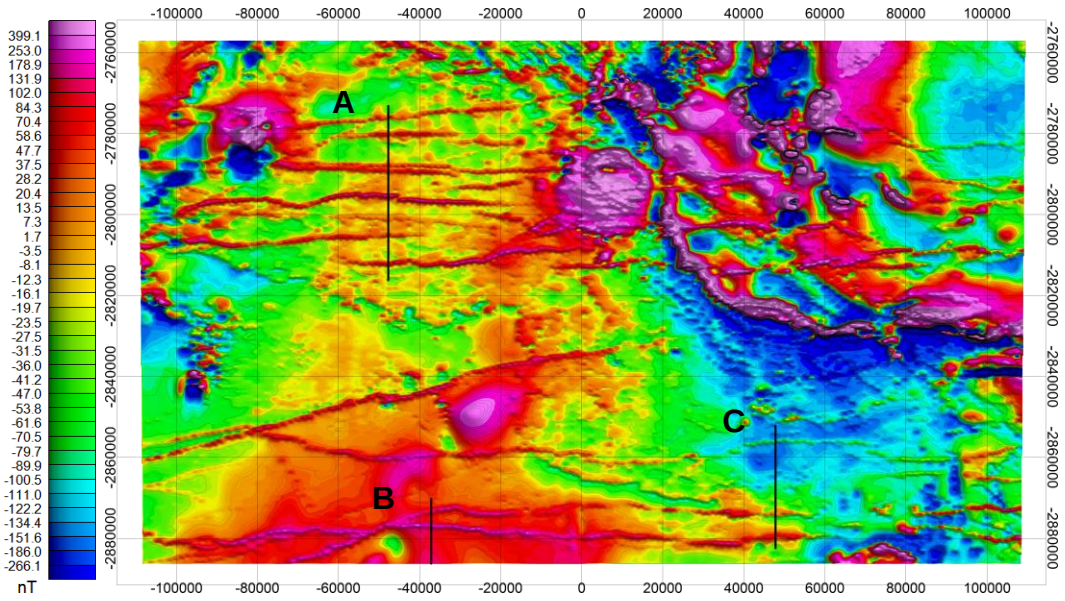


**Figure 48. Pole-reduced total magnetic intensity data over a region of the Bushveld Complex in South Africa showing the three profiles extracted for use in this example.**

**Results of the application of Multi-Scale Tilt Depth Estimation to observed data**

Figure 49 through Figure 54 illustrate the MSTDE results for profiles A through C.

Example 2 – Profile A

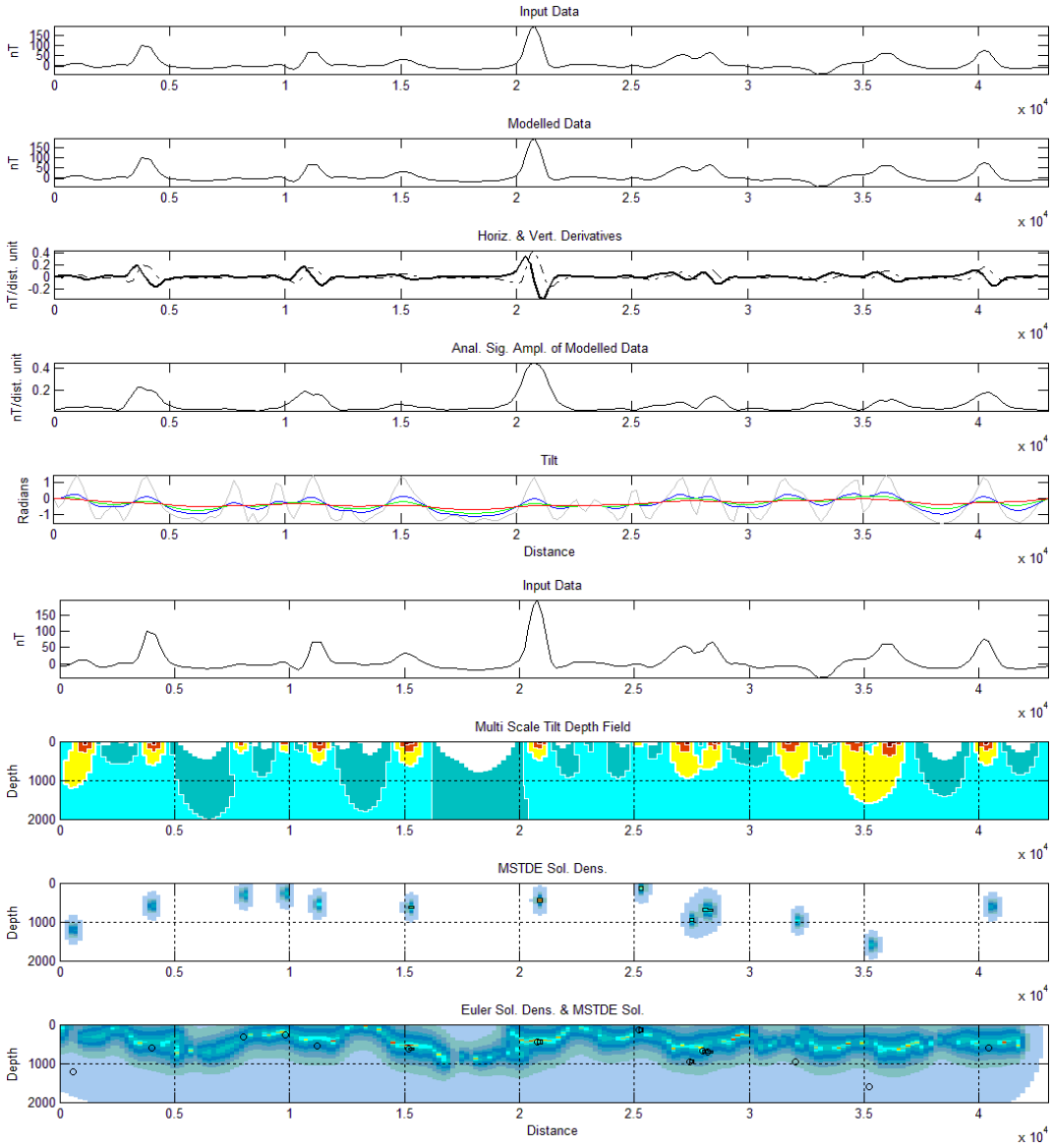


**Figure 49. Observed data (Profile A) with plots of the spatial derivatives, analytic signal amplitude and various continued tilt products (Top), Observed data with MSTD distribution, MSTDE solution density and Euler solution density with MSTDE solution locations (Bottom). The input data to the algorithm was the total magnetic intensity.**

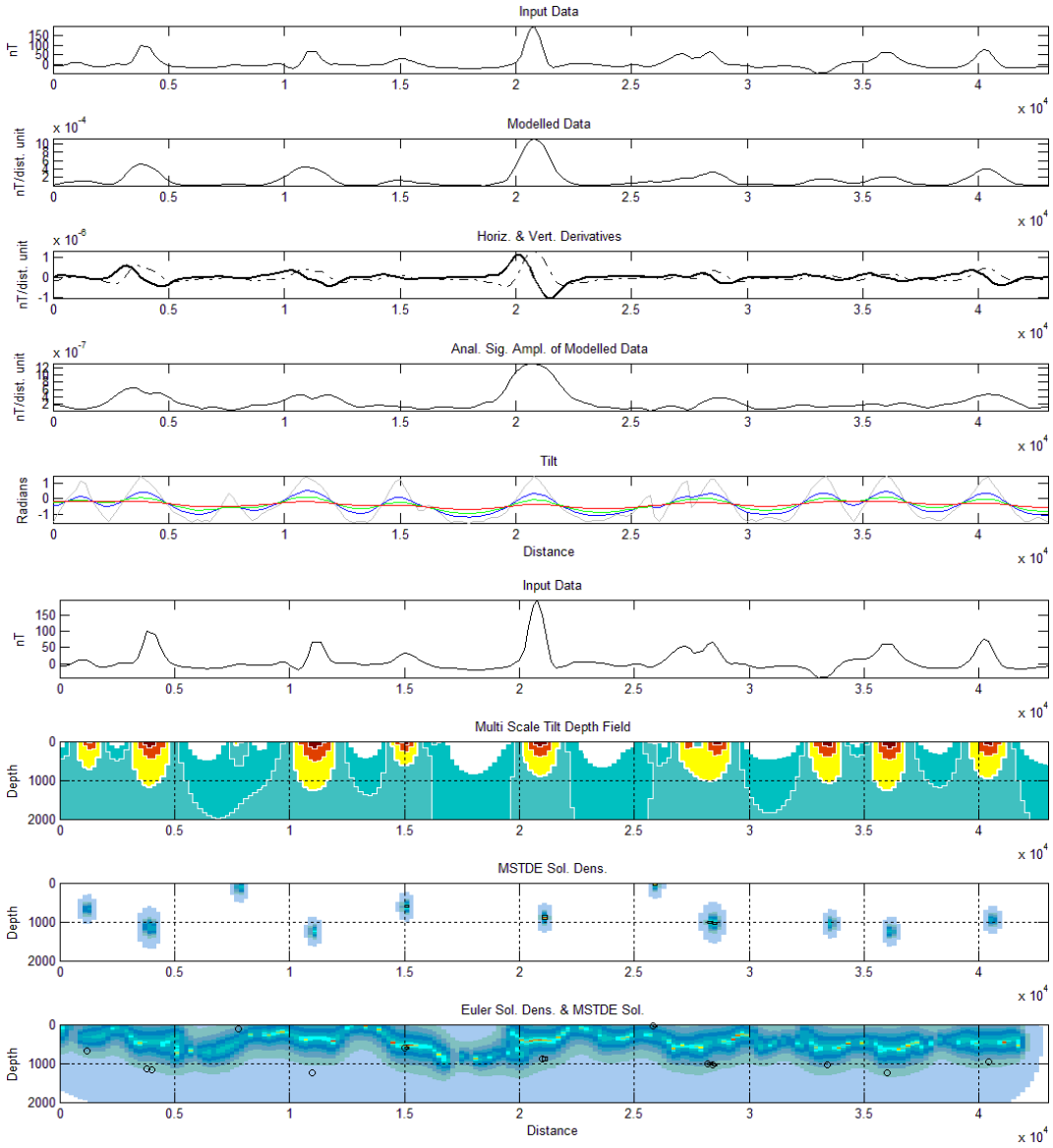


**Figure 50. Observed data (Profile A) with plots of the spatial derivatives, analytic signal amplitude and various continued tilt products (Top), Observed data with MSTD distribution, MSTDE solution density and Euler solution density with MSTDE solution locations (Bottom). The input data to the algorithm was the analytic signal amplitude of the vertical derivative of the pole-reduced total magnetic intensity.**

Example 2 – Profile B

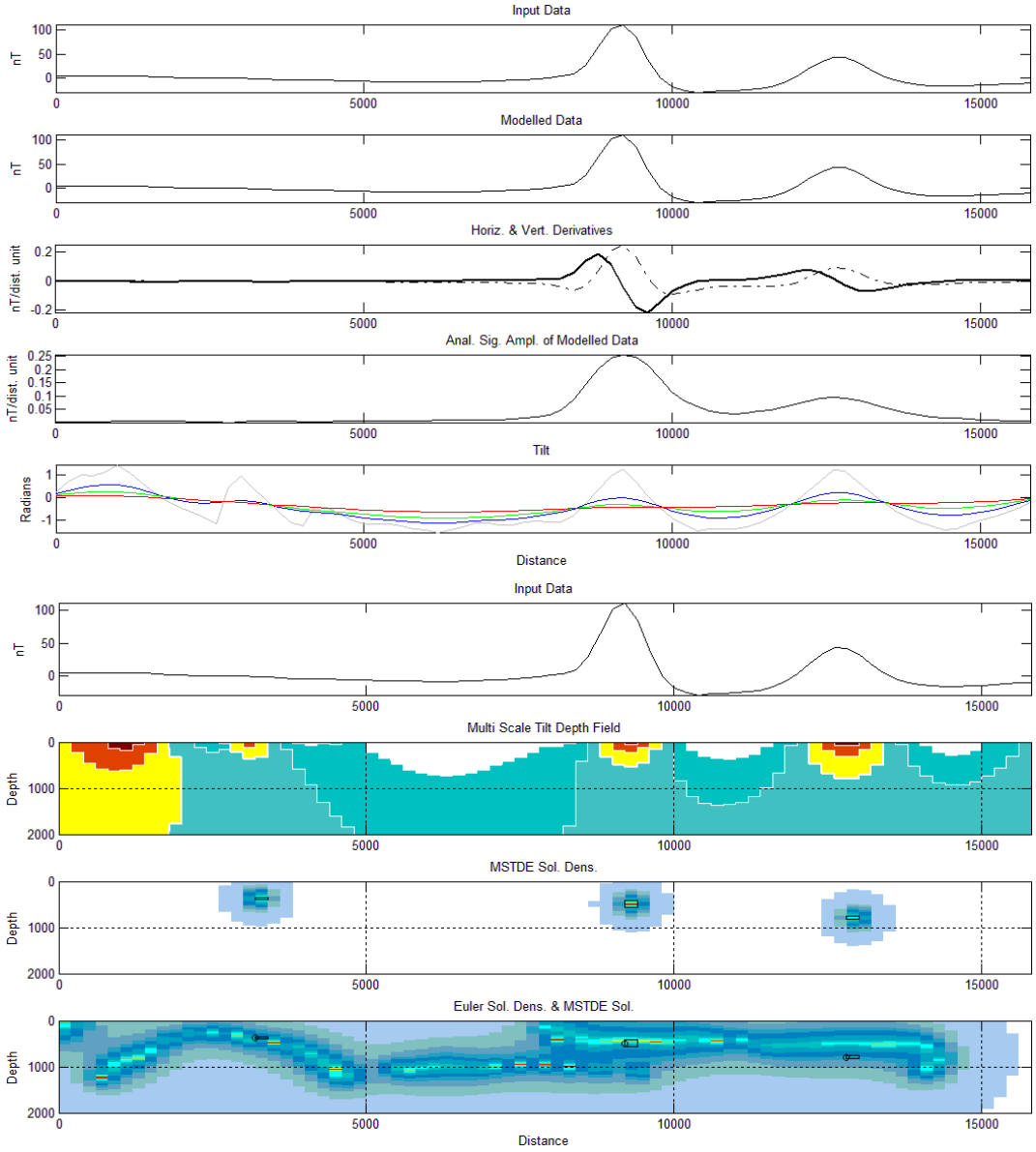


**Figure 51. Observed data (Profile B) with plots of the spatial derivatives, analytic signal amplitude and various continued tilt products (Top), Observed data with MSTD distribution, MSTDE solution density and Euler solution density with MSTDE solution locations (Bottom). The input data to the algorithm was the total magnetic intensity.**

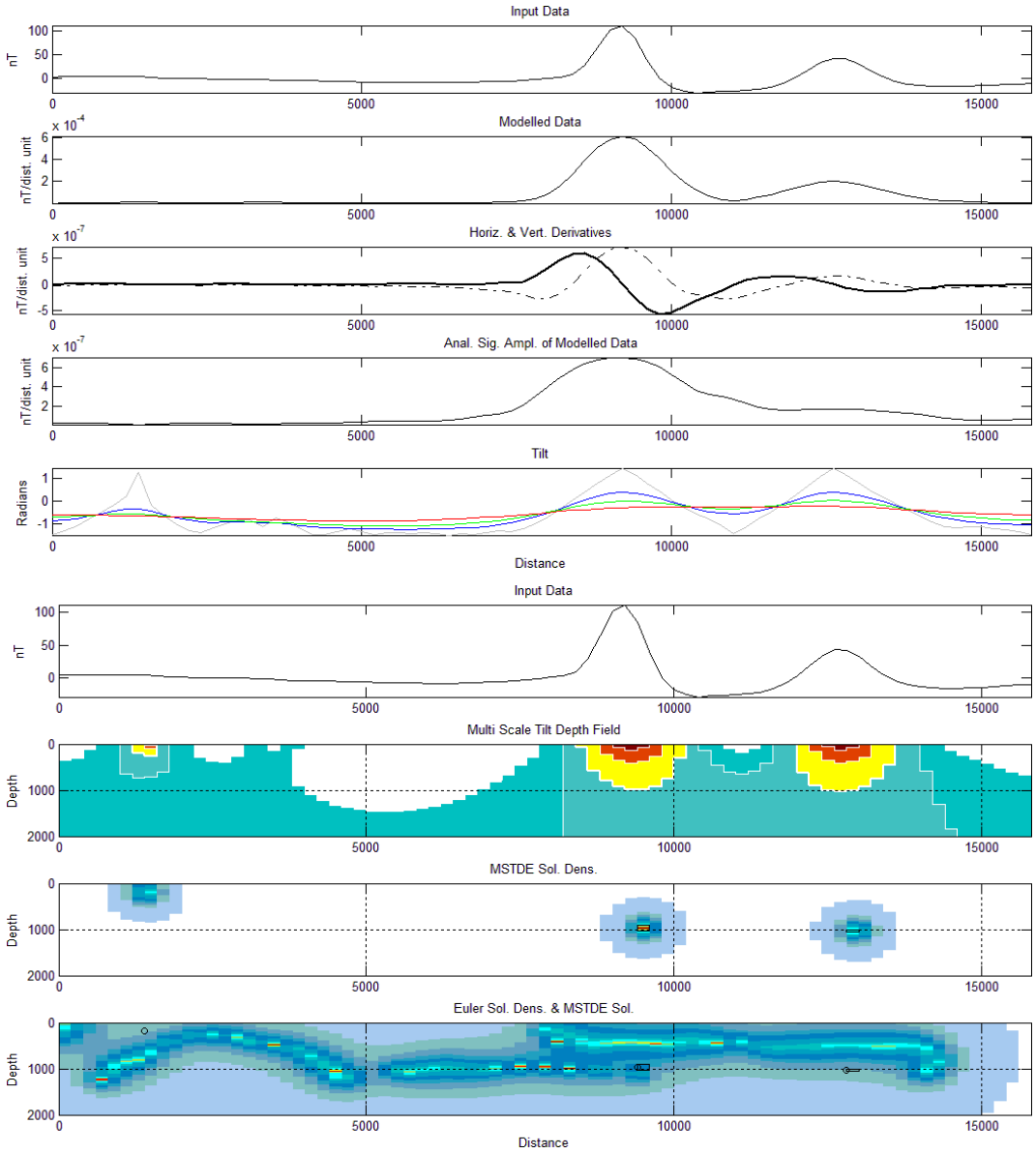


**Figure 52. Observed data (Profile B) with plots of the spatial derivatives, analytic signal amplitude and various continued tilt products (Top), Observed data with MSTD distribution, MSTDE solution density and Euler solution density with MSTDE solution locations (Bottom). The input data to the algorithm was the analytic signal amplitude of the vertical derivative of the pole-reduced total magnetic intensity.**

Example 2 – Profile C

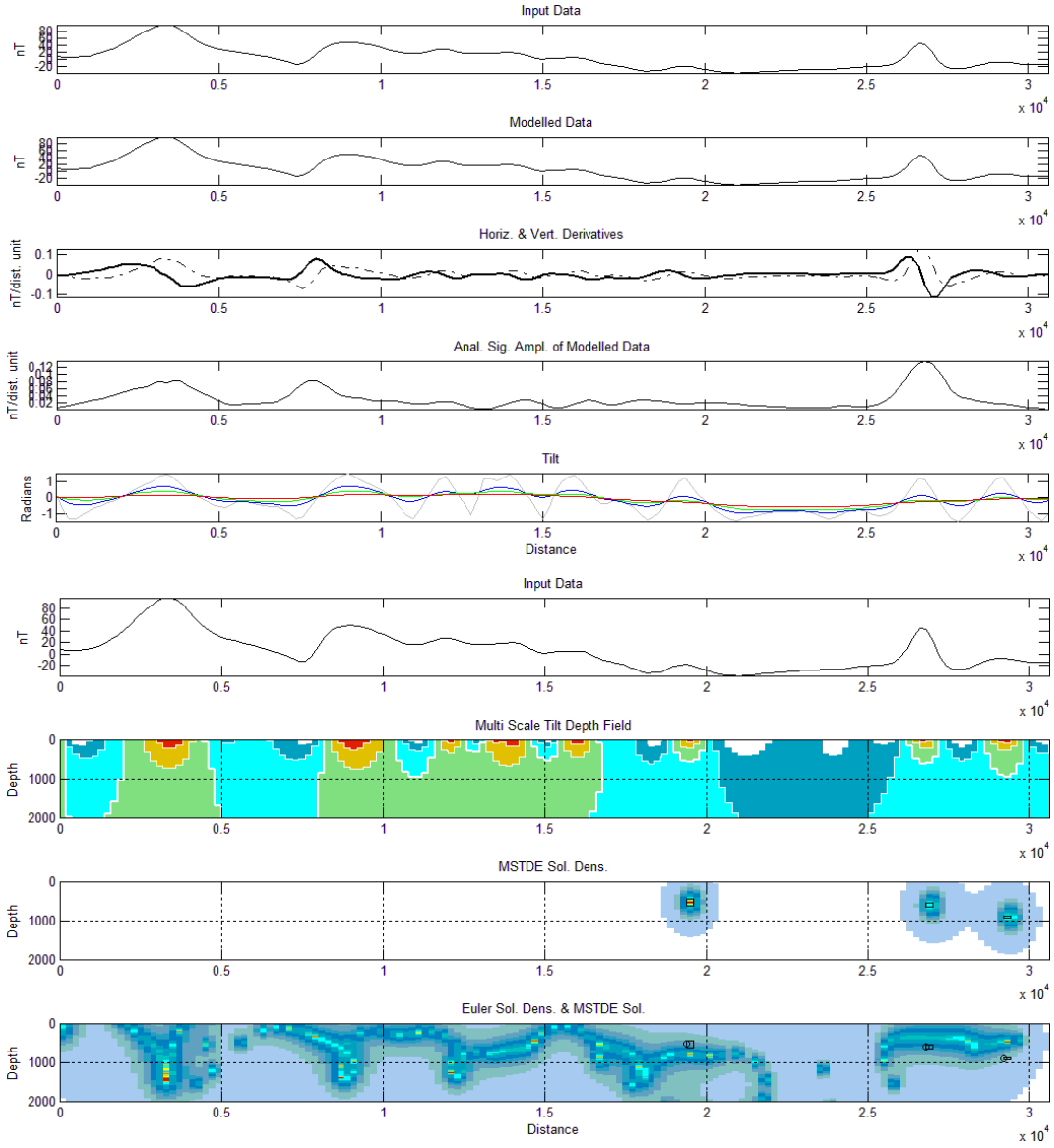


**Figure 53. Observed data (Profile C) with plots of the spatial derivatives, analytic signal amplitude and various continued tilt products (Top), Observed data with MSTD distribution, MSTDE solution density and Euler solution density with MSTDE solution locations (Bottom). The input data to the algorithm was the total magnetic intensity.**

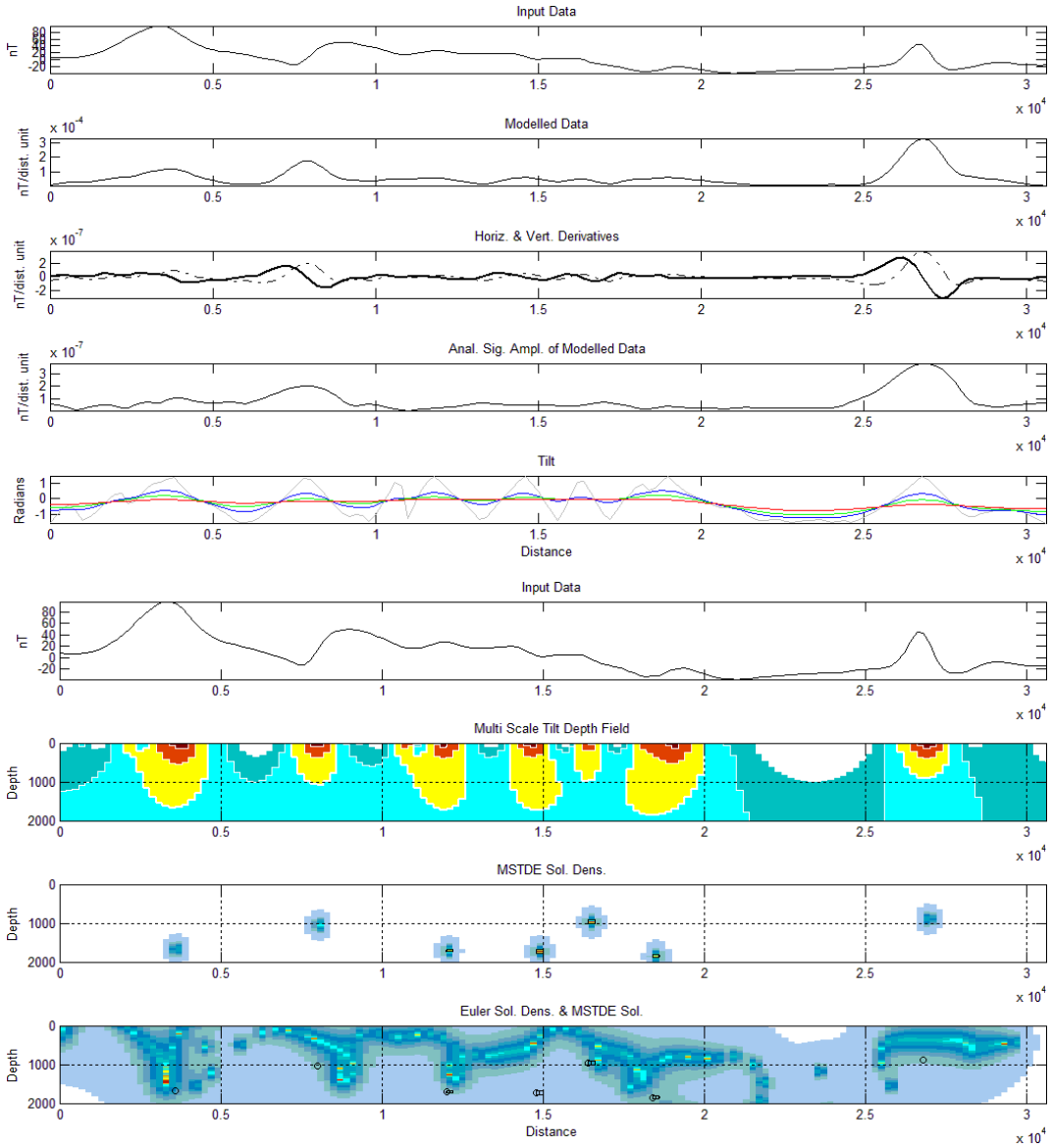


**Figure 54. Observed data (Profile C) with plots of the spatial derivatives, analytic signal amplitude and various continued tilt products (Top), Observed data with MSTD distribution, MSTDE solution density and Euler solution density with MSTDE solution locations (Bottom). The input data to the algorithm was the analytic signal amplitude of the vertical derivative of the pole-reduced total magnetic intensity.**

## Performance of the Multi-Scale Tilt Depth Estimation Method

Presented here is a summary of the performance of the MSTDE method as well as its various implementations during their application to the synthetic and observed data. The method is sensitive, to differing degrees, to a number of factors as stated in Chapter 2. The first is the model type. As seen in the section above, the MSTDE method applied to “thin” sources, i.e. with a large depth:width ratio, performs well, however when applied to “thick” sources the depths are grossly overestimated or undefined when the depth to the turning point is sought. In order to return usable results the method was applied to the AS(VD(TMI)). This approach returned results slightly too shallow for thin sources but correct for sufficiently thick sources.

The second factor was the dip of the structure. Above it is shown that the MSTDE method is quite unstable with respect to varying dip unless the depth is determined at, or close to, the true location of the upper edge. In practice this is achieved in two ways: the first is to query the MSTD distribution at the location of the peak of the analytic signal amplitude as this is less sensitive to the dip of the structure; the second is to apply the MSTDE method to the AS(VD(TMI)). This second approach returned slightly underestimated depths but is relatively stable even to a dip as low as 10°.

The third factor is the sensitivity to the interference due to background signal. This was tested by applying the MSTDE method to total magnetic intensity data generated over two proximal sheet type sources. The distance between these was varied to alter the extent to which the anomalies interfered. From the results it may be seen that when the separation ($s$) between the sources is within the range $0.5d<s<4d$, where $d$ is the true depth to the causative, the depths are substantially

overestimated. This can be attributed to the apparently lower frequency due to the interference of the anomalies. If the separation is less than half of the depth to the sources, the depth is once again well estimated. The application of the MSTDE method to the AS(VD(TMI)) returned more stable results in the range $0.5d<s<4d$, however these are slightly underestimated. The effect of regional residual separation is also addressed, the expected reduction in the estimated depth occurring when low frequency content is removed from the dataset.

The last factor addressed is that of the sensitivity of the method to noise. This was tested by adding simulated white noise to the input data and applying various low-pass / smoothing operations. The method proved highly unstable in the presence of noise, not returning solution locations when the noise had an amplitude of >10% of the standard deviation of the input data. The variable frequency and spatial domain low-pass / smoothing operations improve the result drastically, allowing the method to solve for locations however slightly overestimated. An interesting trend was identified in that the Euler method underestimated the depth when noise is added. The opposite trend is visible in the low-passed / smoothed MSTDE solutions. As the added noise amplitude reduces, the solutions from the MSTDE and Euler methods tend toward the correct depth. This behavior may be utilized to determine an optimal depth via experimentation with added noise.

# CHAPTER 6: CONCLUSIONS

The estimation of magnetic source depths from magnetic data is an extensively studied subject with many, varied approaches adopted. Each of these approaches has been shown to have particular strengths and weaknesses with few implemented on a wide scale, commercial basis. The likes of Euler and Werner deconvolution, shown by Nabighian et al. (2001) to be unified in three dimensions, are the most prevalent techniques employed in the modern geophysical industry. This prevalence does not however preclude the useful application of alternate techniques. Some comments delivered in this work on previous publications include: the work presented in Pasteka (2000) on the use of additional polynomial terms to focus Werner deconvolution solutions on the upper portions of a source; and the solution strategy adopted by Salem (2003). Comment delivered on Pasteka's polynomial addition pertains to extending the concept not only to include low order terms, but to include significantly higher order terms in order to compensate for high frequency noise inevitably present within observed data. Salem (2003) makes use of multiple levels of continuation, a solution set derived from each. It is found that solutions are most focused on different sources at different levels of continuation and the proposal is made that this may be useful for interpreting large scale datasets where sources of differing natures are likely to be found. The comment delivered here is that this solution strategy shows much potential for automation via techniques such as those of automated clustering presented by Ugalde (2008).

The history of multi-scale computation is somewhat diverse and includes much work in the signal processing field. Multi-scale computation appears to have been first applied to geophysical potential fields in 1991 by McGrath. The focus of this work is however the expression and application of a newly developed depth estimation technique dubbed Multi-Scale Tilt Depth Estimation, or here abbreviated as MSTDE. van Buren (2009)

presents a summary of the method which is elaborated upon here. The method has been shown to derive suitable depth estimates when applied to modelled data derived from a range of simple synthetic models. Sensitivity of the method to model type, dip, interference and noise has been presented, as well as mitigating strategies to improve and stabilize the method's performance, which include the application to derivatives of the magnetic intensity. Code for the computation of the required parameters and eventual solution sets is included in Appendix A. Results of the successfully application of the MSTDE method to a field dataset from the Bushveld Complex in South Africa are presented.

## REFERENCES

Abdelrahman, E. M. and El-Araby, T. M. (2001), A new method for shape and depth determinations from gravity data: Geophysics, Vol. 66, No. 6, pp. 1774-1780.

Abdelrahman, E. M. and El-Araby, H. M. (2002), A numerical approach to depth determination from magnetic data: Kuwait J. Sci. Eng. 29, pp. 121-134.

Archibald, N. J. and Gow, P. (1999), Multiscale edge analysis of potential field data: Exploration Geophysics 30, pp. 38-44.

Barbosa, V. C. and Silva, J. B. (1999), Stability analysis and improvement of structural index estimation in Euler deconvolution: Geophysics, Vol. 64, No. 1, pp. 48-60.

Blakely, R. J. and Simpson, R. W. (1986), Approximating edges of source bodies from magnetic or gravity anomalies: Geophysics, Vol. 51, No. 7, pp. 1494-1498.

Boschetti, F. and Horowitz, F. G. Improved edge detection in potential field maps and graphical estimation of depth-to-the-top: SEG 70th Annual Meeting, 2000.

Breiner, S. Magnetic Field Derivatives in Geophysical Interpretation: MSc Thesis, Stanford University, 1962.

Cooper, G. R. J. (2004), Euler Deconvolution applied to Potential Field Gradients: Exploration Geophysics 35, pp. 165-170.

Cooper, G. R. J. (2004), A semi-automatic procedure for the interpretation of geophysical data: Exploration Geophysics 35, pp. 180-185.

Cooper, G. R. J. (2008), Euler Deconvolution with Improved Accuracy and Multiple Different Structural indices: Journal of China University of Geosciences, Vol. 19, No. 1, pp. 72-76.

Cooper, G. R. J. (2004), The stable downward continuation of potential field data: Exploration Geophysics 35, pp. 260-265.

Dawi, M. G. and Tianyou, L. (2004), Depth Estimation of 2-D Magnetic Anomalous Sources by Using Euler Deconvolution Method: American Journal of Applied Sciences 1, pp. 209-214.

Fairhead, J. D. and Bennett, K. J. Euler: Beyond the "Black Box": SEG 64th Annual Meeting, 1994.

Fedi, M. and Florio, G. Multiridge Analysis and Reduced Euler Deconvolution : SEG 77th Annual Meeting, 2007.

FitzGerald, D. and Reid, A. (2004), New discrimination techniques for Euler deconvolution: Computers & Geosciences 30, pp. 461-469.

Florio, G. and Fedi, M. (2006), On the application of Euler deconvolution to the analytic signal: Geophysics, Vol. 71, No. 6, pp. 87-93.

Florio, G. and Fedi, M. Euler deconvolution of vertical profiles of potential field data: SEG 76th Annual Meeting, 2006.

Franklin, J. (1990), Analytic Continuation of the Fast Fourier Transform: SIAM Journal of Scientific and Statistical Computing, Vol. 2, No. 1, pp. 112-122.

Hansen, R. O. and Suciu, L. (2002), Multiple-source Euler Deconvolution: Geophysics, Vol. 67, pp. 525-535.

Hansen, R. O. (2005), 3D multiple-source Werner deconvolution for magnetic data: Geophysics, Vol 70, No. 5, pp. 45-51.

Holden, D. J. and Archibald, N. J. (2000), Inferring Geological Structures Using Wavelet-Based Multiscale Edge Analysis and Forward Models: Exploration Geophysics 31, pp. 67-71.

Keating, P. and Pilkington, M. A comparison of some interpretation techniques for magnetic data: SEG 72nd Annual Meeting, 2002.

Keating, P. and Pilkington, M. (2004), Euler deconvolution of the analytic signal and its application to magnetic interpretation: Geophysical Prospecting 52, pp. 165-182.

Kuttikul, P. Optimization of 3D Euler deconvolution for the interpretation of potential field data: MSc Thesis, ITC, 1995.

Lahti, I. and Karinen, T. (2010), Tilt derivative multiscale edges of magnetic data: The Leading Edge, January 2010, pp. 24-29.

Lee, M. and Morris, B. (2010), Effect of signal amplitude on magnetic depth estimations: The Leading Edge, June 2010, pp. 672-677.

Lee, M. and Ugalde, H. Spatial Domain Filtering of Specific Frequencies: Curvature isolation of potential field signals: SEG 78th Annual Meeting, 2008.

Li, X. (2003), On the use of different methods for estimating magnetic depth: The Leading Edge, November 2003, pp. 1090-1099.

Mallat, S. G. and Zhong, S. Complete Signal Representation with Multiscale Edges: Robotics Research Technical Report, Computer Science Division, NYU, 1989.

Mallat, S. G. and Zhong, S. (1992), Characterization of Signals from Multiscasle Edges: IEEE Transactions on Pattern Analysis and Machine Intelligence, Vol. 14, No. 7, pp. 710-732.

Marson, I. and Klingele, E. E. (1993), Advantages of using the vertical gradient of gravity for 3-D interpretation: Geophysics, Vol. 58, No. 11, pp. 1588-1595.

Mikhailov, V. and Pajot, G. (2007), Tensor deconvolution: A method to locate equivalent sources from full tensor gravity data: Geophysics, Vol. 72, No. 5, pp. 161-169.

Miller, H. G. and Singh, V. (1994), Potential field tilt - a new concept for location of potential field sources: Journal of Applied Geophysics 32, pp. 213-217.

Mushayandebvu, M. F. and van Driel, P. (2001), Magnetic source parameters of two-dimensional structures using extended Euler deconvolution: Geophysics, Vol. 66, No. 3, pp. 814-823.

Mushayandebvu, M. F. and Lesur, V. (2004), Grid Euler deconvolution with constraints for 2D structures: Geophysics, Vol. 69, No. 2, pp. 489-496.

Nabighian, M. N. and Hansen, R. O. (2001), Unification of Euler and Werner deconvolution in three dimensions via the generalized Hilbert transform: Geophysics, Vol. 66, No. 6, pp. 1805-1810.

Nabighian, M. N. (1984), Toward a three-dimensional automatic interpretation of potential field data via generalized Hilbert transforms: Fundamental relations: Geophysics, Vol. 49, No. 6, pp. 780-786.

Pal, D. S. Identification of the Causative Source and Depth from Enhanced Local Wavenumber Analysis: 6th International Conference & Exposition on Petroleum Geophysics, 2006.

Pasteka, R. (2006), The Role of the Interference Polynomial in the Euler Deconvolution Algorithm: Bollettino di Geofisics Teorica ed Applicata, Vol. 47, No. 1-2, pp. 171-180.

Pasteka, R. (2000), 2D Semi-automated Interpretation Methods in Gravimetry and Magnetometry: ACTA Geologica Universitatis Comenianae, Nr. 55, pp. 5-50.

Paterson, N. R. and Kwan, K. C. Use of Euler Deconvolution in Recognizing Magnetic Anomalies of Pipelike Bodies: SEG Extended Abstracts, 1991, pp. 642-645.

Phillips, J. D. Two-step processing for 3D magnetic source locations and structural indices using extended Euler or analytic signal methods: SEG 72nd Annual Meeting, 2002.

Ravat, D. and Kirkham, K. (2002), A source-depth separation filter: Using the Euler method on the derivatives of total intensity magnetic anomaly data: The Leading Edge, April 2002, pp. 360-364.

Reid, A. B. and Allsop, J. M. (1990), Magnetic interpretation in three dimensions using Euler deconvolution: Geophysics, Vol. 55, No 1, pp. 80-91.

Reid, A. B. (2003), Euler magnetic structural index of a thin-bed fault: Geophysics, Vol. 68, No. 4, pp. 1255-1256.

Reid, A. B. Semi-Automated Methods of Potential Field Interpretation – Innovations, and Recent and Future Developments: EGM International Workshop, 2007.

Roest, W. R. and Verhoef, J. (1992), Magnetic interpretation using the 3-D analytic signal: Geophysics, Vol. 57, No. 1, pp. 116-125.

Salem, A. and Ravat, D. (2003), A combined analytic signal and Euler method (AN-EUL) for automatic interpretation of magnetic data: Geophysics, Vol. 68, No. 6, pp. 1952-1961.

Salem, A. and Ravat, D. (2004), Linearized least-squares method for interpretation of potential-field data from sources of simple geometry: Geophysics, Vol. 69, No. 3, pp. 783-788.

Salem, A. and Smith, R. Generalized magnetic tilt-Euler deconvolution: SEG 72nd Annual Meeting, 2007.

Salem, A. and Williams, S. E. (2008), Interpretation of magnetic data using tilt-angle derivatives: Geophysics, Vol. 73, No. 1, pp. 1-10.

Salem, A. and Williams, S. E. (2007), Tilt-depth method: A simple depth estimation method using first-order magnetic derivatives: The Leading Edge, December 2007, pp. 1502-1505.

Shaw, R. K. and Agarwal, B. N. (2007), Use of Walsh transforms in estimation of depths of idealized sources from total field magnetic anomalies: Journal of Computers & Geosciences, Vol. 33, No. 7, pp. 966-975.

Shi-Zhe, X. (2007), A Comparison of Effects Between the Iteration Method and FFT for Downward Continuation of Potential Fields: Chinese Journal of Geophysics Vol.50, No.1, pp. 270-274.

Slack, H. A. and Lynch, V. M. (1968), Discussion on 'The Geomagnetic Gradiometer': Geophysics, Vol. 33, No.4 , pp. 680-683.

Smith, R. S. and Thurston, J. B. (1998), iSPI™ - the improved source parameter imaging method: Geophysical Prospecting 46, pp. 141-151.

Stavrev, P. and Gerovska, D. Euler inversion of magnetic anomalies using analytical continuation: SEG 74th Annual Meeting, 2004.

Stavrev, P. and Reid, A. (2007), Degrees of homogeneity of potential fields and structural indices of Euler deconvolution: Geophysics, Vol. 72, No. 1, pp. 1-12.

Stavrev, P. and Gerovska, D. (2006), Automatic inversion of magnetic anomalies from two height levels using finite-difference similarity transforms: Geophysics, Vol. 71, No. 6, pp. 75-86.

Thompson, D. T. (1982), EULDPH: A new technique for making computer-assisted depth estimates from magnetic data : Geophysics, Vol. 47, No. 1, pp. 31-37.

Thurston, J. B. and Smith, R. S. (2007), Source location using total-field homogeneity: Introducing the SLUTH method for depth estimation: The Leading Edge, October 2007, pp. 1272-1277.

Thurston, J. B. and Smith, R. S. (1997), Automatic conversion of magnetic data to depth, dip, and susceptibility contrast using the SPI (TM) method: Geophysics, Vol. 62, No. 3, pp. 807-813.

Ugalde, H. and Morris, B. Cluster analysis of Euler deconvolution solutions: new filtering techniques and actual link to geological structure: SEG 78th Annual Meeting, 2008.

Vallée, M. A. and Keating, P. Magnetic depth estimates using the continuous wavelet transform: SEG 72nd Annual Meeting, 2002.

van Buren, R. Multi-Scale Depth Estimation: 11th SAGA Biennial Technical Meeting, 2009.

Werner, S. Interpretation of Magnetic Anomalies at Sheet-like Bodies: Sveriges Geologiska Undersokning, Arsbok 43, No. 6, 1953.

Williams, S. E. and Fairhead, J. D. (2005), Comparison of grid Euler deconvolution with and without 2D constraints using a realistic 3D magnetic basement model: Geophysics, Vol. 70, No. 3, pp. 13-21.

# APPENDIX A

Matlab source code for the program developed to compute the Multi-Scale Tilt Depth estimates follows.

```
% Program to compute Multi-Scale Tilt Depth Estimates
% by Reece van Buren, submitted in 2013 to the University
% of the Witwatersrand as part of the requirements for the
% degree of Master of Science in Geophysics.
%%
% Environment setup
clear
format long
delete('DepthSolutions.csv');
load('MSTDEColourmap.mat','cmap')
%%
% User Input
fprintf('\nEnter the fully qualified name of data file \n');
fileName = input(' ... including extension: ','s');
fprintf('\nPerform AS conversion (0 = No | > 0 = Yes) \n');
ASC = input(' ... ');
ASC=floor(ASC);
fprintf('\nEnter the maximum depth \n');
zMax = input(' ... in meters ');
zMax=abs(fix(zMax));
zMaxNeg=-zMax;
levels=floor(zMax/1); % Denominator controls the vertical
resolution
fprintf('\nEnter the amplitude of the noise to be added\n');
fprintf('in percent of standard deviation of the data\n');
ampN = input(' ... ');
fprintf('\nEnter the # of iterations of noise addition and
smoothing\n');
iter = input(' ... ');
if iter<1 iter=1; else iter=floor(iter); end
deltaSmoothIter=0;
if iter>1
    fprintf('\nEnter the smoothing increment per iteration (0 =
No change)\n');
    deltaSmoothIter = input(' ... ');
end
fprintf('\nInitial # of smoothing iterations (0 = No | > 0 = FD &
SD) \n');
smoothIter = input(' ... ');
smoothIter = ceil(smoothIter);
fprintf('\nRemove a regional (0 = No | > 0 = Yes) \n');
regRem = input(' ... ');
regRem = ceil(regRem);
%%
% Read Input Data File
Tp = csvread(fileName);
%%
% Fix Tp length
if floor(length(Tp)/2)<(length(Tp)/2)
    Tp=[Tp;Tp(length(Tp),1)+(Tp(length(Tp),1)-Tp(length(Tp)-1,1))
Tp(length(Tp),2)+(Tp(length(Tp),2)-Tp(length(Tp)-1,2))];
```

```
end
%%
% Setup Variables
x = Tp(:,1);
Tp = Tp(:,2);
n=length(x);
n2 = floor(n/2);
m2=n2+n;
flen=4*n;
dx=abs((max(x)-min(x))/(n-1));
fnyq=0.5/dx;
df=2*fnyq/(flen-1);
f=[-fnyq:df:fnyq];
k=2*pi*f;
%%
% Reject outlying values
cTp=Tp;
for i=2:length(Tp)-1
    data=Tp(i-1:i+1);
    med=median(data);
    sd=std(data);
    if abs(Tp(i)-med)>sd
        cTp(i)=interp1([Tp(i-1) Tp(i+1)],1.5,'linear');
    end
end
Tp=cTp;
%%
% Interpolate to a fixed data spacing
intX=min(x):dx:max(x);
int=interp1(x,Tp,intX,'spline');
Tp=int';
Tp=Tp-mean(Tp);
x=intX';
profLen=max(x)-min(x);
origData=Tp;
%%
% Fix outliers at Tp edges
Tp(2)=(Tp(3)-Tp(4))+(Tp(3)+Tp(4))/2;
Tp(1)=(Tp(2)-Tp(3))+(Tp(2)+Tp(3))/2;
Tp(n-1)=(Tp(n-2)-Tp(n-3))+(Tp(n-2)+Tp(n-3))/2;
Tp(n)=(Tp(n-1)-Tp(n-2))+(Tp(n-1)+Tp(n-2))/2;
%%
% Padding
pTp=[zeros(n2+1,1);(-flipud(Tp(2:n))+2*Tp(1)).*((sin([-
pi/2:(pi/2)/(n2-1):pi/2])+1)/2)'; Tp; (-flipud(Tp(1:n-
1))+2*Tp(n)).*flipud(((sin([-pi/2:(pi/2)/(n2-
1):pi/2])+1)/2)');zeros(n2+1,1)];
%%
% Remove Regional
if regRem>0
    fh=exp(-abs(profLen/8)*abs(k)); % UC by 1/8 of profile length
    pUc=real(ifft(fft(pTp,flen).*fftshift(fh')));
    Tp=pTp(m2+1:m2+n)-pUc(m2+1:m2+n);
    pTp=[zeros(n2+1,1);(-flipud(Tp(2:n))+2*Tp(1)).*((sin([-
pi/2:(pi/2)/(n2-1):pi/2])+1)/2)'; Tp; (-flipud(Tp(1:n-
1))+2*Tp(n)).*flipud(((sin([-pi/2:(pi/2)/(n2-
1):pi/2])+1)/2)');zeros(n2+1,1)];
end
%%
```

```
% Define Taper
taper=(sin([-pi/2:(pi/2)/(n-1)*2:pi/2])+1)/2;
taper=[taper';ones(length(pTp)-
2*length(taper'),1);flipud(taper')];
%%
% Set Up Iterations
statData=pTp;
for q=1:iter
    pTp=statData;
%%
% Add Random Noise
for i=1:flen
    pTp(i)=(pTp(i)+rand*ampN/100*std(pTp))*taper(i);
end
%%
% Store Copy Of Input Data For Plotting
inputData=pTp(m2+1:m2+n);
%%
% Perform VDAS Conversion Of Data
if ASC>0
    % Spatial Smoothing
    for sm=1:max(smoothIter,1)
        pSwop=pTp;
        for i=2:flen-1
            pTp(i)=0.25*pSwop(i-1)+0.5*pSwop(i)+0.25*pSwop(i+1);
        end
    end

    % Calculate The HD & VD Of The Data
    pHd=gradient(pTp,dx);
    pVd=imag(hilbert(pHd));

    % Fix VD Edges
    Vd=pVd(m2+1:m2+n);
    Vd(2)=(Vd(3)-Vd(4))+(Vd(3)+Vd(4))/2;
    Vd(1)=(Vd(2)-Vd(3))+(Vd(2)+Vd(3))/2;
    Vd(n-1)=(Vd(n-2)-Vd(n-3))+(Vd(n-2)+Vd(n-3))/2;
    Vd(n)=(Vd(n-1)-Vd(n-2))+(Vd(n-1)+Vd(n-2))/2;

    % Repad The VD
    pVd=[zeros(n2+1,1);(-flipud(Vd(2:n))+2*Vd(1)).*((sin([-
pi/2:(pi/2)/(n2-1):pi/2])+1)/2)'; Vd; (-flipud(Vd(1:n-
1))+2*Vd(n)).*flipud(((sin([-pi/2:(pi/2)/(n2-
1):pi/2])+1)/2)');zeros(n2+1,1)]; % zero padding

    % Calculate The HD & VD Of The VD
    pHd=gradient(pVd,dx);
    pVd=imag(hilbert(pHd));

    % Calculate The AS Of The VD And Replace The Input Data
    pTp=sqrt(pVd.^2+pHd.^2);

    % Spatial Smoothing
    pSwop=pTp;
    for i=2:flen-1
        pTp(i)=0.25*pSwop(i-1)+0.5*pSwop(i)+0.25*pSwop(i+1);
    end
end
```

```
%%
% Retaper Output Data
pTp=pTp.*taper;
Tp=pTp(m2+1:m2+n);
%%
% Set up 2D Array
smpTp=pTp*ones(1,levels);
%%
% Perform Variable Smoothing
if smoothIter > 0 % Perform variable frequency domain smoothing
(Preferred)
    for Step=1:levels
        lamda=Step*zMax/levels*2;
        numOnes=min(floor(1/lamda/df/2),length(f)/2-1);
        sinVectLen=floor(min(length(f)/2-numOnes,length(f)/16));
        sinVect=[0:1/sinVectLen:1];
        filt=[ones(numOnes-
1,1);sin(pi/2+sinVect*pi)'/2+0.5;zeros(length(f)/2-numOnes-
sinVectLen,1)];
        filtmirror=[filt;flipud(filt)];
        smpTp(:,Step)=real(ifft(fft(pTp,flen).*filtmirror));
    end
    if smoothIter>levels % Perform variable spatial domain
smoothing
        for step = 1:levels
            for sm=1:ceil(smoothIter/levels)
                pSwop=smpTp(:,step);
                for i=2:flen-1
                    smpTp(i,step)=0.25*pSwop(i-
1)+0.5*pSwop(i)+0.25*pSwop(i+1);
                end
            end
            if step<levels
                smpTp(:,step+1)=smpTp(:,step);
            end
        end
    else
        for step = 1:levels
            if smoothIter>0
                for sm=1:ceil(smoothIter*step/levels)
                    pSwop=smpTp(:,step);
                    for i=2:flen-1
                        smpTp(i,step)=0.25*pSwop(i-
1)+0.5*pSwop(i)+0.25*pSwop(i+1);
                    end
                end
            end
        end
    end
end
smTp=smpTp(m2+1:m2+n,:);
%%
% Calculate HD & VD For Each Level
for step = 1:levels
    pHd(:,step)=gradient(smpTp(:,step),dx);
    pVd(:,step)=imag(hilbert(pHd(:,step)));
end
%%
% Calculate 2D Tilt Array
```

```
pTilt=atan(pVd./sqrt(pHd.*pHd));
Vd2D=pVd(m2+1:m2+n,:);
Hd2D=pHd(m2+1:m2+n,:);
Tilt=pTilt(m2+1:m2+n,:);
%%
% Calculate Upward-Continuation For Each Level
for step = 1:levels
    fh=exp(abs(k)*step*zMaxNeg/levels);
    pUc=real(ifft(fft(pTilt(:,step),flen).*fftshift(fh')));
    msDepths(levels+1-step,:)=pUc(m2+1:m2+n);
end
%%
% Use 10% Smoothed Level To Compute VD & HD For Display
Hd=gradient(smpTp(:,ceil(0.1*levels)),dx);
Vd=imag(hilbert(Hd));
Hd=Hd(m2+1:m2+n);
Vd=Vd(m2+1:m2+n);
As=sqrt(Vd.^2+Hd.^2);
%%
% Find Zero Contour & Peak Locations
zeroc=zeros(1,n);
for i=3:n-2
        for j=1:levels
            if msDepths(j,i)>0 & zeroc(i)>-1
                    zeroc(i)=-levels+j;
            end
        end
end
j=1;
Peak=[0 0];
dzeroc=gradient(zeroc,dx);
for i = 2 : n-2
    if zeroc(i)<0 & zeroc(i+1)<0 & zeroc(i)>-levels+1 &
zeroc(i+1)>-levels+1 & (dzeroc(i)*dzeroc(i+1)<0 |
dzeroc(i)*dzeroc(i+1)==0)
        Peak(j,1)=i;
        Peak(j,2)=-zeroc(i)*zMaxNeg/levels+(0.5*zMaxNeg/levels);
        j=j+1;
    end
end
%%
% Write Solution File
Sol=[Peak(:,1)*dx+min(x) Peak(:,2)];
dlmwrite('DepthSolutions.csv',Sol,'-append');
if deltaSmoothIter>0
    smoothIter=smoothIter+deltaSmoothIter;
end
disp([int2str(ceil(q/iter*100)) '% complete']);
end
%%
%  Read Back Solutions For Imaging
disp('Plotting figures');
SolStatRand = csvread('DepthSolutions.csv');
% The dataDensity Funtion Was Obtained From The Matlab Code
Sharing Site
SolDens=dataDensity(SolStatRand(:,1),SolStatRand(:,2),(max(x)-
min(x))/dx+1,levels,[min(x) max(x) 0 zMaxNeg],dx);
%%
% Calculate Euler Solutions
```

```
% The CalcEulSol Function Was Modified From Code Supplied By G.
R. J. Cooper.
% The Author Has Not Received Permission To Divulge The Details
Of The Code
% But May State That The Implimentation Is That Of Standard Euler
Deconvolution
[EulX EulZ]=CalcEulSol([intX' statData(m2+1:m2+n)],11,1);
EulSolDens=dataDensity(EulX,EulZ,(max(x)-
min(x))/dx+1,levels,[min(x) max(x) 0 zMaxNeg],dx);
%%
% Stretch Images
msDepthsStr=zeros(zMax,profLen);
SolDensStr=zeros(zMax,profLen);
EulSolDensStr=zeros(zMax,profLen);
for i=1:profLen
    for j=1:zMax

msDepthsStr(j,i)=msDepths(ceil(j/zMax*(levels)),floor(i/profLen*(
profLen/dx)+1));

SolDensStr(j,i)=SolDens(ceil(j/zMax*(levels)),floor(i/profLen*(pr
ofLen/dx)+1));

EulSolDensStr(j,i)=EulSolDens(ceil(j/zMax*(levels)),floor(i/profL
en*(profLen/dx)+1));
    end
end
%%
% Plot Figures Summarising Data & Results
figure(1);
clf(figure(1));
whitebg([1 1 1]);
subplot(5,1,1);
plot(x,inputData,'k');
hold on;
axis([min(x) max(x) -Inf Inf]);
title('Input Data');
ylabel('nT');
subplot(5,1,2);
plot(x,Tp,'k');
axis([min(x) max(x) -Inf Inf]);
title('Modelled Data');
if ASC>0
    ylabel('nT/dist. unit');
else
    ylabel('nT')
end
subplot(5,1,3);
plot(x,Hd,'k','LineWidth',2);
axis([min(x) max(x) -Inf Inf]);
hold on;
plot(x,Vd,'-.k');
axis([min(x) max(x) -Inf Inf]);
title('Horiz. & Vert. Derivatives');
ylabel('nT/dist. unit');
subplot(5,1,4);
plot(x,As,'k');
axis([min(x) max(x) -Inf Inf]);
title('Anal. Sig. Ampl. of Modelled Data');
```

```
ylabel('nT/dist. unit');
subplot(5,1,5);
axis([min(x) max(x) -Inf Inf]);
title('Tilt');
ylabel('Radians');
hold on;
plot(x,msDepths(levels,:),'Color',[0.8 0.8 0.8]);
plot(x,msDepths(ceil(levels*0.75),:),'b');%'Color',[0.6 0.6
0.6]);
plot(x,msDepths(ceil(levels*0.5),:),'g');%'Color',[0.3 0.3 0.3]);
plot(x,msDepths(1,:),'r');%'Color',[0 0 0]);
xlabel('Distance');
box('on');

figure(2);
clf(figure(2));
subplot(4,1,1);
plot(x,inputData,'k');
hold on;
axis([min(x) max(x) -Inf Inf]);
title('Input Data');
ylabel('nT');
subplot(4,1,2);
imagesc(SolDensStr);
hold on;
contourf(flipud(msDepthsStr));
title('Multi Scale Tilt Depth Field');
ylabel('Depth');
grid;
axis ij;
axis([min(x) max(x) 0 zMax]);
contour(flipud(msDepthsStr),'w');
contour(flipud(msDepthsStr),[0 0],'w','LineWidth',2);
subplot(4,1,3);
imagesc(sqrt(SolDensStr));
colormap(cmap);
hold on;
contour(SolDensStr,[max(max(SolDensStr))/10],'-k','LineWidth',1);
axis ij;
axis([min(x) max(x) 0 zMax]);
plot(intX,zeroc*zMax/levels,'k')
title('MSTDE Sol. Dens.');
ylabel('Depth');
grid;
subplot(4,1,4);
imagesc(sqrt(EulSolDensStr));
title('Euler Sol. Dens. & MSTDE Sol.');
xlabel('Distance');
ylabel('Depth');
grid;
axis ij;
axis([min(x) max(x) 0 zMax]);
hold on;
plot(Peak(:,1)*dx+min(x),-Peak(:,2),'ok','MarkerSize',5);
contour(SolDensStr,[max(max(SolDensStr))/10],'-k','LineWidth',1);

figure(3);
clf(figure(3));
```

```
bins=[0:zMax/50:zMax];
hist(-SolStatRand(:,2),bins);
axis tight;
hold on;
xlabel('Depth');
ylabel('MSTDE Solution Count');
title('Histogram');
colormap(flipud(gray));

figure(4);
clf(figure(4));
hist(-EulZ,bins);
axis tight;
hold on;
xlabel('Depth');
ylabel('Euler Solution Count');
title('Histogram');
colormap(flipud(gray));
%%
% Export Figures
for i=1:4
    outFile = char(['Figure' num2str(i) '(' fileName ').fig']);
    saveas(figure(i),outFile);
    outFile = char(['Figure' num2str(i) '(' fileName ').bmp']);
    saveas(figure(i),outFile);
end
```

# APPENDIX B

Appendix B contains a list of figures (Figure 55 - Figure 89) depicting the various data used to test the Multi-Scale Tilt Depth Estimation method and the results thereof. All figures shown within Appendix B make use of the total magnetic intensity as the input component to the algorithm.

## Vertical sheet at various depths

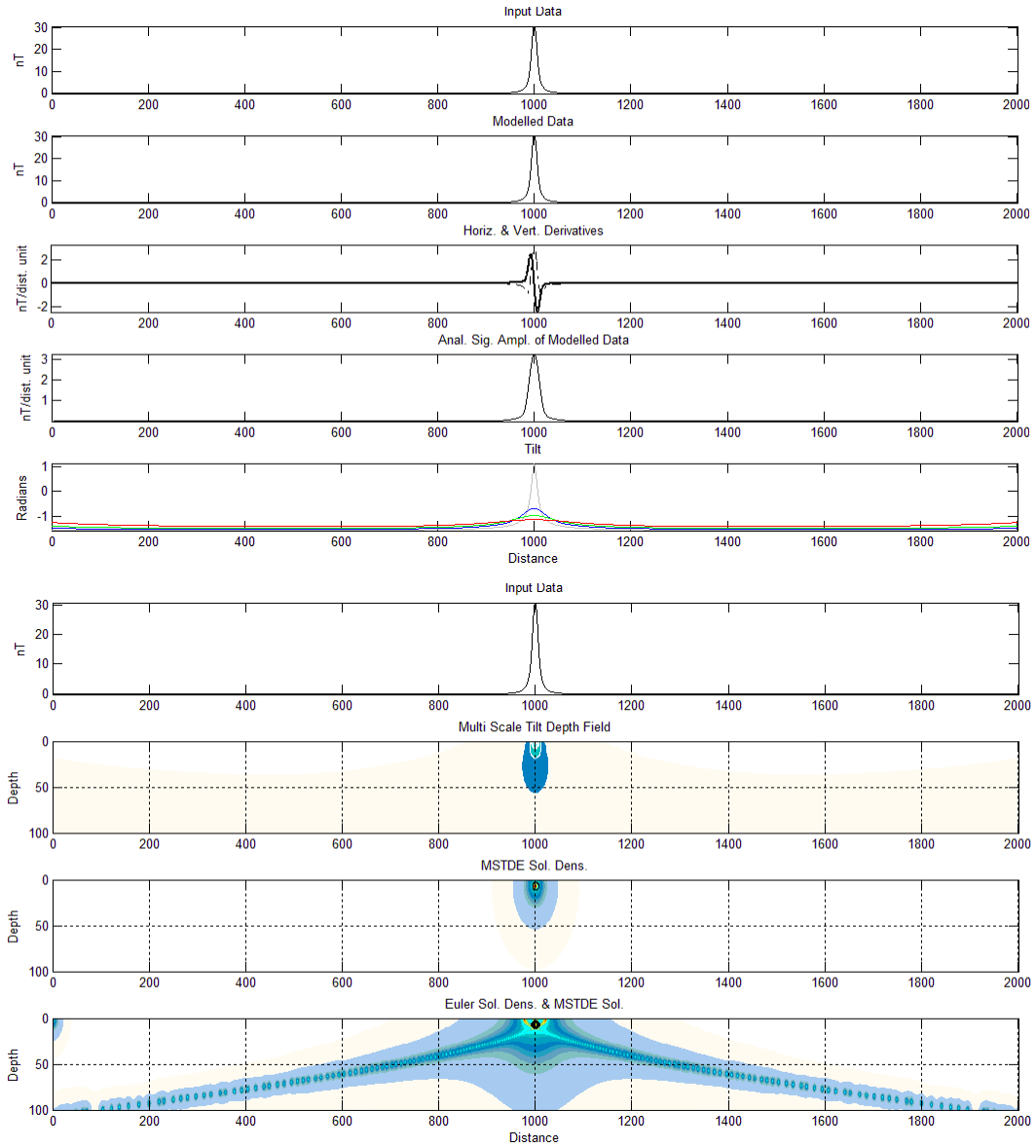


**Figure 55. Synthetic model data (Depth of 5 dist. units) with plots of the spatial derivatives, analytic signal amplitude and various continued tilt products (Top), Synthetic model data with MSTD distribution, MSTDE solution density and Euler solution density with MSTDE solution locations (Bottom).**

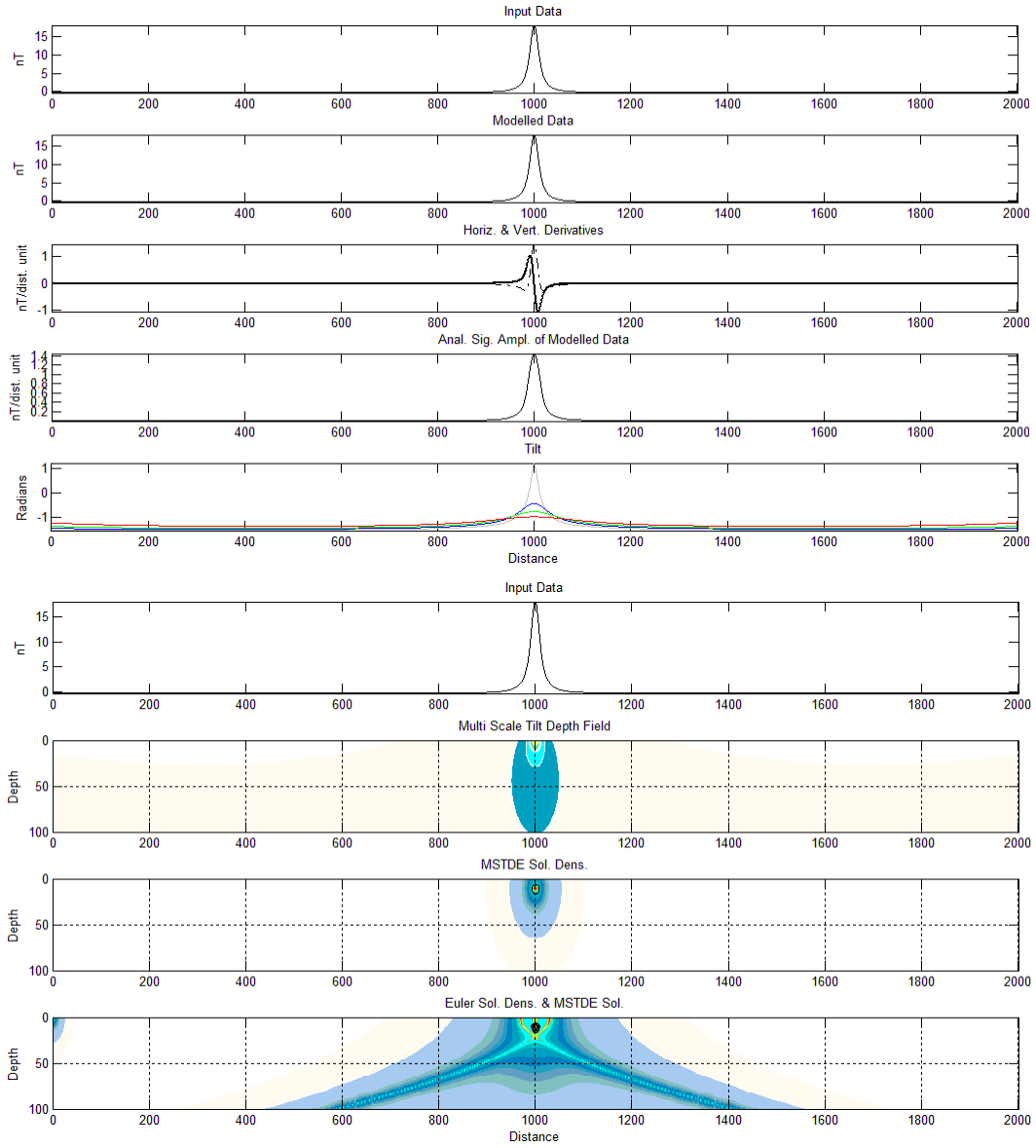


**Figure 56. Synthetic model data (Depth of 10 dist. units) with plots of the spatial derivatives, analytic signal amplitude and various continued tilt products (Top), Synthetic model data with MSTD distribution, MSTDE solution density and Euler solution density with MSTDE solution locations (Bottom).**

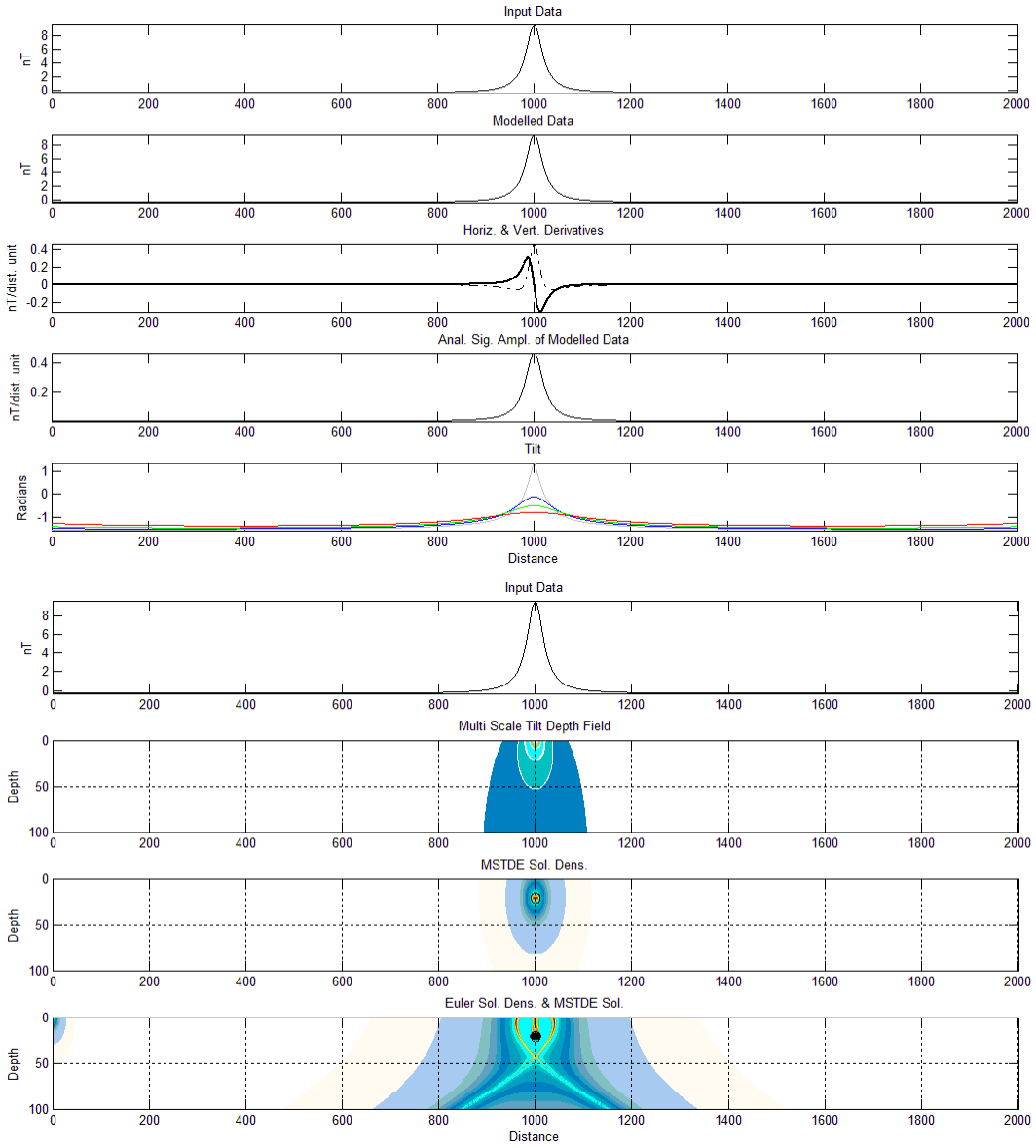


**Figure 57. Synthetic model data (Depth of 20 dist. units) with plots of the spatial derivatives, analytic signal amplitude and various continued tilt products (Top), Synthetic model data with MSTD distribution, MSTDE solution density and Euler solution density with MSTDE solution locations (Bottom).**

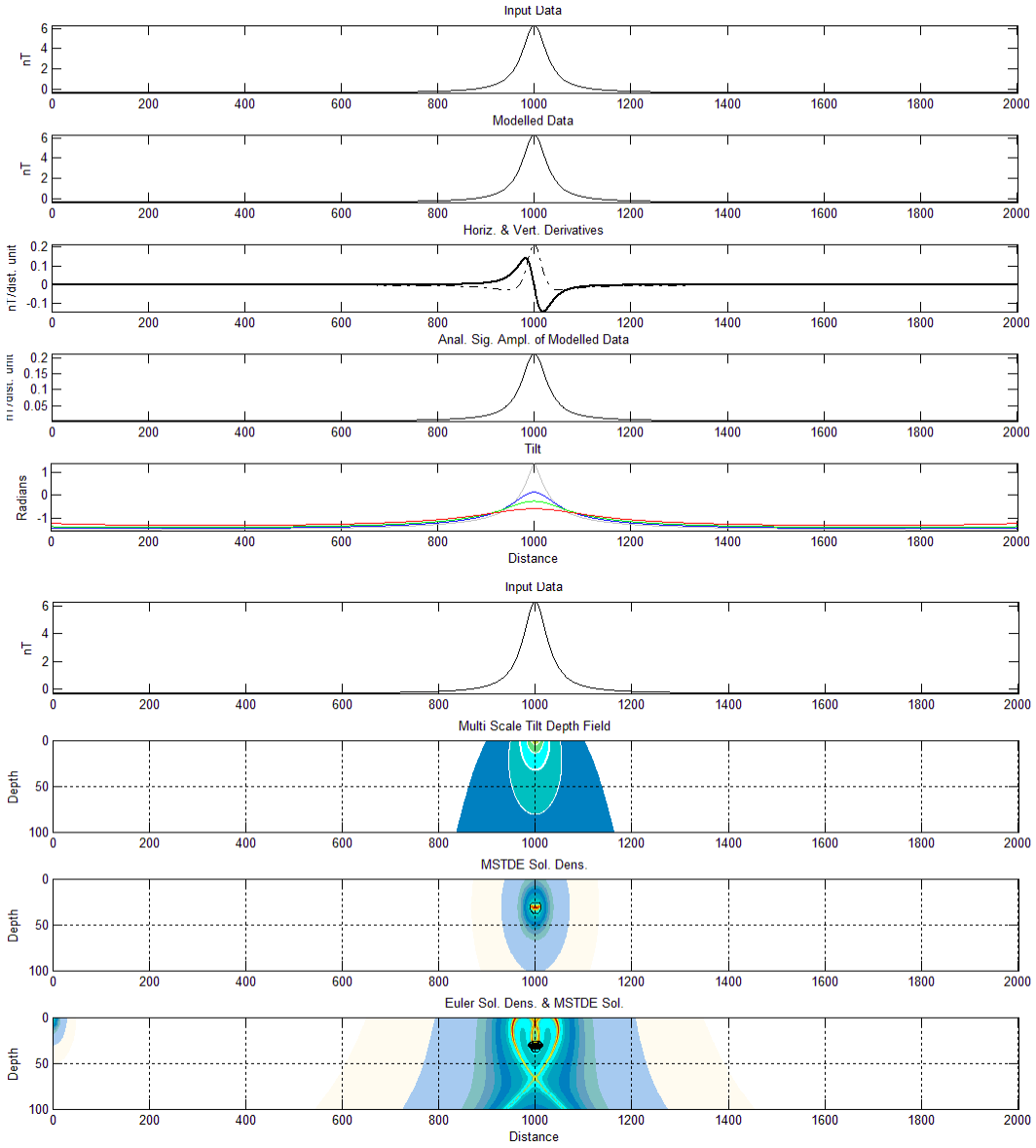


**Figure 58. Synthetic model data (Depth of 30 dist. units) with plots of the spatial derivatives, analytic signal amplitude and various continued tilt products (Top), Synthetic model data with MSTD distribution, MSTDE solution density and Euler solution density with MSTDE solution locations (Bottom).**

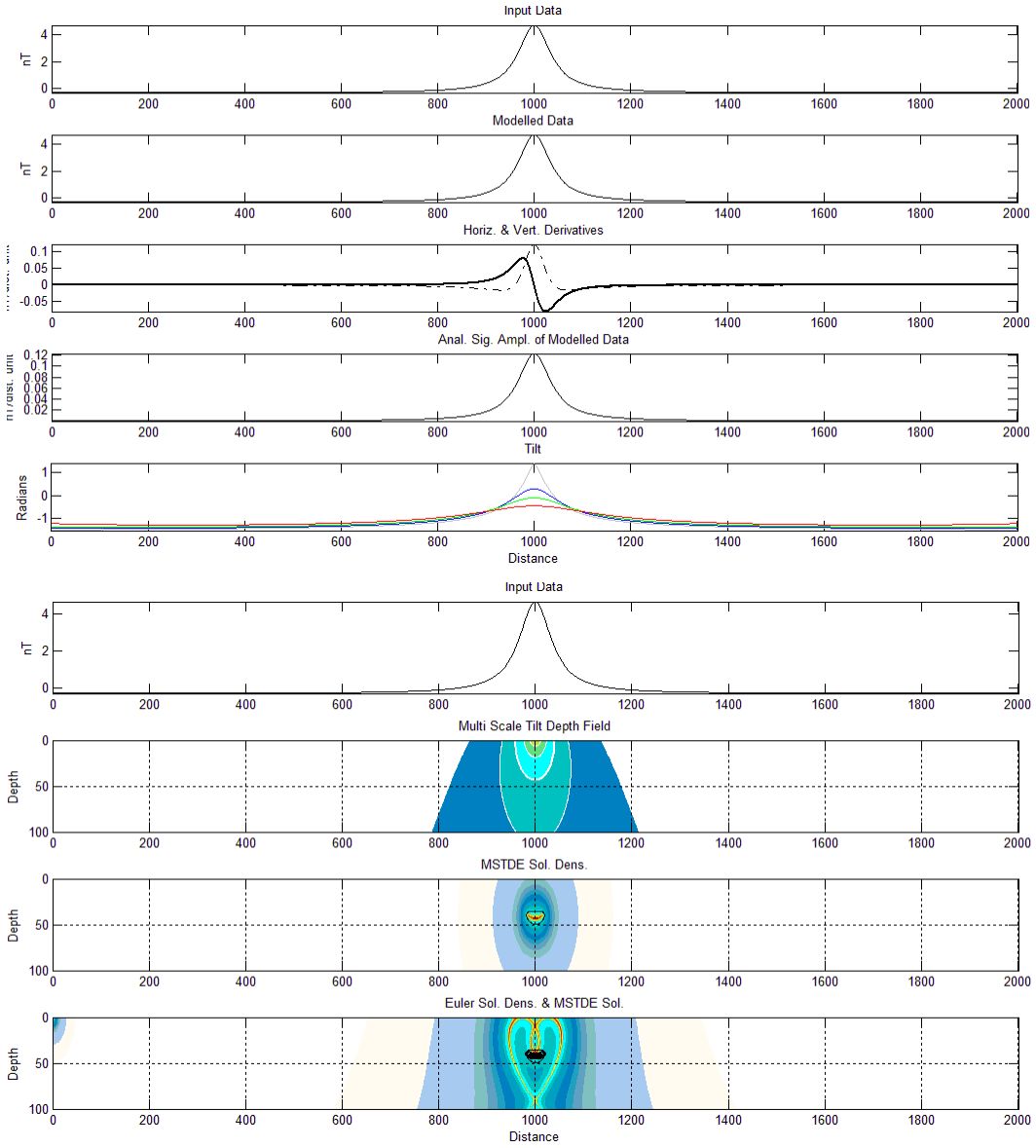


**Figure 59. Synthetic model data (Depth of 40 dist. units) with plots of the spatial derivatives, analytic signal amplitude and various continued tilt products (Top), Synthetic model data with MSTD distribution, MSTDE solution density and Euler solution density with MSTDE solution locations (Bottom).**

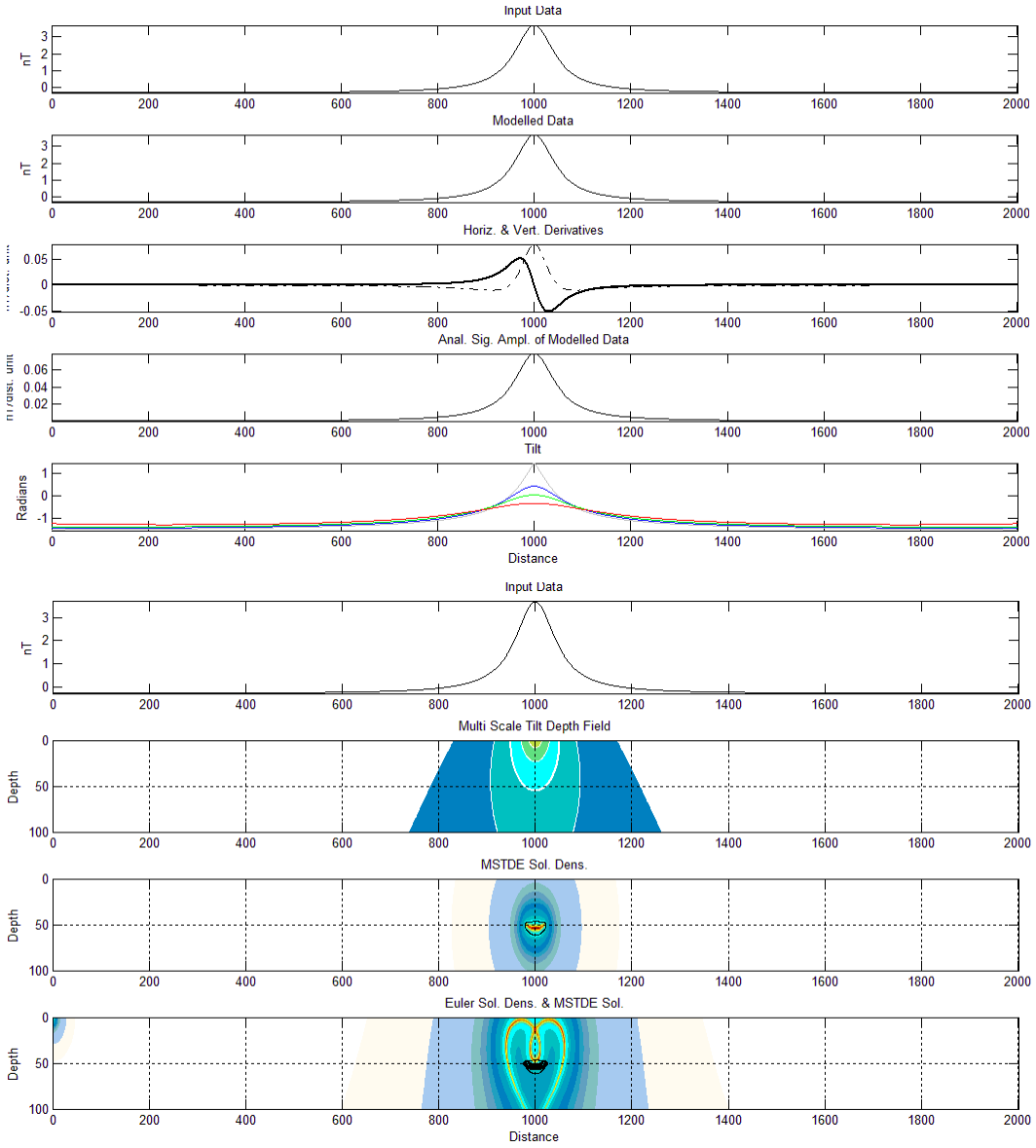


**Figure 60. Synthetic model data (Depth of 50 dist. units) with plots of the spatial derivatives, analytic signal amplitude and various continued tilt products (Top), Synthetic model data with MSTD distribution, MSTDE solution density and Euler solution density with MSTDE solution locations (Bottom).**

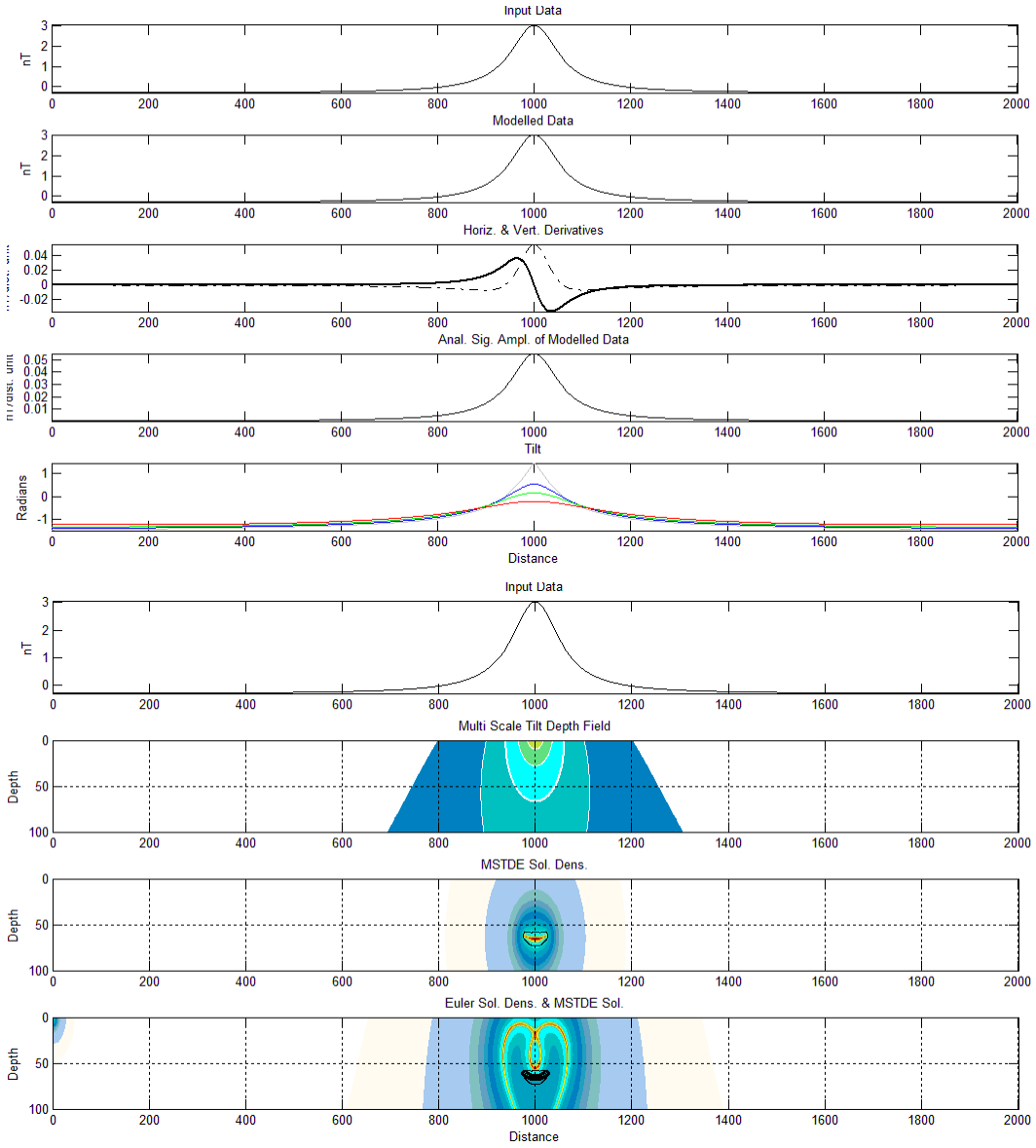


**Figure 61. Synthetic model data (Depth of 60 dist. units) with plots of the spatial derivatives, analytic signal amplitude and various continued tilt products (Top), Synthetic model data with MSTD distribution, MSTDE solution density and Euler solution density with MSTDE solution locations (Bottom).**

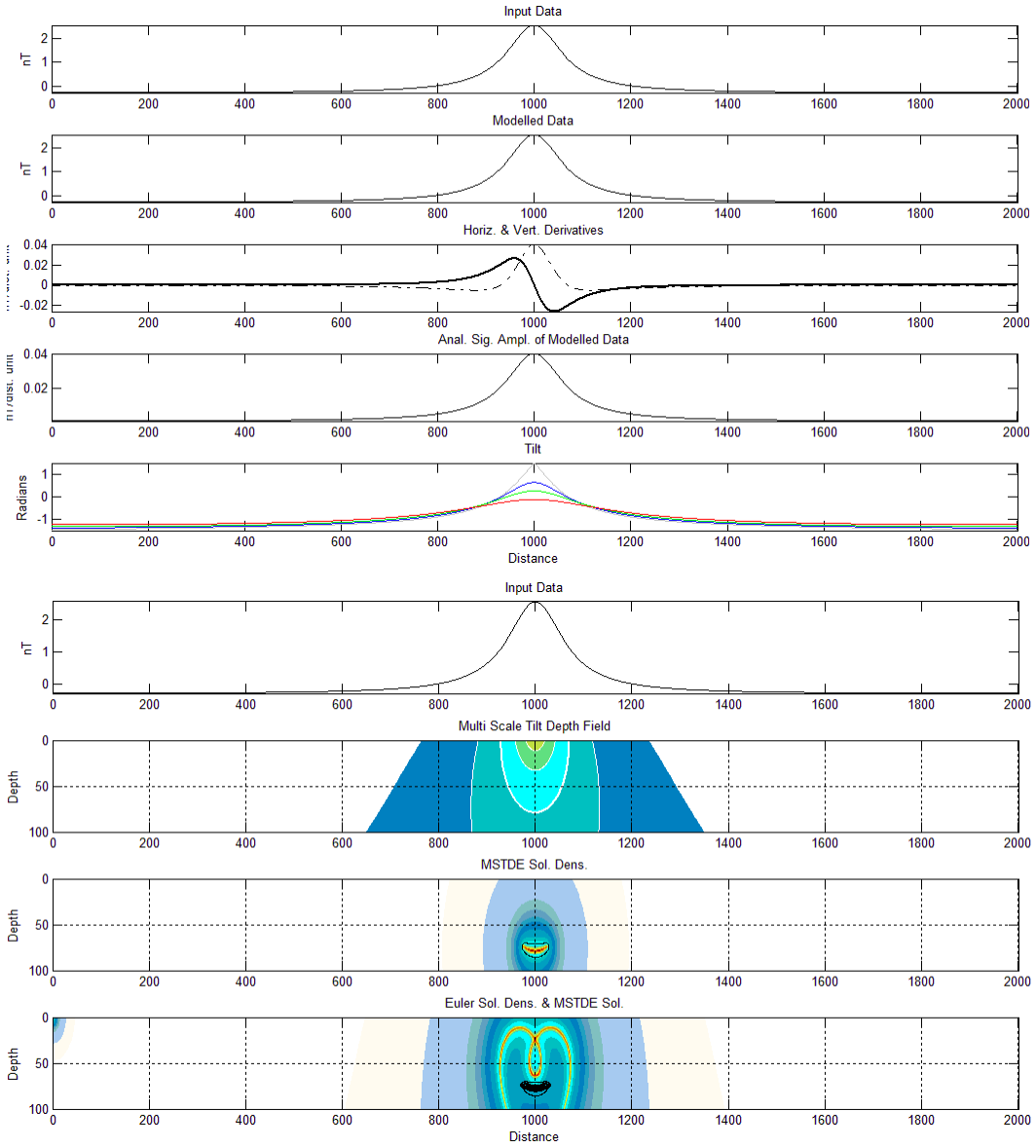


**Figure 62. Synthetic model data (Depth of 70 dist. units) with plots of the spatial derivatives, analytic signal amplitude and various continued tilt products (Top), Synthetic model data with MSTD distribution, MSTDE solution density and Euler solution density with MSTDE solution locations (Bottom).**

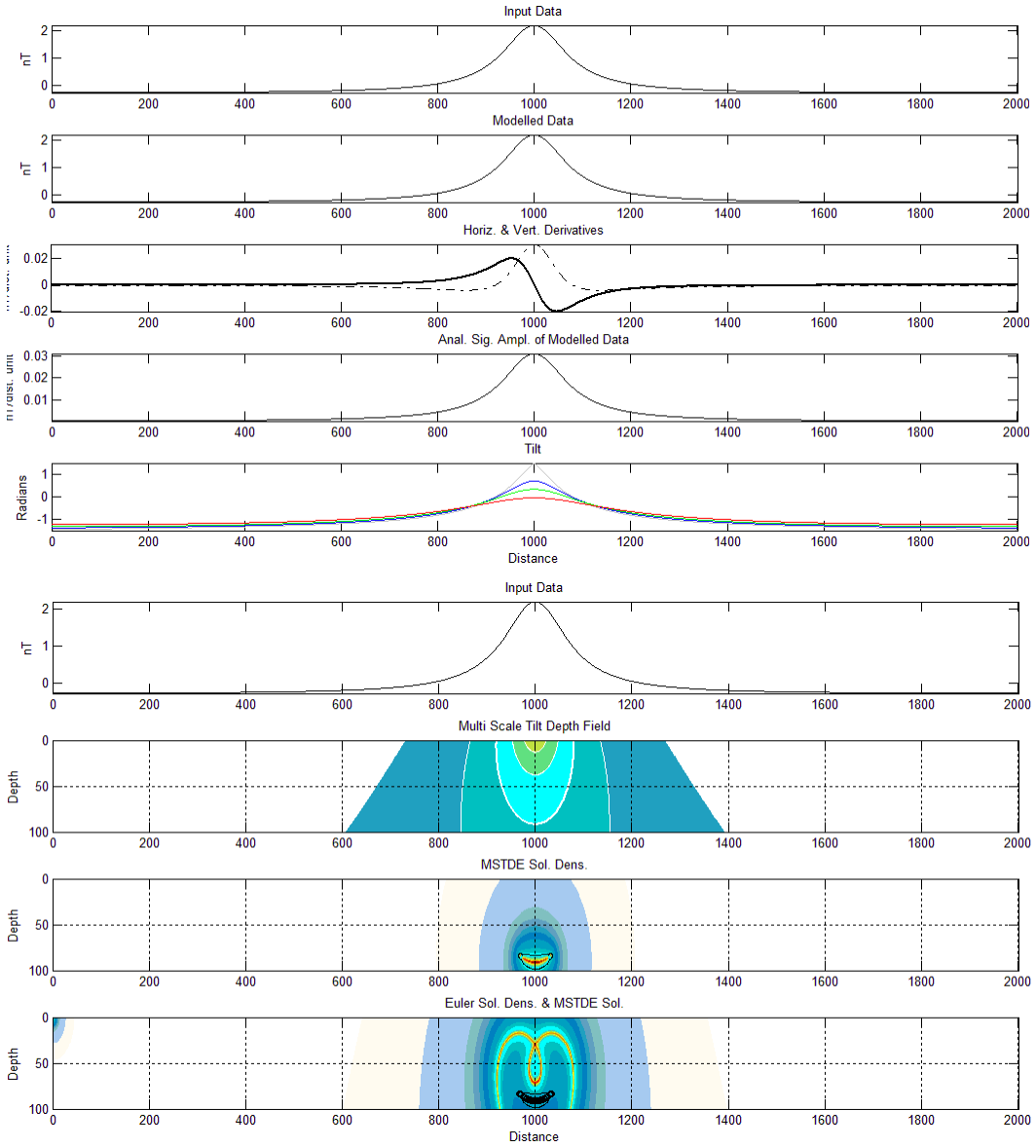


**Figure 63. Synthetic model data (Depth of 80 dist. units) with plots of the spatial derivatives, analytic signal amplitude and various continued tilt products (Top), Synthetic model data with MSTD distribution, MSTDE solution density and Euler solution density with MSTDE solution locations (Bottom).**

## Sheet with various dips

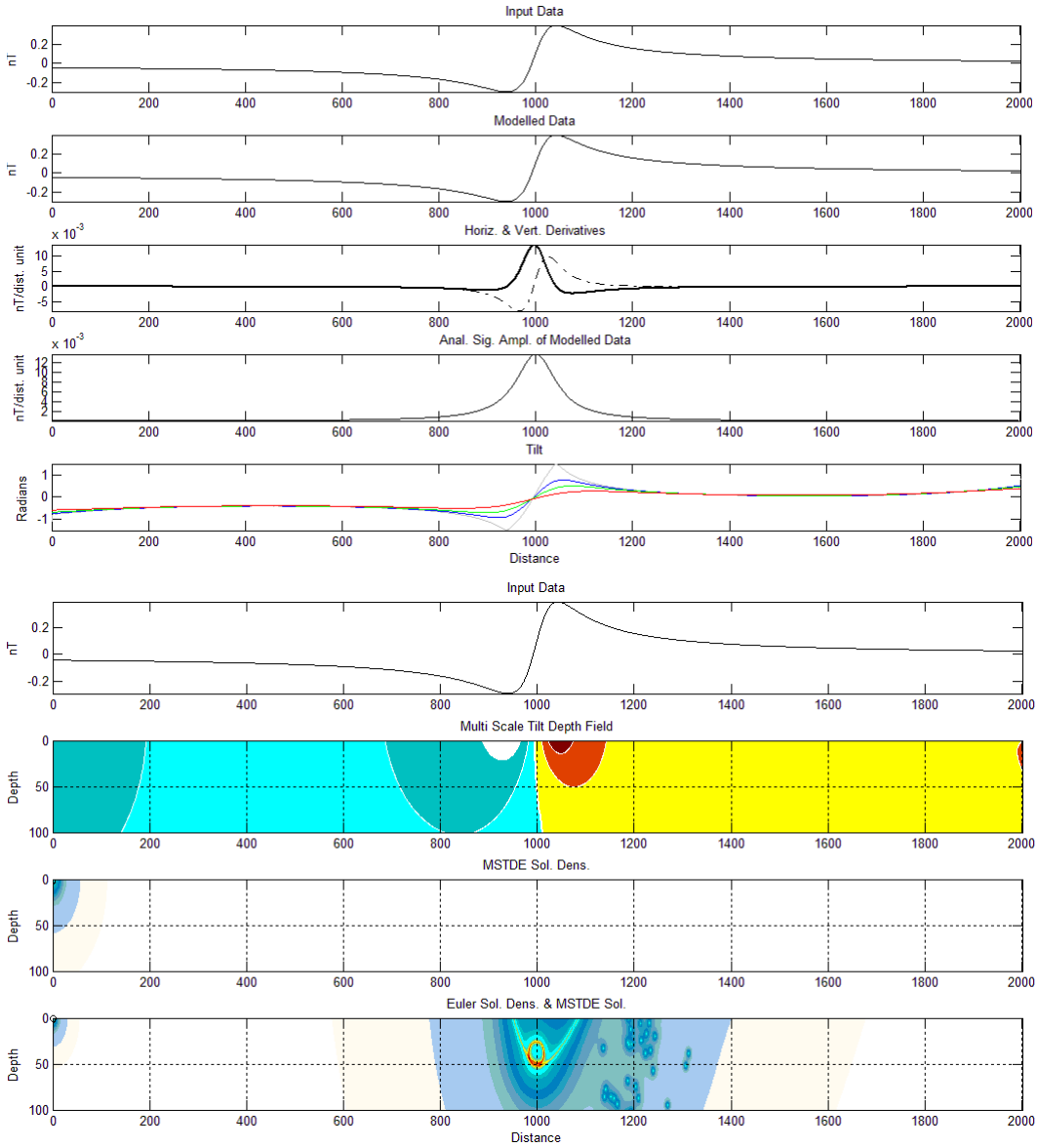


**Figure 64. Synthetic model data (Dip of 10°, Depth of 50 dist. units) with plots of the spatial derivatives, analytic signal amplitude and various continued tilt products (Top), Synthetic model data with MSTD distribution, MSTDE solution density and Euler solution density with MSTDE solution locations (Bottom).**

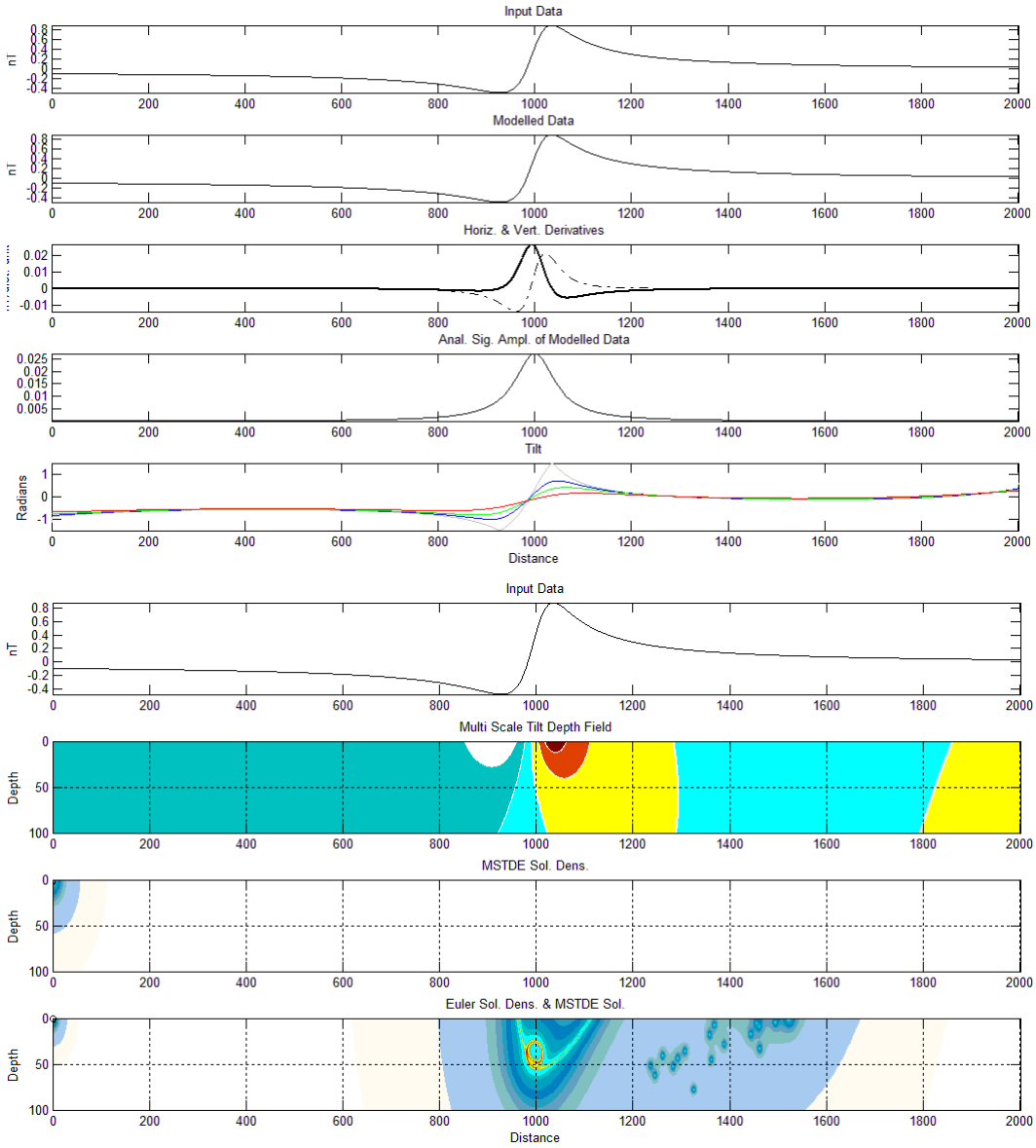


**Figure 65. Synthetic model data (Dip of 20°, Depth of 50 dist. units) with plots of the spatial derivatives, analytic signal amplitude and various continued tilt products (Top), Synthetic model data with MSTD distribution, MSTDE solution density and Euler solution density with MSTDE solution locations (Bottom).**

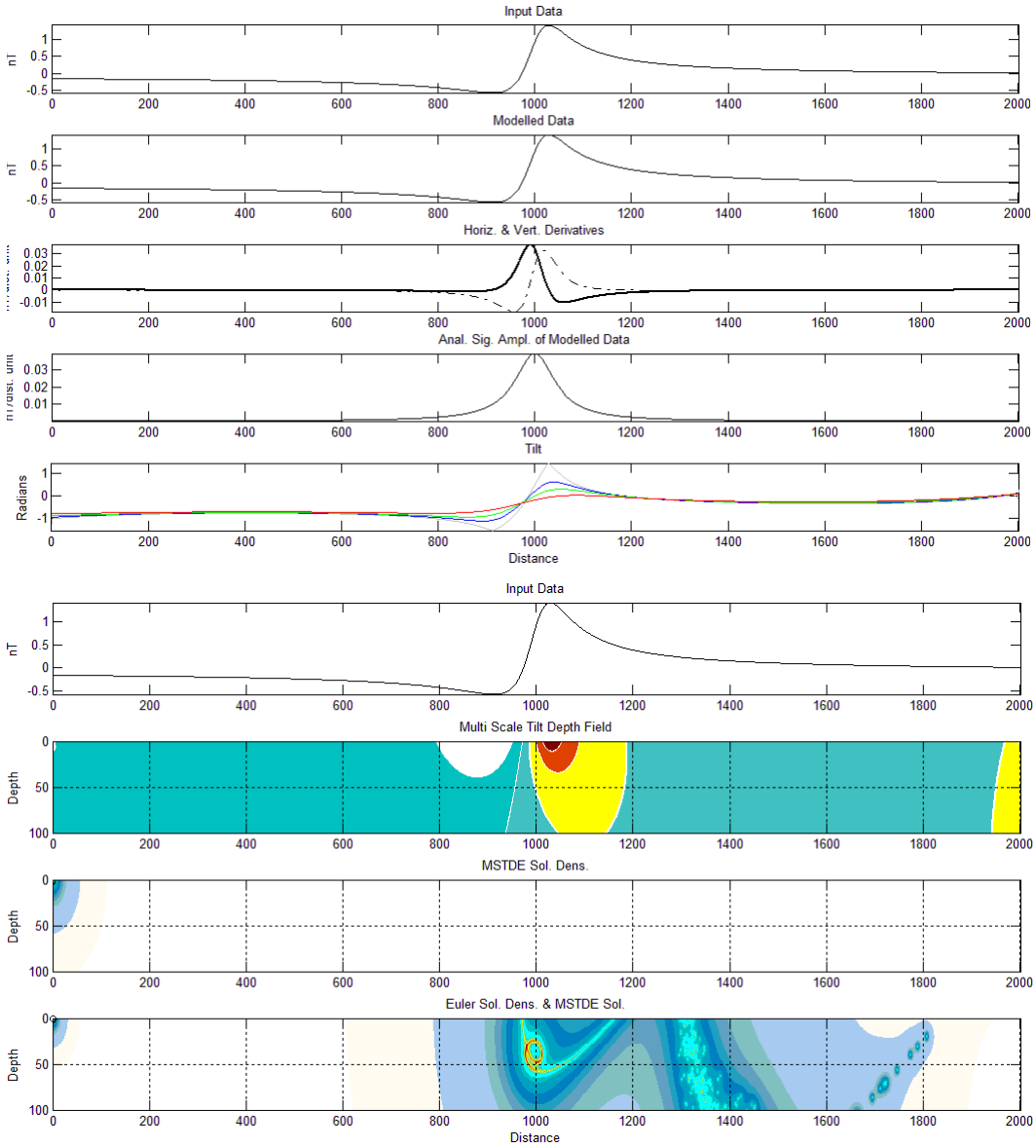


**Figure 66. Synthetic model data (Dip of 30°, Depth of 50 dist. units) with plots of the spatial derivatives, analytic signal amplitude and various continued tilt products (Top), Synthetic model data with MSTD distribution, MSTDE solution density and Euler solution density with MSTDE solution locations (Bottom).**

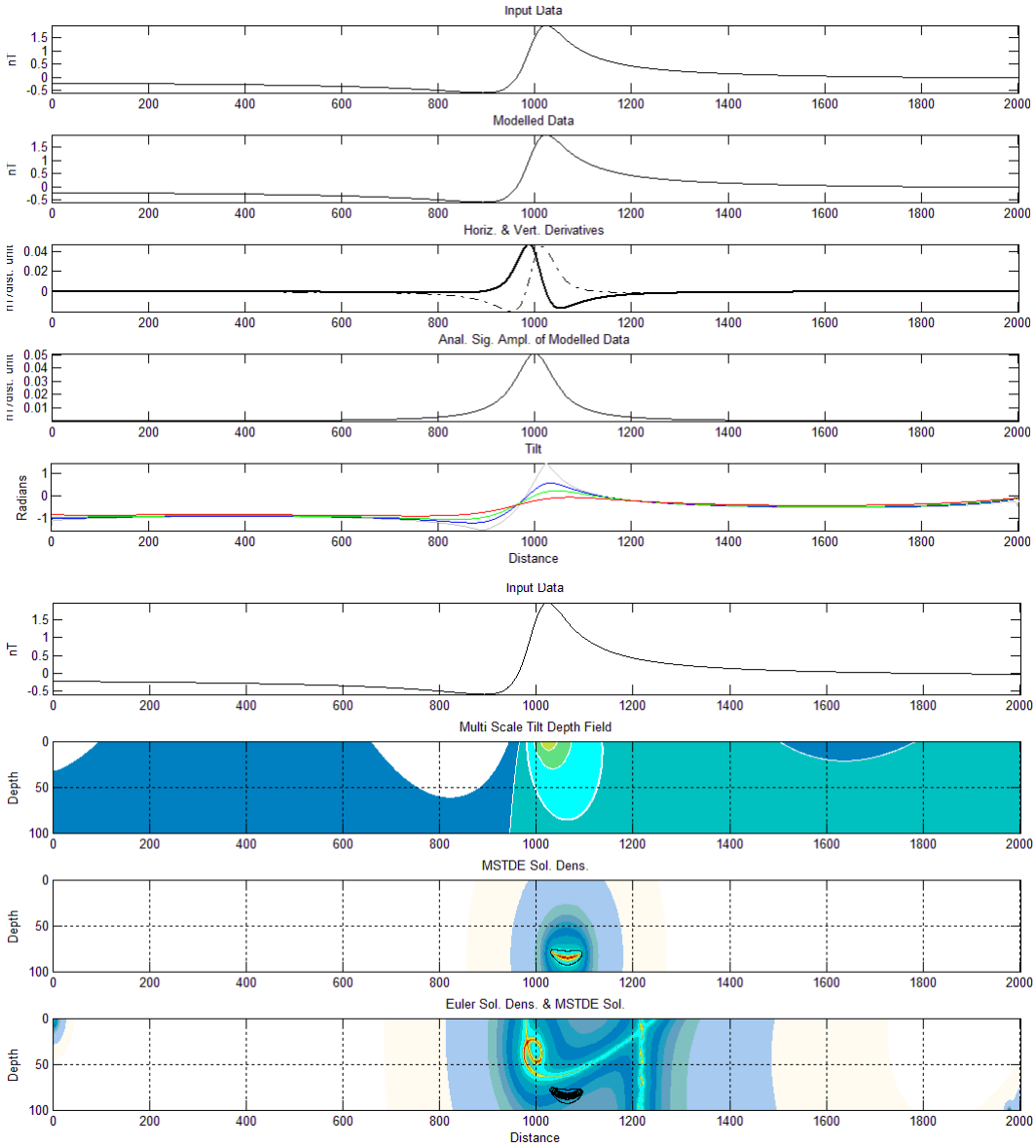


**Figure 67. Synthetic model data (Dip of 40°, Depth of 50 dist. units) with plots of the spatial derivatives, analytic signal amplitude and various continued tilt products (Top), Synthetic model data with MSTD distribution, MSTDE solution density and Euler solution density with MSTDE solution locations (Bottom).**

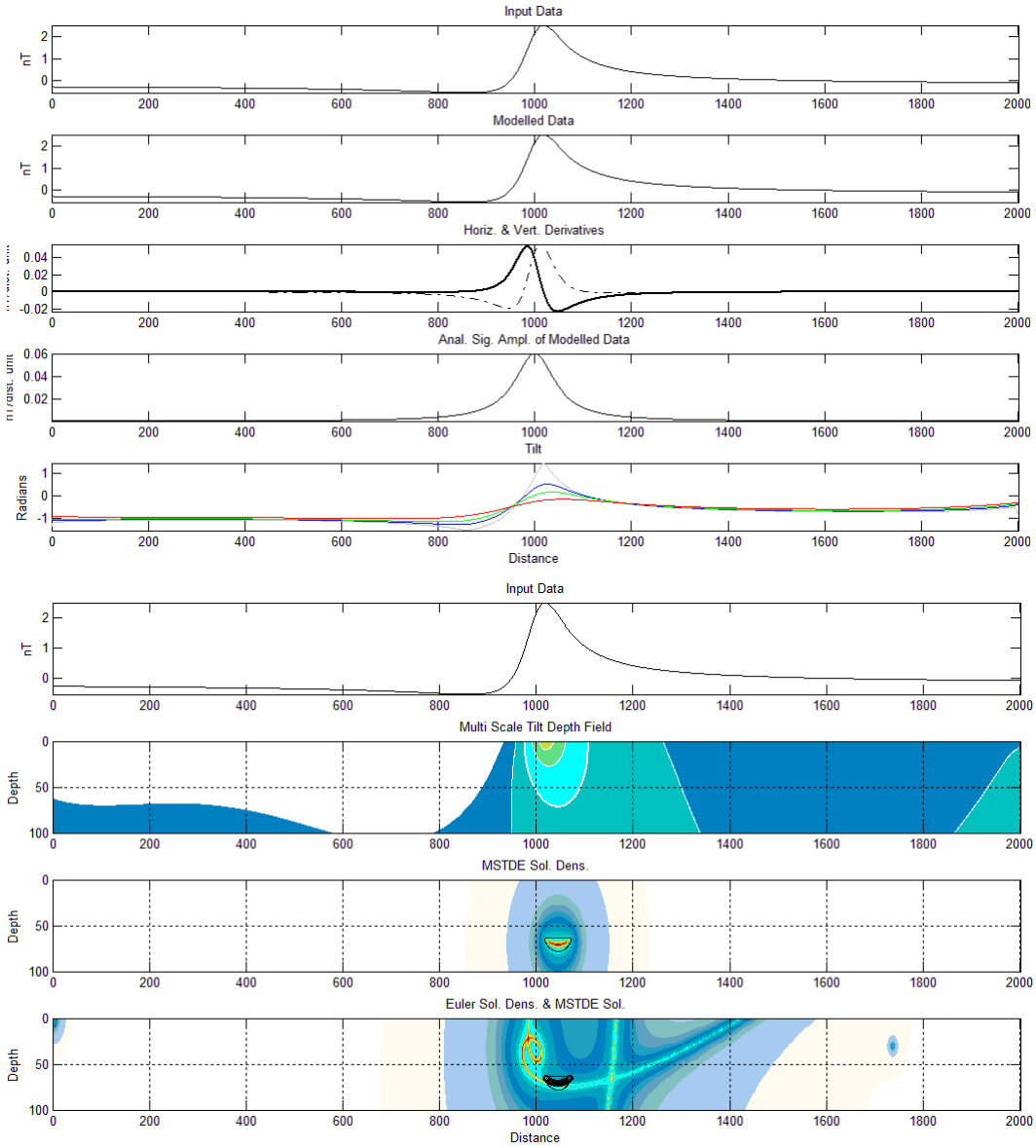


**Figure 68. Synthetic model data (Dip of 50°, Depth of 50 dist. units) with plots of the spatial derivatives, analytic signal amplitude and various continued tilt products (Top), Synthetic model data with MSTD distribution, MSTDE solution density and Euler solution density with MSTDE solution locations (Bottom).**

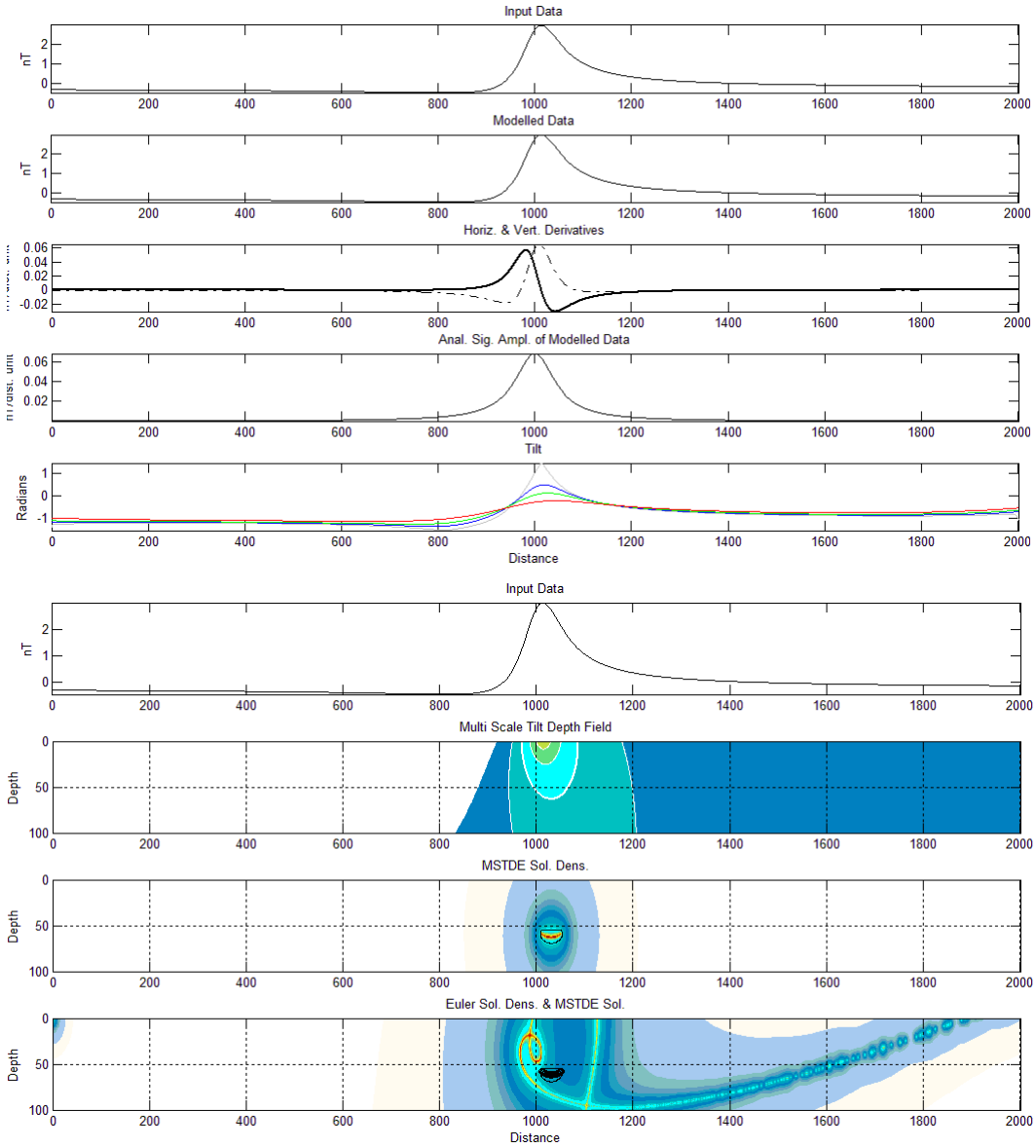


**Figure 69. Synthetic model data (Dip of 60°, Depth of 50 dist. units) with plots of the spatial derivatives, analytic signal amplitude and various continued tilt products (Top), Synthetic model data with MSTD distribution, MSTDE solution density and Euler solution density with MSTDE solution locations (Bottom).**

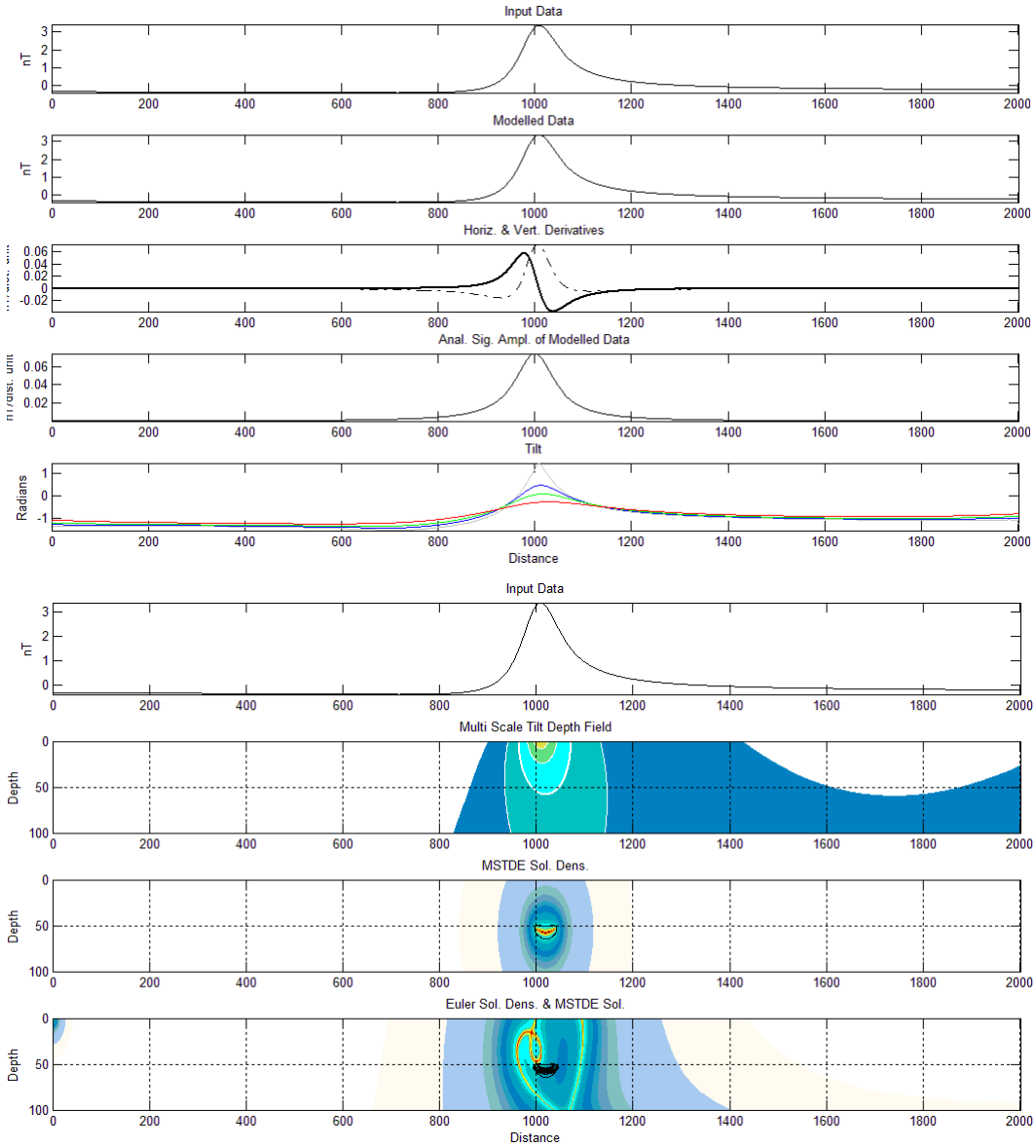


**Figure 70. Synthetic model data (Dip of 70°, Depth of 50 dist. units) with plots of the spatial derivatives, analytic signal amplitude and various continued tilt products (Top), Synthetic model data with MSTD distribution, MSTDE solution density and Euler solution density with MSTDE solution locations (Bottom).**

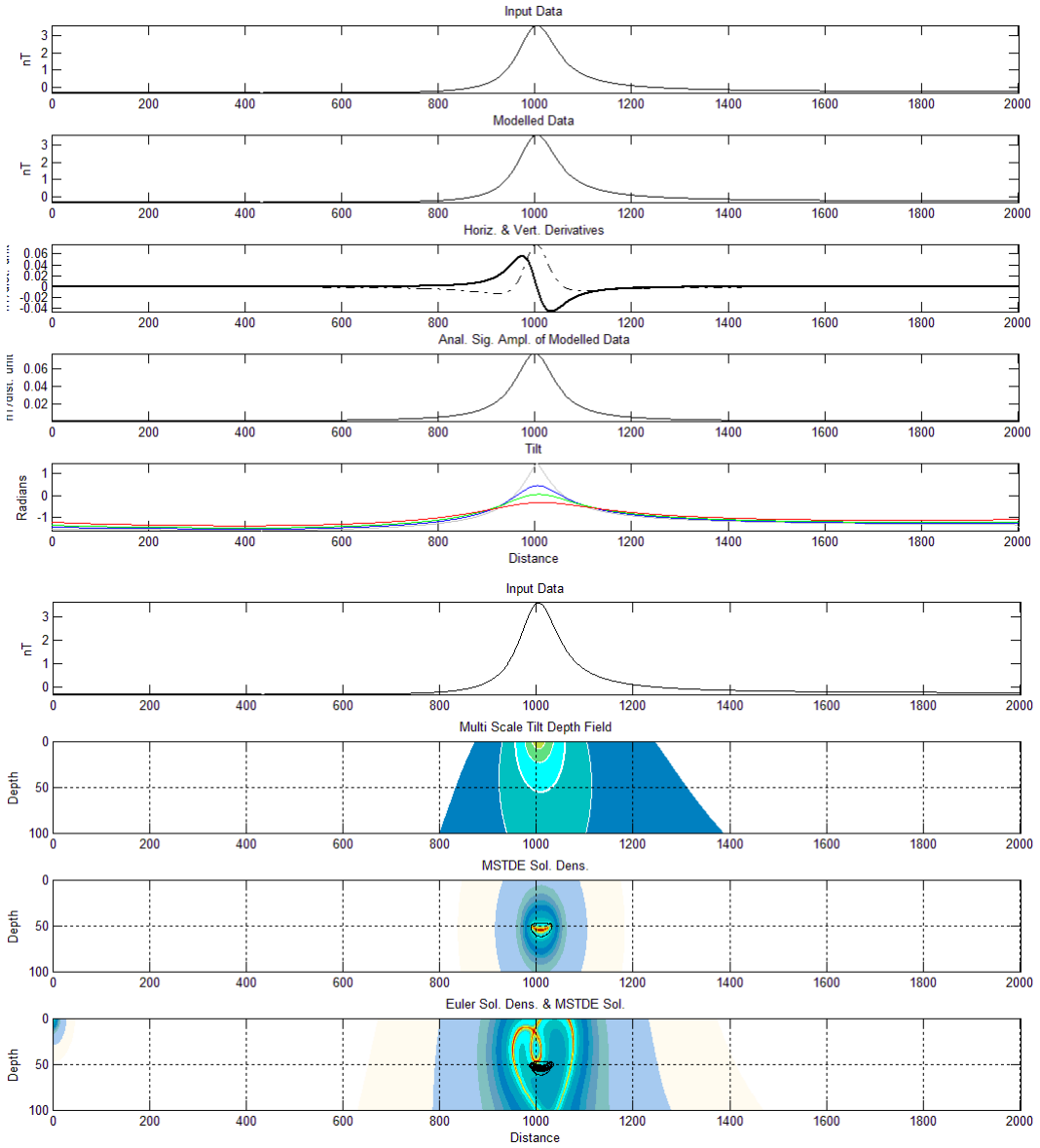


**Figure 71. Synthetic model data (Dip of 80°, Depth of 50 dist. units) with plots of the spatial derivatives, analytic signal amplitude and various continued tilt products (Top), Synthetic model data with MSTD distribution, MSTDE solution density and Euler solution density with MSTDE solution locations (Bottom).**

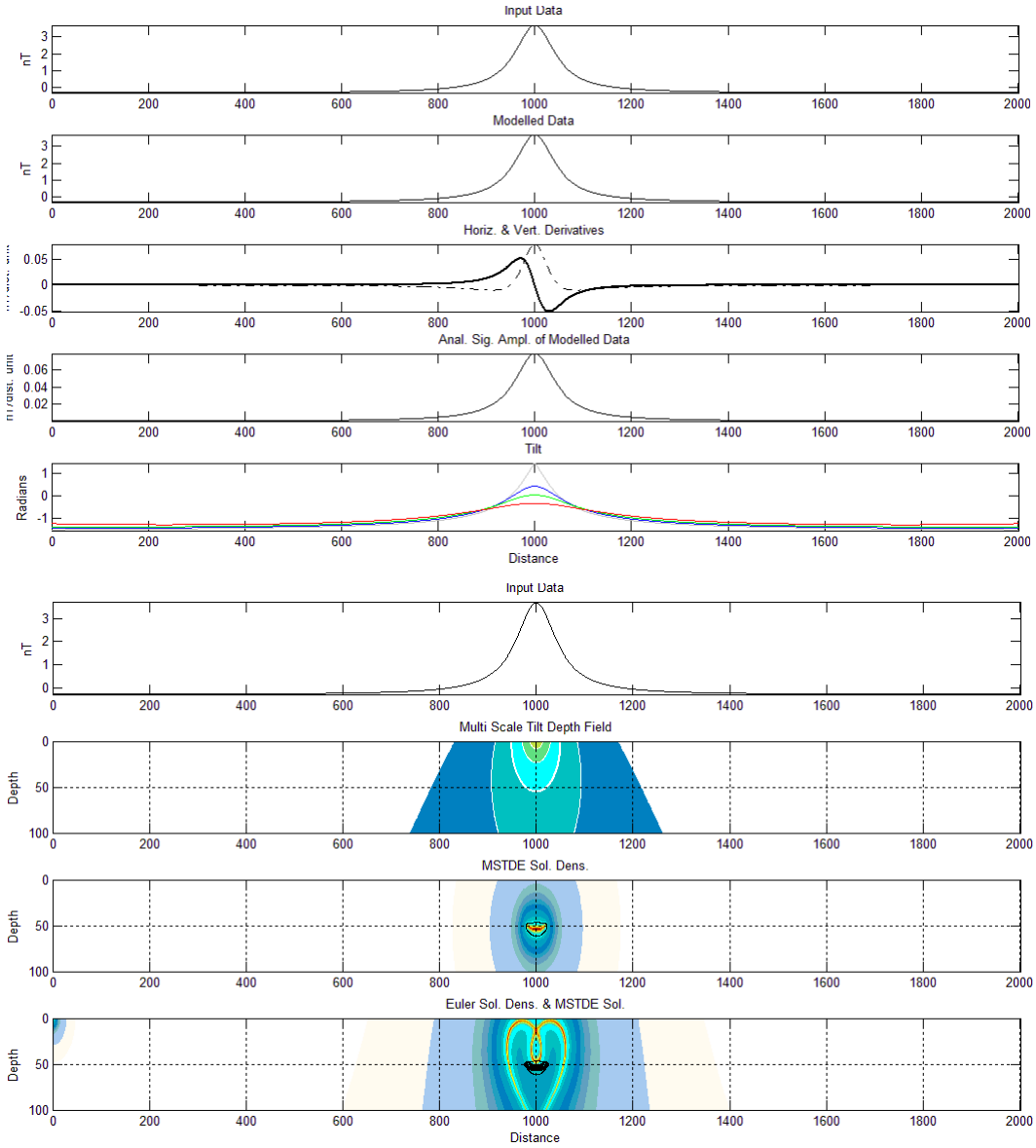


**Figure 72. Synthetic model data (Dip of 90°, Depth of 50 dist. units) with plots of the spatial derivatives, analytic signal amplitude and various continued tilt products (Top), Synthetic model data with MSTD distribution, MSTDE solution density and Euler solution density with MSTDE solution locations (Bottom).**

## Vertical sheet with various noise amplitudes – No smoothing

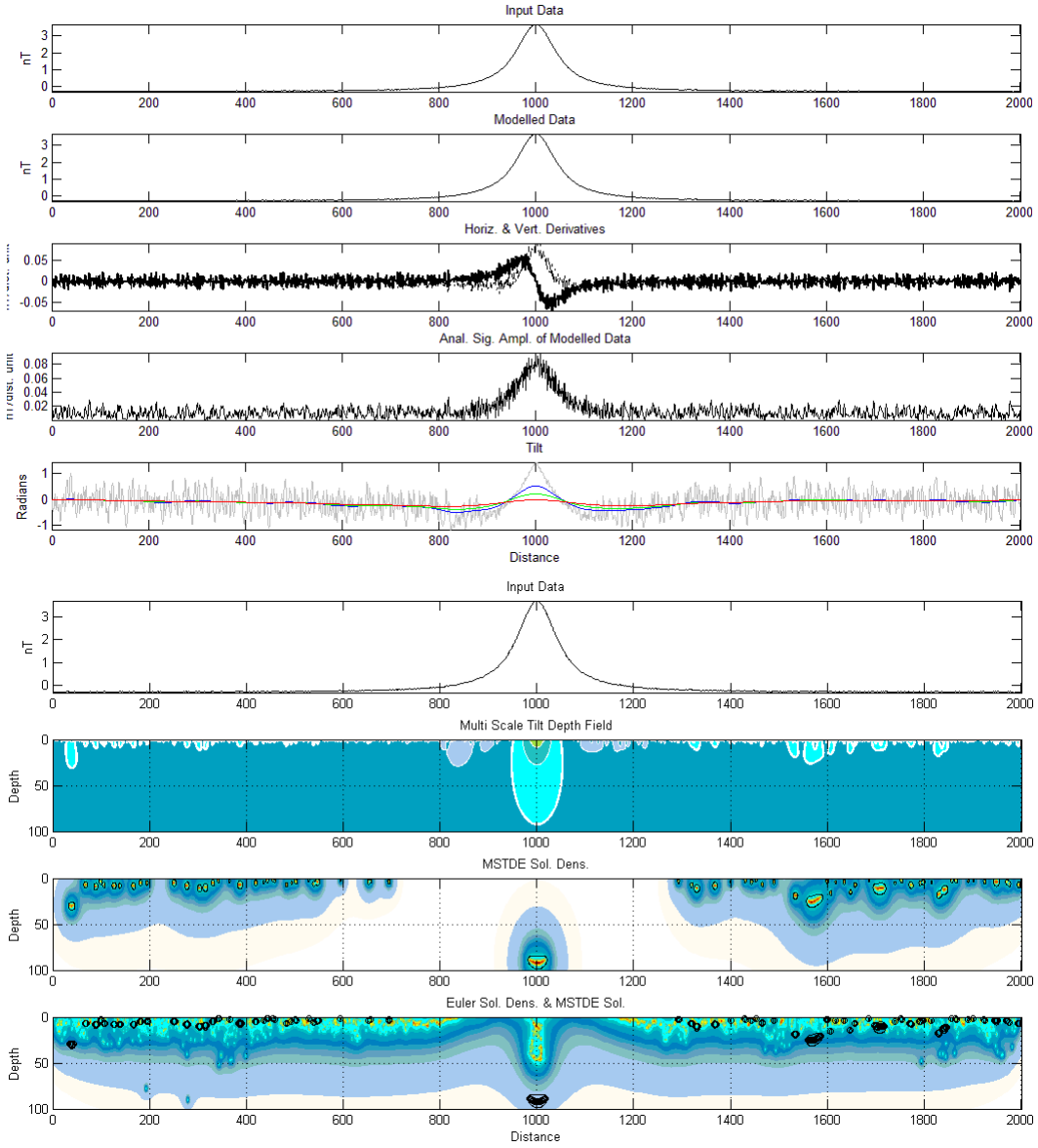


**Figure 73. Synthetic model data (Noise range of 10% of the standard deviation, Depth of 50 dist. units) with plots of the spatial derivatives, analytic signal amplitude and various continued tilt products (Top), Synthetic model data with MSTD distribution, MSTDE solution density and Euler solution density with MSTDE solution locations (Bottom). No smoothing has been applied to the data.**

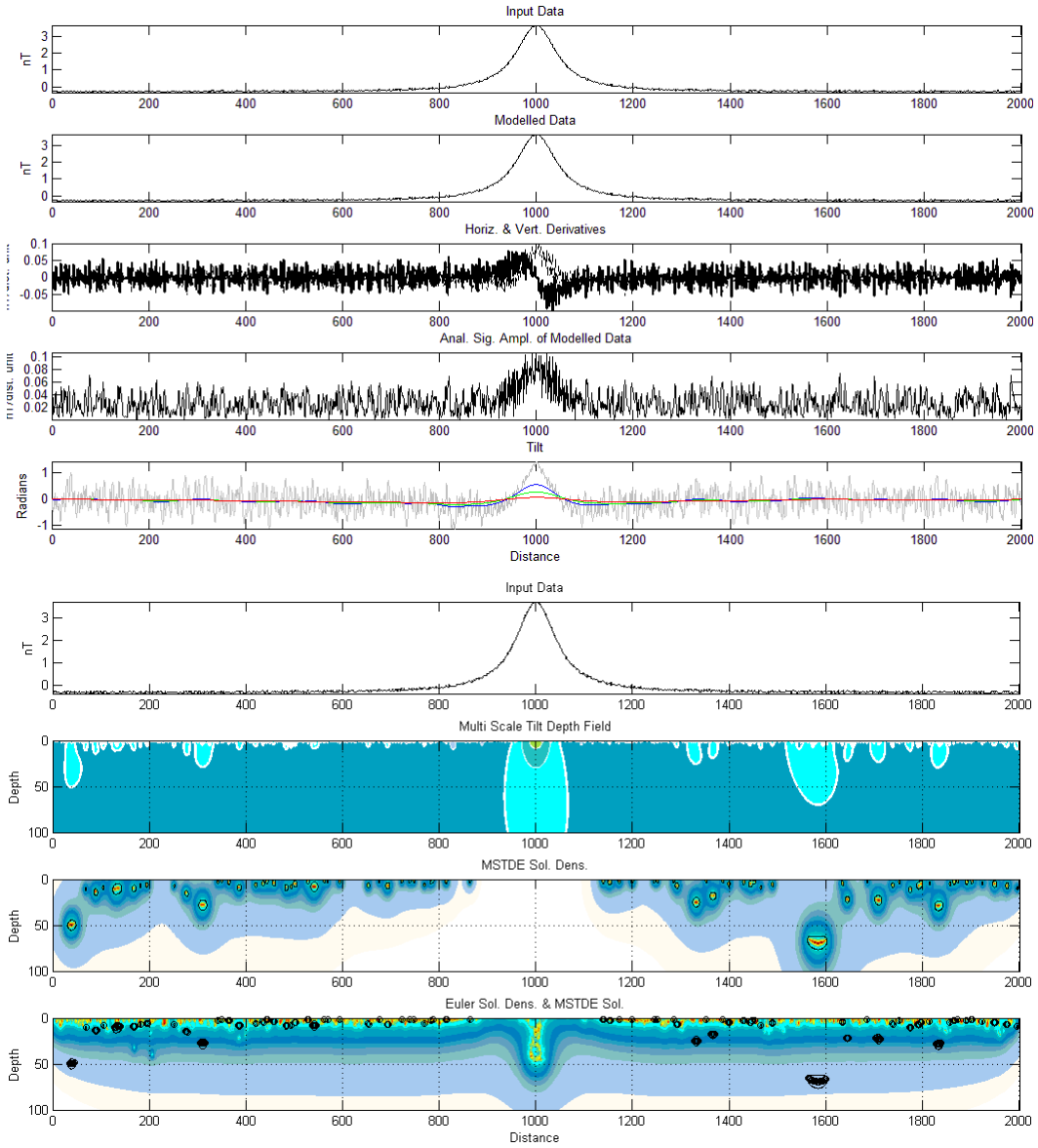


**Figure 74. Synthetic model data (Noise range of 25% of the standard deviation, Depth of 50 dist. units) with plots of the spatial derivatives, analytic signal amplitude and various continued tilt products (Top), Synthetic model data with MSTD distribution, MSTDE solution density and Euler solution density with MSTDE solution locations (Bottom). No Smoothing has been applied to the data. No smoothing has been applied to the data.**

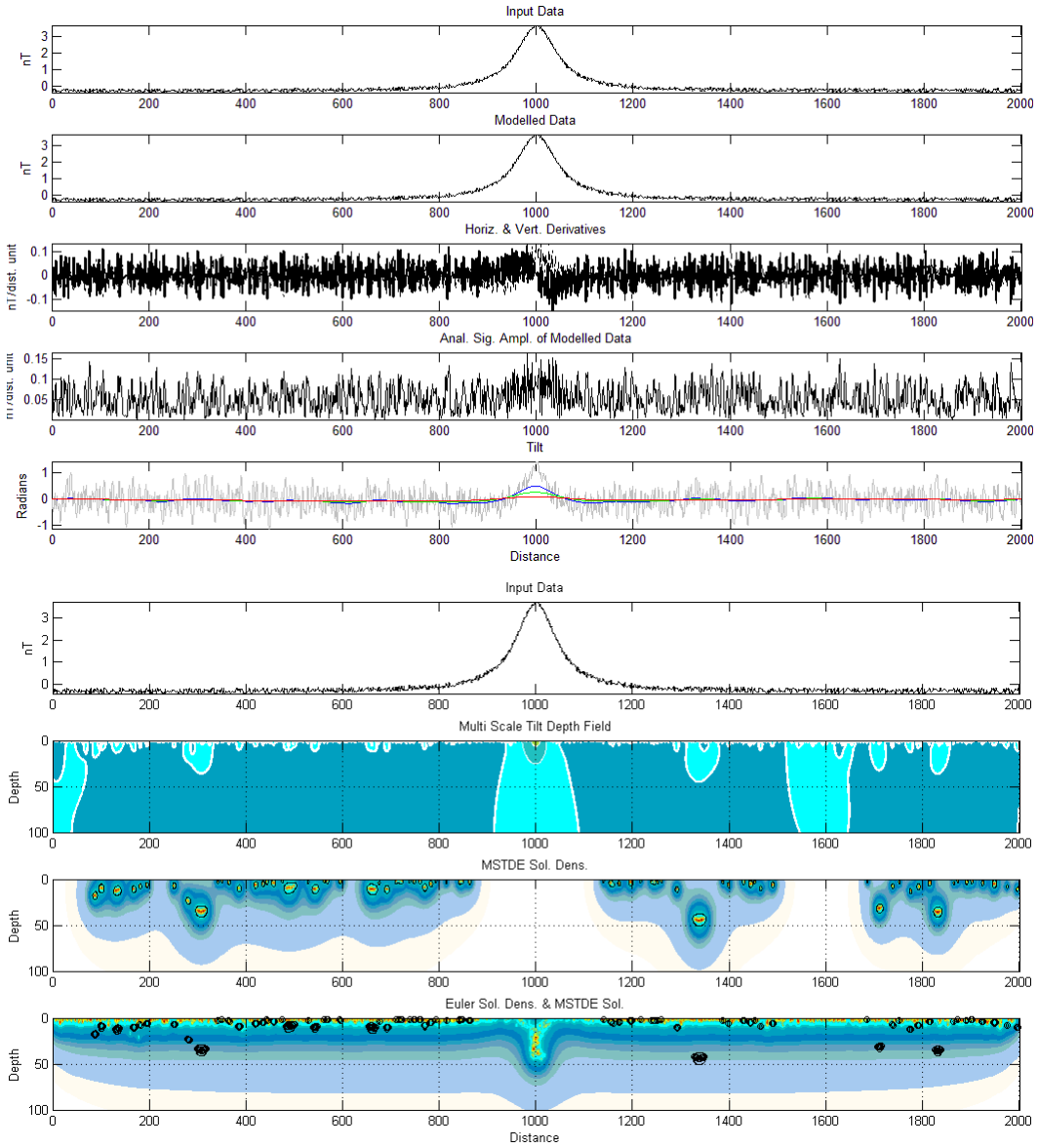


**Figure 75. Synthetic model data (Noise range of 50% of the standard deviation, Depth of 50 dist. units) with plots of the spatial derivatives, analytic signal amplitude and various continued tilt products (Top), Synthetic model data with MSTD distribution, MSTDE solution density and Euler solution density with MSTDE solution locations (Bottom). No smoothing has been applied to the data.**

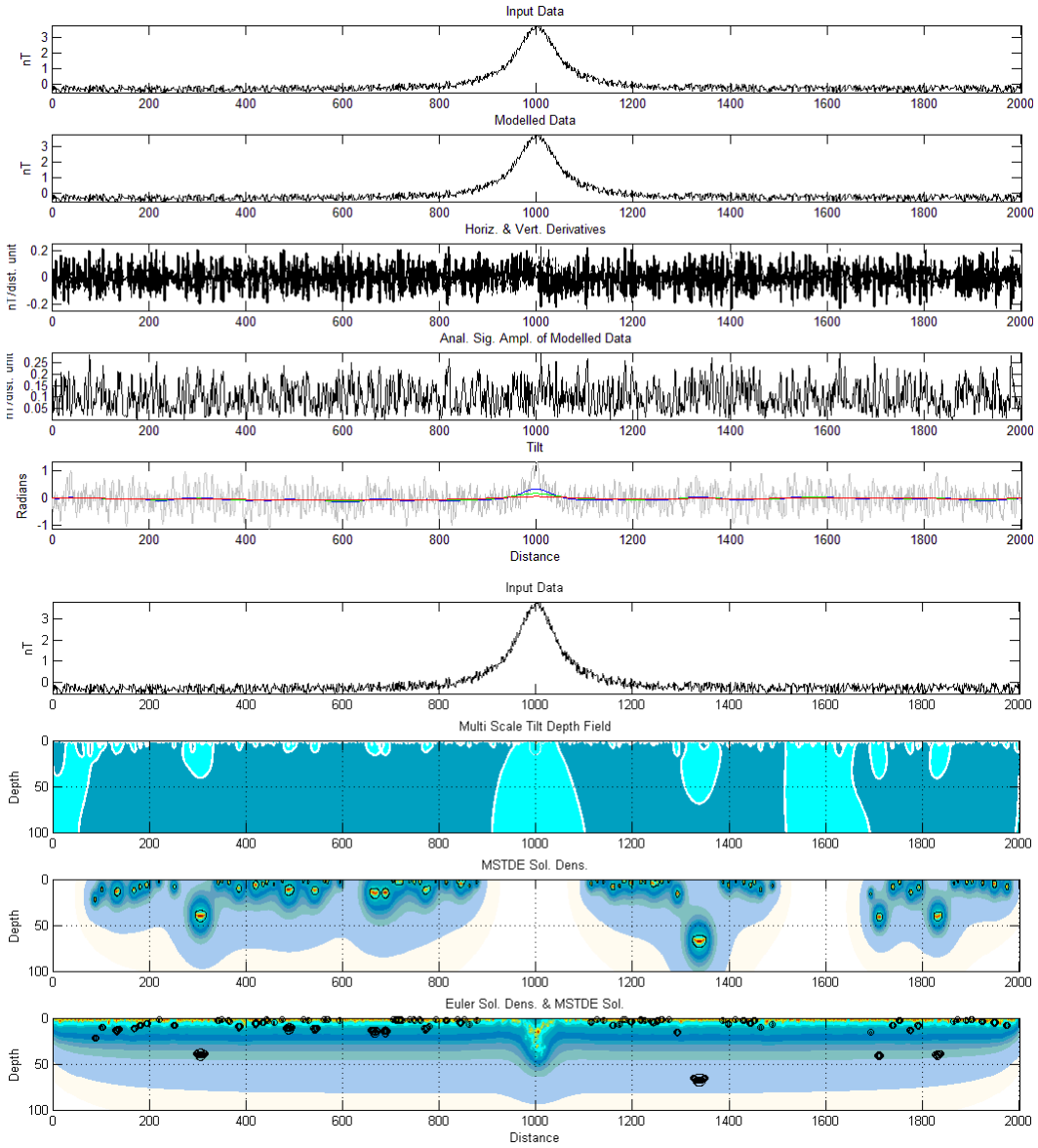


**Figure 76. Synthetic model data (Noise range of 100% of the standard deviation, Depth of 50 dist. units) with plots of the spatial derivatives, analytic signal amplitude and various continued tilt products (Top), Synthetic model data with MSTD distribution, MSTDE solution density and Euler solution density with MSTDE solution locations (Bottom). No smoothing has been applied to the data.**

## Vertical sheet with various noise amplitudes – Frequency domain smoothing

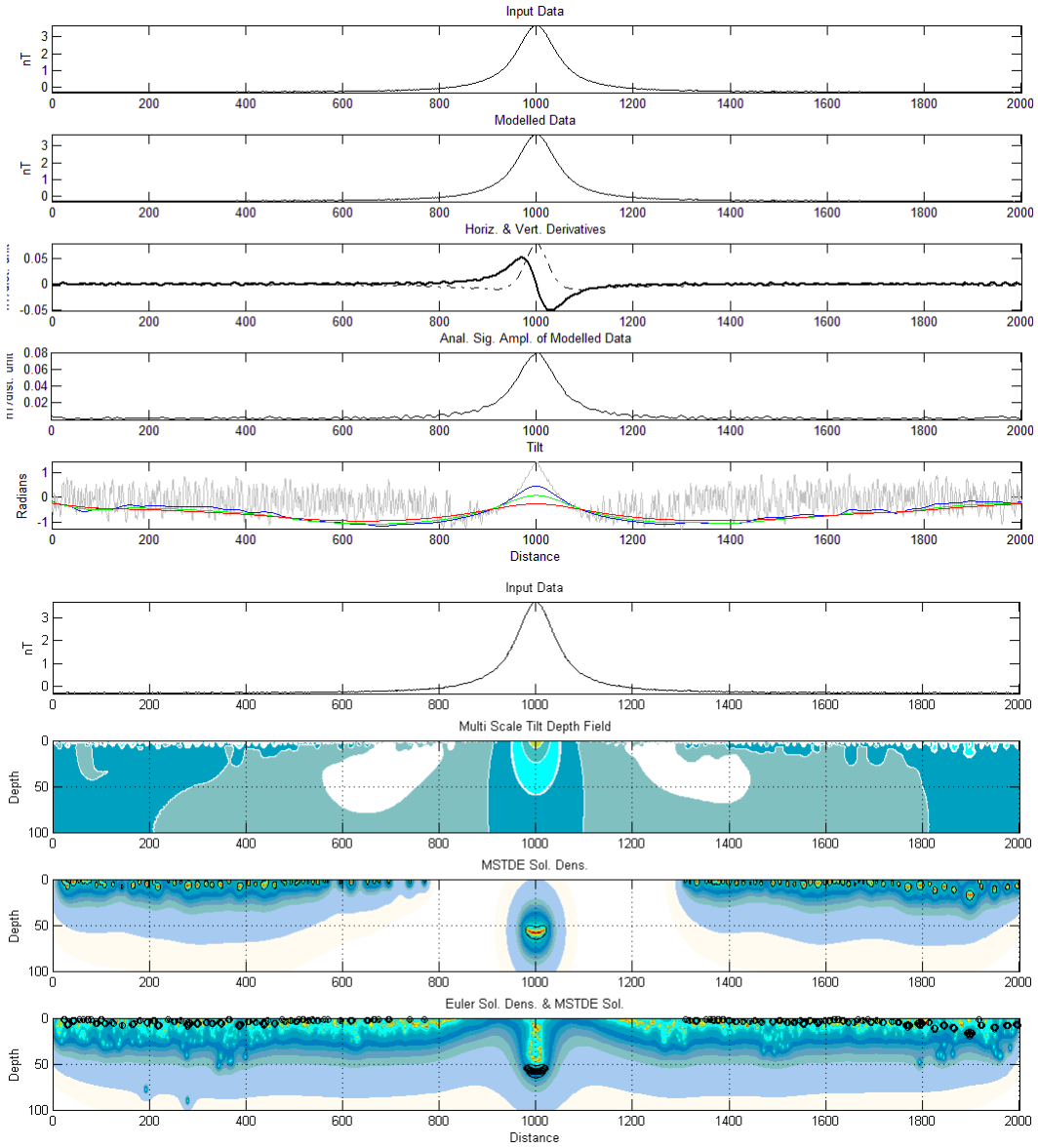


**Figure 77. Synthetic model data (Noise range of 10% of the standard deviation, Depth of 50 dist. units) with plots of the spatial derivatives, analytic signal amplitude and various continued tilt products (Top), Synthetic model data with MSTD distribution, MSTDE solution density and Euler solution density with MSTDE solution locations (Bottom). Frequency domain smoothing has been applied to the data.**

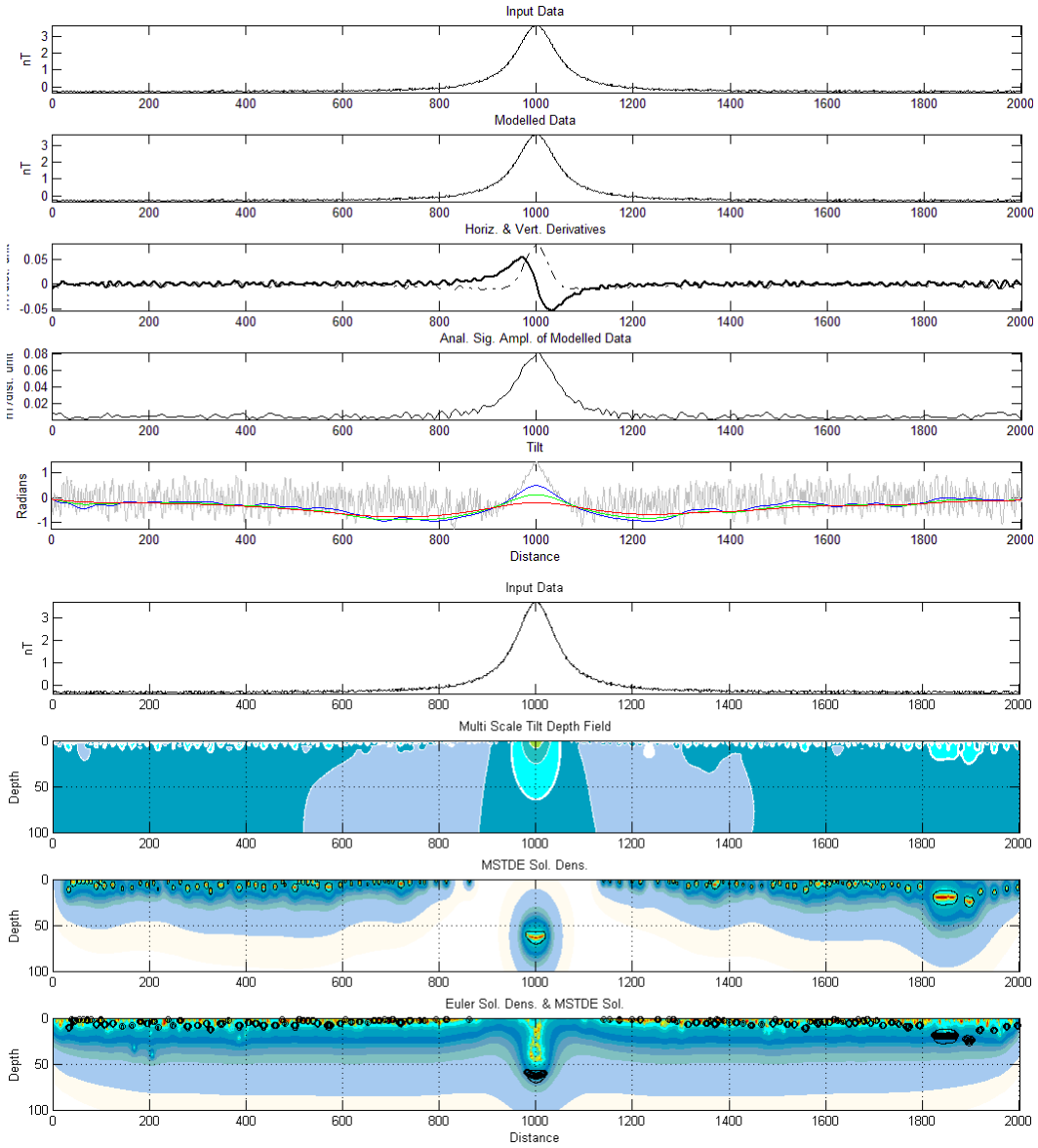


**Figure 78. Synthetic model data (Noise range of 25% of the standard deviation, Depth of 50 dist. units) with plots of the spatial derivatives, analytic signal amplitude and various continued tilt products (Top), Synthetic model data with MSTD distribution, MSTDE solution density and Euler solution density with MSTDE solution locations (Bottom). Frequency domain smoothing has been applied to the data.**

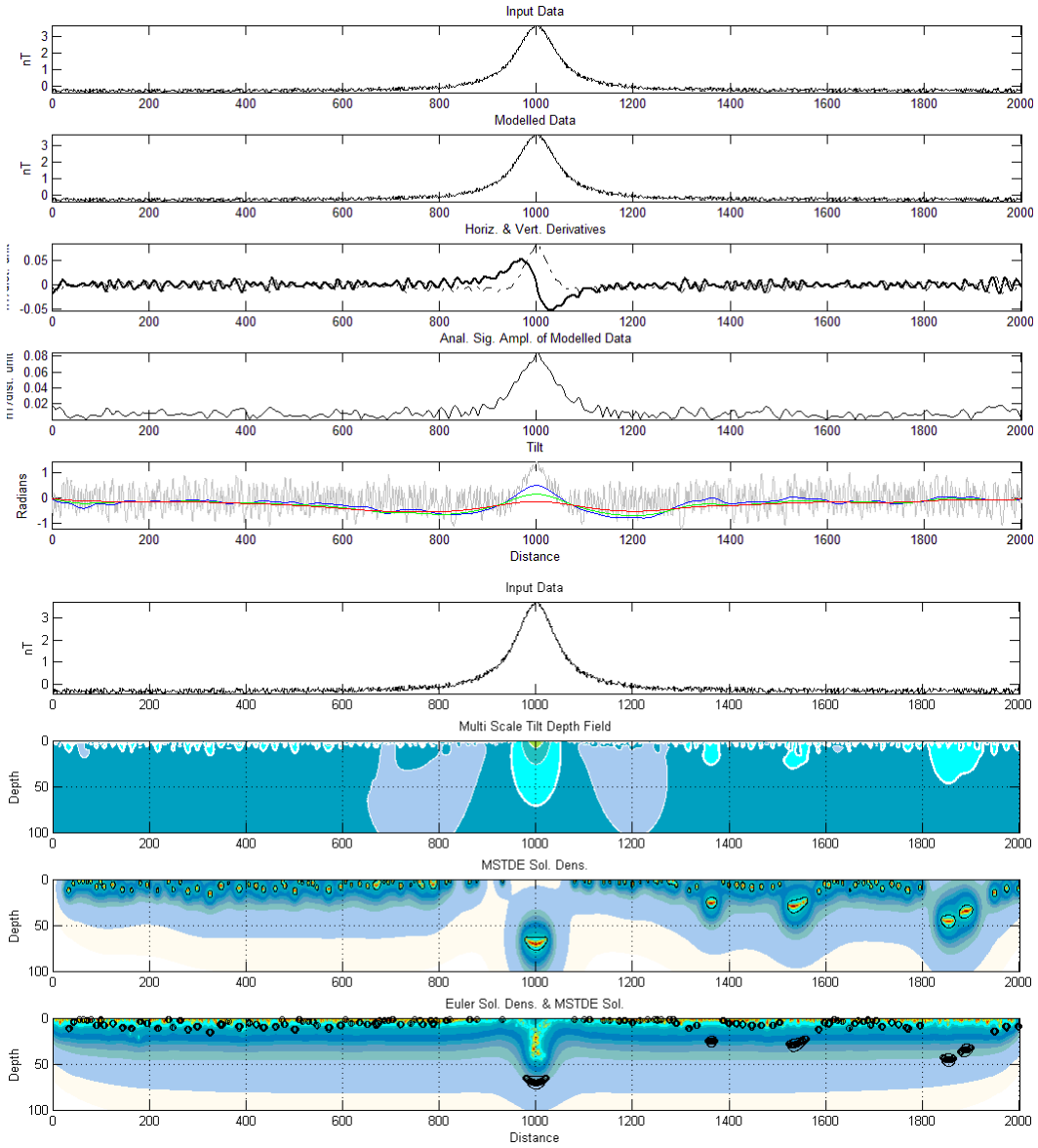


**Figure 79. Synthetic model data (Noise range of 50% of the standard deviation, Depth of 50 dist. units) with plots of the spatial derivatives, analytic signal amplitude and various continued tilt products (Top), Synthetic model data with MSTD distribution, MSTDE solution density and Euler solution density with MSTDE solution locations (Bottom). Frequency domain smoothing has been applied to the data.**

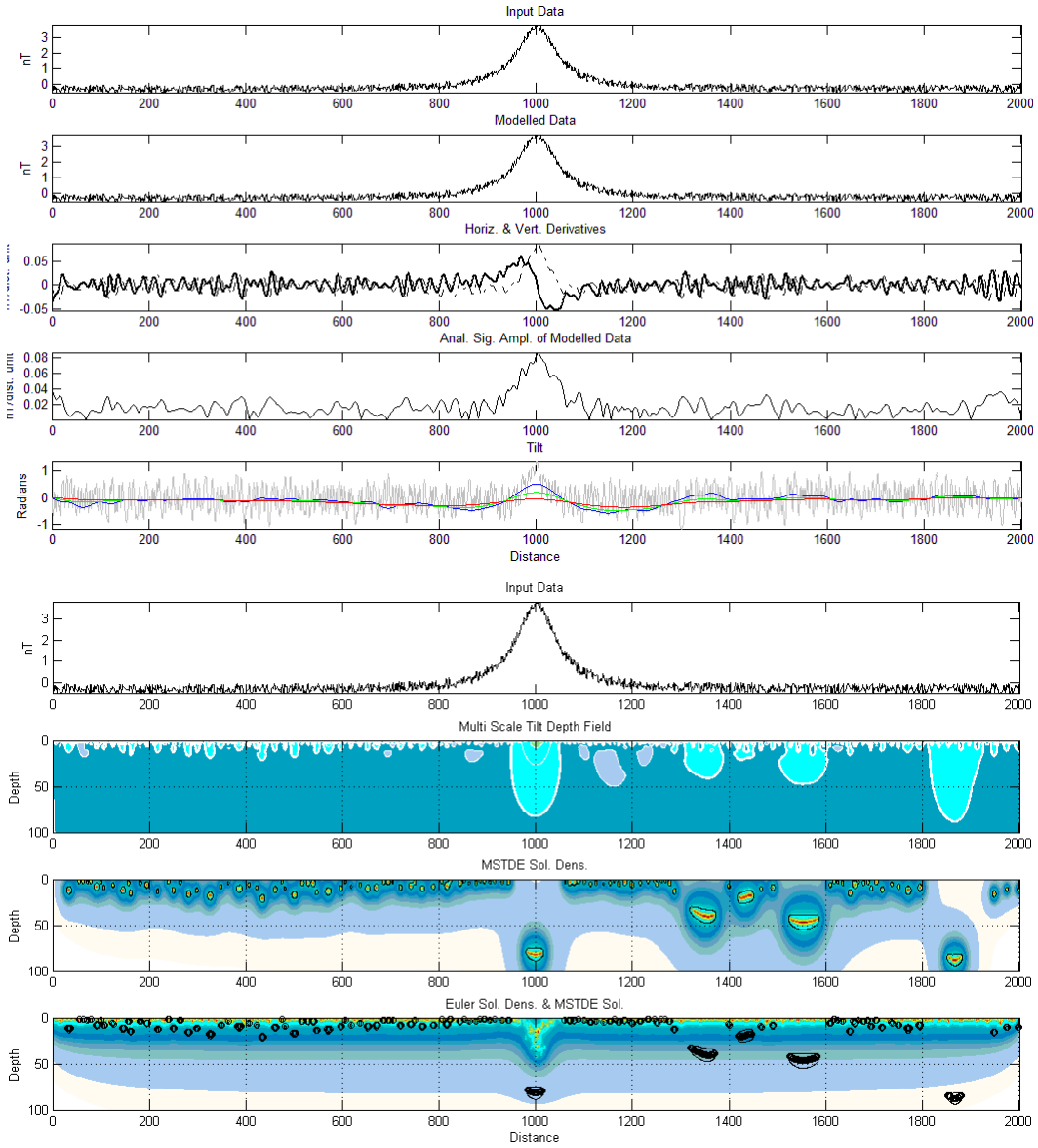


**Figure 80. Synthetic model data (Noise range of 100% of the standard deviation, Depth of 50 dist. units) with plots of the spatial derivatives, analytic signal amplitude and various continued tilt products (Top), Synthetic model data with MSTD distribution, MSTDE solution density and Euler solution density with MSTDE solution locations (Bottom). Frequency domain smoothing has been applied to the data.**

## Vertical sheet with various noise amplitudes – Frequency domain and 100 iterations of spatial domain smoothing

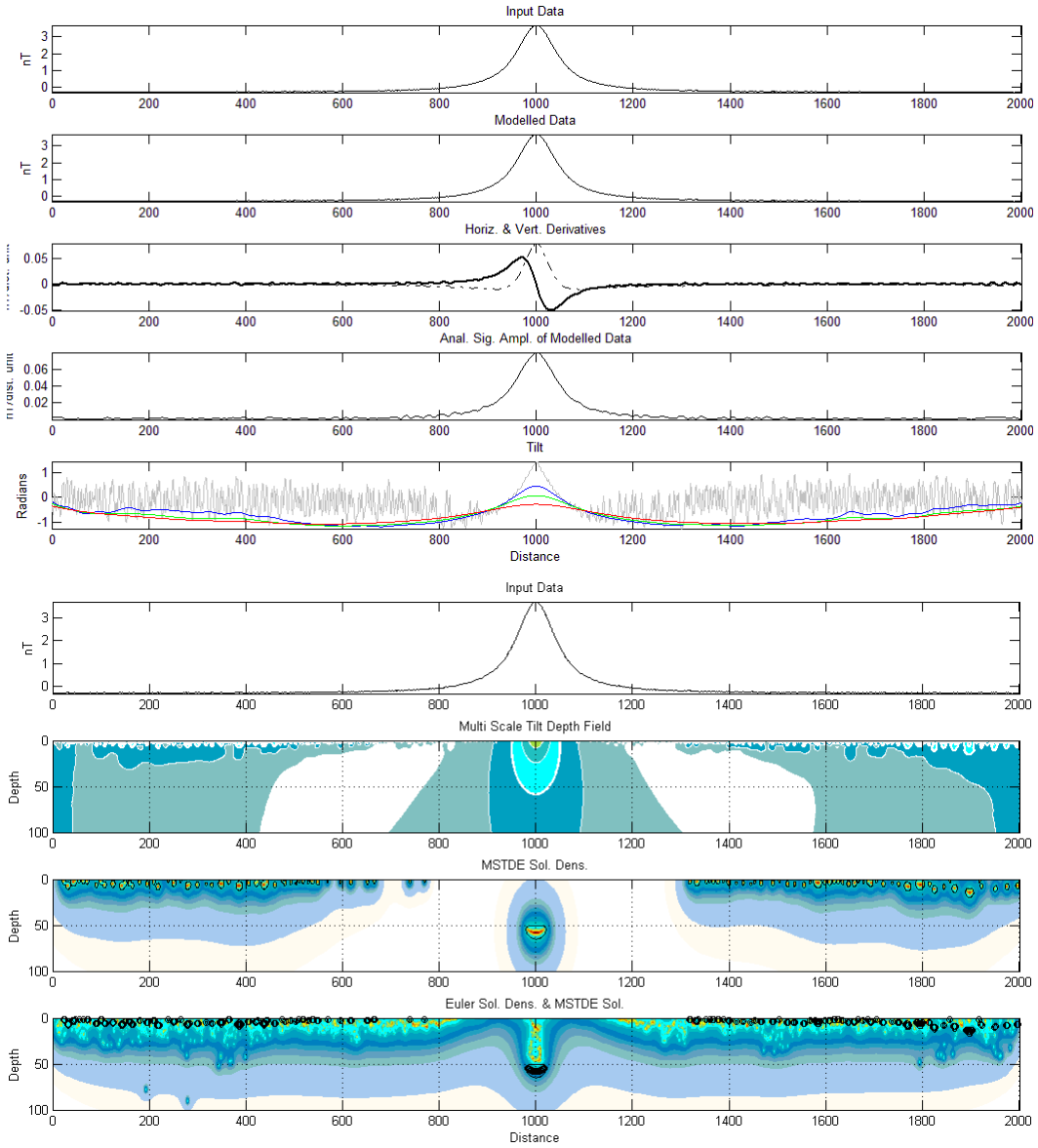


**Figure 81. Synthetic model data (Noise range of 10% of the standard deviation, Depth of 50 dist. units) with plots of the spatial derivatives, analytic signal amplitude and various continued tilt products (Top), Synthetic model data with MSTD distribution, MSTDE solution density and Euler solution density with MSTDE solution locations (Bottom). Frequency domain and up to 100 iterations of spatial domain smoothing have been applied to the data.**

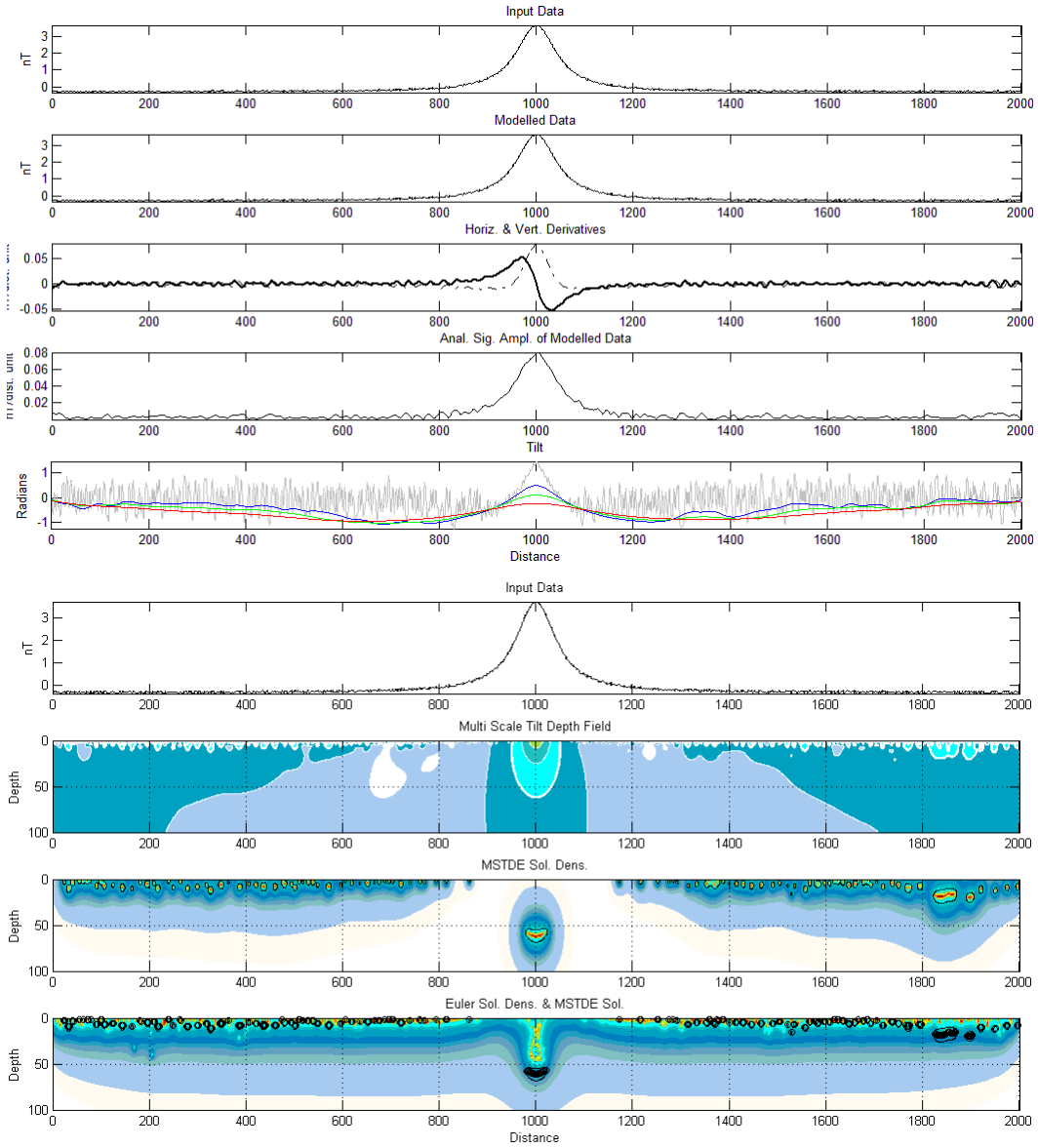


**Figure 82. Synthetic model data (Noise range of 25% of the standard deviation, Depth of 50 dist. units) with plots of the spatial derivatives, analytic signal amplitude and various continued tilt products (Top), Synthetic model data with MSTD distribution, MSTDE solution density and Euler solution density with MSTDE solution locations (Bottom). Frequency domain and up to 100 iterations of spatial domain smoothing have been applied to the data.**

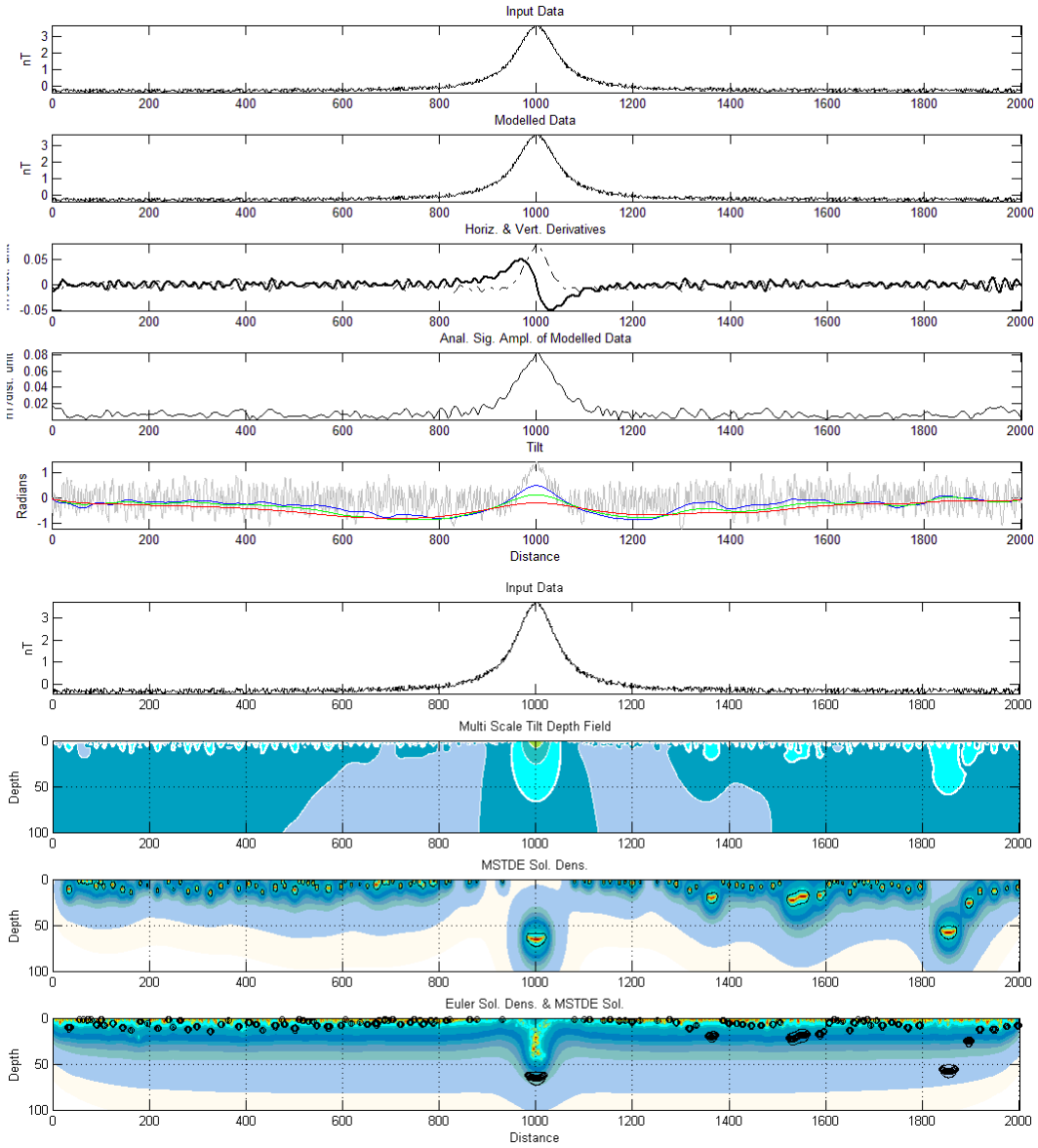


**Figure 83. Synthetic model data (Noise range of 50% of the standard deviation, Depth of 50 dist. units) with plots of the spatial derivatives, analytic signal amplitude and various continued tilt products (Top), Synthetic model data with MSTD distribution, MSTDE solution density and Euler solution density with MSTDE solution locations (Bottom). Frequency domain and up to 100 iterations of spatial domain smoothing have been applied to the data.**

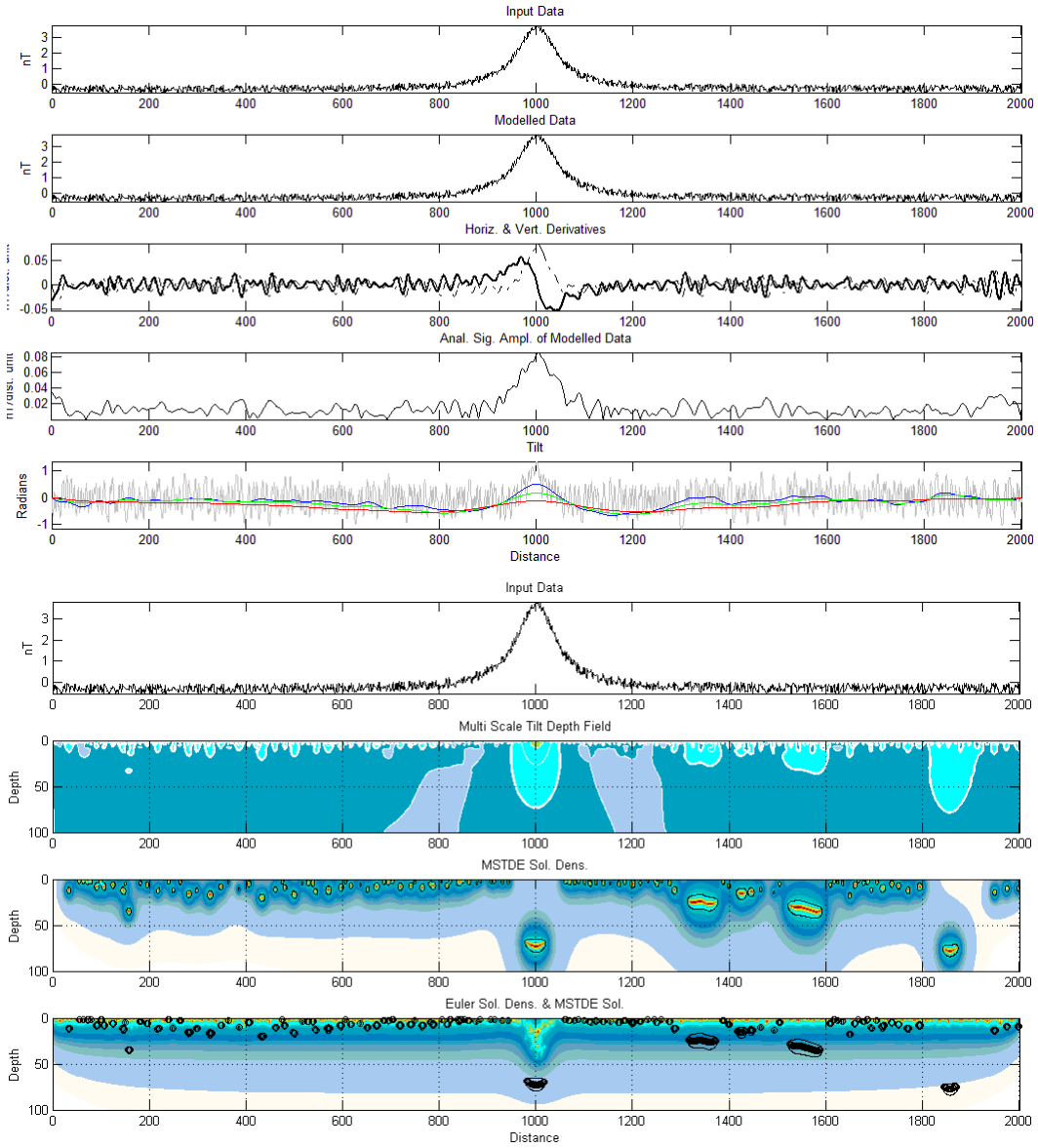


**Figure 84. Synthetic model data (Noise range of 100% of the standard deviation, Depth of 50 dist. units) with plots of the spatial derivatives, analytic signal amplitude and various continued tilt products (Top), Synthetic model data with MSTD distribution, MSTDE solution density and Euler solution density with MSTDE solution locations (Bottom). Frequency domain and up to 100 iterations of spatial domain smoothing have been applied to the data.**

## Multiple vertical sheets with various separations

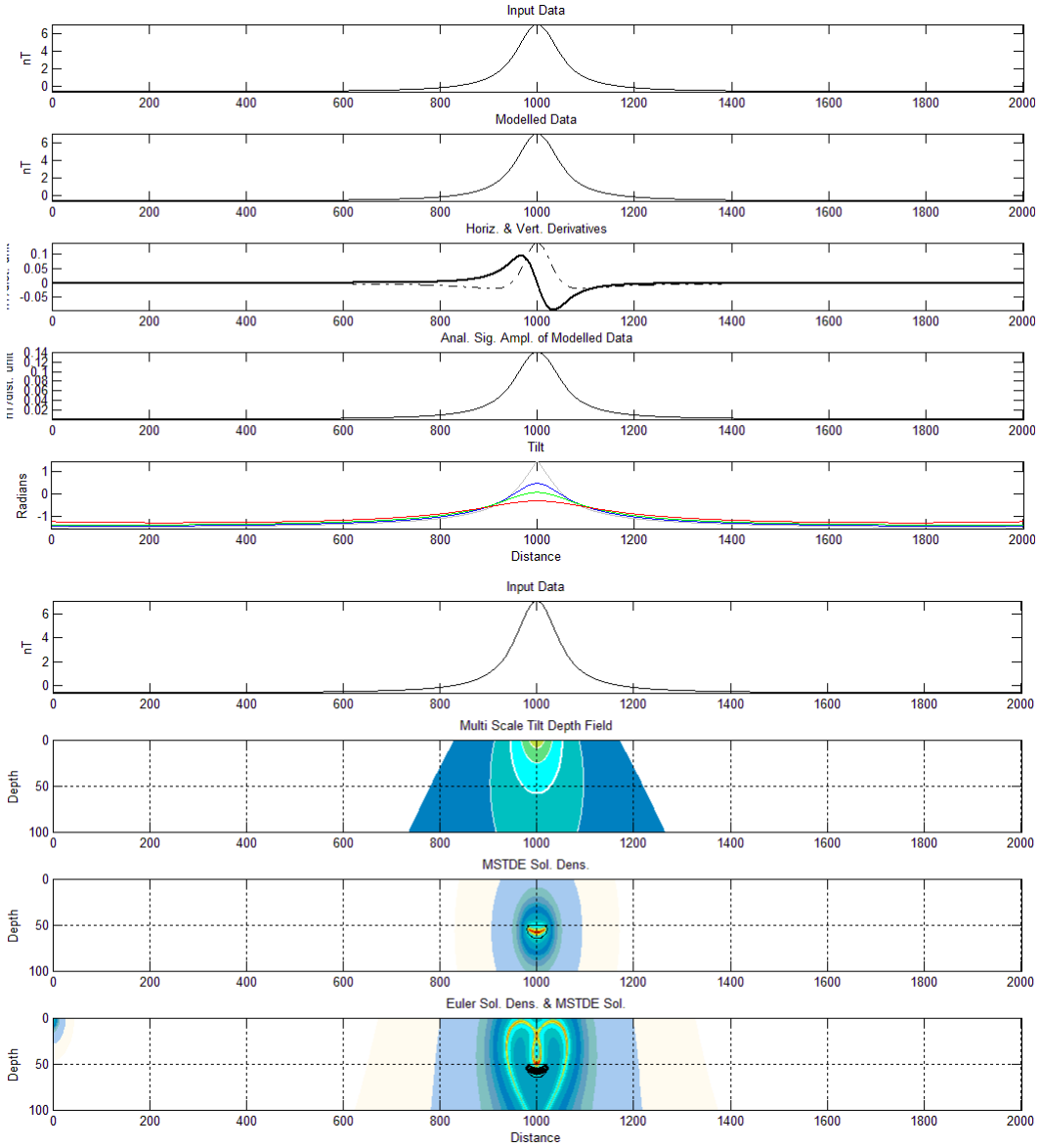


**Figure 85. Synthetic model data (Separation of 20 dist. units, Depth of 50 dist. units) of two vertical sheets, the centres separated by 100 distance units. Plots of the spatial derivatives, analytic signal amplitude and various continued tilt products (Top), Synthetic model data with MSTD distribution, MSTDE solution density and Euler solution density with MSTDE solution locations (Bottom).**

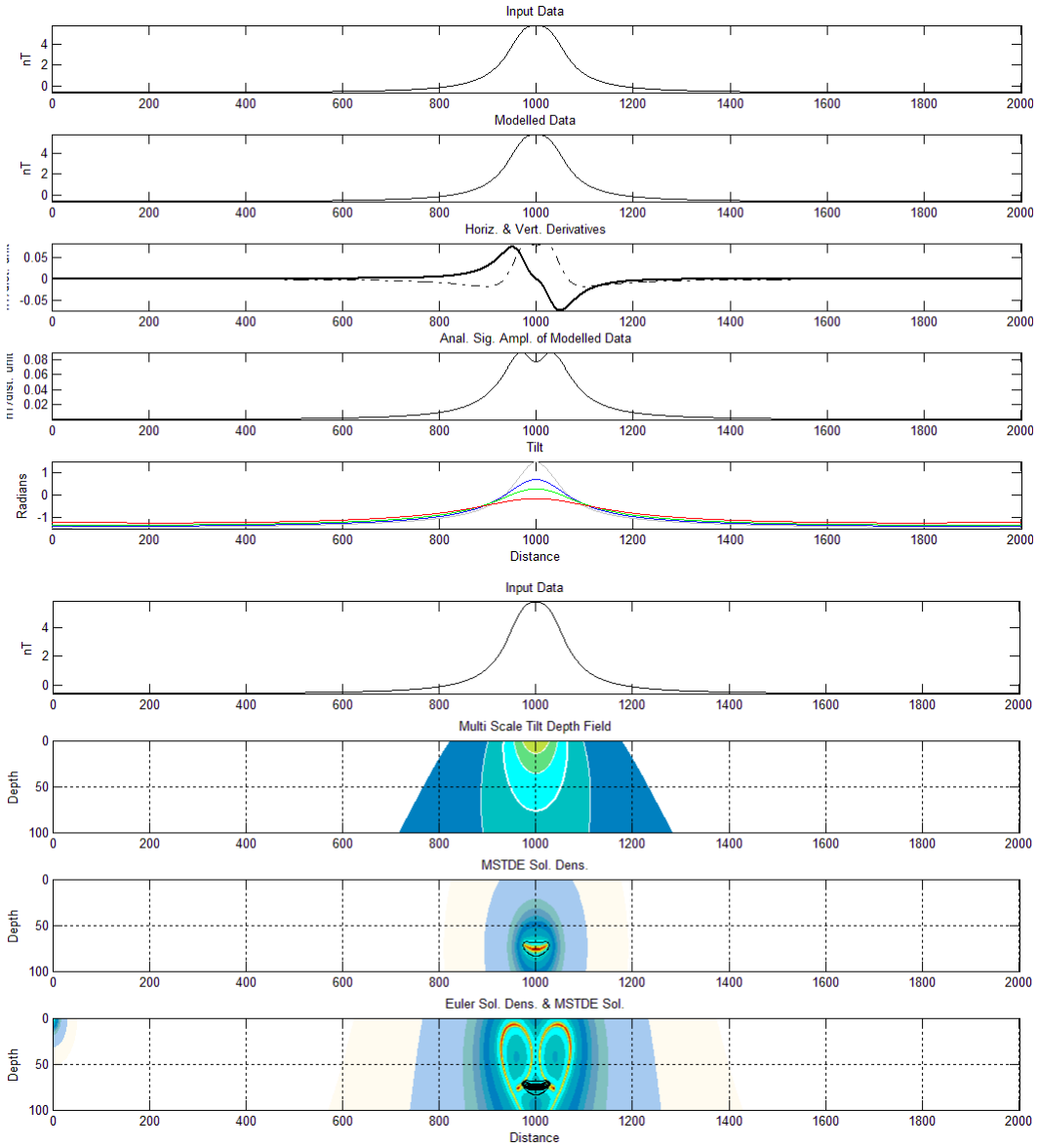


**Figure 86. Synthetic model data (Separation of 50 dist. units, Depth of 50 dist. units) of two vertical sheets, the centres separated by 100 distance units. Plots of the spatial derivatives, analytic signal amplitude and various continued tilt products (Top), Synthetic model data with MSTD distribution, MSTDE solution density and Euler solution density with MSTDE solution locations (Bottom).**

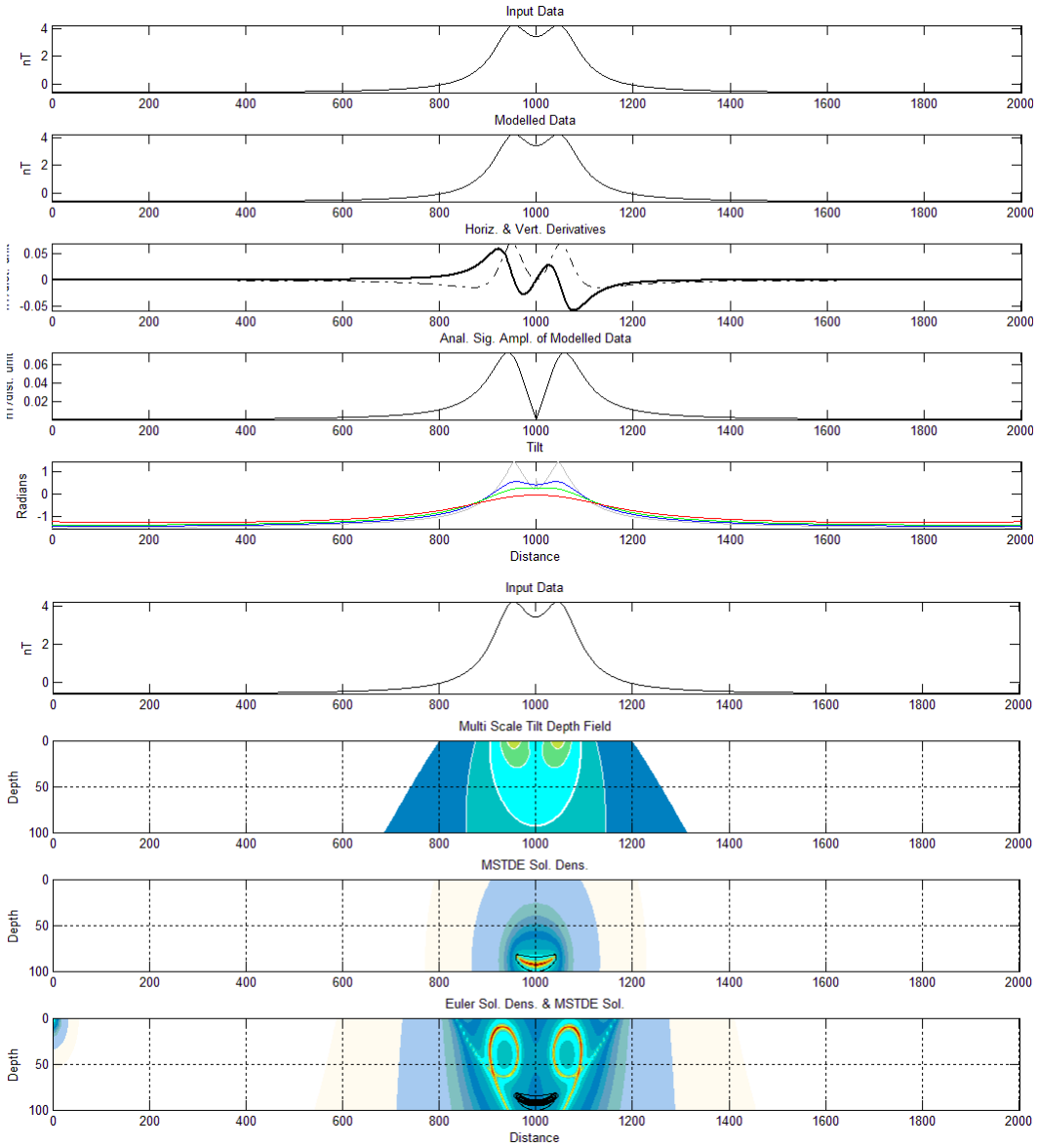


**Figure 87. Synthetic model data (Separation of 100 dist. units, Depth of 50 dist. units) of two vertical sheets, the centres separated by 100 distance units. Plots of the spatial derivatives, analytic signal amplitude and various continued tilt products (Top), Synthetic model data with MSTD distribution, MSTDE solution density and Euler solution density with MSTDE solution locations (Bottom).**

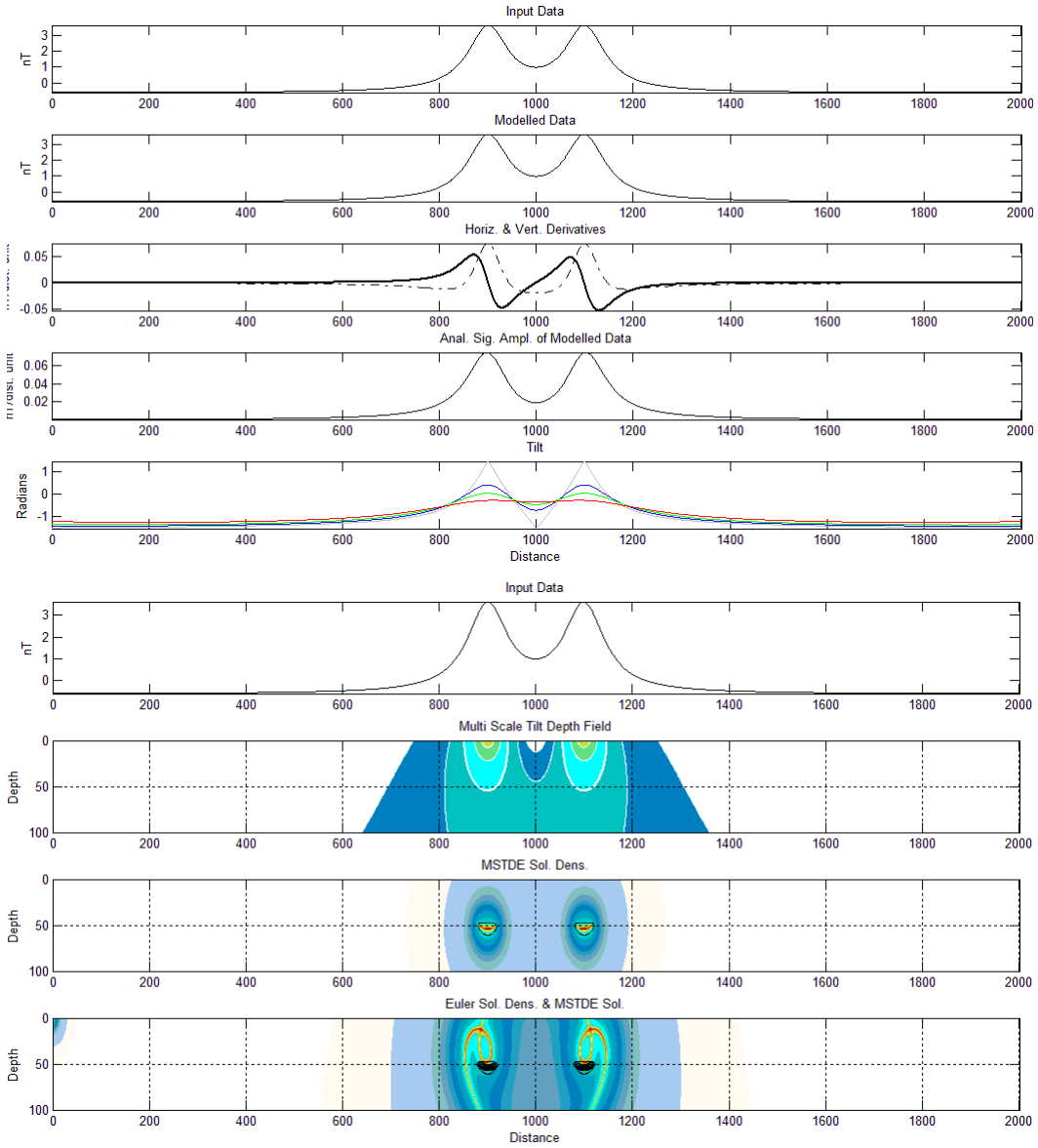


**Figure 88. Synthetic model data (Separation of 200 dist. units, Depth of 50 dist. units) of two vertical sheets, the centres separated by 100 distance units. Plots of the spatial derivatives, analytic signal amplitude and various continued tilt products (Top), Synthetic model data with MSTD distribution, MSTDE solution density and Euler solution density with MSTDE solution locations (Bottom).**

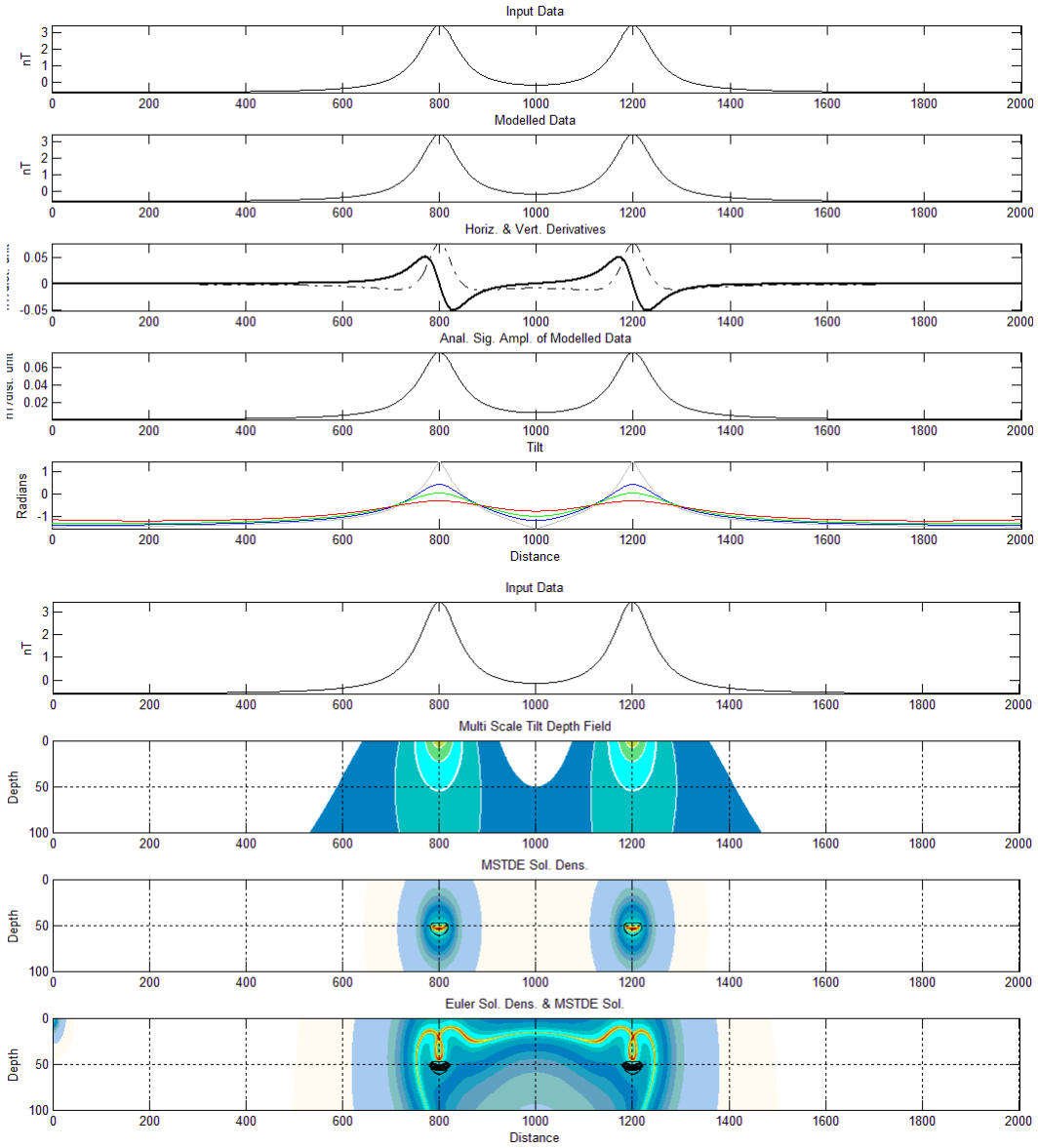


**Figure 89. Synthetic model data (Separation of 400 dist. units, Depth of 50 dist. units) of two vertical sheets, the centres separated by 100 distance units. Plots of the spatial derivatives, analytic signal amplitude and various continued tilt products (Top), Synthetic model data with MSTD distribution, MSTDE solution density and Euler solution density with MSTDE solution locations (Bottom).**

# APPENDIX C

Appendix C contains a list of figures (Figure 90 - Figure 124) depicting the various data used to test the Multi-Scale Tilt Depth Estimation method and the results thereof. All figures shown within Appendix C make use of the analytic signal amplitude of the vertical derivative of the total magnetic intensity as the input component to the algorithm.

## Vertical sheet at various depths

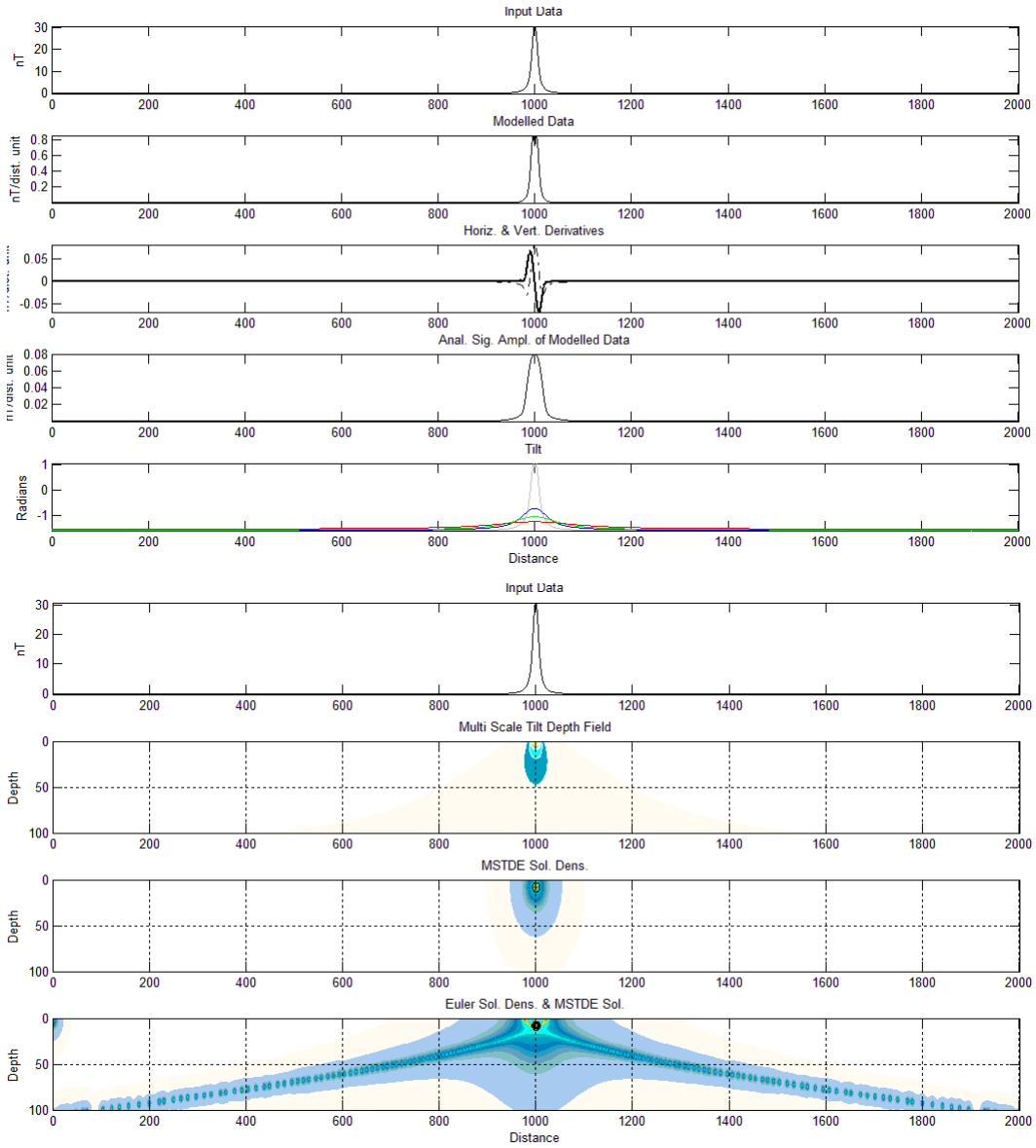


**Figure 90. Synthetic model data (Depth of 5 dist. units) with plots of the spatial derivatives, analytic signal amplitude and various continued tilt products (Top), Synthetic model data with MSTD distribution, MSTDE solution density and Euler solution density with MSTDE solution locations (Bottom).**

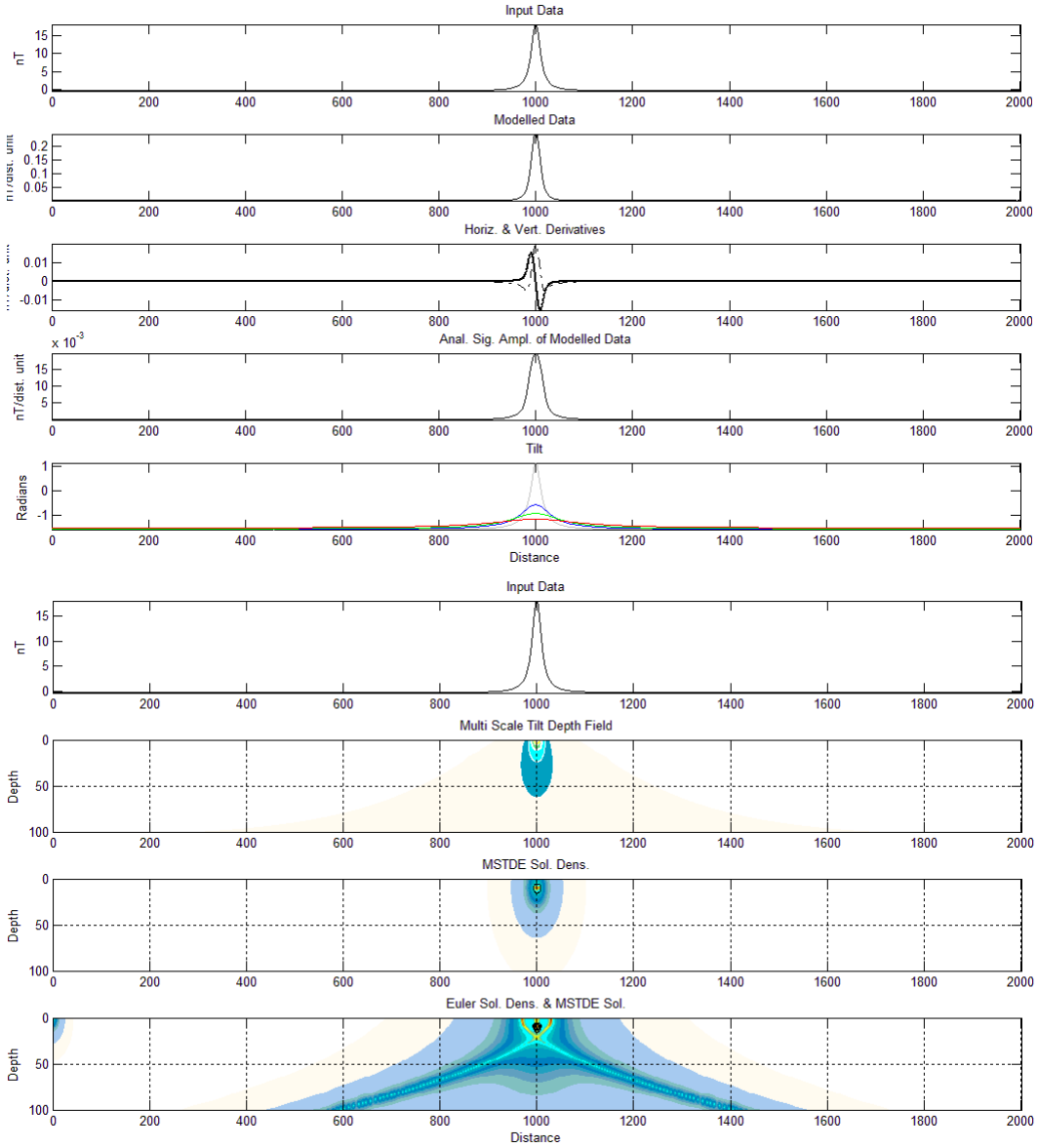


**Figure 91. Synthetic model data (Depth of 10 dist. units) with plots of the spatial derivatives, analytic signal amplitude and various continued tilt products (Top), Synthetic model data with MSTD distribution, MSTDE solution density and Euler solution density with MSTDE solution locations (Bottom).**

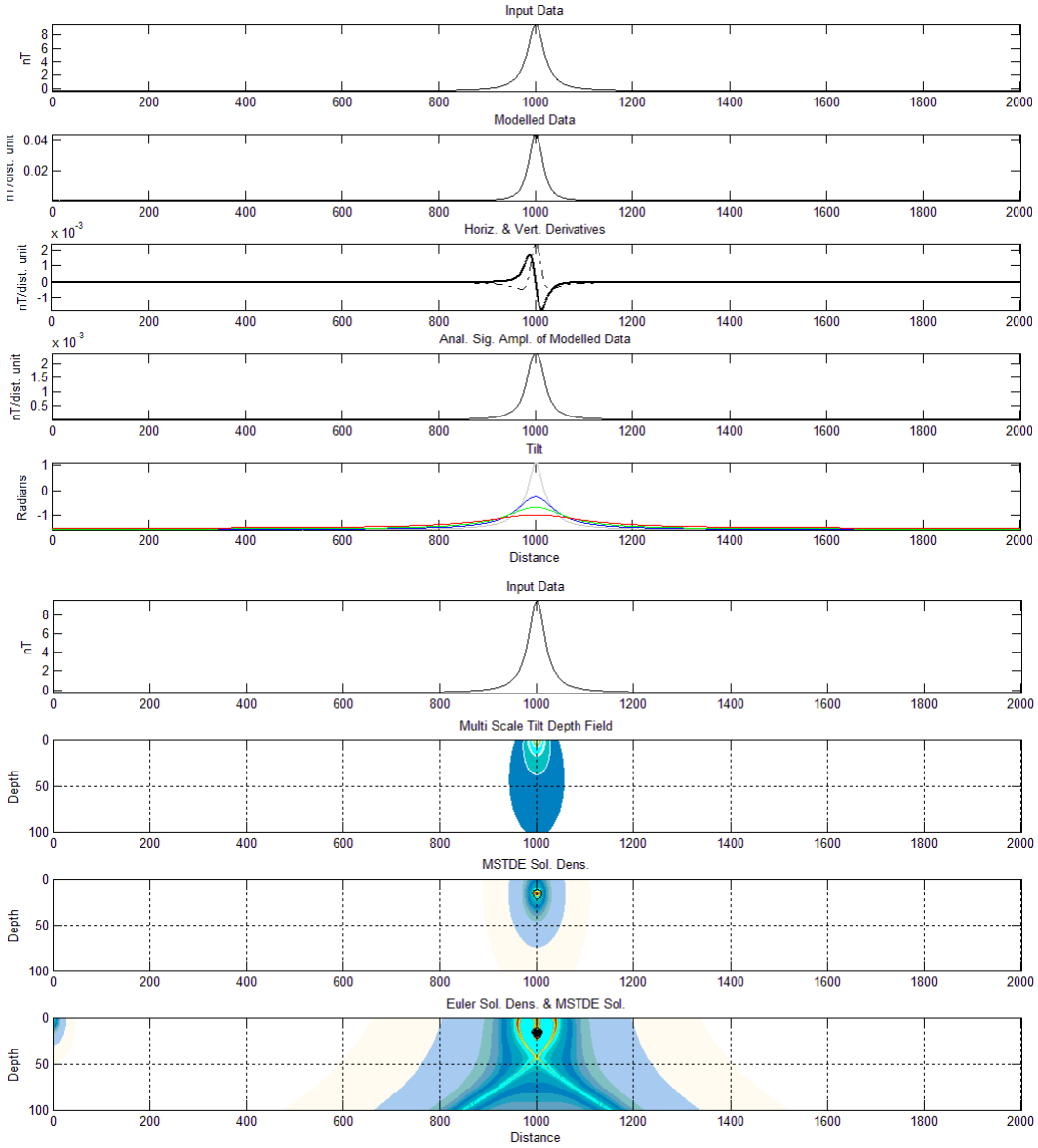


**Figure 92. Synthetic model data (Depth of 20 dist. units) with plots of the spatial derivatives, analytic signal amplitude and various continued tilt products (Top), Synthetic model data with MSTD distribution, MSTDE solution density and Euler solution density with MSTDE solution locations (Bottom).**

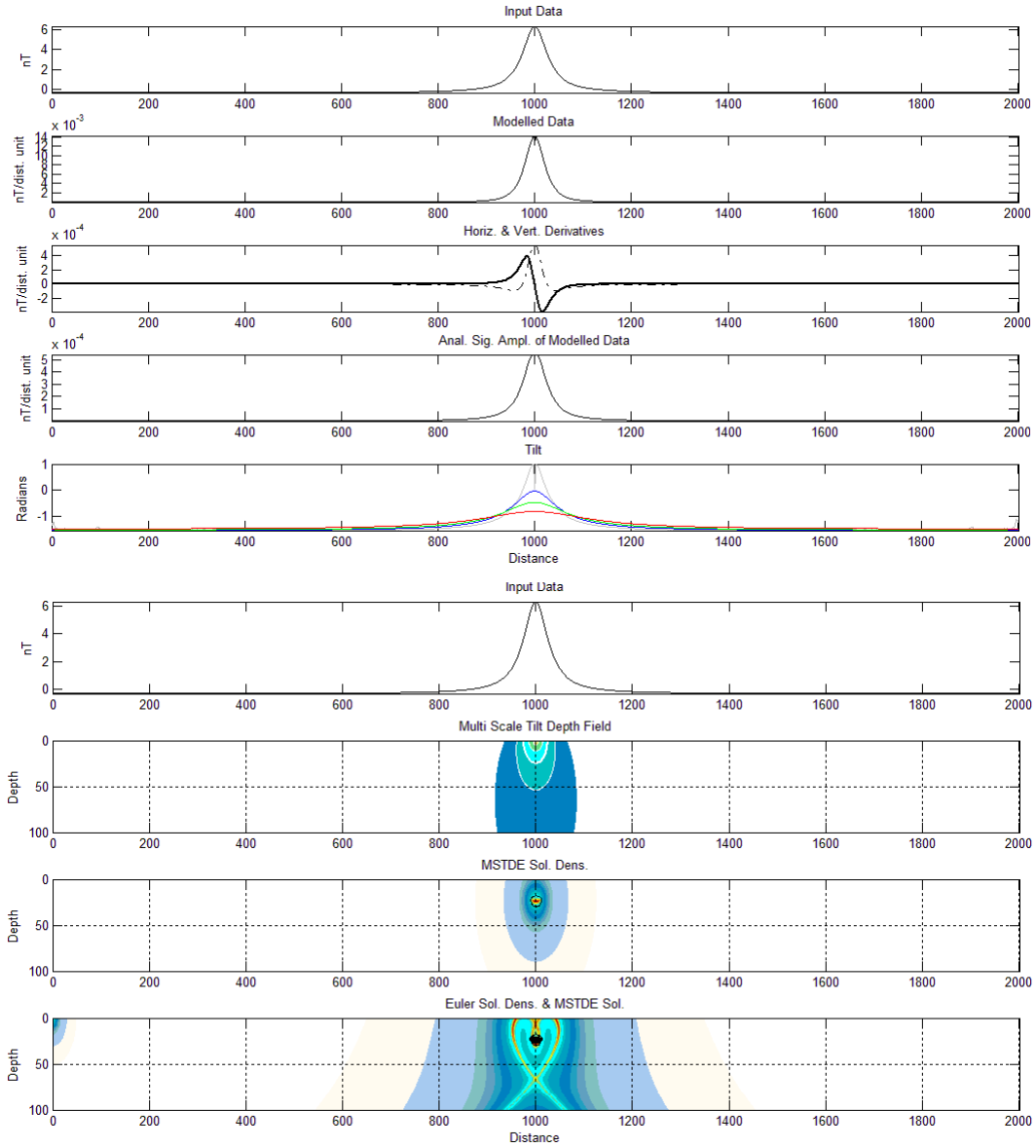


**Figure 93. Synthetic model data (Depth of 30 dist. units) with plots of the spatial derivatives, analytic signal amplitude and various continued tilt products (Top), Synthetic model data with MSTD distribution, MSTDE solution density and Euler solution density with MSTDE solution locations (Bottom).**

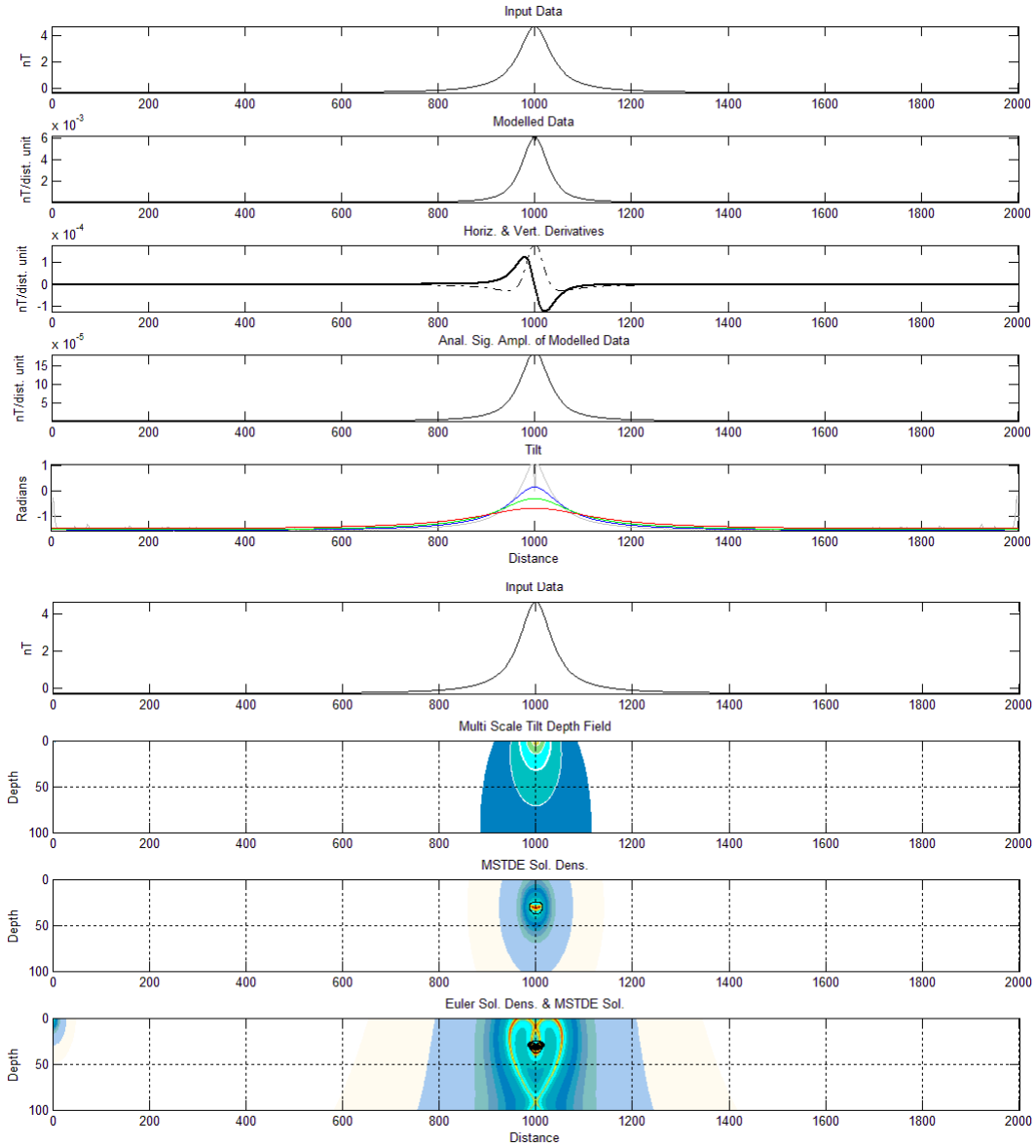


**Figure 94. Synthetic model data (Depth of 40 dist. units) with plots of the spatial derivatives, analytic signal amplitude and various continued tilt products (Top), Synthetic model data with MSTD distribution, MSTDE solution density and Euler solution density with MSTDE solution locations (Bottom).**

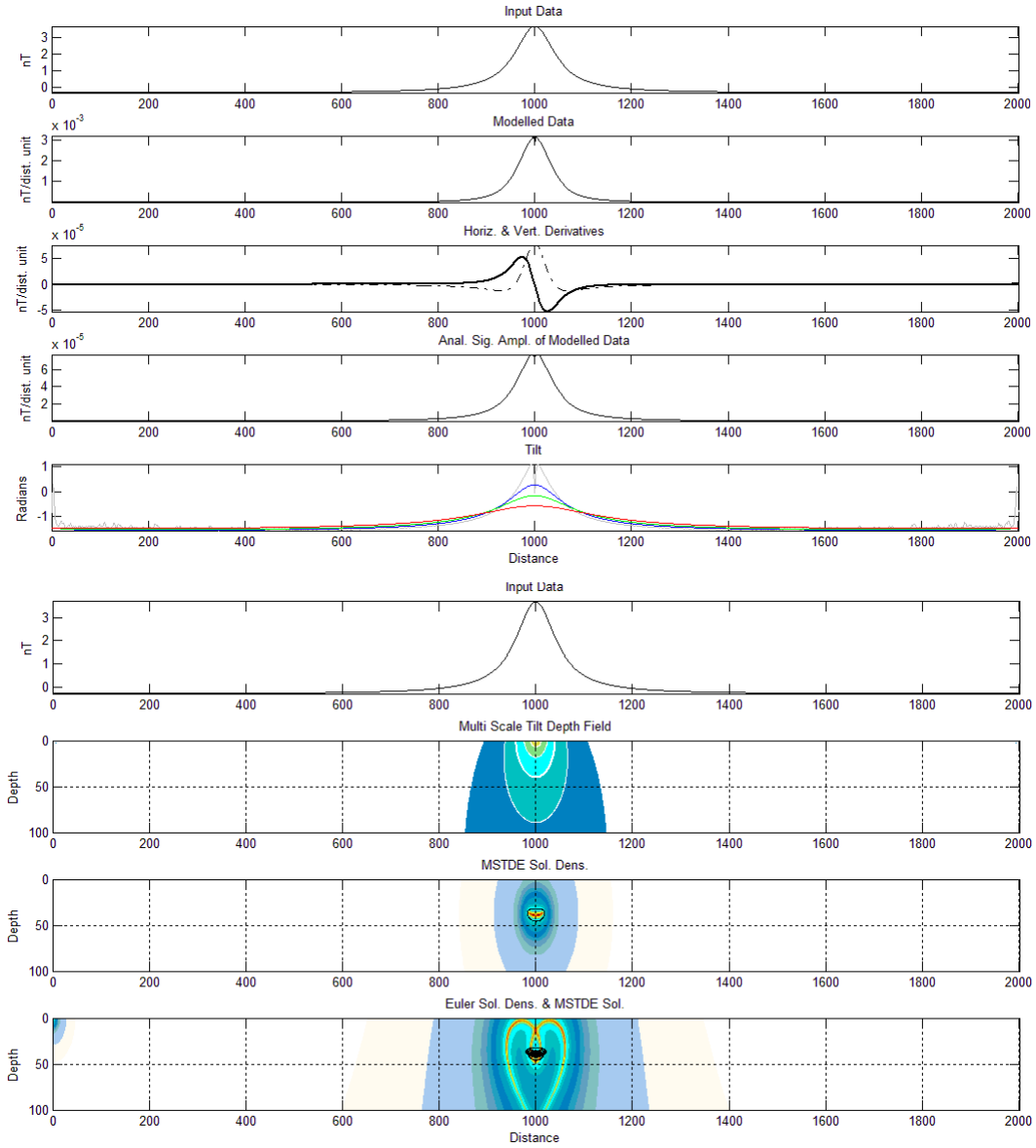


**Figure 95. Synthetic model data (Depth of 50 dist. units) with plots of the spatial derivatives, analytic signal amplitude and various continued tilt products (Top), Synthetic model data with MSTD distribution, MSTDE solution density and Euler solution density with MSTDE solution locations (Bottom).**

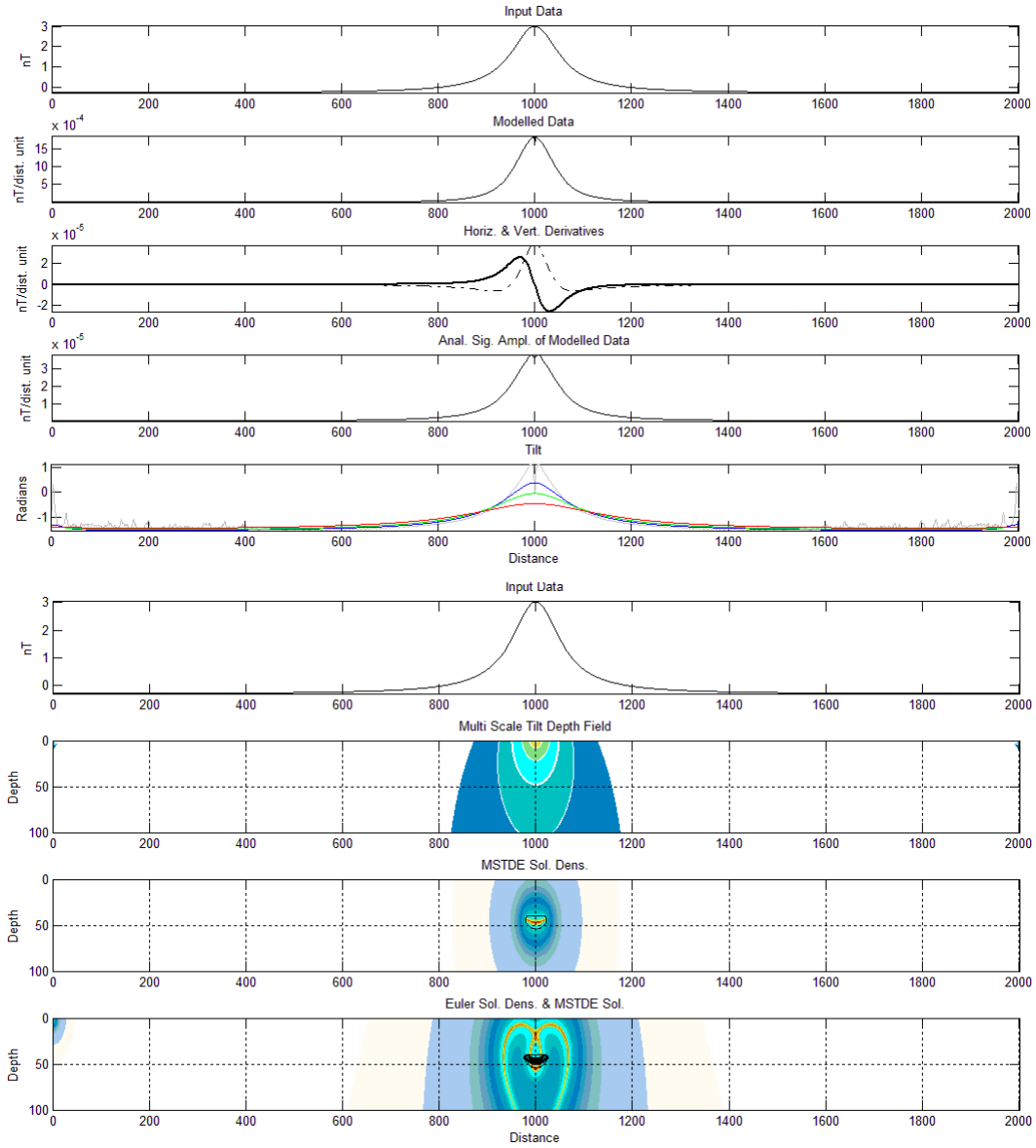


**Figure 96. Synthetic model data (Depth of 60 dist. units) with plots of the spatial derivatives, analytic signal amplitude and various continued tilt products (Top), Synthetic model data with MSTD distribution, MSTDE solution density and Euler solution density with MSTDE solution locations (Bottom).**

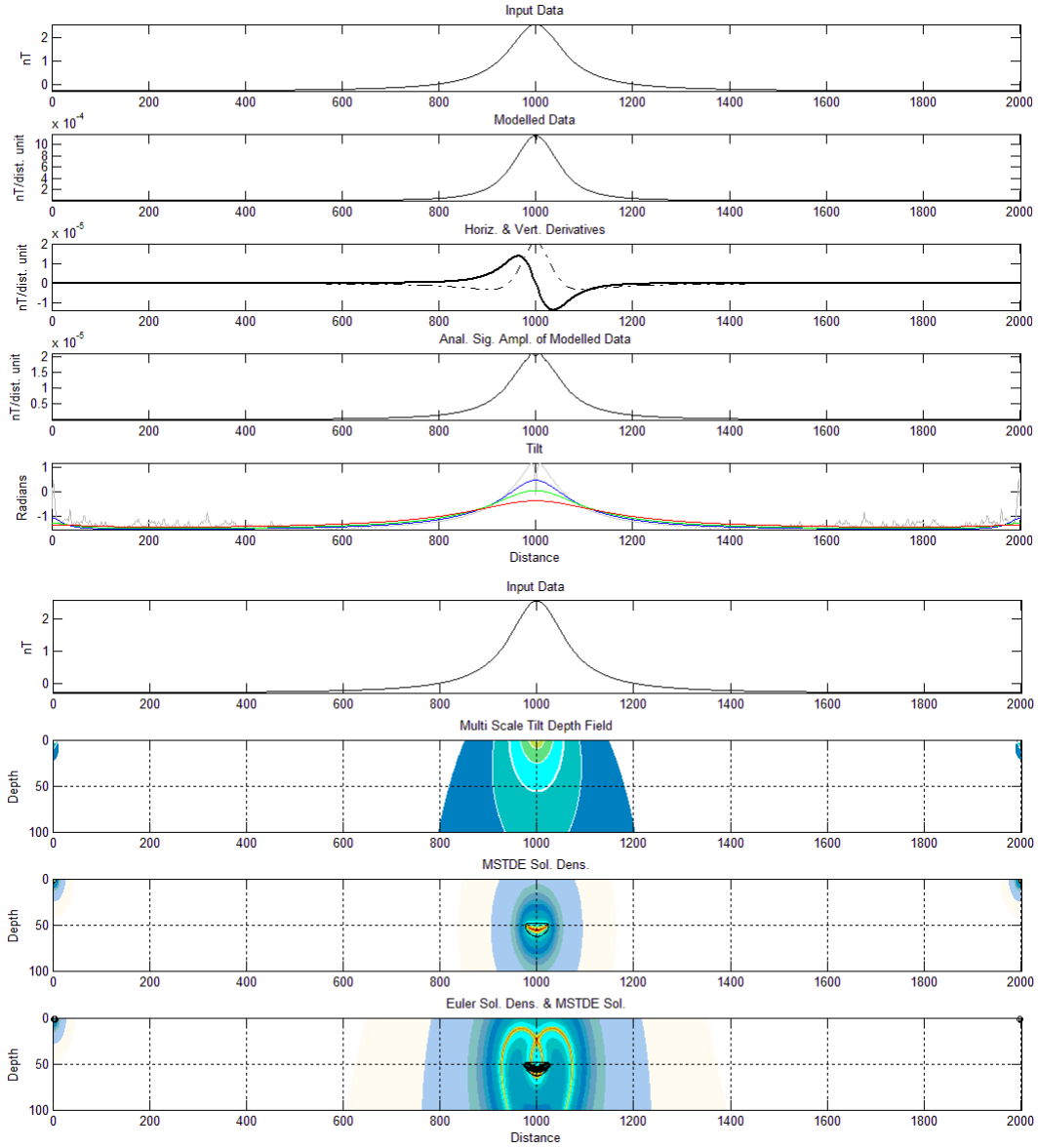


**Figure 97. Synthetic model data (Depth of 70 dist. units) with plots of the spatial derivatives, analytic signal amplitude and various continued tilt products (Top), Synthetic model data with MSTD distribution, MSTDE solution density and Euler solution density with MSTDE solution locations (Bottom).**

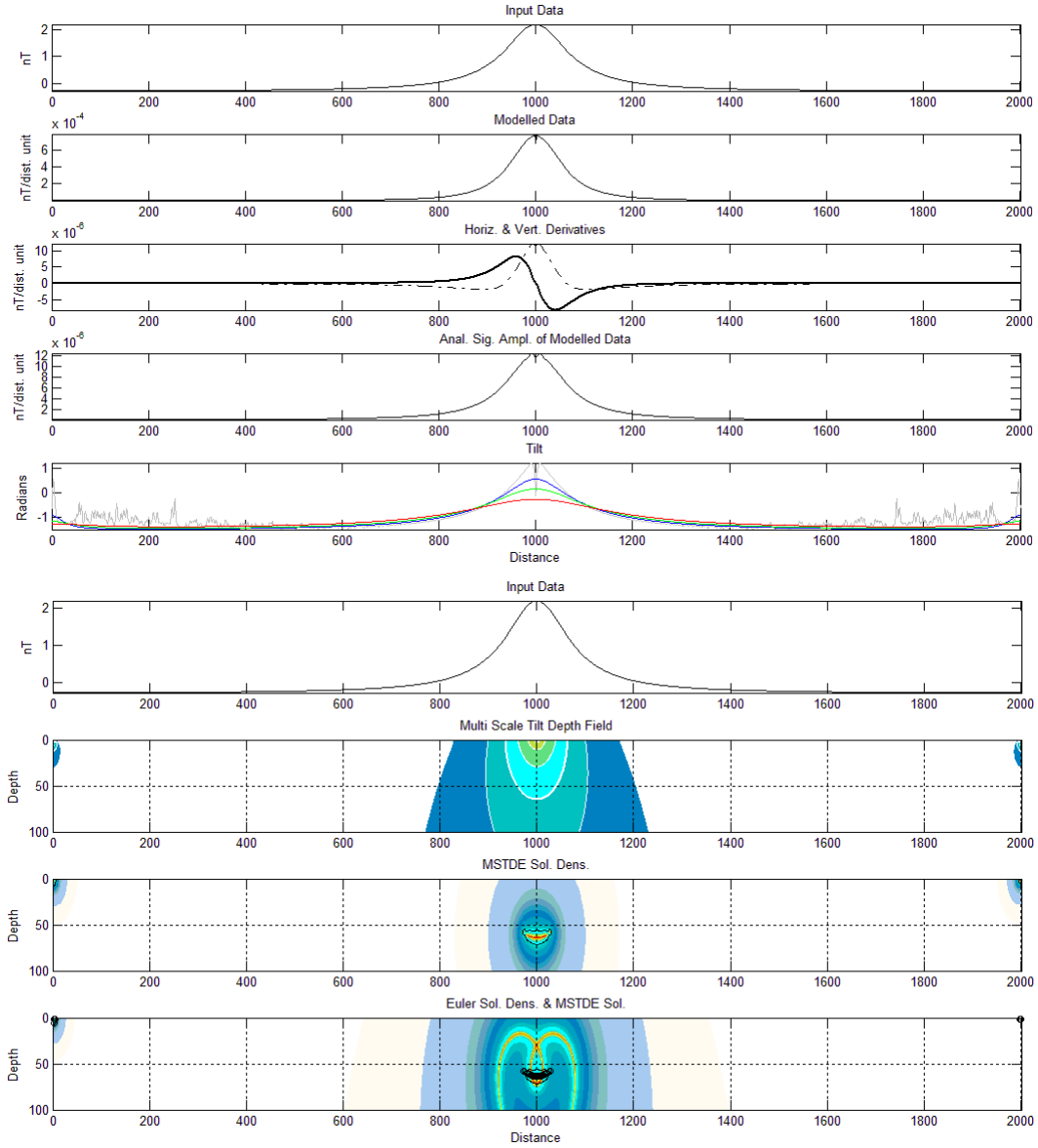


**Figure 98. Synthetic model data (Depth of 80 dist. units) with plots of the spatial derivatives, analytic signal amplitude and various continued tilt products (Top), Synthetic model data with MSTD distribution, MSTDE solution density and Euler solution density with MSTDE solution locations (Bottom).**

## Sheet with various dips

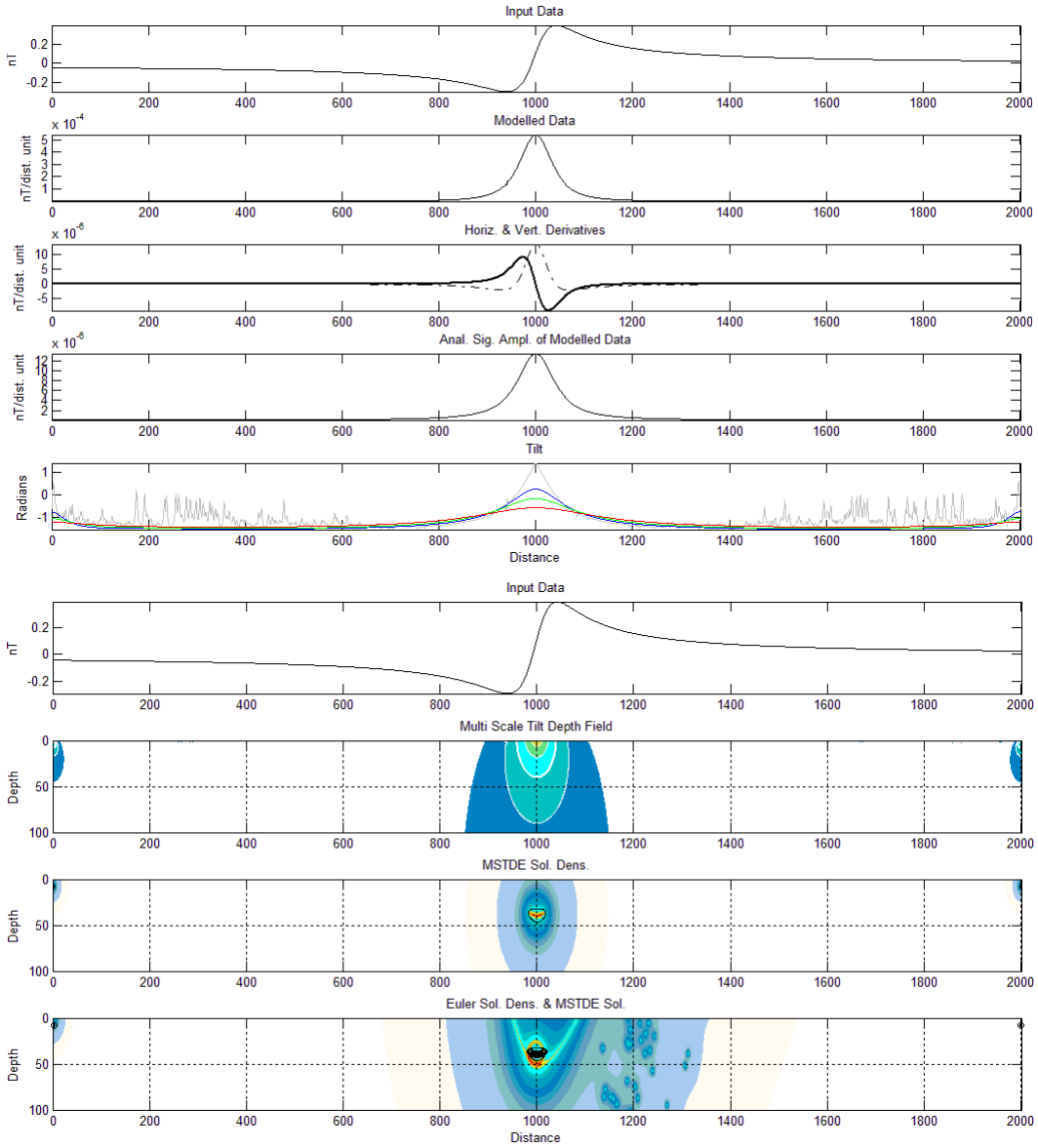


**Figure 99. Synthetic model data (Dip of 10°, Depth of 50 dist. units) with plots of the spatial derivatives, analytic signal amplitude and various continued tilt products (Top), Synthetic model data with MSTD distribution, MSTDE solution density and Euler solution density with MSTDE solution locations (Bottom).**

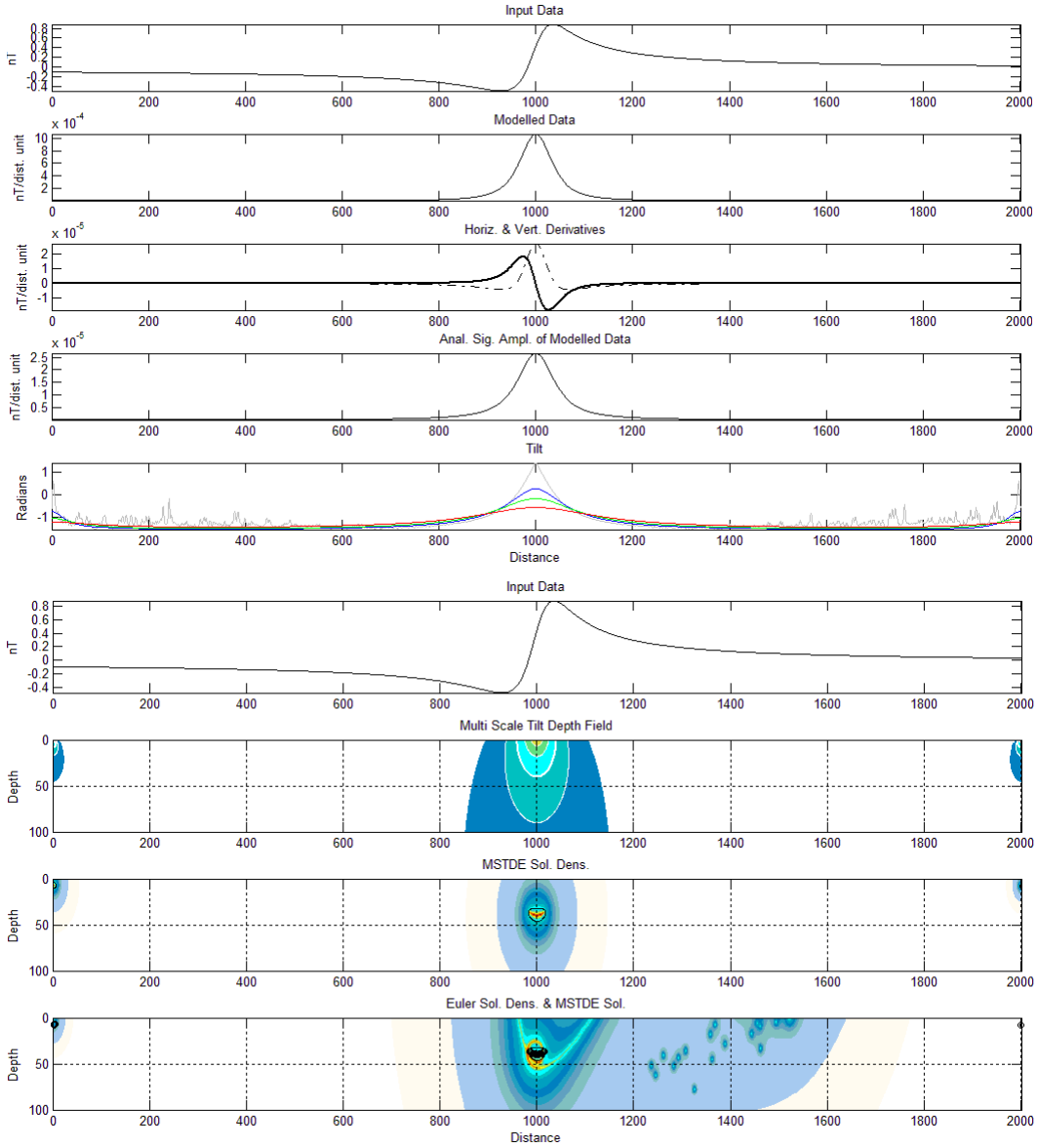


**Figure 100. Synthetic model data (Dip of 20°, Depth of 50 dist. units) with plots of the spatial derivatives, analytic signal amplitude and various continued tilt products (Top), Synthetic model data with MSTD distribution, MSTDE solution density and Euler solution density with MSTDE solution locations (Bottom).**

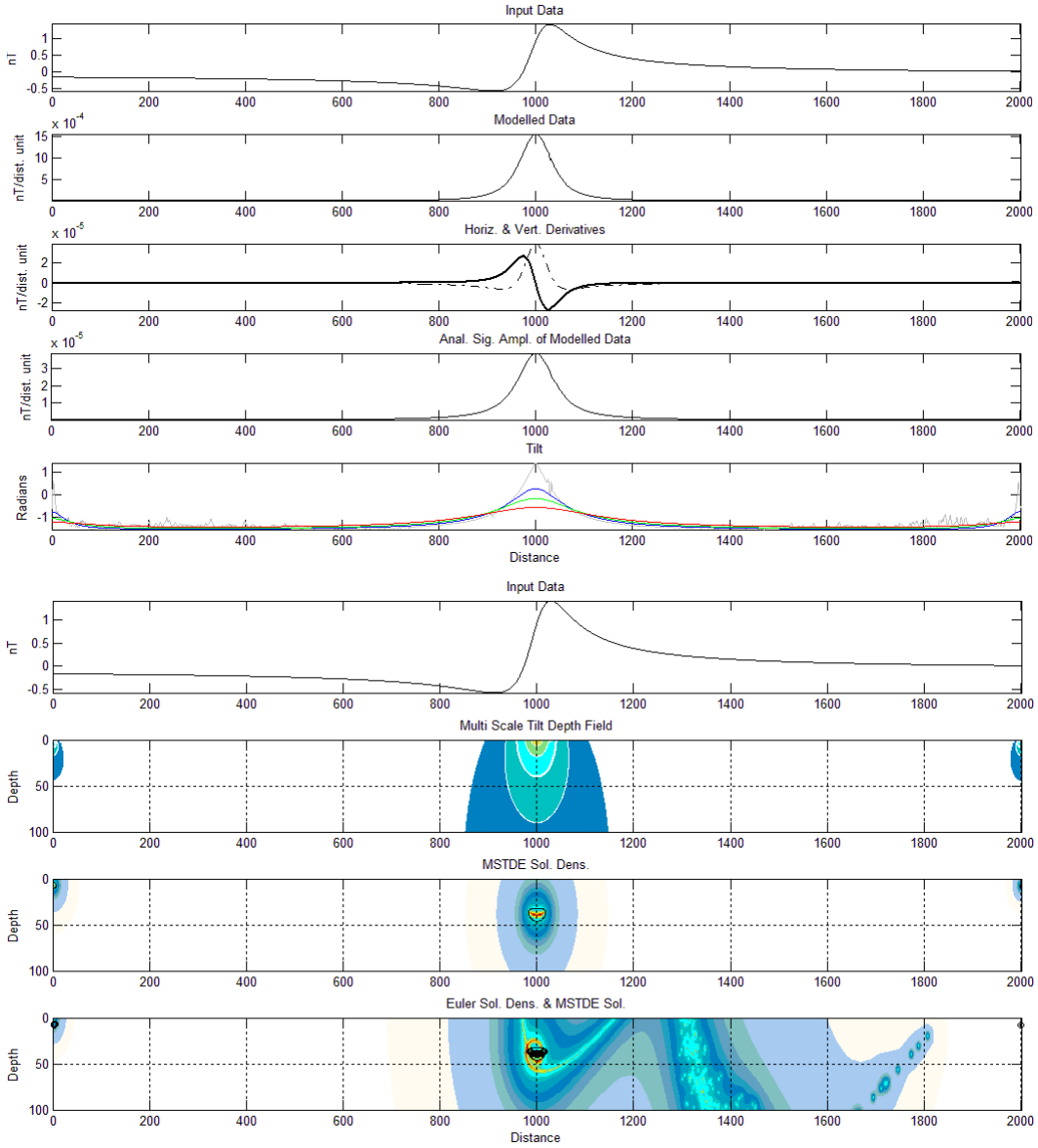


**Figure 101. Synthetic model data (Dip of 30°, Depth of 50 dist. units) with plots of the spatial derivatives, analytic signal amplitude and various continued tilt products (Top), Synthetic model data with MSTD distribution, MSTDE solution density and Euler solution density with MSTDE solution locations (Bottom).**

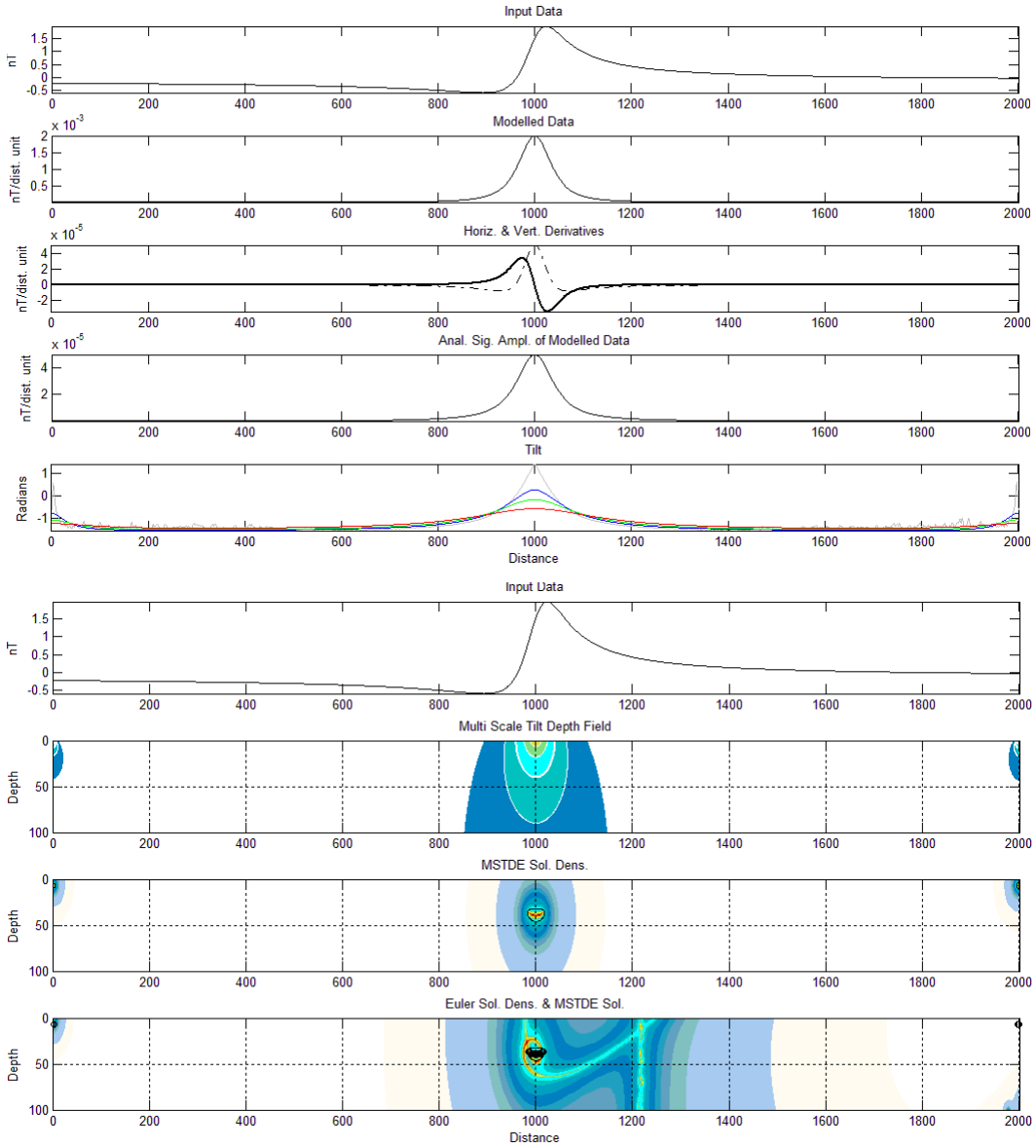


**Figure 102. Synthetic model data (Dip of 40°, Depth of 50 dist. units) with plots of the spatial derivatives, analytic signal amplitude and various continued tilt products (Top), Synthetic model data with MSTD distribution, MSTDE solution density and Euler solution density with MSTDE solution locations (Bottom).**

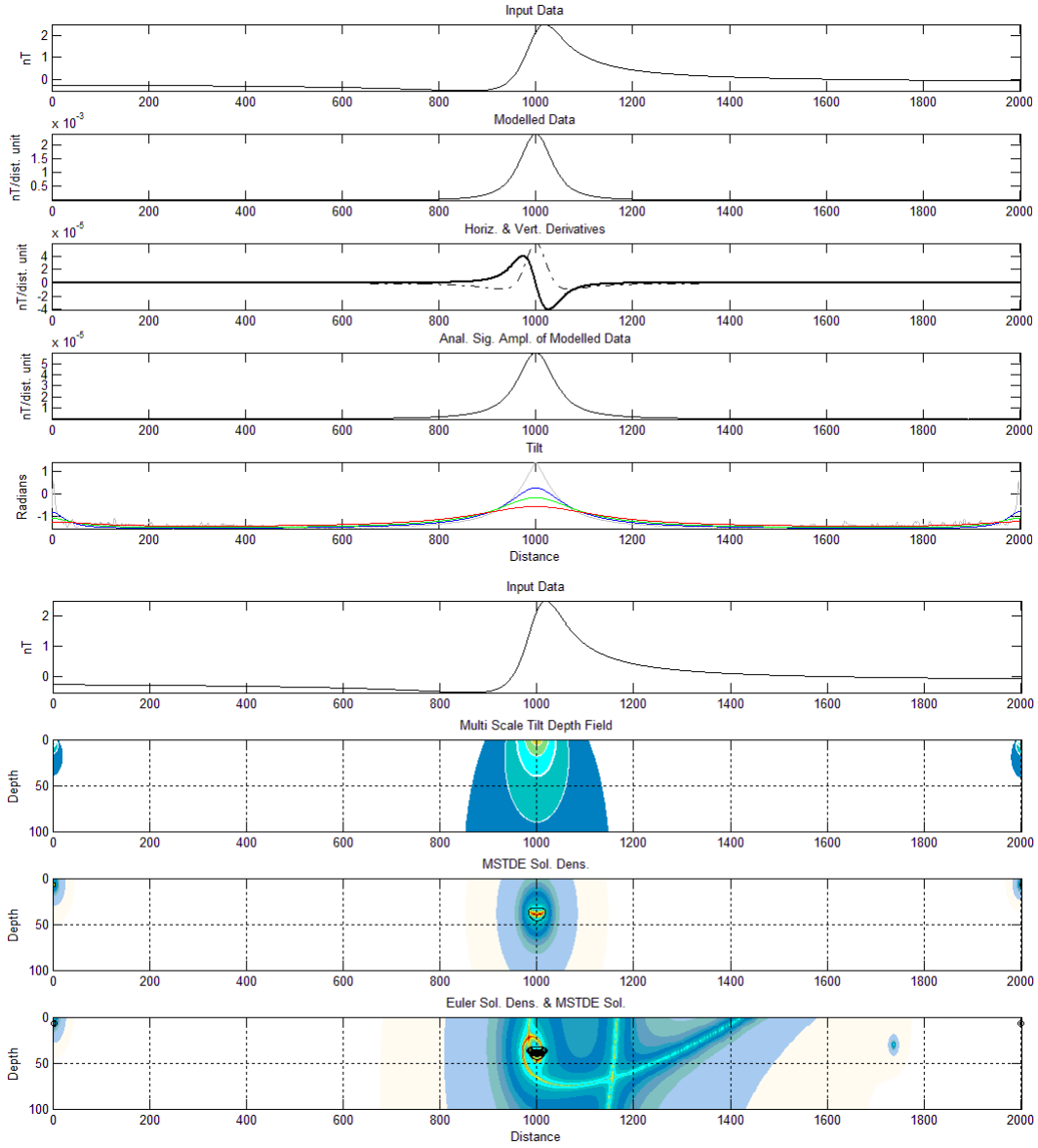


**Figure 103. Synthetic model data (Dip of 50°, Depth of 50 dist. units) with plots of the spatial derivatives, analytic signal amplitude and various continued tilt products (Top), Synthetic model data with MSTD distribution, MSTDE solution density and Euler solution density with MSTDE solution locations (Bottom).**

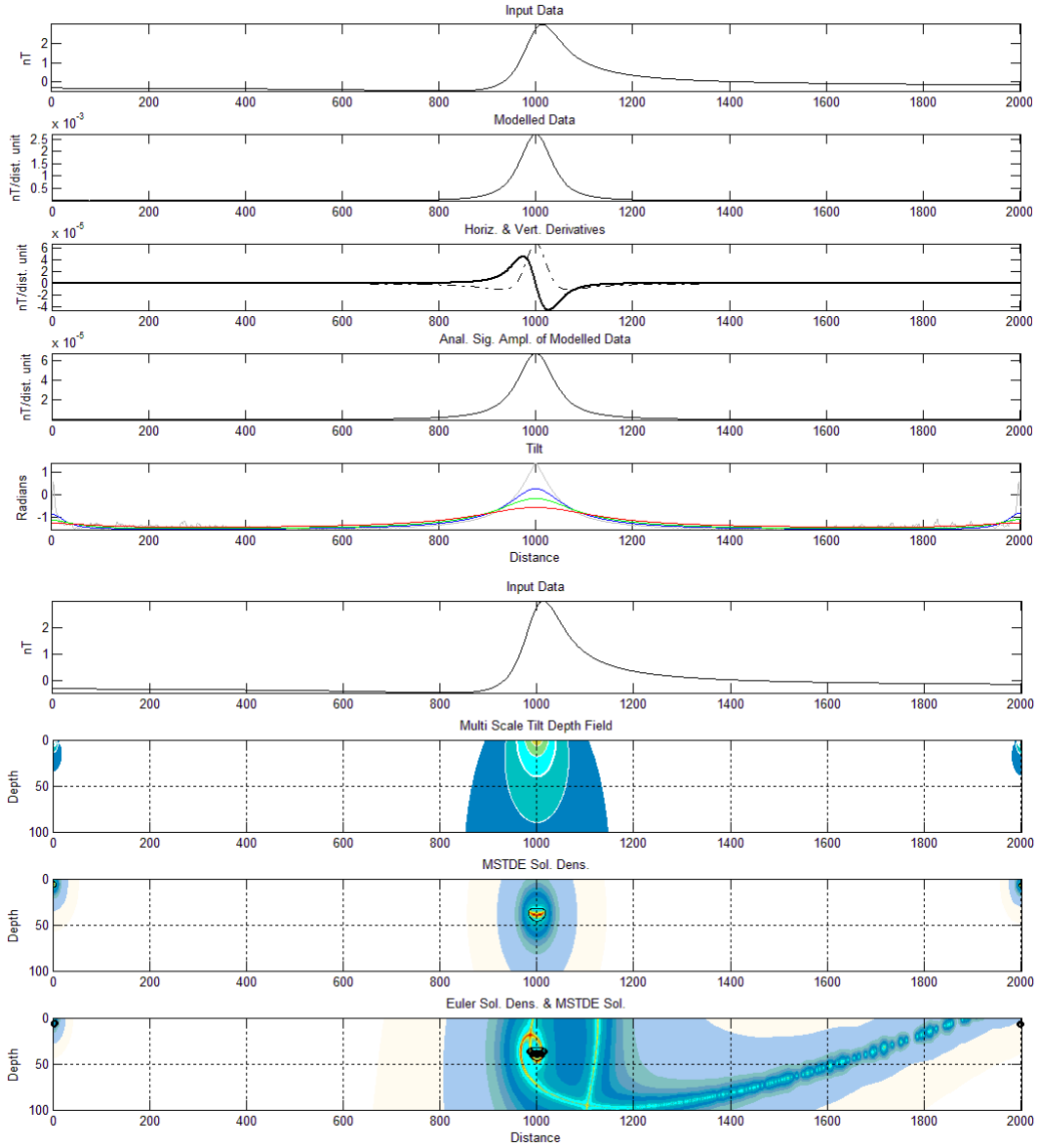


**Figure 104. Synthetic model data (Dip of 60°, Depth of 50 dist. units) with plots of the spatial derivatives, analytic signal amplitude and various continued tilt products (Top), Synthetic model data with MSTD distribution, MSTDE solution density and Euler solution density with MSTDE solution locations (Bottom).**

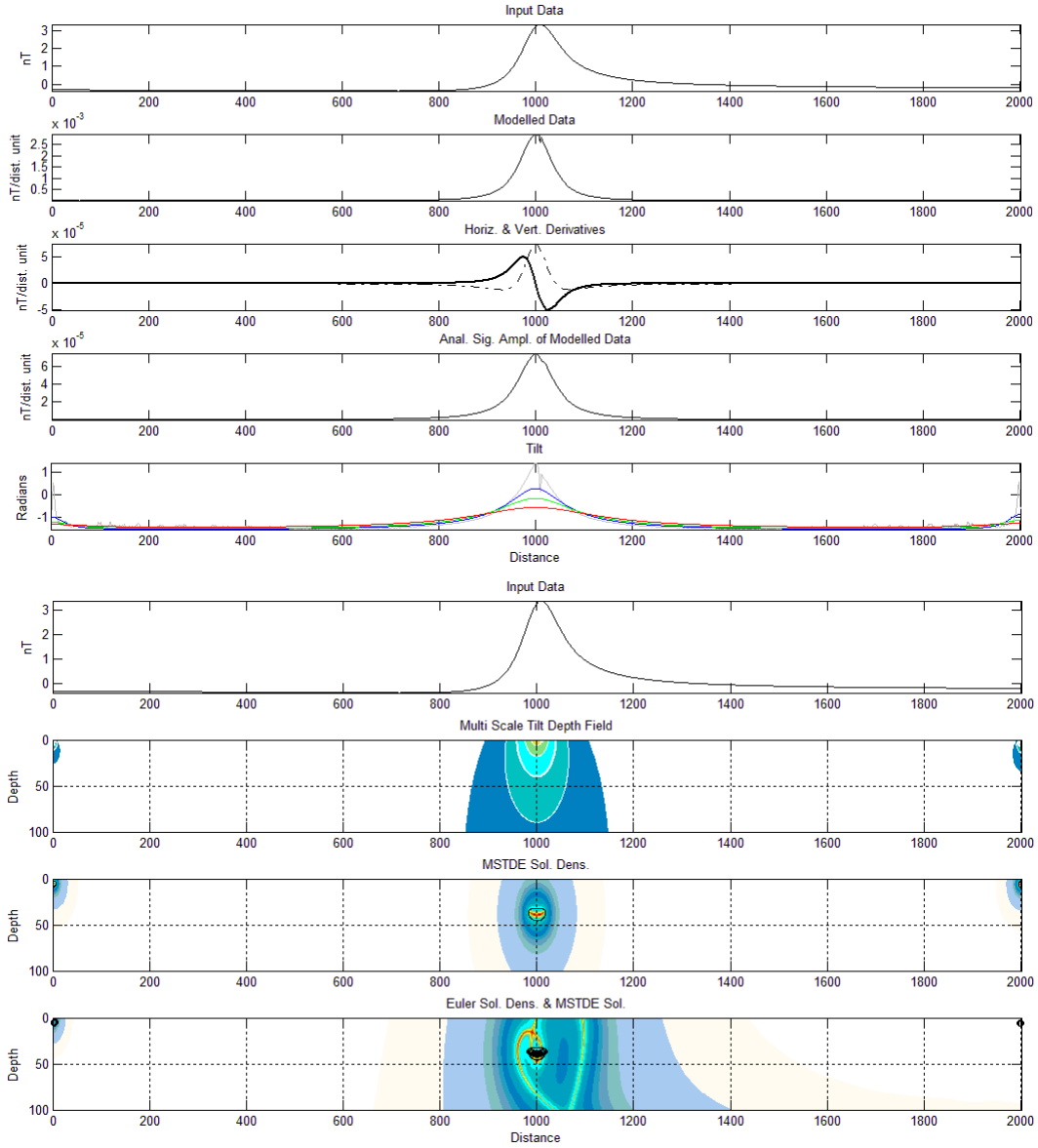


**Figure 105. Synthetic model data (Dip of 70°, Depth of 50 dist. units) with plots of the spatial derivatives, analytic signal amplitude and various continued tilt products (Top), Synthetic model data with MSTD distribution, MSTDE solution density and Euler solution density with MSTDE solution locations (Bottom).**

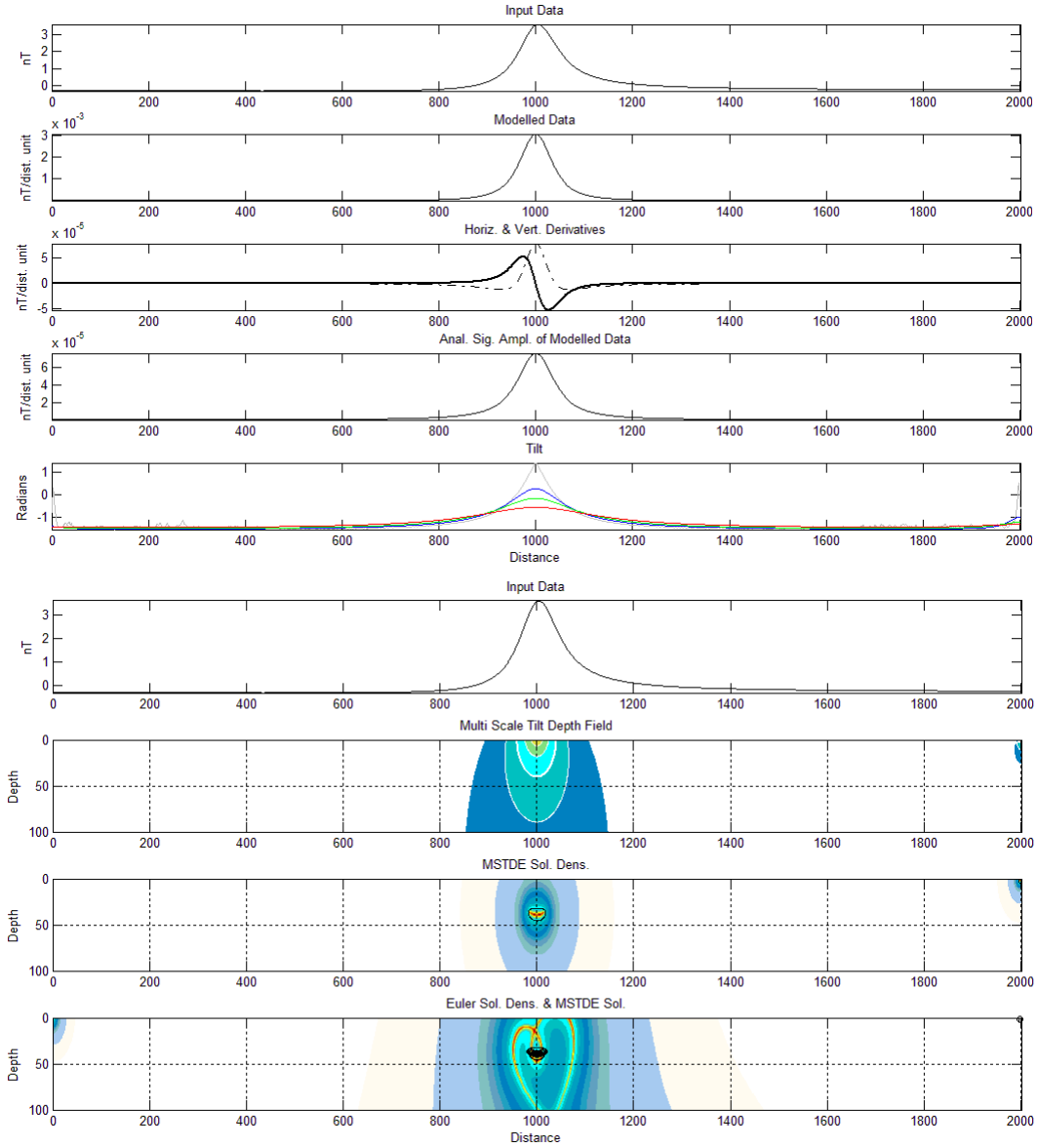


**Figure 106. Synthetic model data (Dip of 80°, Depth of 50 dist. units) with plots of the spatial derivatives, analytic signal amplitude and various continued tilt products (Top), Synthetic model data with MSTD distribution, MSTDE solution density and Euler solution density with MSTDE solution locations (Bottom).**

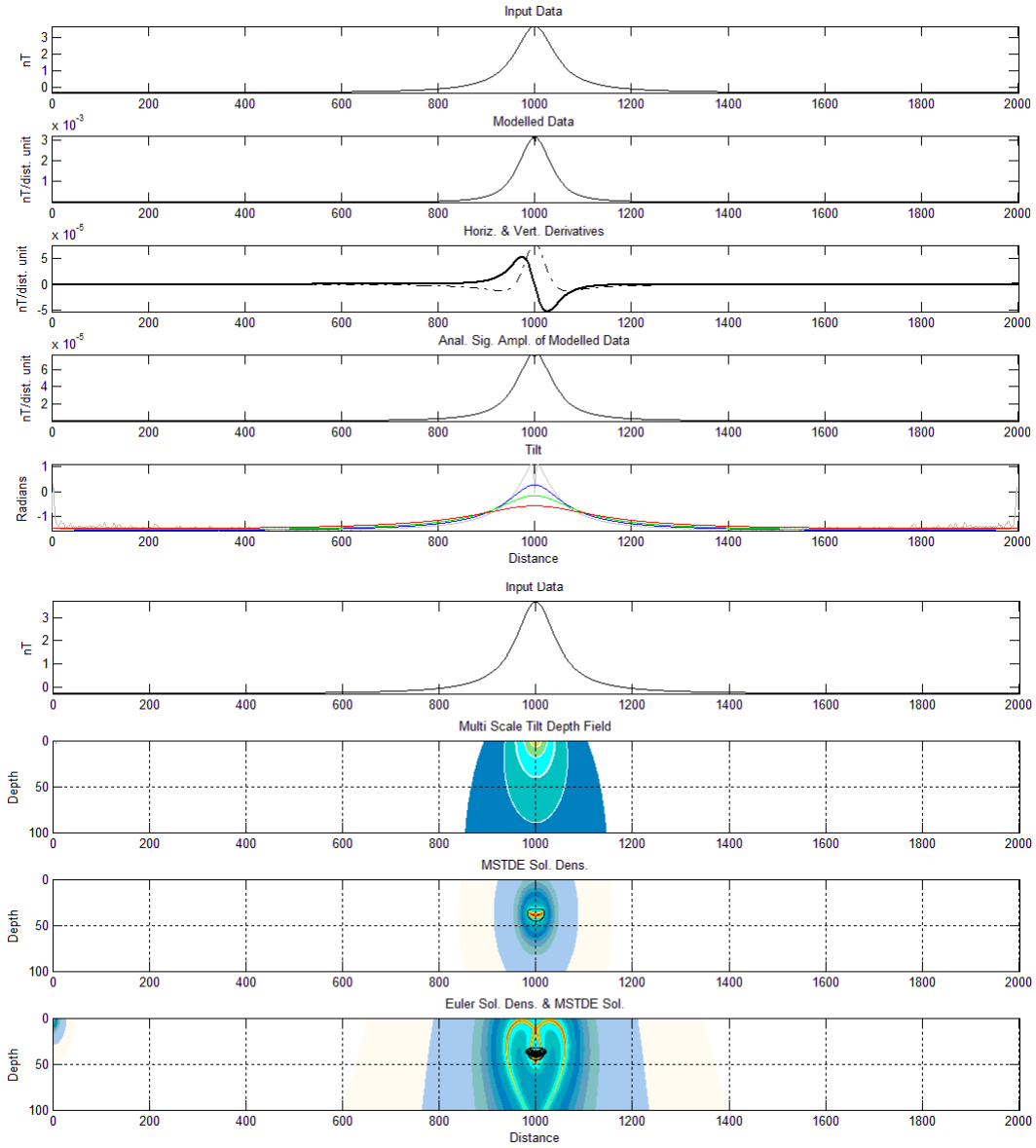


**Figure 107. Synthetic model data (Dip of 90°, Depth of 50 dist. units) with plots of the spatial derivatives, analytic signal amplitude and various continued tilt products (Top), Synthetic model data with MSTD distribution, MSTDE solution density and Euler solution density with MSTDE solution locations (Bottom).**

## Vertical sheet with various noise amplitudes – No smoothing

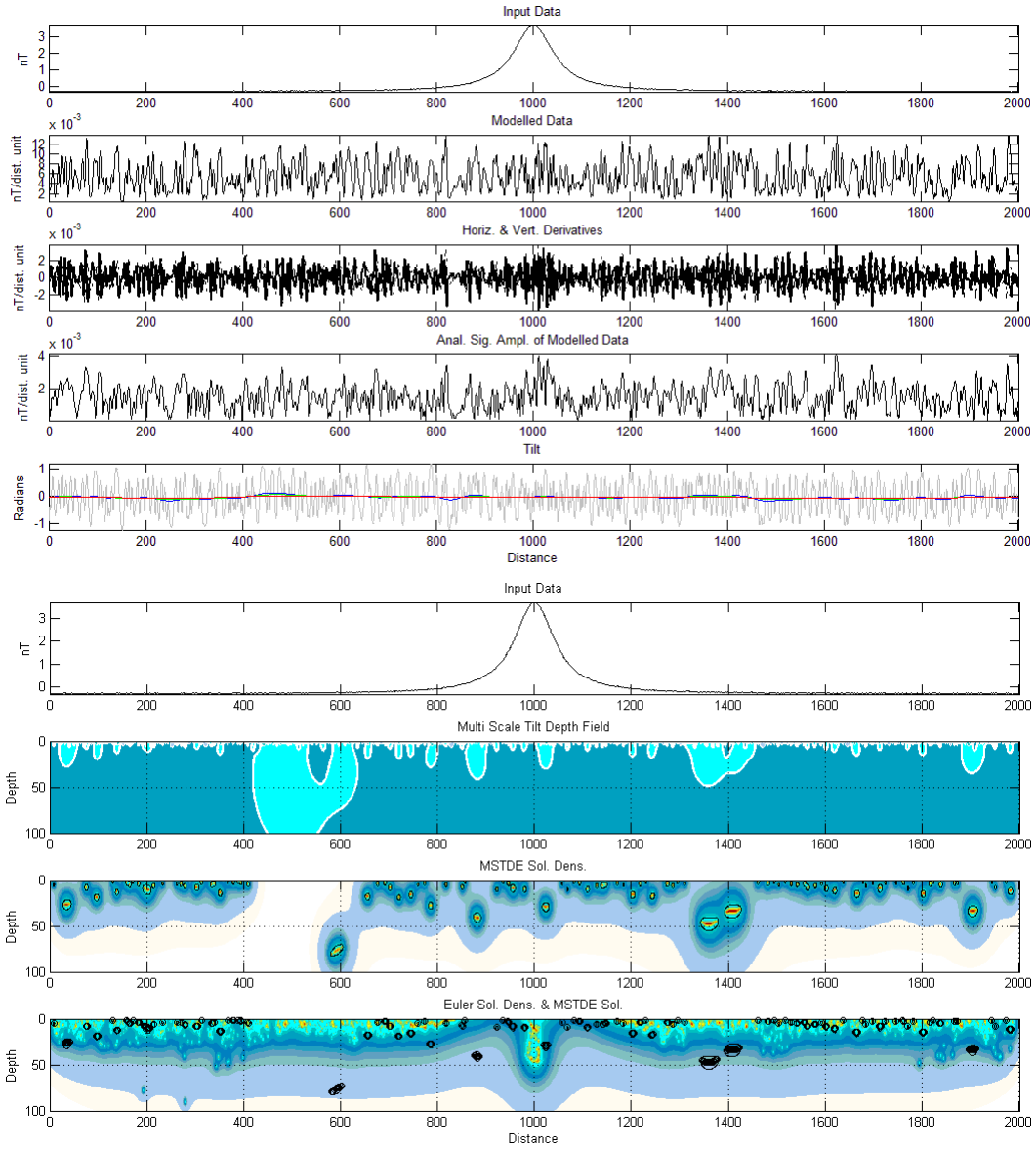


**Figure 108. Synthetic model data (Noise range of 10% of the standard deviation, Depth of 50 dist. units) with plots of the spatial derivatives, analytic signal amplitude and various continued tilt products (Top), Synthetic model data with MSTD distribution, MSTDE solution density and Euler solution density with MSTDE solution locations (Bottom). No smoothing has been applied to the data.**

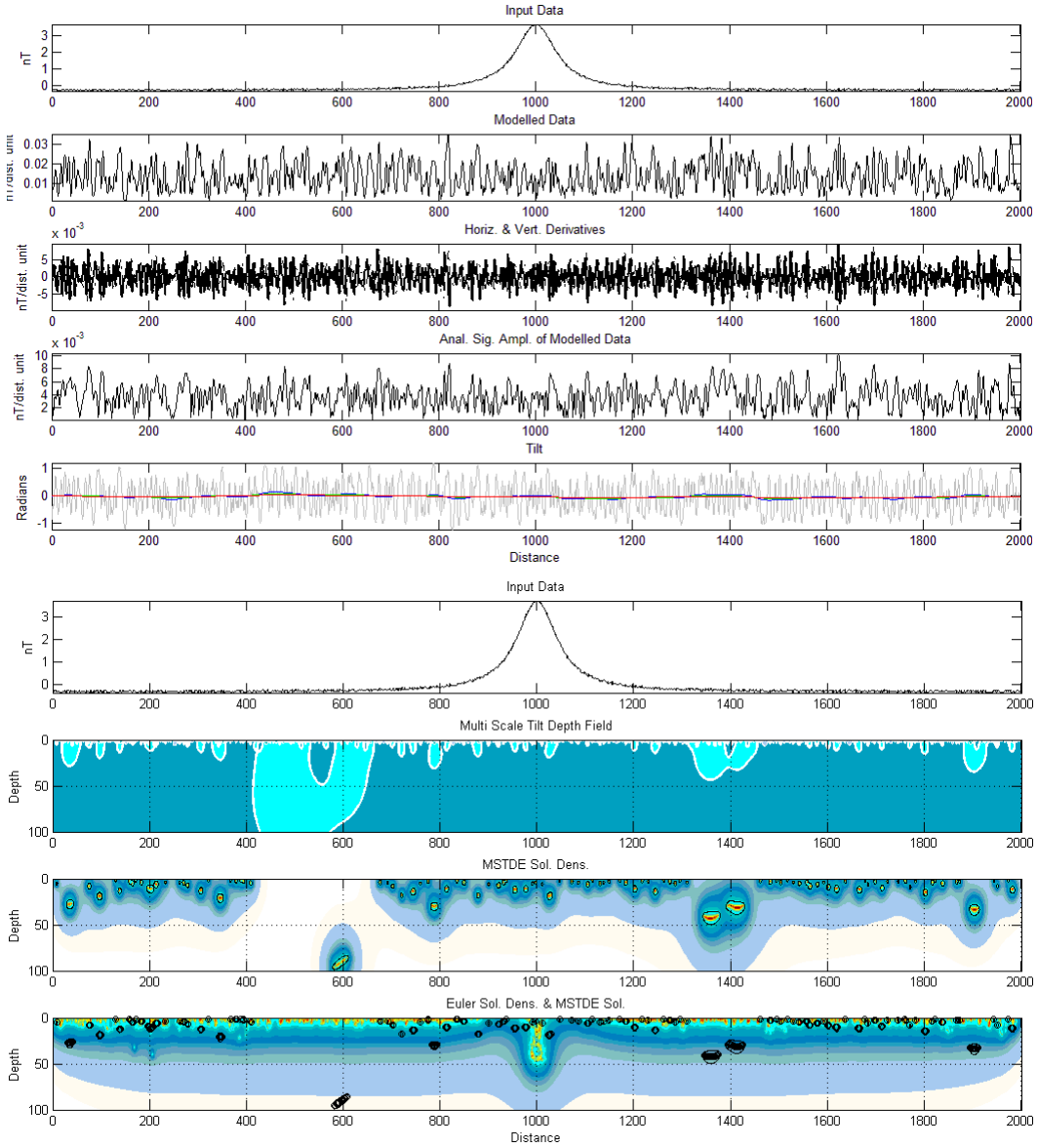


**Figure 109. Synthetic model data (Noise range of 25% of the standard deviation, Depth of 50 dist. units) with plots of the spatial derivatives, analytic signal amplitude and various continued tilt products (Top), Synthetic model data with MSTD distribution, MSTDE solution density and Euler solution density with MSTDE solution locations (Bottom). No Smoothing has been applied to the data.. No smoothing has been applied to the data.**

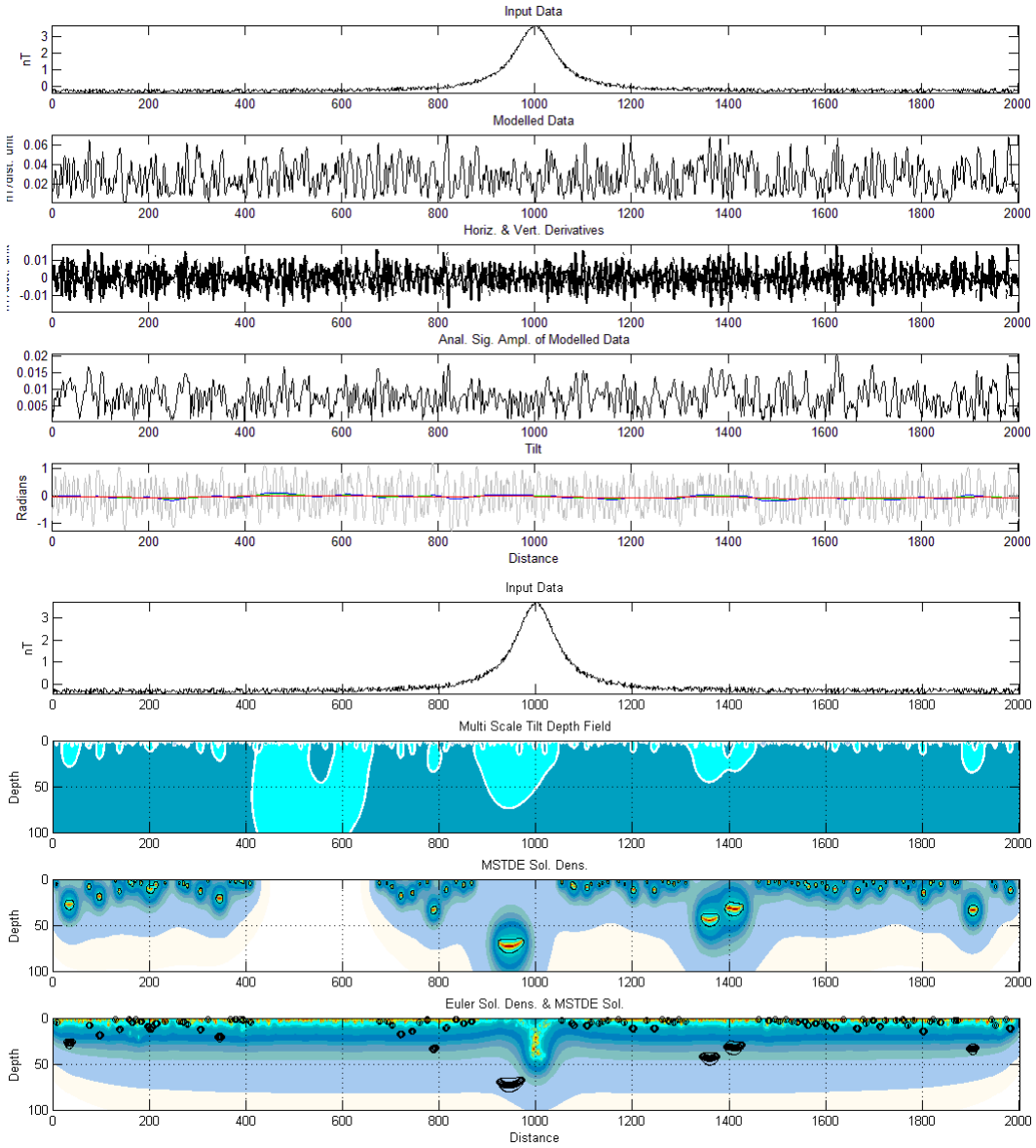


**Figure 110. Synthetic model data (Noise range of 50% of the standard deviation, Depth of 50 dist. units) with plots of the spatial derivatives, analytic signal amplitude and various continued tilt products (Top), Synthetic model data with MSTD distribution, MSTDE solution density and Euler solution density with MSTDE solution locations (Bottom). No smoothing has been applied to the data.**

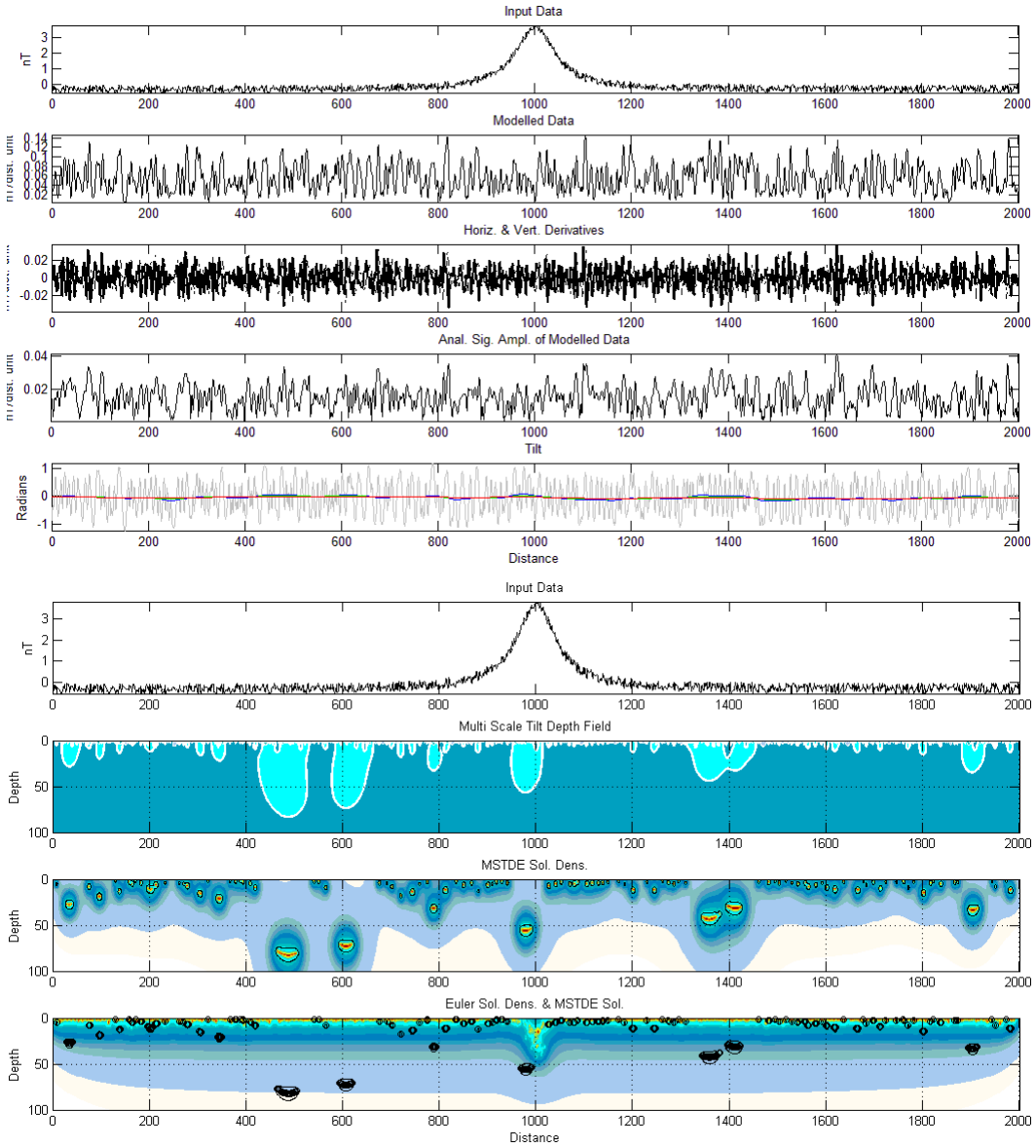


**Figure 111. Synthetic model data (Noise range of 100% of the standard deviation, Depth of 50 dist. units) with plots of the spatial derivatives, analytic signal amplitude and various continued tilt products (Top), Synthetic model data with MSTD distribution, MSTDE solution density and Euler solution density with MSTDE solution locations (Bottom). No smoothing has been applied to the data.**

## Vertical sheet with various noise amplitudes – Frequency domain smoothing

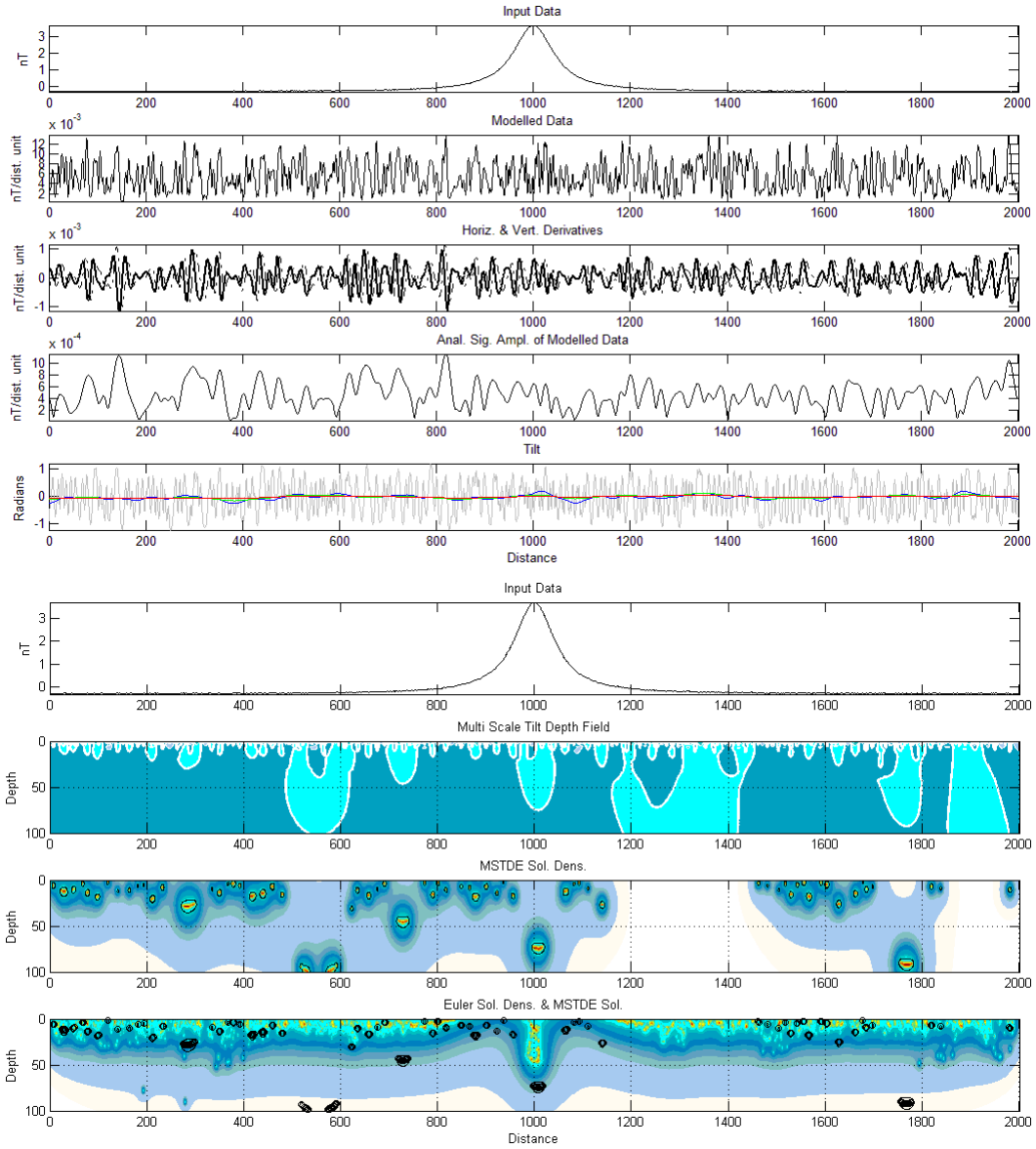


**Figure 112. Synthetic model data (Noise range of 10% of the standard deviation, Depth of 50 dist. units) with plots of the spatial derivatives, analytic signal amplitude and various continued tilt products (Top), Synthetic model data with MSTD distribution, MSTDE solution density and Euler solution density with MSTDE solution locations (Bottom). Frequency domain smoothing has been applied to the data.**

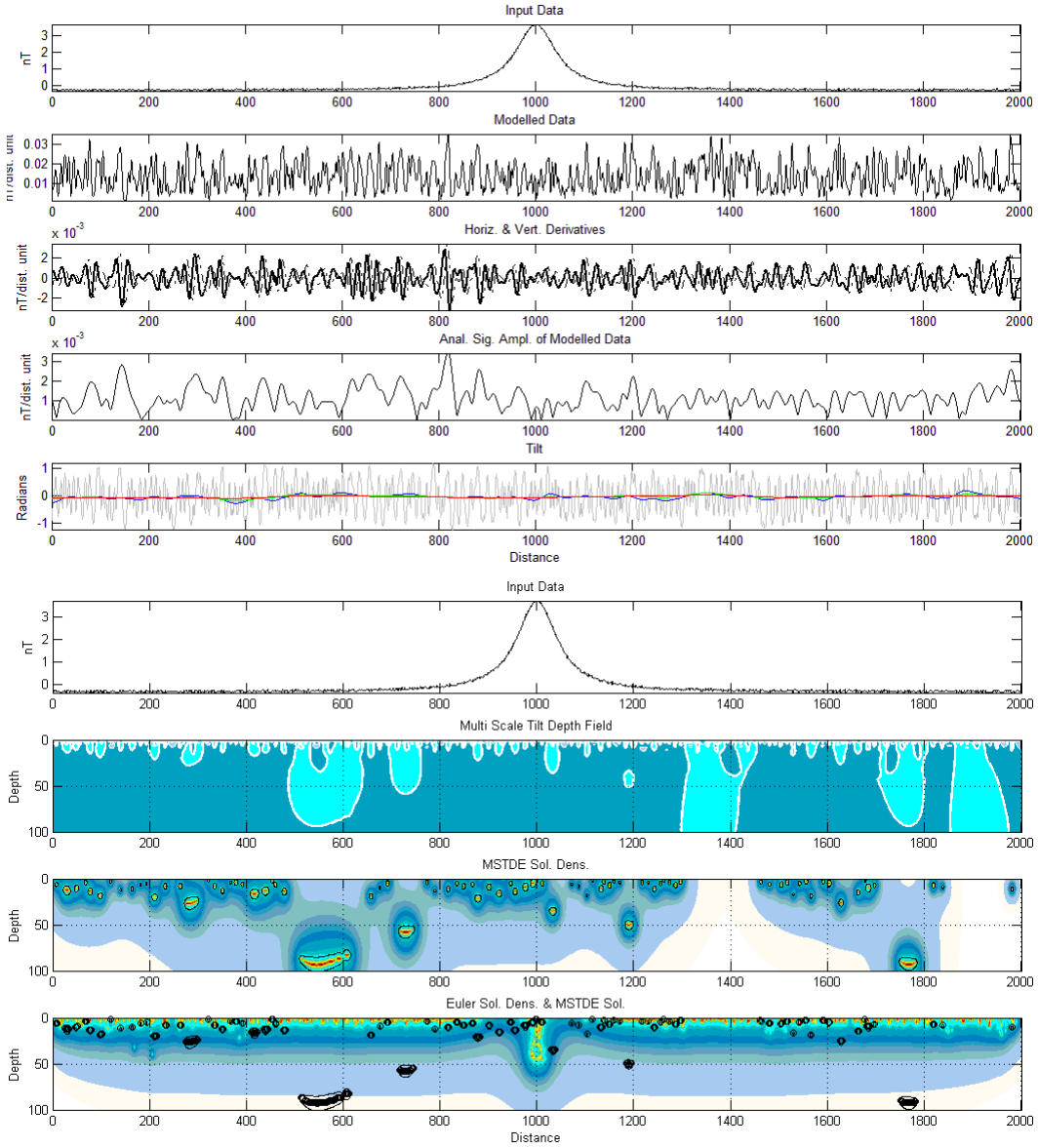


**Figure 113. Synthetic model data (Noise range of 25% of the standard deviation, Depth of 50 dist. units) with plots of the spatial derivatives, analytic signal amplitude and various continued tilt products (Top), Synthetic model data with MSTD distribution, MSTDE solution density and Euler solution density with MSTDE solution locations (Bottom). Frequency domain smoothing has been applied to the data.**

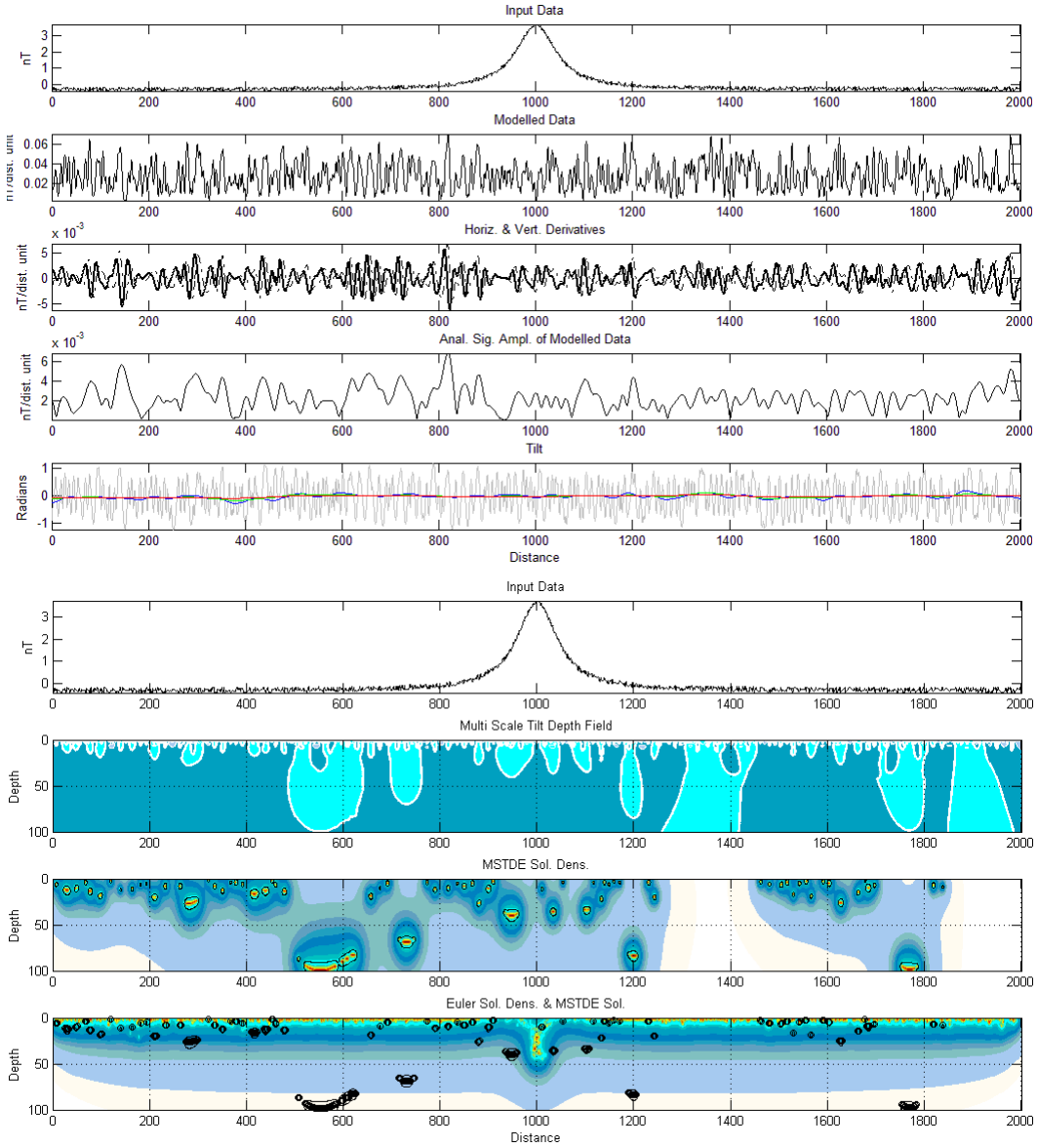


**Figure 114. Synthetic model data (Noise range of 50% of the standard deviation, Depth of 50 dist. units) with plots of the spatial derivatives, analytic signal amplitude and various continued tilt products (Top), Synthetic model data with MSTD distribution, MSTDE solution density and Euler solution density with MSTDE solution locations (Bottom). Frequency domain smoothing has been applied to the data.**

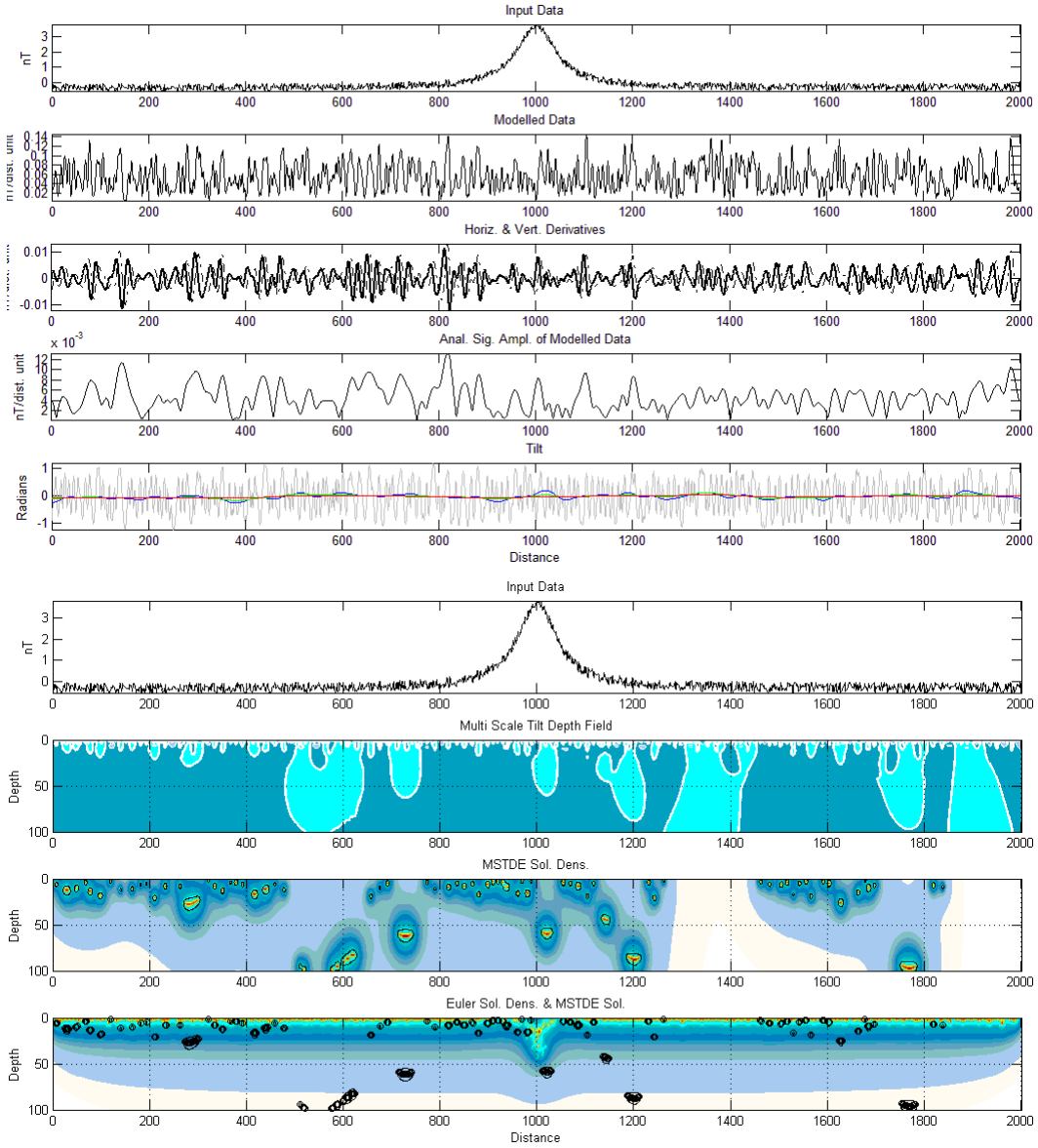


**Figure 115. Synthetic model data (Noise range of 100% of the standard deviation, Depth of 50 dist. units) with plots of the spatial derivatives, analytic signal amplitude and various continued tilt products (Top), Synthetic model data with MSTD distribution, MSTDE solution density and Euler solution density with MSTDE solution locations (Bottom). Frequency domain smoothing has been applied to the data.**

**Vertical sheet with various noise amplitudes – Frequency domain and 100 iterations of spatial domain smoothing**

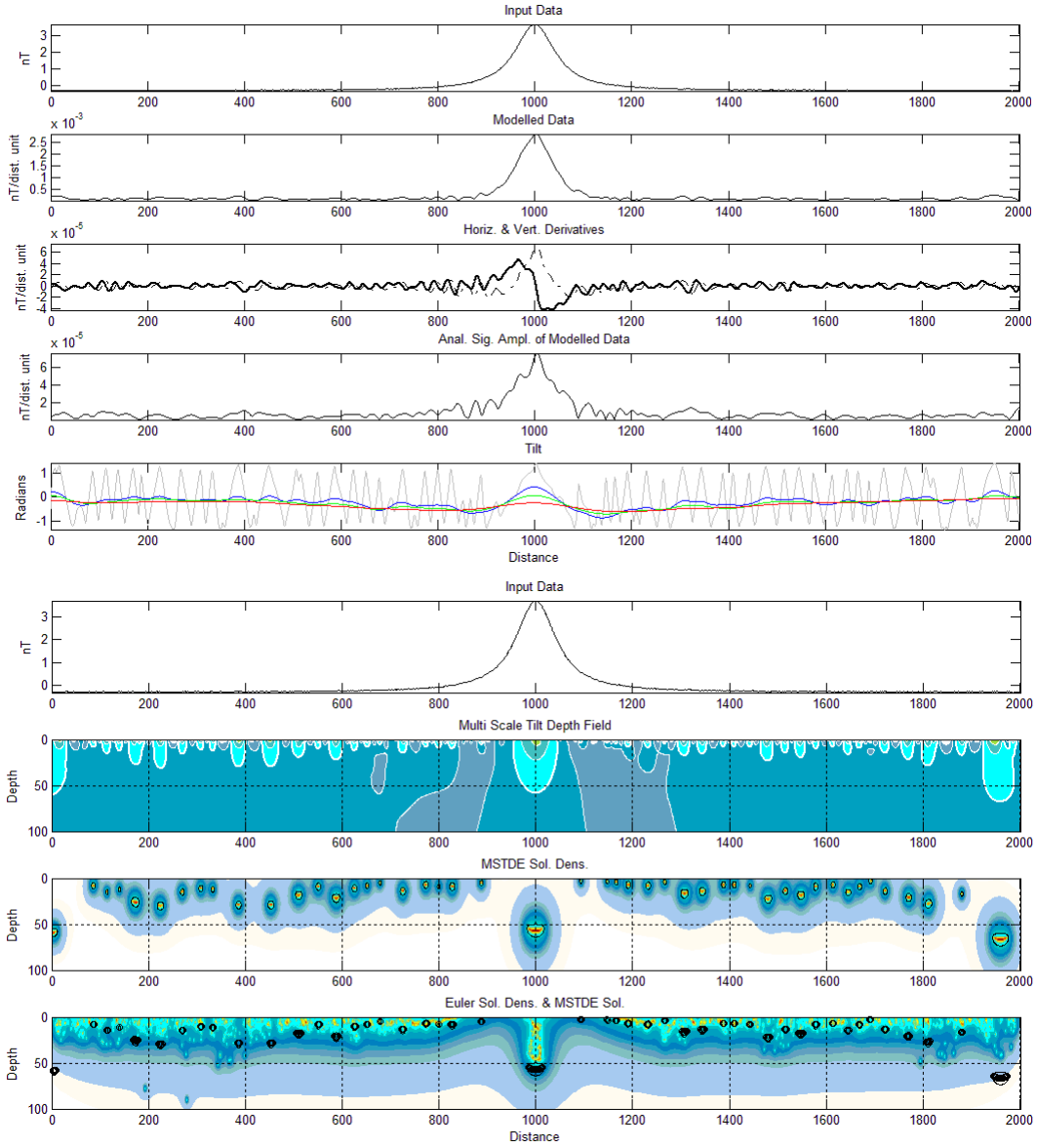


**Figure 116. Synthetic model data (Noise range of 10% of the standard deviation, Depth of 50 dist. units) with plots of the spatial derivatives, analytic signal amplitude and various continued tilt products (Top), Synthetic model data with MSTD distribution, MSTDE solution density and Euler solution density with MSTDE solution locations (Bottom). Frequency domain and up to 100 iterations of spatial domain smoothing have been applied to the data.**

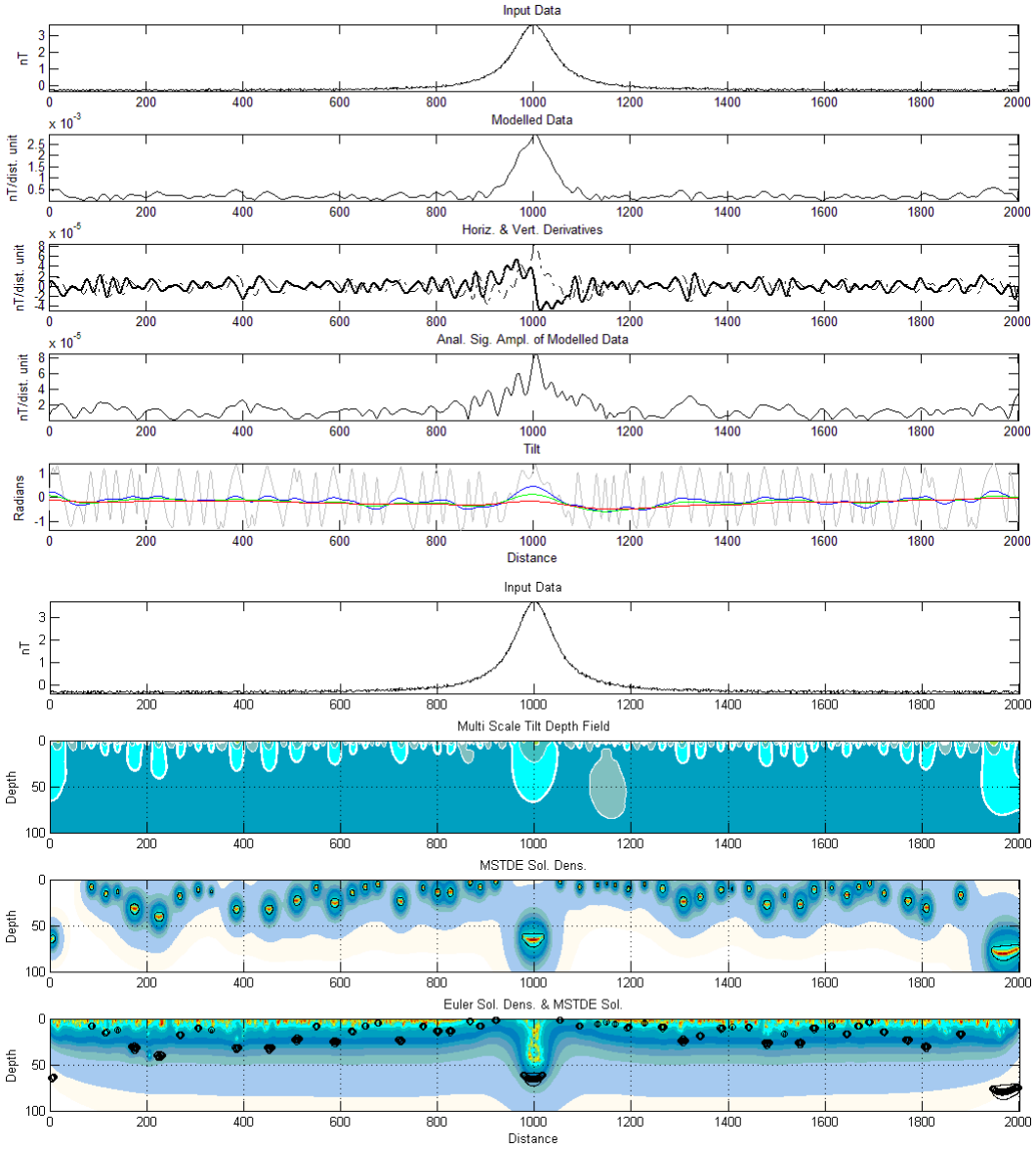


**Figure 117. Synthetic model data (Noise range of 25% of the standard deviation, Depth of 50 dist. units) with plots of the spatial derivatives, analytic signal amplitude and various continued tilt products (Top), Synthetic model data with MSTD distribution, MSTDE solution density and Euler solution density with MSTDE solution locations (Bottom). Frequency domain and up to 100 iterations of spatial domain smoothing have been applied to the data.**

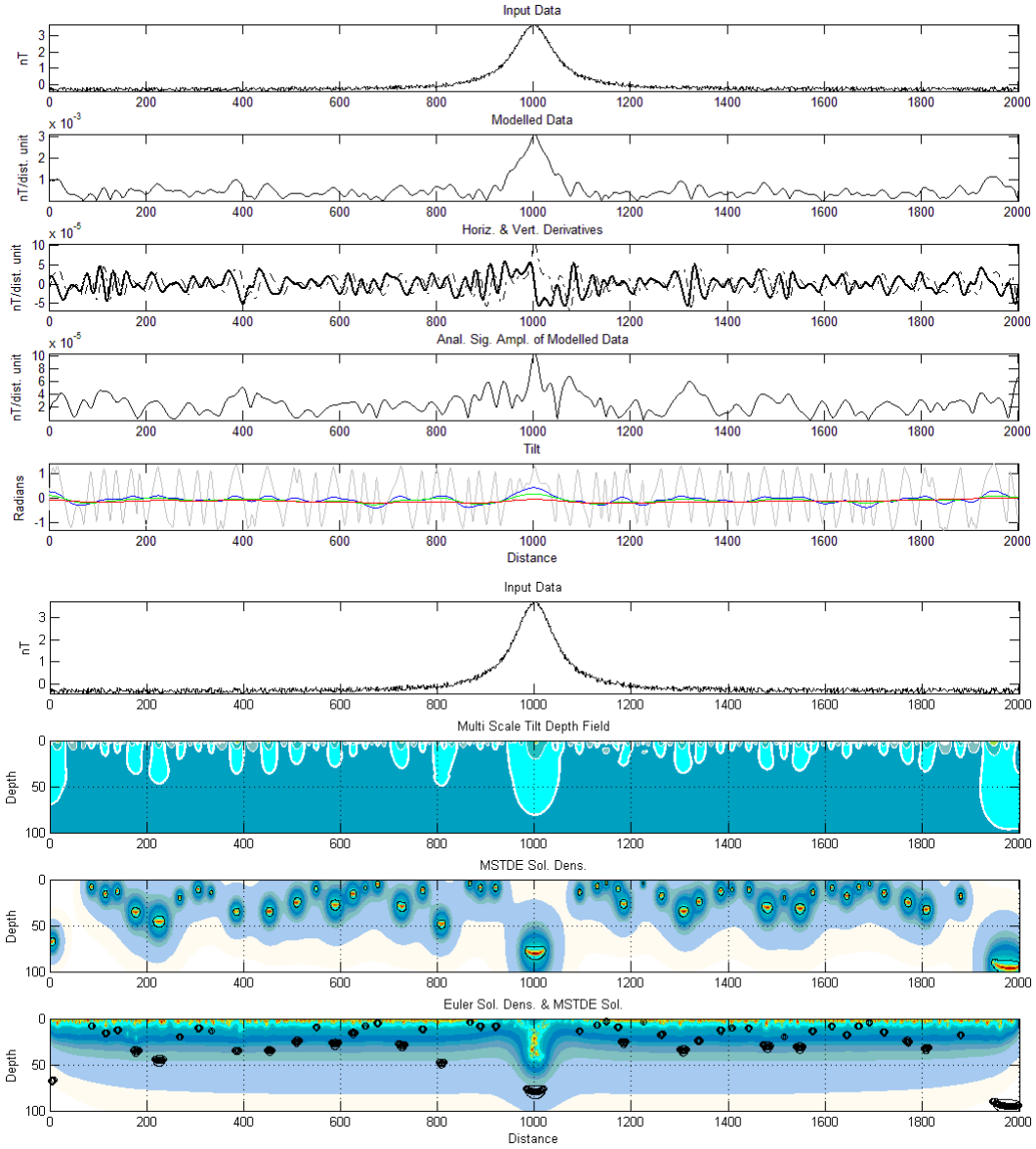


**Figure 118. Synthetic model data (Noise range of 50% of the standard deviation, Depth of 50 dist. units) with plots of the spatial derivatives, analytic signal amplitude and various continued tilt products (Top), Synthetic model data with MSTD distribution, MSTDE solution density and Euler solution density with MSTDE solution locations (Bottom). Frequency domain and up to 100 iterations of spatial domain smoothing have been applied to the data.**

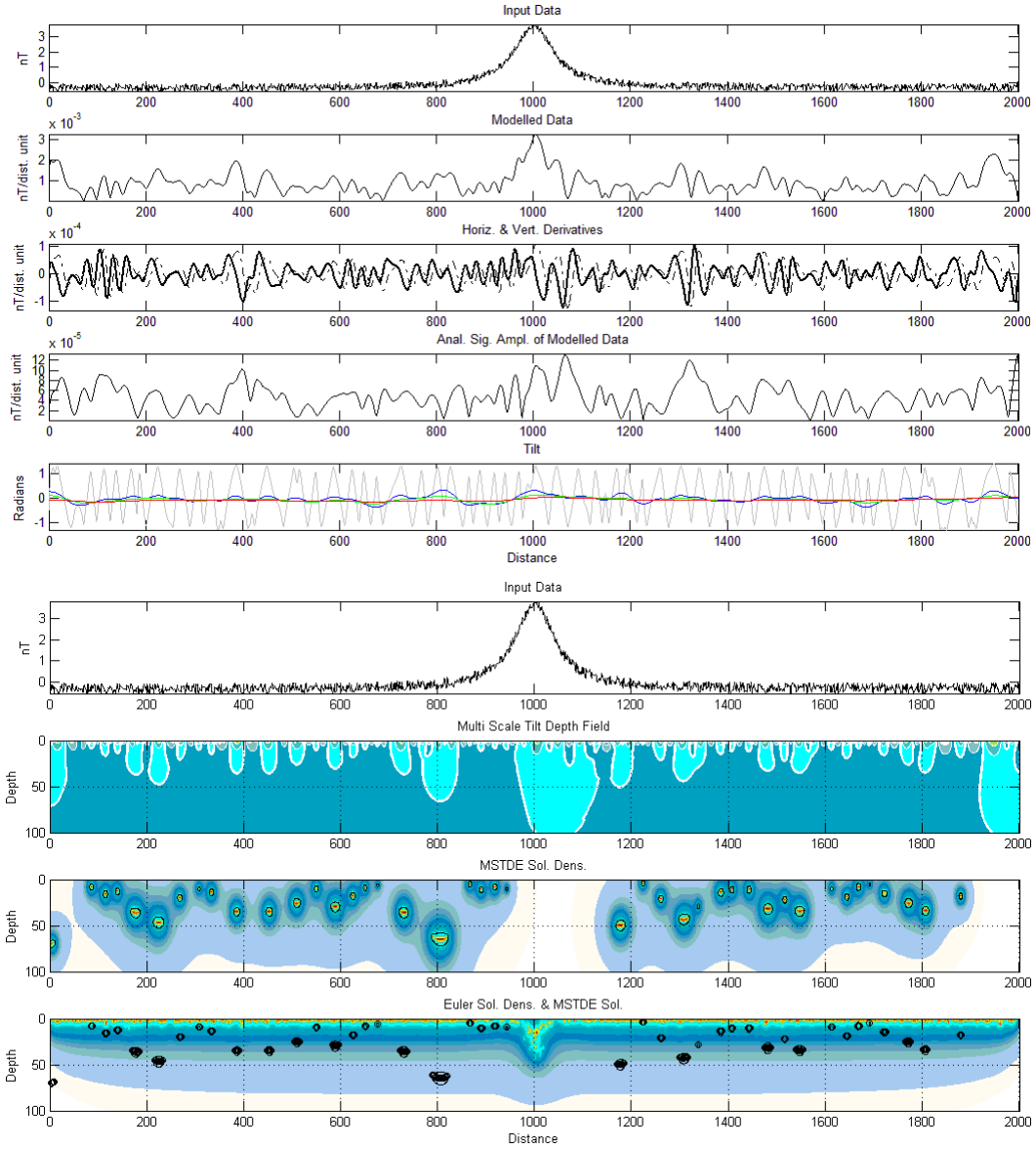


**Figure 119. Synthetic model data (Noise range of 100% of the standard deviation, Depth of 50 dist. units) with plots of the spatial derivatives, analytic signal amplitude and various continued tilt products (Top), Synthetic model data with MSTD distribution, MSTDE solution density and Euler solution density with MSTDE solution locations (Bottom). Frequency domain and up to 100 iterations of spatial domain smoothing have been applied to the data.**

## Multiple vertical sheets with various separations

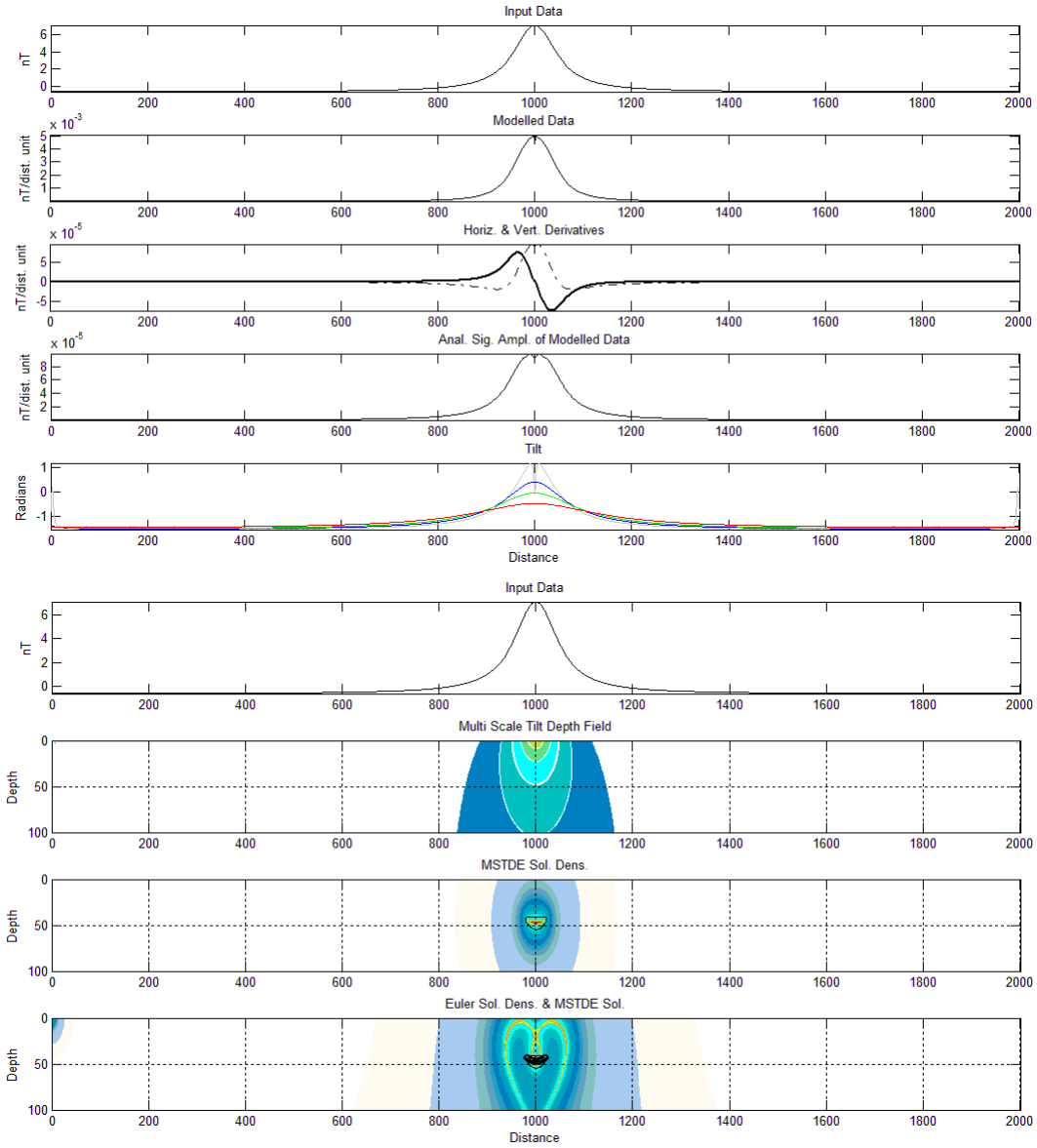


**Figure 120. Synthetic model data (Separation of 20 dist. units, Depth of 50 dist. units) of two vertical sheets, the centres separated by 100 distance units. Plots of the spatial derivatives, analytic signal amplitude and various continued tilt products (Top), Synthetic model data with MSTD distribution, MSTDE solution density and Euler solution density with MSTDE solution locations (Bottom).**

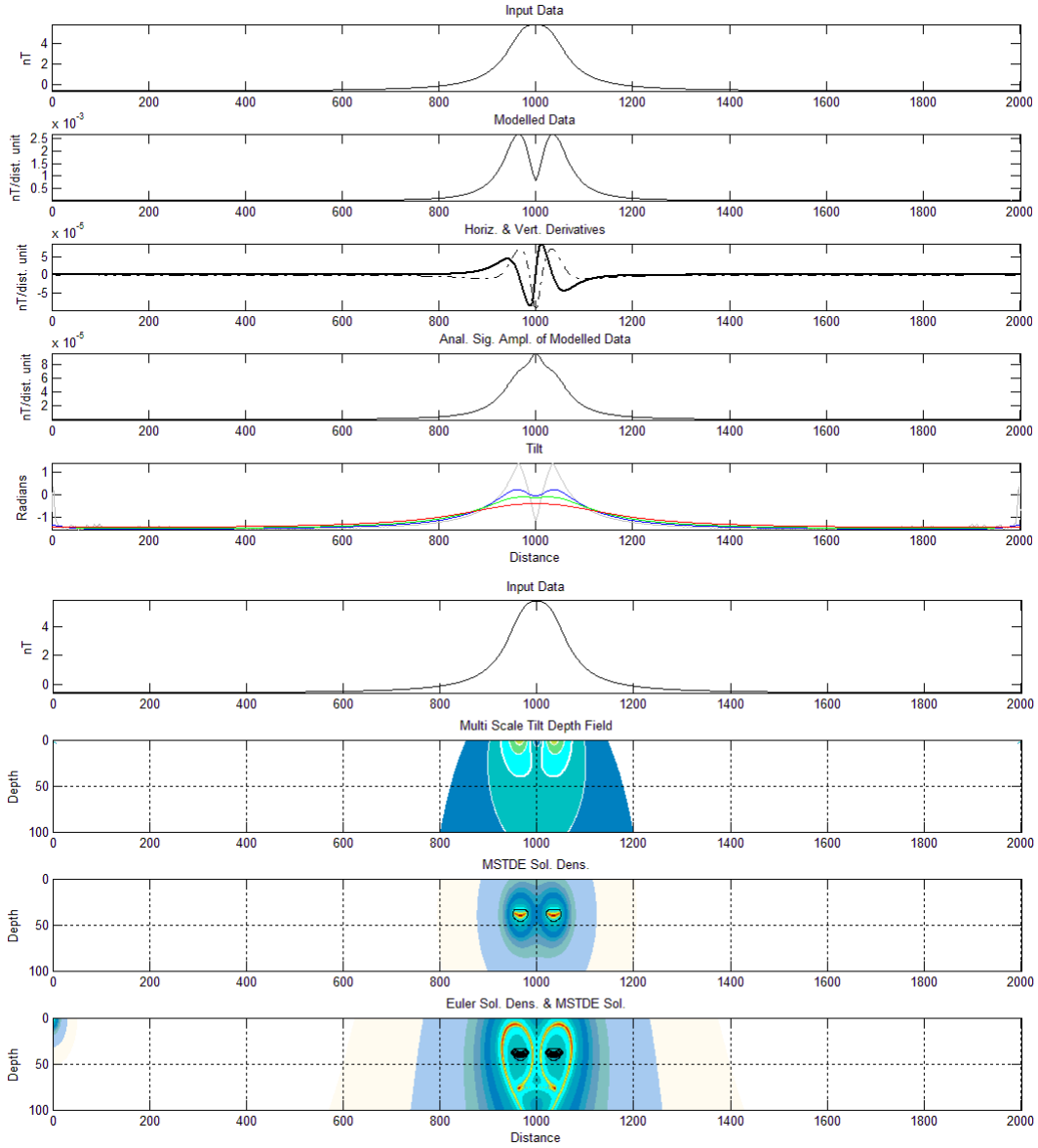


**Figure 121. Synthetic model data (Separation of 50 dist. units, Depth of 50 dist. units) of two vertical sheets, the centres separated by 100 distance units. Plots of the spatial derivatives, analytic signal amplitude and various continued tilt products (Top), Synthetic model data with MSTD distribution, MSTDE solution density and Euler solution density with MSTDE solution locations (Bottom).**

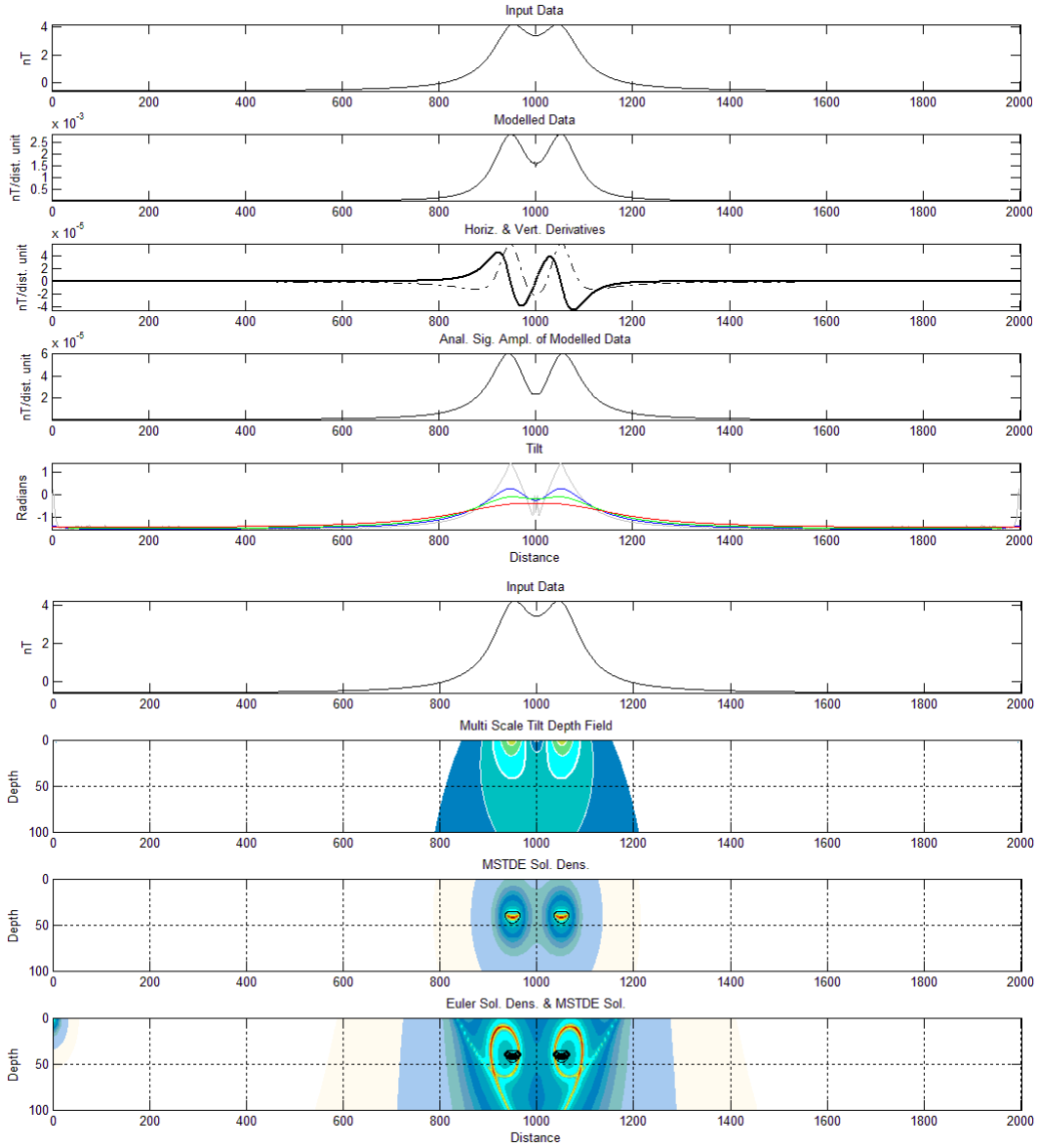


**Figure 122. Synthetic model data (Separation of 100 dist. units, Depth of 50 dist. units) of two vertical sheets, the centres separated by 100 distance units. Plots of the spatial derivatives, analytic signal amplitude and various continued tilt products (Top), Synthetic model data with MSTD distribution, MSTDE solution density and Euler solution density with MSTDE solution locations (Bottom).**

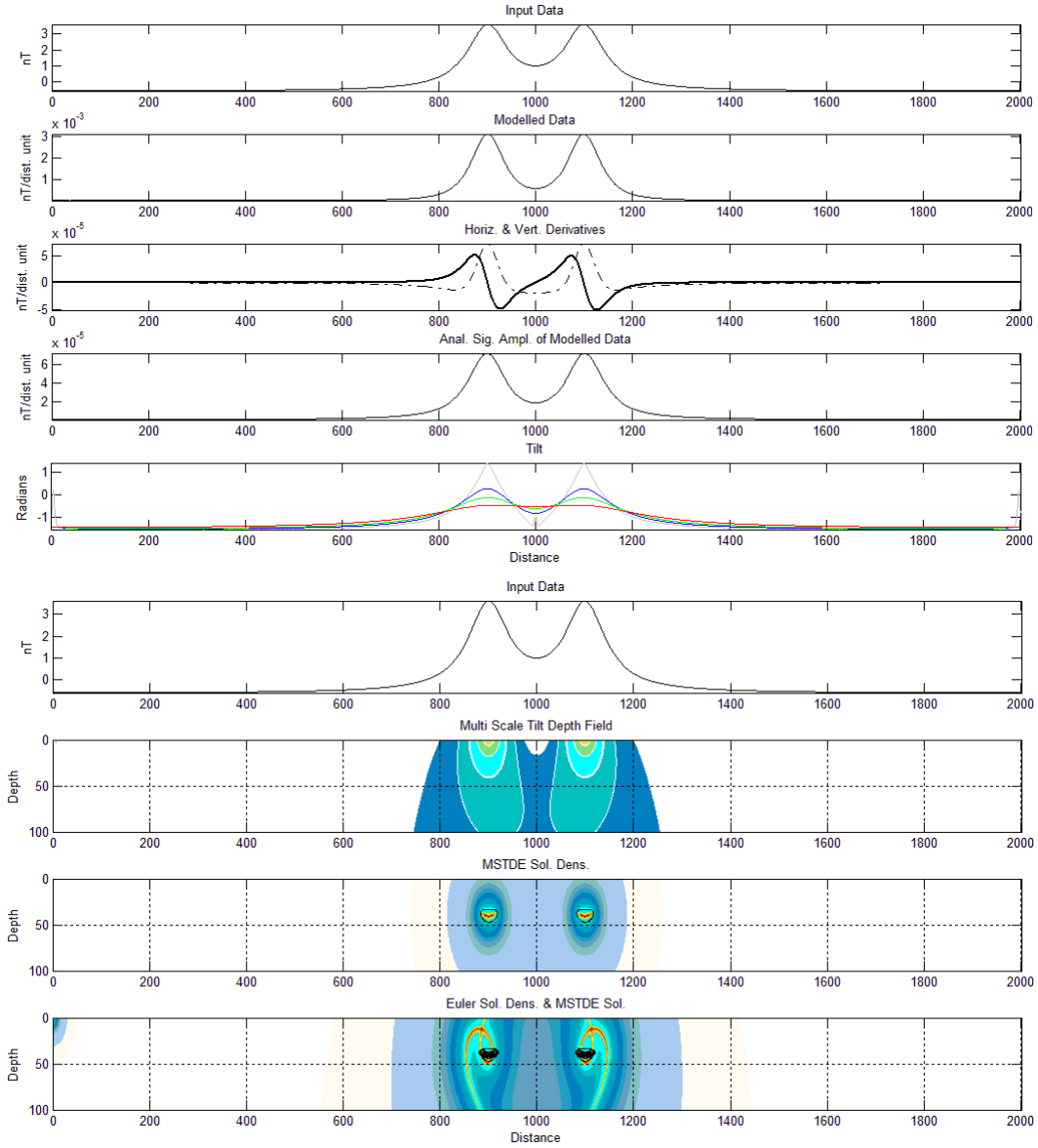


**Figure 123. Synthetic model data (Separation of 200 dist. units, Depth of 50 dist. units) of two vertical sheets, the centres separated by 100 distance units. Plots of the spatial derivatives, analytic signal amplitude and various continued tilt products (Top), Synthetic model data with MSTD distribution, MSTDE solution density and Euler solution density with MSTDE solution locations (Bottom).**

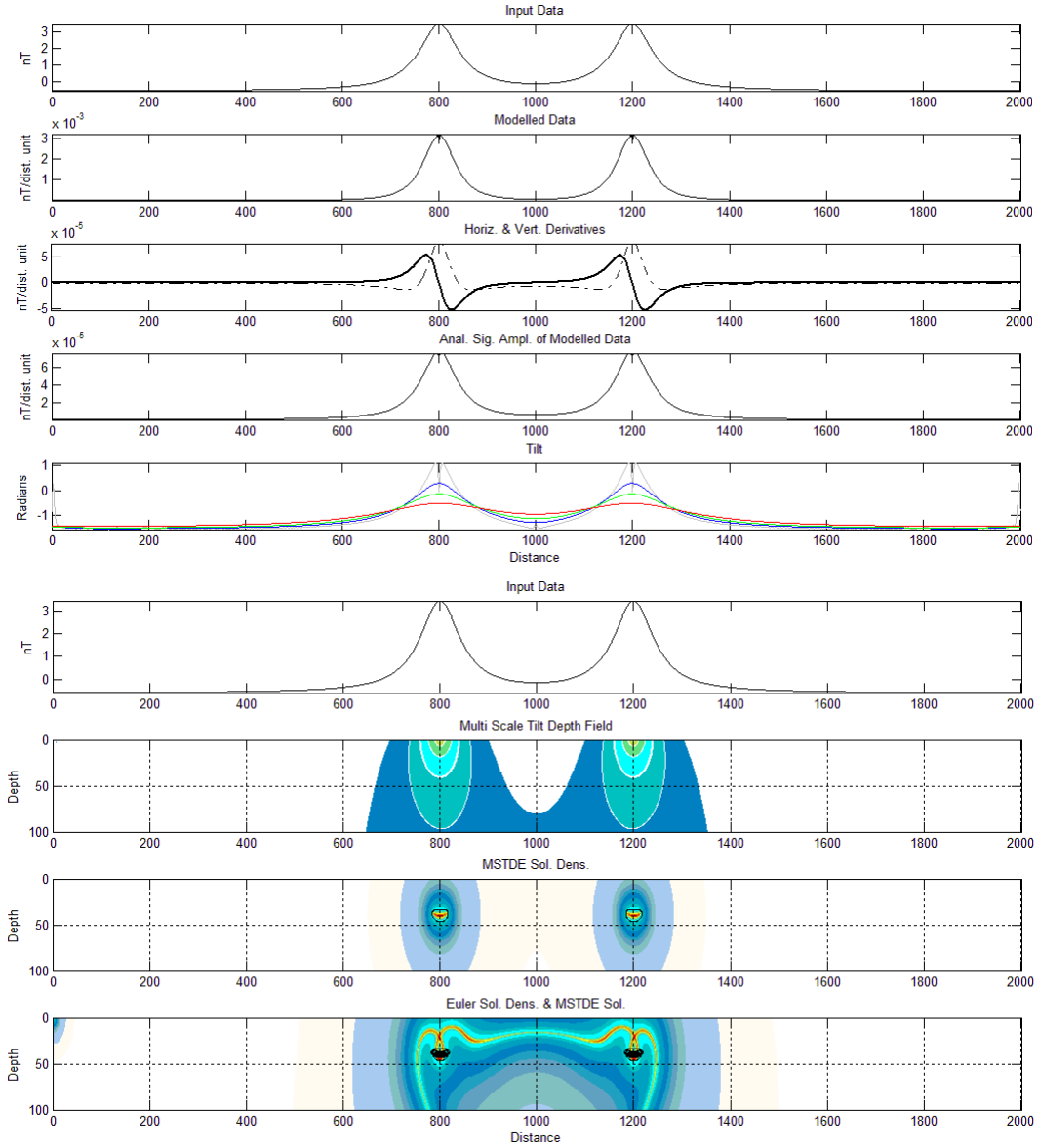


**Figure 124. Synthetic model data (Separation of 400 dist. units, Depth of 50 dist. units) of two vertical sheets, the centres separated by 100 distance units. Plots of the spatial derivatives, analytic signal amplitude and various continued tilt products (Top), Synthetic model data with MSTD distribution, MSTDE solution density and Euler solution density with MSTDE solution locations (Bottom).**

# APPENDIX D

Appendix D contains the original paper published by van Buren (2009) at the 11th SAGA Biennial Technical Meeting, which to my knowledge remains the only prior mention of this methodology to date. This work was bestowed the Best Poster award at the Meeting.

# Multi-Scale Depth Estimation

**R. van Buren**

1. De Beers Technical Services, South Africa, Reece.vanBuren@debeersgroup.com

## ABSTRACT

This paper documents the development of an empirical depth estimation technique applicable to potential field data. The technique is demonstrated by application to synthetic magnetic data generated from bodies with varying properties. Application to a sample field dataset is also documented. The estimates produced by the technique and its various derivatives are compared with Euler results providing a benchmark. The results are encouraging and comparable to those obtained from the 3D (grid) Euler method. Although the robust nature of the technique is illustrated, it requires more development in order to formalise the methodology and to provide a theoretical understanding of the observations.

**Key words:** Multi-Scale, Depth Estimation, Magnetic Data

## INTRODUCTION

The Multi-Scale depth estimation method is at present an empirical technique to approximate the depth to the causative of a magnetic anomaly. The method requires more interrogation to better formalise the methodology and provide theoretical justification for the observations, but similarities may be drawn with SPI™ methods (Thurston and Smith, 1997) employing the wave number and local phase. The results obtained from the application of this method to synthetic data are presented herein and compared with those obtained from 3D (grid) Euler deconvolution.

## THE METHOD

This method utilises the upward-continued tilt derivative of the reduced-to-pole magnetic data. The "AREA" of the tilt derivative (TDR, Figures 2 & 5) is computed at each of the upward continued levels. These data are then combined into an array with associated depths (derived directly from upward continued distances).

$$TDR(f) = \tan^{-1}[VD/HD], VD = \partial f/\partial z, HD = \sqrt{(\partial f/\partial x)^2 + (\partial f/\partial y)^2} \quad (1)$$

$$AREA = \tan^{-1}\left[\tan\left[\frac{\pi}{2} - \tan^{-1}(RTP\_TDR)\right]\right], RTP\_TDR = TDR(RTP) \quad (2)$$

The distance intervals used in the upward-continuation were: 0, 10, 20, 30, 50, 75, …, 275, 300m. These correspond to depths of 0, 10, 20m etc. The choice of these intervals is arbitrary and should correspond to likely depths of causatives. The interval differences can be increased with depth due to decreased resolution.

A farm of susceptible bodies was created to test the accuracy of the method and is shown in Figure 1. The magnetic forward response (TMI) of the farm was computed and the vertical derivative (VD) of this is presented in Figure 2.

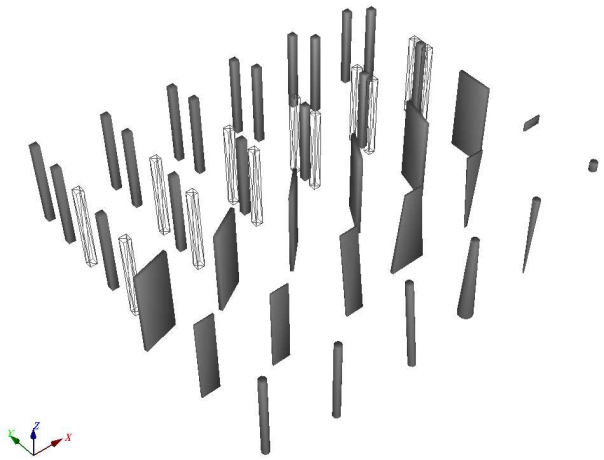

**Figure 1 Farm of susceptible bodies illustrating variations in the X direction:**
**Row 1 – Pipe (depth, dip, size at depth, depth extent)**
**Row 2 – Linear (as with Row 1)**
**Row 3 – Variation in strike**
**Row 4 – Variation in proximity**
**Row 5 – Variation in susceptibility**
**Row 6 – Variation in depth**
**(Row no.'s increase in the +Y direction, Column no.'s in the +X direction)**

The method was also tested in the presence of noise by adding a pseudo-random noise component to the computed TMI (Figures 3 & 4). The VD of the TMI is seen in Figure 2.

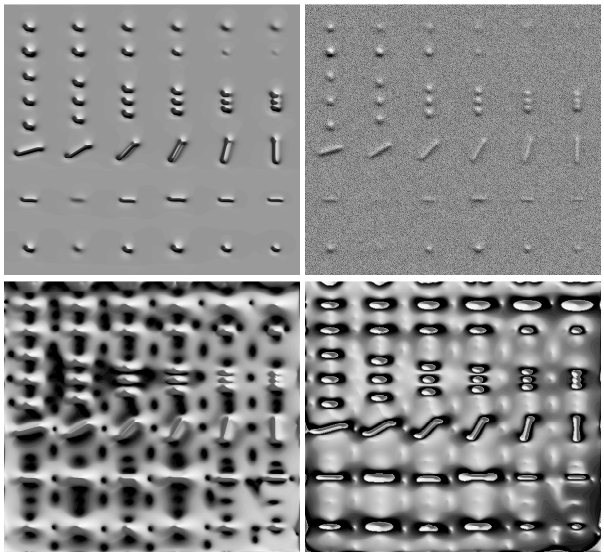

**Figure 2 VD of the TMI (Top Left) with noise added (Top Right), RTP_TDR (Bottom Left) & AREA (Bottom Right)**

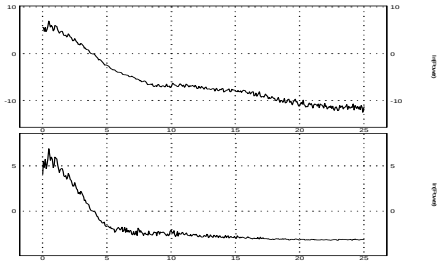

**Figure 3 Power spectra of the TMI (Top) & TMI with noise (Bottom)**

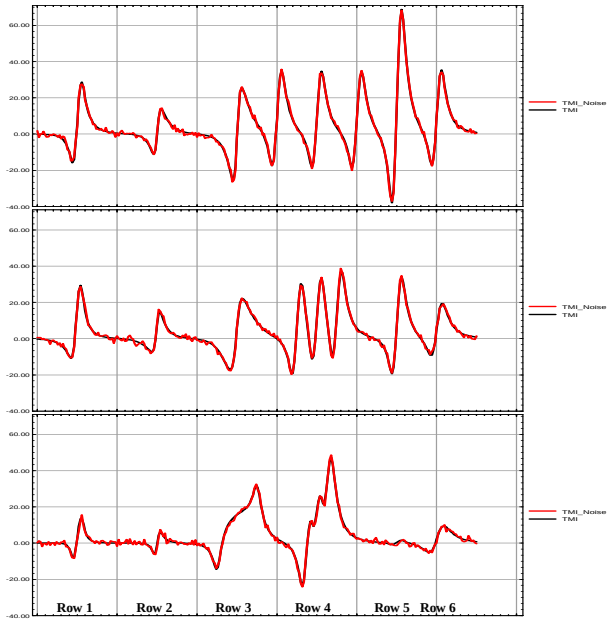


**Figure 4 TMI profiles with (Red) & without noise (Black) for Columns 1, 3 & 6**

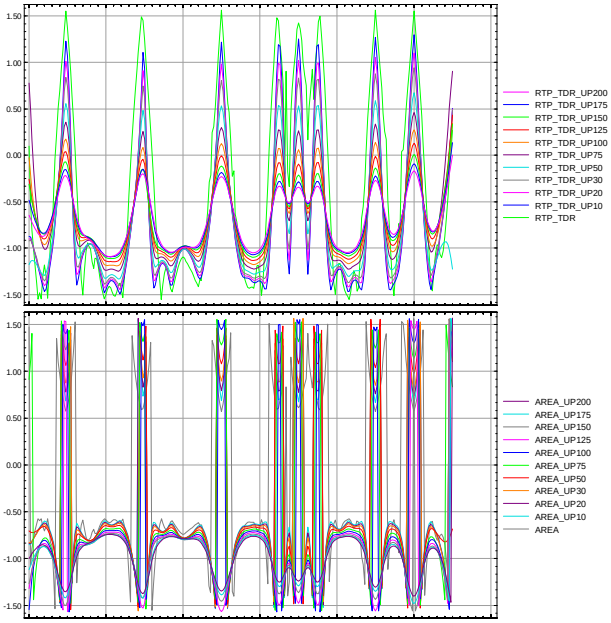


**Figure 5 RTP_TDR & AREA graphs for Column 3, depths of 0-200m are graphed**

The AREA filter can be equated to the local phase in some respects, but does not invert at the centre of the target, rather at the inflection points. As with the phase, there is a discontinuity in the AREA filter centred on 0, which implies it is either very positive or very negative with extremely large gradients separating these regions. The size of the positive region generated by the area filter reduces as the data is upward continued. At some point in the upward continuation the positive area vanishes and all values become negative. This "vanishing depth" is extracted for each column of cells in the array and a grid is created from these points (Figure 6). This grid is then queried at specific positions for depth. The positions found to be most useful are derived from the peaks of the analytic signal amplitude (ASA, also used for 3D Euler calculations). These positions correspond to the lateral centre of the body when the depth / width ratio is greater than 1, and to the edges when this ratio is 1 or below.

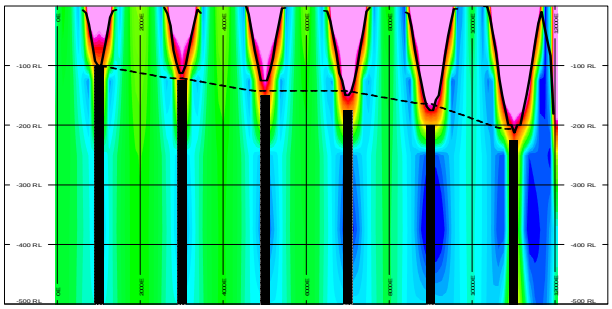

**Figure 6 A vertical section through Row 6 illustrating the positive "cones" formed by the AREA filter extending down to the causative bodies. The "vanishing depth" grid (Solid) and the final depth grid (Dashed) are overlain**

## RESULTS

The results of the various implementations of this method are presented within the set of graphs found at the end of the paper in Figure 9. Three implementations of this method are presented below:

1. MSDepth – the standard algorithm (centre position)
2. MSDepth_RG – designed as a response to the poor performance of the traditional algorithm in the case of added noise
3. MSDepth_E3D – positions derived from the peaks of the ASA (as with 3D Euler)

Also plotted are:

1. E3DDepth_SI1 – 3D Euler depth with a SI of 1
2. SPIDepth – SPI depth

The aim of MSDepth_RG implementation is to reduce the effect of the high frequency noise. This is achieved by conservatively, spatially low-pass filtering the RTP by the upward continued distance, for each elevation step before computing the TDR. This approach gave drastically improved results with scope for improvement by better defining the wavelength of interest. (Note: no attempt was made to de-noise the data before running 3D Euler) The SPI™ method also suffers from the presence of noise due to its dependence upon higher order derivatives. The SPI™ derived depth for Row 6 may be seen in the bottom left graph of Figure 9. It was computed in the case with noise, but no meaningful result was obtained and is therefore not shown. I intend to apply a similar approach to the SPI™ calculation in order to determine if any improvement can be achieved.

### Field Example

The method has been applied to a sample field dataset (Figure 7) and compared with results obtained from the 2D An-Euler method (Figure 8). Depths to magnetic causative across the region are expected at ~100m.

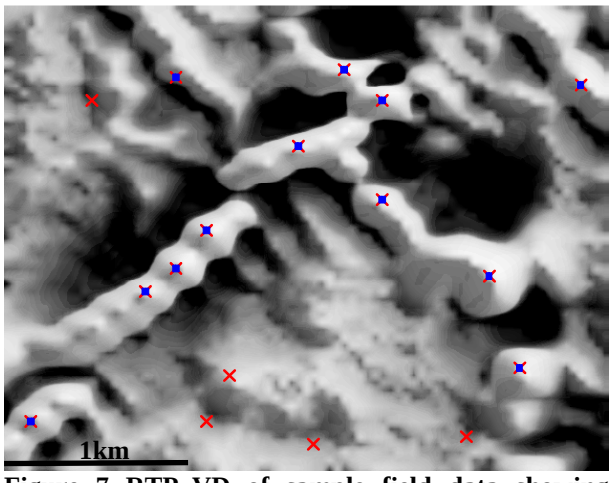


**Figure 7 RTP_VD of sample field data showing solution positions**

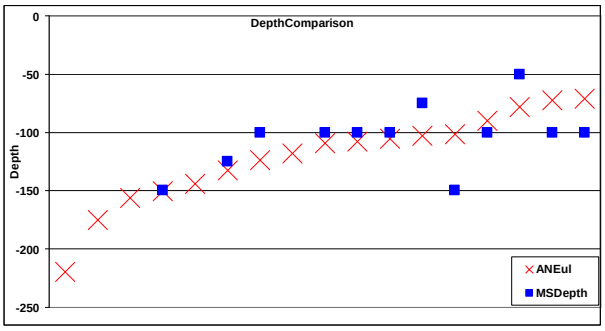


**Figure 8 Graph comparing An-Euler solutions to Multi-Scale depth results for positions shown in Figure 7**

## CONCLUSIONS

In general the Multi-Scale depth estimation method seems to work well. A few shortcomings were observed, one being the strong relationship to strike. This issue is related to a small (<1) depth / width ratio and is overcome by querying the depth surface at the ASA peak positions. The method is also sensitive to the depth extent of the causative. Thus, an improvement may be achieved by application to the vertical derivative which is an implementation to be investigated. Special attention should be given to the anomaly in Row 5, Column 6 seen in Figure 4. The Multi-Scale method has retrieved a satisfactory depth estimate (Figure 9) despite its extremely small signal / noise amplitude ratio. As mentioned, further investigation of the theory is required to justify the success of this approach.

## REFERENCES

Thurston, J. and Smith, R., 1997, Automatic conversion of magnetic data to depth, dip, and susceptibility contrast using the SPI ™ method: Geophysics Vol. 62, No. 3, 807 - 813.

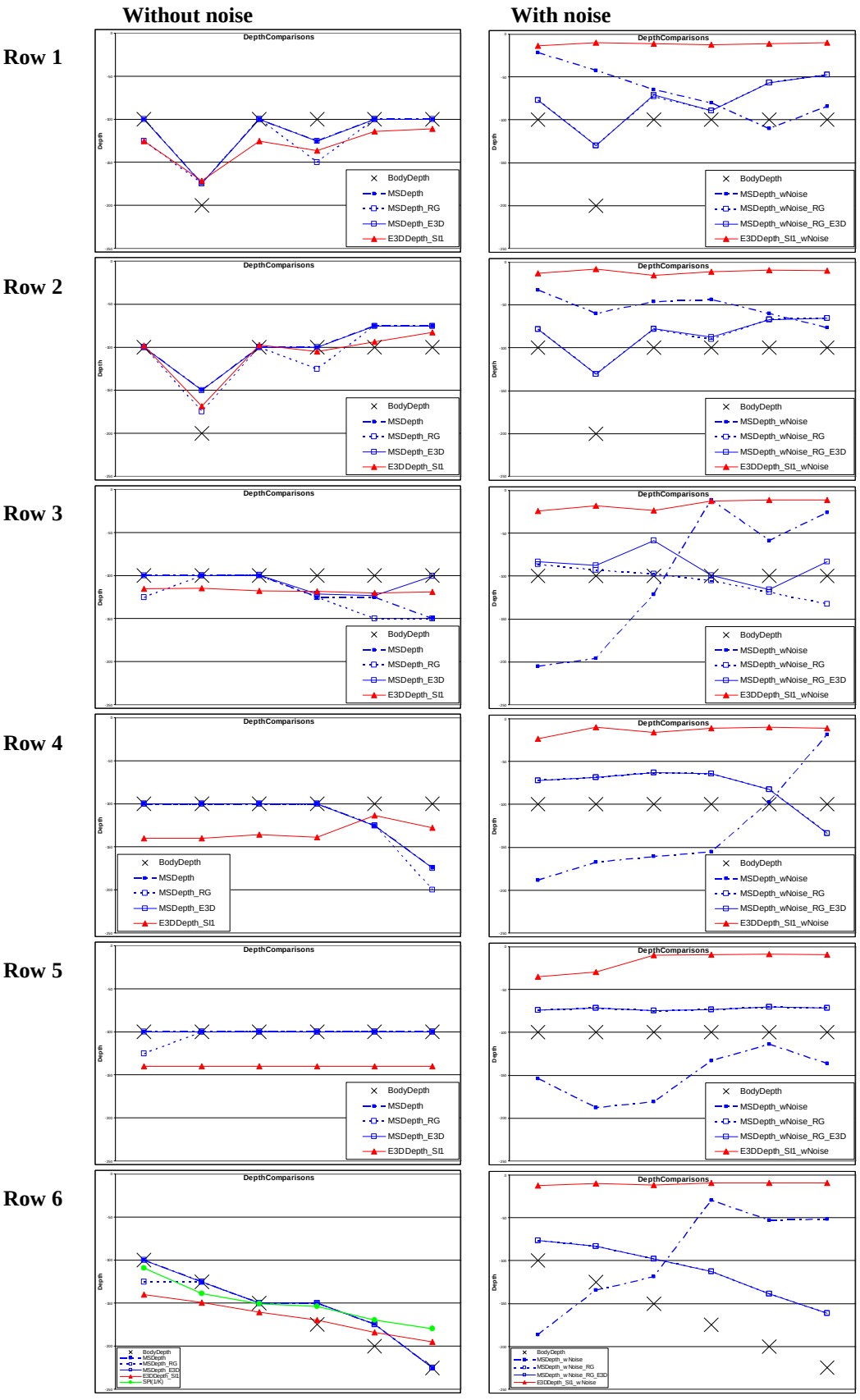


**Figure 9 Graphs showing depths derived from the various implementations of the Multi-Scale depth estimation, 3D Euler & SPI™ methods. Each "row" corresponds to a row in the X direction within the farm. The case without noise is presented on the left whilst the case with noise is on the right**

**Without noise**

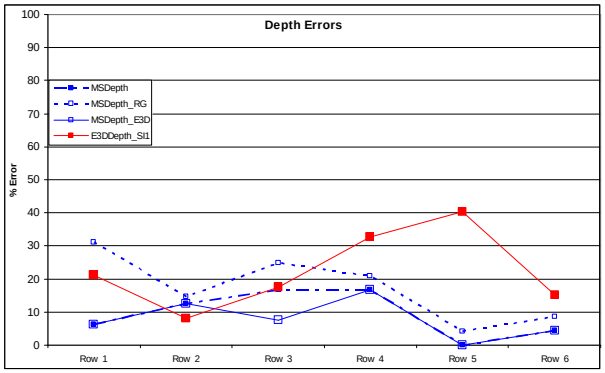


**With noise**

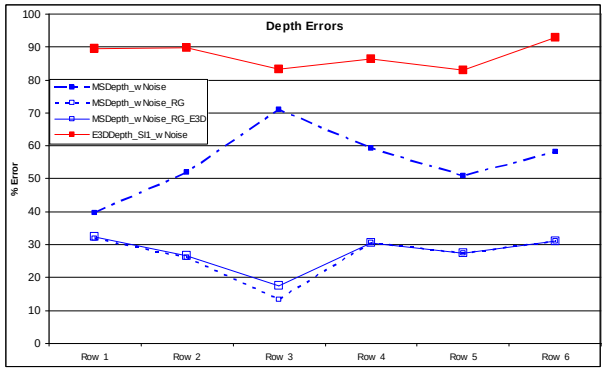


**Figure 10 Graphs showing the average % error in the depth estimates for the various rows of the farm, again, with and without noise**

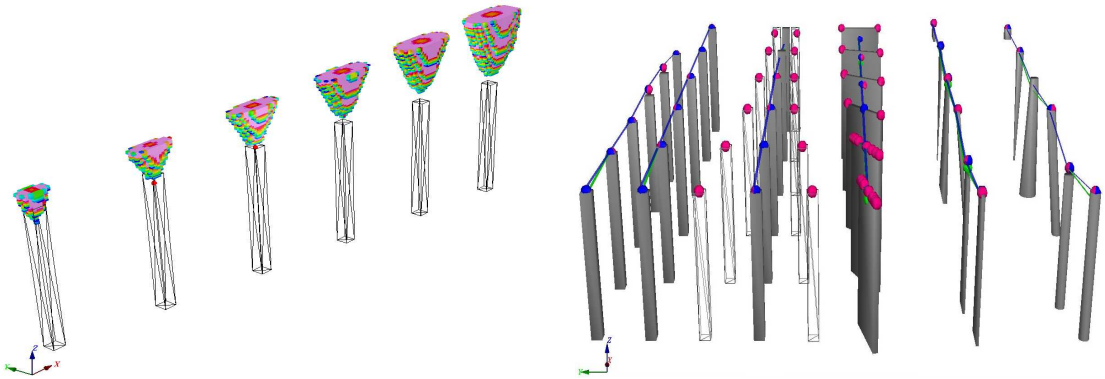

**Figure 11 Positive "cones" produced from AREA filter above causative bodies of Row 6 (Left), results obtained over the farm of bodies using the 3 differing implementations (Right, Blue – MSDepth, Green – MSDepth_RG, Pink – MSDepth_E3D)**